Improved Vehicle Dynamics Sensing during Cornering for Trajectory Tracking using Robust Control and Intelligent Tires

Anish S. Gorantiwar

Dissertation submitted to the Faculty of the
Virginia Polytechnic Institute and State University
in partial fulfillment of the requirements for the degree of

Doctor of Philosophy
in
Mechanical Engineering

Saied Taheri, Chair
John Ferris
Kaveh Akbari Hamed
Anuj Karpatne

August 4, 2023
Blacksburg, Virginia

Keywords: Fiala Tire Model, Lateral Dynamics, Vertical Dynamics, Intelligent Tires, Tire Tread Wear, Pneumatic Trail, Model Predictive Control

Improved Vehicle Dynamics Sensing during Cornering for Trajectory Tracking using Robust Control and Intelligent Tires

Anish S. Gorantiwar

(ABSTRACT)

Tires, being the only component of the vehicle in contact with the road surface, are responsible for generating the forces for maintaining the vehicle pose, orientation and stability of the vehicle. Additionally, the on-board advanced chassis control systems require estimation of these tire-road interaction properties for their operation. Extraction of these properties becomes extremely important in handling limit maneuvers such as Double Lane Change (DLC) and cornering wherein the lateral force transfer is dependent upon these computations. This research focuses on the development of a high-fidelity vehicle-tire model and control algorithm framework for vehicle trajectory tracking for vehicles operating in this limit handling regime. This combined vehicle-tire model places an emphasis on the lateral dynamics of the vehicle by integrating the effects of relaxation length on the contact patch force generation. The vertical dynamics of the vehicle have also been analyzed, and a novel double damper has been mathematically modeled and experimentally validated. Different control algorithms, both classical and machine learning-based, have been developed for optimizing this vertical dynamics model. Experimental data has been collected by instrumenting a vehicle with in-tire accelerometers, IMU, GPS, and encoders for slalom and lane change maneuvers. Different state estimation techniques have been developed to predict the vehicle side slip angle, tire slip angle, and normal load to further assist the developed vehicle-tire model. To make the entire framework more robust, Machine Learning algorithms have been developed to classify between different levels of tire wear. The effect of tire tread wear on

the pneumatic trail of the tire has been further evaluated, which affects the aligning moment and lateral force generation. Finally, a Model Predictive Control (MPC) framework has been developed to compare the performance between the conventional vehicle models and the developed vehicle models in tracking a reference trajectory.

Improved Vehicle Dynamics Sensing during Cornering for Trajectory Tracking using Robust Control and Intelligent Tires

Anish S. Gorantiwar

(GENERAL AUDIENCE ABSTRACT)

In our rapidly advancing world, self-driving or autonomous vehicles are no longer a vision of the future but a reality of today. As we grow more reliant on these vehicles, ensuring their safety and reliability becomes increasingly critical. Unlike traditional vehicles, self-driving cars operate without human intervention. Consequently, the onus of passenger and pedestrian safety falls squarely on the vehicle's control systems. The efficiency and effectiveness of these control systems are pivotal in preventing accidents and ensuring a smooth ride. One vital aspect of these control systems lies in understanding the tires' behavior, the only parts of the vehicle that are in contact with the road surface. A tire's interaction with the road surface significantly impacts the vehicle's handling and stability. Information such as how much of the tire is in contact with the road, the forces and moments generated at this contact point, becomes valuable for optimizing the vehicle's performance. This is particularly crucial when a vehicle is turning or cornering, where the forces developed between the tires and the road are key to maintaining control and stability. In this research, a framework has been designed to improve the vehicle performance, primarily by improving the modeling of tire lag dynamics. This refers to the delay or 'lag' between a change in tire conditions (such as pressure, wear, and temperature) and the corresponding change in tire behavior. In addition, in this research a vertical dynamics model of the vehicle has also been developed incorporated with a novel double damper suspension system. To complete the entire framework, the effect of tire wear over time and how this affects its performance and safety characteristics

has also been examined. By estimating and understanding this wear, we can predict how it will affect the dynamic properties of the tire, thus improving the reliability and efficiency of our autonomous vehicles. The last piece of this framework comprises the development of an MPC controller to track a reference trajectory and evaluate the performance of the developed model.

Dedication

This dissertation is dedicated to my parents and my sisters who have always stood by me, supported me and pushed me to achieve my goals no matter the circumstances.

"Nothing is invented, for it's written in nature first. Originality consists of returning to the origin" - Antonio Gaudi

Acknowledgments

First and foremost, I would really like to thank my advisor Dr. Saied Taheri for all his help throughout my time as a student at Virginia Tech. He not only helped me to obtain in-depth knowledge on tire mechanics and vehicle dynamics, but at the same time gave me a different perspective in analyzing various research topics. His thinking of '*to always think outside the box no matter the constraints*', really pushed me to explore different avenues of this research which otherwise I would not have even imagined. I would also like to thank all of my committee members, Dr. John Ferris, Dr. Kaveh Hamed Akbari, and Dr. Anuj Karpatne for their guidance and support throughout my research.

I would also like to acknowledge all my lab colleagues, both current and former, for their continuous guidance and support, especially Utkarsh, Karthik, Jyotirmoy and Shivam. Our discussions always helped me approach a solution and get a different perspective in solving the problem. I am also grateful to my friends, Mohit, Kushal, Anshul, and Diksha for helping me enjoy and cherish my time at Virginia Tech.

Finally, none of this would have been possible without my parents and my sister . Their belief in me is what pushed me to continuously expand my limits and strive toward excellence.

Contents

List of Figures

List of Tables

List of Abbreviations

$(\frac{CS}{FZ})$ Normalized derivative of longitudinal force with respect to the longitudinal slip

α Slip Angle

β Vehicle Side Slip Angle

γ Tire Camber Angle

μ Coefficient of Friction

ω Wheel Speed

σ Composite Slip Function

θ, ϕ CG Pitch and Roll Angle

a_{p0} Static Contact Patch Length

a_p Contact Patch Length

C_1, C_2, C_3, C_4 Passive Damping Coefficients

$F(\sigma)$ Composite Force Function

$F_{t1}, F_{t2}, F_{t3}, F_{t4}$ Tire forces at individual wheels

F_x Longitudinal Force

f_x Unit Longitudinal Force

F_y Lateral Force

f_y Unit Lateral Force

F_{zt} Tire Design Load

F_z Normal Load

K_1, K_2, K_3, K_4 Vertical Stiffness Coefficients of the Suspension System

K_c Lateral Stiffness

K_s Longitudinal Stiffness

L_f, L_r, t Distance from the front axle to vehicle CG, distance from rear axle to vehicle CG, vehicle track width

L_y Lateral Slip Relaxation Length

m_1, m_2, m_3, m_4 Unsprung Mass Values

M_s Sprung Mass Value

R_{re} Effective Rolling Radius

S Slip Ratio

T_p Tire Pressure

T_w Tire width

V_x Longitudinal Vehicle Speed

V_y Lateral Vehicle Speed

x_1, x_2, x_3, x_4 Sprung Mass Displacements

x_5, x_6, x_7, x_8 Unsprung Mass Displacements

x_b CG Displacement

Y_γ Tire Camber Coefficient

CenTiRe Center for Tire Research

CNN Convolution Neural Networks

DAQ Data Acquisition System

DD Double Damper

DL Deep Learning

DLC Double Lane Change

DYC Direct Yaw Control

ESC Electronic Stability Control

FNR False Negative Rate

GNB Gaussian Naive Bayes

GPS Global Positioning System

IMU Inertial Measurement Unit

IT Intelligent Tire

LiDAR Light Detection and Ranging

LSTM Long Short Term Memory

LTV Linear Time Varying

ML Machine Learning

MMPC Multi-constrained Model Predictive Control

MPC Model Predictive Control

MSV Mean Square Value

NNMPC Neural Network based Model Predictive Control

PDB Power Distribution Board

PID Proportional Derivative Integral

RGB Red Green Blue

RMC Rollover Mitigation Control

RMS Root Mean Square

RUL Remaining Useful Life

TPR True Positive Rate

Chapter 1

Introduction

This chapter introduces the proposed research and outlines the structure of the dissertation. Primary novel contributions along with journals and conferences published during the course of the research have also been listed.

1.1 Motivation

The automotive industry has been on a revolutionizing trend ever since the invention of the first gasoline engine power vehicle in 1879 [6]. The industry has taken huge strides, moving from these gasoline engine powered vehicles to electric battery-operated systems. This revolution has resulted in the total number of vehicles in the world reaching a staggering number of 1.446 billion, with an estimated of 19% of this within the United States alone [7]. To keep up with technological advancements and to ensure passenger safety, different on-board control systems have been implemented. These comprise of an array of safety systems ranging from Electronic Stability Control (ESC), Anti-lock Braking System (ABS), Direct Yaw Control (DYC), Rollover Mitigation Control (RMS), among others. The need for these control frameworks has become even more profound with the advent of autonomous vehicles.

With the development of Autonomous Vehicles (AV), it has become extremely important to improve existing vehicle models so that the AV would perform as closely to an actual human being driving the vehicle. Modules such as Advanced Driver Assistance Systems

(ADAS), which in itself comprises of a large array of safety features - lane departure warning, adaptive cruise control, etc. have received a big boost in the recent years [8]. For the optimal functioning of these systems, especially at abnormal operating regimes like limits of handling, it becomes of prime importance to properly understand the vehicle and tire dynamics.

As research into these fields grows, there is a shared opportunity to dive into the depths of this research. Existing research and architectures in this field are ultimately limited; they provide critical information about the dynamics of the vehicle and tire, but not across all operating regimes. Also, there is a need for a combined system that does the following:

- Combines the vehicle lateral and vertical dynamics with high fidelity tire models.
- Utilizing the tire as an active sensor of the vehicle and extracting tire-road interaction properties useful for developing the above models.
- Need of a tire health detection system to allow for implementation of different control strategies based upon the condition of the tire.

The purpose of this dissertation is to work towards achieving the above system and further expand the horizons of automotive control systems as the industry moves towards autonomous vehicles.

1.2 Dissertation Outline

The dissertation has been organized as follows:

- Chapter 1 and Chapter 2 provides a comprehensive review of different vehicle models and tire models focusing on vertical dynamics and vehicle lateral dynamics. Along

with this, an extensive review on tire wear and defect monitoring is also presented. These chapters also provide an insight on different control algorithms used at the limit handling performance of the vehicle and also sheds some information on the concept of the "Intelligent Tire Technology".

- Chapter 3 has been divided into three broad sections. In Section 3.1, a high fidelity modified Fiala tire model and an STI tire model have been developed focusing on the higher slip angle operating regime. A comparative analysis has been drawn between the two models via simulation tools such as CarSim and Simulink. Section 3.3 discusses the development of an 11-DoF vertical dynamics model for analyzing the vehicle pose and orientation along the vertical axis. Section 3.4 discusses the development and testing of a 5-DoF lateral dynamics model encompassing the effects of relaxation length and tire lag dynamics into the model.

- Chapter 4 comprises of three broad sections. The first section describes the mathematical modelling of a novel "Double Damper" system to analyze the road holding and ride comfort characteristics of the damper. Different control algorithms have been implemented and compared with conventional passive and semi-active monotube dampers. In the second section, the model has been validated via in-house run experiments on a Shock Dyno setup. Finally, Science Guided Machine Learning (SGML) based control algorithms have been developed to further improve the performance of this double damper.

- Chapter 5 details the instrumentation of the vehicle with different proprioceptive and exteroceptive sensors to collect both tire and chassis motion data. Along with this, the development of a scaled UGV platform for testing different control algorithms has also been discussed. Finally, the last section of this chapter talks about the development of an in-house test rig for Structure Health Monitoring (SHM) which has been further

extended for tire defect and wear monitoring analysis.

- Chapter 6 discusses the different data processing techniques used in time domain to analyze the tire accelerometer, IMU, and encoder data. Along with this, different state estimation techniques have been developed in this chapter to estimate the tire slip angle, vehicle side slip angle, and dynamic normal load.

- Development of a framework for defect type and intensity classification has been discussed in Chapter 7. This framework comprises of different time-domain and time-frequency domain-based features which have been fed to different supervised Machine Learning (ML) classification algorithms. This framework has been first tested on a classifying between different defects on a machine bearing and later extended to classifying between a new tire and a worn out tire.

- Chapter 8 discusses the development of analytical and data-driven models to estimate the pneumatic trail of the tire. Along with this, the effect of tire wear on the pneumatic trail has also been analyzed via the "intelligent tire" setup.

- Chapter 9 discusses the implementation of an MPC algorithm for trajectory tracking of the vehicle using the new vehicle-tire plant model. The primary objective of this chapter is to compare the performance between existing vehicle models and the developed vehicle model in tracking a reference trajectory.

- Chapter 10 summarizes the work which has been presented so far in this dissertation. This chapter lays out the significant results of each system - vehicle model, tire model, vertical dynamics model, state estimation and tire health monitoring. Along with this, the chapter also comprises of the future work which can be conducted considering this research as the foundation.

1.3 Dissertation Contributions

The primary contributions of this dissertation are as follows:

- Development and enhancement of the Fiala Tire Model combined with a relaxation length fused 5-DoF vehicle model for analyzing the lateral dynamics of the vehicle during cornering.
- Modeling and experimental validation of a novel double damper semi-active suspension system combined with an 11-DoF vertical vehicle dynamics model. Along with this, a Science Guided Machine Learning (SGML) based control algorithm framework has also been developed and compared against existing control architectures.
- Development of an experimental setup and test matrix on an instrumented VW Jetta to perform a slalom maneuver at the limits of vehicle handling.
- Development of a tire-health detection system, focusing on tire tread wear, using time domain based data processing methodologies and Deep Learning algorithms.
- Development of a framework to analytically and experimentally estimate the pneumatic trail of a tire and its relationship with the tire tread depth.

1.4 Publications, Patents and Awards

The following publications, patents and competition awards have been achieved during the process of this research:

- Anish Gorantiwar, Utkarsh Gupta, Saied Taheri. Intelligent Tire-Based Tire Wear Estimation and its Effect on Pneumatic Trail. *Tire Society 2023 - Submitted*

- Utkarsh Gupta, Anish Gorantiwar, Saied Taheri. Vehicle Suspension Control using Physics Guided Machine Learning *IEEE HORA 2023*

- Anish Gorantiwar, Utkarsh Gupta, Saied Taheri. Real Time Tire Wear Detection using Intelligent Tires. *ASME IMECE Conference 2023* - Accepted

- Anish Gorantiwar, Saied Taheri, Bijan Moslehi, and Feraidoon Zahiri. Real Tire Bearing Defect Classification using Time Domain Analysis and Deep Learning Algorithms. *SAE Technical Paper SAE WCX 2023*

- Anish Gorantiwar, Mohit Shenvi, Corina Sandu, Saied Taheri. Vibration Characteristics and Control Algorithm for Semi-Active Suspension of Space Exploration Vehicles. *Noise and Vibration Conference Exhibition - Low Frequency NVH- Body - Chassis Structure and Components, 2023*

- Anish Gorantiwar, Rajvardhan Nalawade, Arash Nouri, Saied Taheri, Vahid Sotoudeh, William Price, and Feraidoon Zahiri. Fiber Optic Sensor System for Defect Classification using Novel Physics based Modelling and Data Driven Approach. *IEEE Aerospace Conference 2022*

- Rajvardhan Nalawade, Arash Nouri, Utkarsh Gupta, Anish Gorantiwar, and Saied Taheri. Improved Vehicle Longitudinal Velocity Estimation Using Accelerometer Based Intelligent Tire. *39th Annual Business Meeting and Conference on Tire Science and Technology, 2022*

- Saied Taheri, Anish Gorantiwar, Rajvardhan Nalawade, Arash Nouri. Automotive double damper suspension system. *US Patent: US20220410646A1, 2022*

- Anish Gorantiwar, Rajvardhan Nalawade, Arash Nouri, and Saied Taheri. Experimental analysis of a novel double damper system with semi-active control. *Electronics,*

9(9):1518,2020.

- Anish Gorantiwar, Jyotirmoy Mukherjee, Saied Taheri - Tire Wet Traction Improvement using Intelligent Tires, *Monte Jade Innovation Competition 2020 - 2nd Place Winners*

- Anish Gorantiwar, Utkarsh Gupta, Saied Taheri - Tire Wear Detection using Intelligent Tires, *Monte Jade Innovation Competition 2022 - 2nd Place Winners*

- Anish Gorantiwar, Jyotirmoy Mukherjee, Arash Nouri, Sunish Vadakkeveetil, and Saied Taheri, Measuring Tire Contact Mechanics Parameters for Intelligent Vehicle Applications. *Cornell Cup - Arm Embedded Competition - Semi-finalists 2019*

- Anish Gorantiwar, Saied Taheri, Improved Vehicle Dynamics Sensing during Cornering for Optimized Motion Planning using Robust Control and Intelligent Tires. *Walter O'Brien Graduate Student Symposium, Virginia Tech, 2022*

Chapter 2

Review of Literature

2.1 Tire Modelling

2.1.1 Tire Construction

Tires, being the only component of the vehicle in contact with the road surface, play a crucial role in terms of deciding different vehicle dynamic properties at the contact patch - lateral and longitudinal forces, slip angle, aligning moments and torque amongst others. Therefore, it is of prime importance to accurately model the tire to ensure that the correct force input can be given to the vehicle model. Before analyzing different types of tire models, it is necessary to understand the construction of pneumatic tires and how each component operates on a system level [9, 10]. Figure 2.1 shows a typical schematic diagram of pneumatic tire construction.

Some of the key components of the tire and their effects on contact patch properties have been listed below

- Tread: The tire tread is one of the crucial parts of the tire responsible for providing the traction force as well as road holding properties of the vehicle.
- Sidewall: The sidewall protects the cord plies of the tire and forms an essential element for lateral force generation. The phenomenon of ”relaxation length” is brought by the

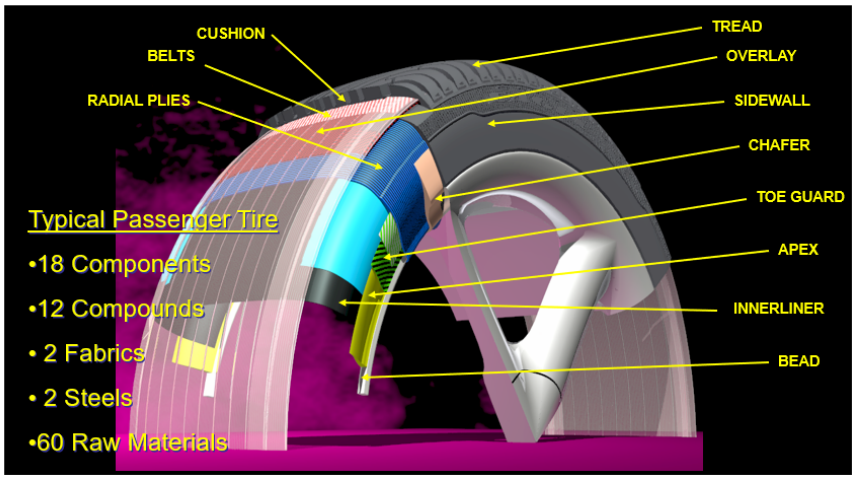

Figure 2.1: Tire Construction [1]

tire sidewall and its thickness decides the compliance of the tire during turning.

- Shoulder: The tire radial plies play a crucial role in determining the rolling resistance, durability and the resistance to the tread wear of the tire.

- Mold shape: The mold shape of the tire can be characterized by the tire crown radius. For a given value of normal load, a tire having a flat crown will have greater footprint area as compared to that of tire having a round crown. Flatter crown increases the tire stiffness resulting greater footprint area.

- Overlay: Overlay is basically an addition rubberized cords circumferentially over the top of belts and below treads to prevent tread separation. For a given value of normal load and longitudinal speed, addition of an overlay makes the footprint shape more rounder.

- Belt Stiffness: Tire belts are rubber-coated layers of steel, and other materials between the tire tread and plies, crisscrossing at angles, having the function of holding the plies in place. For a given sidewall stiffness, a soft belt has a wider footprint as compared to a stiffer belt.

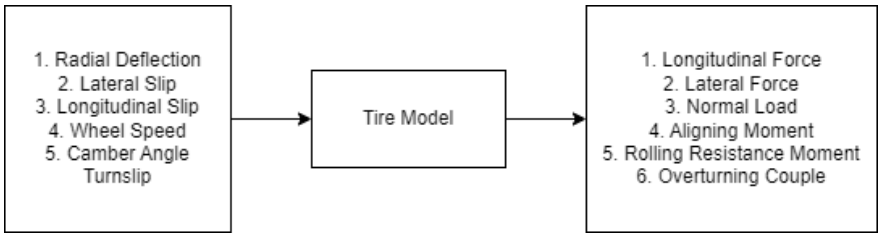

Figure 2.2: Tire Model Input Output Relationship

Based upon the above summarization of some of the key tire components, the next step comprises of modelling the tire to determine the forces transmitted to the vehicle chassis.

2.1.2 Tire Modelling Methodology

As discussed in Section 2.1.1, the primary function of the tire is the transmission of forces from the road to the vehicle chassis. Along with this, the tire itself has its own stiffness and damping properties which directly affects the vertical dynamics of the vehicle in terms of its ride comfort and road holding characteristics. These material properties of the tire also affect the tread wear and deformation of the tire across different cross-section areas. To analyze each one of these phenomena, a mathematical model of the tire is required. Figure 2.2, derived from [2], shows the input parameters to be fed into the mathematical tire model for getting the forces and the moments transmitted to the chassis.

Taking all of these parameters into consideration, different steady state, dynamic, semi-empirical, Finite Element Analysis (FEA)-based and transient tire models have been developed. Figure 2.3 shows the four categories of possible approaches to modeling the tire.

The tire models can also be classified based upon which part of vehicle dynamics they focus on. Table 2.1 summarizes these tire models.

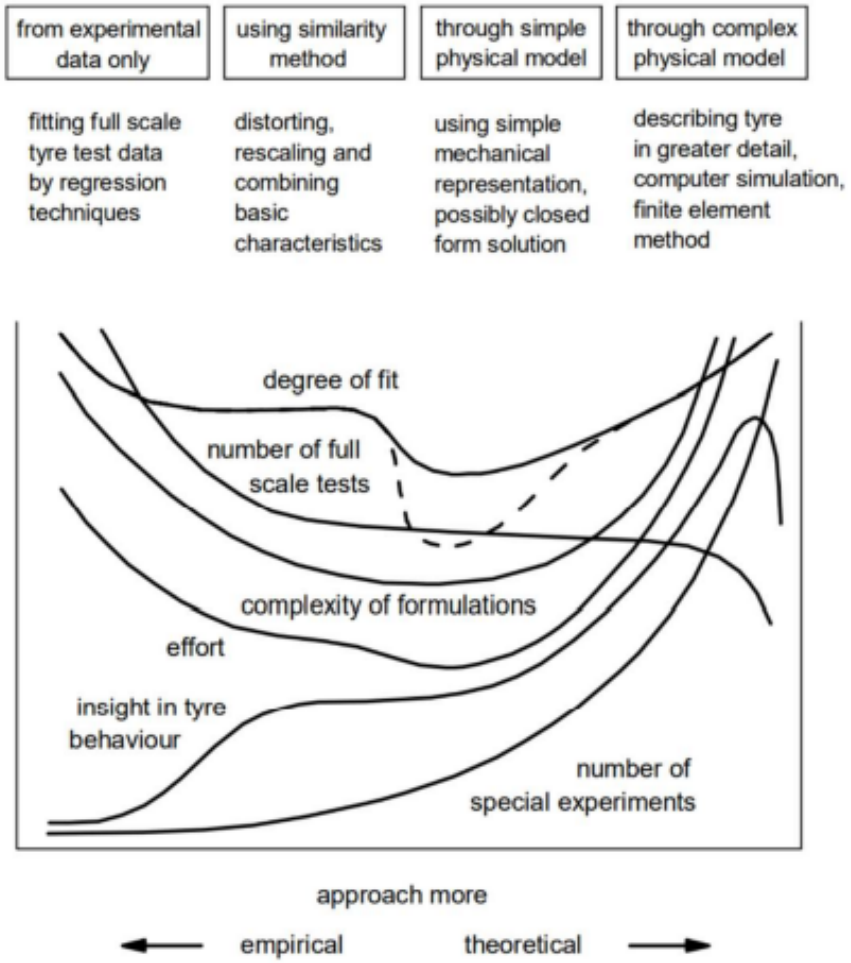

Figure 2.3: Tire Model Classification [2]

Table 2.1: Tire Models Classification based upon vehicle dynamics

Parameter	**Tire Models**
Handling Models	Dugoff Model
-	STI Model
-	Brush Model
-	String on Elastic Foundation Model
-	Pacejka Model
Ride Models	Point Contact
-	Roller Contact Model
-	Rigid Ring Model
-	Flexible Ring Model
Traction Models	LuGre Model

Steady State Tire Models

The steady state tire models, as described in [11], are valid for those conditions wherein the input parameters - tire slip angle, vehicle load, and vehicle speed have minimal variations. These models are extensively used in simulations as well as in real-time applications because of their less complexity and being computationally inexpensive. Pacejka (Magic Formula) Tire Model and TMeasy tire model [12, 13, 14] fall in this category.

The general formulation of the Pacejka Tire Model is shown in Equation 2.1.

$$y = D\sin[C\arctan[(1-E)*Bx + E\arctan(Bx)]] \tag{2.1}$$

where: B = Stiffness Factor

C = Shape Factor

D = Peak Value

E = Curvature Factor

S_h = Horizontal Shift

S_v = Vertical Shift

x = Input variable: Longitudinal slip or tire slip angle

Y = Output variable: Lateral or longitudinal force

Similarly, the general formulation of the TMeasy tire model is given by Equation 2.2.

$$F(s) = \begin{cases} \mathrm{s}^M dF^0 \frac{\sigma}{1+\sigma(\sigma+dF^0\frac{s^M}{F^M}-2)}, & \text{if } \sigma = \frac{s}{s^M}, 0 \leq s \leq \mathrm{s}^M \\ \mathrm{F}^M - (F^M - F^S)\sigma^2(3-2\sigma), & \text{if } \sigma = \frac{s-s^M}{s^S-s^M}, \mathrm{s}^M \leq s \leq \mathrm{s}^S \\ \mathrm{F}^S, & \mathrm{s} \gg \mathrm{s}^S \end{cases} \tag{2.2}$$

Transient State Tire Models

The transient response tire models are required for for transient events such as slalom maneuvers and double lane change maneuvers. The primary reason for this is the effect of lag in the longitudinal and lateral force generation of the tire. These lags need to be modelled by a first order equation governing the relaxation length of the tire [15, 16, 17]. The transient tire models are much more accurate in determining the forces and the moments at the contact patch but are computationally expensive. Brush Tire model [18, 19] and LuGre tire model [20, 21] are some of the extensively used transient tire models

2.2 Vertical Dynamics

The automotive suspension system plays a crucial role in maintaining the vehicle dynamics of the car for changes in road input and variations in the normal weight distribution. An effective suspension system ensures passenger ride comfort for unpredictable input variations, and allows a sufficient amount of tire-road contact for proper road handling. Damper design and analysis is the most pivotal part when analyzing any suspension system. There are three commonly used suspension systems-passive, semi-active, and active with each one having its advantages and limitations over the other. Conventional passive suspension systems come with the inherent limitation that they cannot cater to both road-holding and ride comfort at the same time. For example, a soft suspension system may be better at providing ride comfort but will not perform as well in handling as compared to a harder, stiffer suspension and vice-versa [22]. A numerical simulation study conducted by [23] also shows that for obtaining the best performance from any particular type of suspension for a spectrum of different operating conditions such as road undulations, vehicle speed variations, and fixed working space, requires the adjustment of suspension parameters through wide ranges.

Active suspension systems affect the changes in the system by altering the damping coefficient of the vehicle suspension with the help of hydraulic or electric actuators, thereby applying an external force to the system [24]. These controlled external forces alter the ride and handling characteristics of the system in real-time. Due to the external forcing element, these active systems are expensive and require a complex setup. These controlled forces help in modifying the ride and handling characteristics at every instant in real-time. A study performed by Xue et al. [25] compared the four different configurations of suspensions systems-passive, semi-active, hydraulic, or pneumatic active and electromagnetic active. They concluded that even though the hydraulic active suspension systems have slightly better ride comfort and handling characteristics, it comes with inherent drawbacks of having a complex structure and a very high cost. Along with this, the use of different control algorithms for semi-active dampers has increased their reliability over the active suspension systems. These advantages of semi-active dampers have justified their use for commercial vehicle applications [26, 27, 28].

Semi-active suspension systems lie between passive and active in terms of performance, cost, and complexity. They can vary the damping characteristics by either using a variable orifice [29] or variable viscosity fluids [30, 31]. Variable orifice semi-active suspension systems use a position control valve to adjust the orifice area through which the damper fluid flows [32]. This variation in orifice area is directly proportional to the damping coefficient, which in turn varies the force transmitted to the vehicle chassis. Variable fluid viscosity semi-active dampers, on the other hand, make use of Electrorheological (ER) or Magnetorheological (MR) fluids to vary the damping force. When subjected to a magnetic field, the MR fluids change their properties and act as a semi-solid material, thus altering the damping properties of the damper [33].

Sabino et al. [34] used a Magne-Ride Delphi damper, which is an MR damper for testing

three specific control algorithms; on-off Skyhook control, continuous Skyhook control and Skyhook algorithm based fuzzy logic control. However, these MR dampers have inherent limitations of particle settling within the damper, causing abrasions. These abrasions along the inner wall of the damper may lead to wearing damper material resulting in decreased life.

Peng et al. [35] also made use of MR dampers for semi-active suspension control using Skyhook Control. They used a B class vehicle and replaced the conventional four hydraulic dampers with MR dampers and utilized eight accelerometers—four for sprung and four for unsprung mass accelerations. They were able to reduce the peak vertical acceleration of the driver's seat to 0.32 g. Tang et al. [36] developed a state-observer based fuzzy controller for a MR damper. The validation of the algorithm was done on a quarter car test rig which had provisions for collecting the sprung and unsprung mass acceleration data.

Krauze et al. [37], along with using accelerometers, also made use of Linear Variable Differential Transformer (LVDT) for measuring the vertical deflection of the suspension on an instrumented All-Terrain Vehicle. They used a sampling frequency of 500 Hz and frequency of excitation between 1.5–12 Hz. An important conclusion derived was that accelerometer-based velocity estimation gave better results for Skyhook Control, whereas, the Groundhook control performed better with LVDT based measurement methods. Gong and Chen [38] implemented variable damping control strategy on a variable orifice damper. They essentially made use of displacement sensors as a feedback unit upon which the variable damping control strategy was based. A reduction in the body, roll and pitch angle accelerations were found in comparison with a passive damper.

Different controlling methods have been extensively researched and developed for controlling the suspension damping coefficient. These methodologies are essentially Hardware-in-the-Loop (HIL) systems in which the damping coefficient is varied by varying the orifice area through which the fluid passes. The control algorithms have an objective function of reduc-

ing the sprung mass displacement and improving the vertical vehicle dynamics. Skyhook-Groundhook [39, 40, 41] is one of the most studied algorithms which take into account the unsprung and sprung mass velocities to reduce the displacement. Similarly, algorithms such as Acceleration Driven Damper [42] and Power-Driven Damper [43] are used to improve ride comfort and road holding. However, all these algorithms are data-driven approaches in which the dynamics of the system are not captured. Hence this field has now evolved into hybrid systems with Physics Guided Models as the backbone of the system architecture. [44]

Such a physics guided approach is gradually entering the vehicle dynamics phase with more and more efforts being put into developing an accurate model encompassing all the dynamics of the system. One such published work talks about the development of structured, unstructured, and recurrent neural network models combined with the time-invariant vehicle models to estimate the longitudinal dynamics [45]. A similar modeling approach can be seen in [46] in which physics-based models have been developed to track a vehicle path up to its friction limits.

2.3 Intelligent Tire Technology

As discussed in Section 2.1, measurement of tire forces and moments is key in determining the dynamics of the vehicle. There are two approaches to gather the relevant tire-road contact information. The first approach comprises of the development of physics based and semi-empirical mathematical models as discussed in Section 2.1.2. These models tend to be computationally and time expensive when it comes to real-time deployment. Along with this, the initialization of these models required an extensive parameter estimation. In order to overcome this, the concept of ”Intelligent Tire Technology” is used in conjunction with the tire models to improve the computation time.

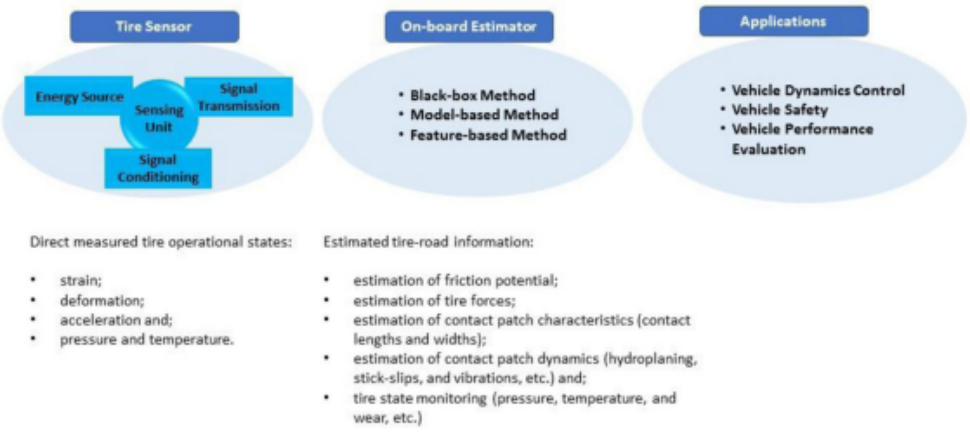

Figure 2.4: Tire Sensor System Structure [3]

An extensive review on the concept of intelligent tires and tire characterization has been discussed in [47]. A similar review has been conducted by [3, 48], wherein the use and the potential of in-tire sensors for vehicle control system development has been discussed. Figure 2.4 shows the overall structure of the intelligent tire system comprising of the in-tire sensor, different state estimation algorithms and its corresponding applications.

Intelligent Tire Technology essentially comprises of having different optical and vibration sensors mounted inside the tire for collecting tire-road interaction data. The primary objectives of any of these sensor systems is the following [49]:

- The sensors in itself should not vary the tire-road interaction properties: should have low mass values and minimal interference with the tire construction.
- Should be robust in construction.
- The sensitivity and the resolution of the sensor should be low enough to get important tire-road data at different frequencies.

Keeping these under consideration, the literature for intelligent tires comprises of an array of sensors used. Yilmazoglu et al. [50] used magnetic field sensors to get the tire-road in-

formation. Pohl et al. [51] and Zhang et al. [52] utilized wireless passive Surface Acoustic Wave (SAW) sensors to get the tire deformation as well as the tire pressure-temperature data. Optical sensors utilizing photo-diode surface resistance have also been used to measure tire carcass deflections [53]. These sensors are mounted on the tire rim rather than on the inner-lining of the tire for recording the measurements.

With advancements in the size, measuring range, and the resolution capabilities, accelerometers have also been used as the in-tire sensors [49, 54]. Accelerometers have an added advantage of measuring the tread deflections in all the three directions allowing for getting more indirect measurements in terms of aligning, rollover and pitching moments.

2.4 Structural Health Monitoring

2.4.1 Bearing Defect Analysis

Condition based maintenance (CBM) is a maintenance strategy which essentially suggests maintenance decisions based on the information collected through health monitoring. This information is collected through an array of sensors both exteroceptive - which give information of the surrounding relative to machine body and proprioceptive - which give information regarding the machine itself.

Two important aspects of CBM lie in defect classification and Remaining Useful Life (RUL) estimation which essentially corresponds to structural health monitoring and machine prognosis [55]. Rolling element bearings play a crucial role in various mechanical engineering assemblies ranging from small gearboxes to heavy industrial equipment. A defect in any portion of the bearing may result in the overall breakdown of the machine and hence it is of prime importance to detect these defects early during the machine operation. In order to

sense these vibration signals, different sensors can be used, the selection of which depends upon various parameters such as frequency range, resolution and the required sensitivity amongst others.

In [56], piezoelectric based accelerometers along with a load cell have been used for bearing defect classification via time and frequency domain features. To overcome the inherent frequency range limitation of accelerometers, Fiber Bragg Gratings (FBG's) have just being started to use for condition health monitoring.

In [57], a review consisting of an experimental setup comprising of a network of FBG sensors for temperature and strain monitoring is discussed. The sensors also provide information on the loading and traffic status of the passenger cars, temperature-induced stresses and deformations on rails and carriages, dynamic axle vibrations due to corrosion and bearing wear, and other parameters relevant to rail road health monitoring. A key outcome of this work is that the FBG sensors can easily capture high frequency dynamic strains.

For defect classification, different approaches have been considered which make use of time, frequency and time-frequency domain features, to extract meaningful information from the vibration data ([58, 59, 60]).

Researchers in [61] extracted time domain based statistical features from the vibration signals and trained multi-class Support vector Machines (SVM's) to classify between the different bearing defects. In accordance with this, Jack and Nandi [62] developed Artificial Neural Networks (ANN's) combined with genetic algorithms to select the most significant input parameters from a larger set of input features for bearing defect monitoring.

In [63], statistical features from time and frequency domains were used in combination with Hilbert transforms to get a feature matrix and further using Principal Component Analysis (PCA) for dimensionality reduction. This approach extended further from the previous work

wherein features from both domains were used and a Fuzzy C-means clustering method to determine the classification efficacy.

In a study [64], degradation signals considered focused on the evolution of the Root Mean Square (RMS) vibration level over time. This information was then used to train neural network models on predicting bearing operating times. The proposed methodology in [65] uses time domain features extracted from vibration signals as health indicators. The degradation states in bearings are detected by an unsupervised classification technique called artificial ant clustering. The imminence of the next degradation state in bearings is given by hidden Markov models, and the estimation of the remaining time before the next degradation state is given by the multi-step time series prediction and the adaptive neuro-fuzzy inference system.

Studies have also been conducted in using time-frequency domain based approach by utilizing wavelets for feature extraction. In [66], the authors show the use of complex wavelet analysis for feature extraction and further developing SVM and ANN for bearing defect classification. Research has also been carried out in defect identification in gears by using genetic algorithms for selecting the optimum mother wavelet and carrying out comparison studies between different wavelet types([67, 68, 69]).

Along with using standard machine algorithms, Convolutional Neural Networks (CNN's) have also been used to identify different types of bearing faults. Vibration data acquired from accelerometers have been stacked together to form 2-D matrices and then passed to different convolution and pooling layers. Use of scaled-Fourier Transforms and adaptive CNN's have also been developed for better feature extraction and classification([70, 71, 72, 73].

The final step for bearing health detection and classification comprises of determining the algorithm efficiency in a real-time environment. For this, it is of prime importance to have

computationally faster algorithms, robust hardware, and data collection systems [74, 75].

2.4.2 Tire Wear/Defect Modelling and Analysis

The field of tire wear has been studied primarily for two reasons, understanding its effect on the vehicle performance and for the enhancement of vehicle-road safety. The effect of tire wear on the dynamics of the vehicle can be seen in terms of the lateral, longitudinal forces and the aligning moment generated at the contact patch [76, 77]. Tires undergo wear continuously and this effect becomes even more profound while operating the vehicle at constant limits of handling. This results in the formation of different types of wear patterns such as feathered wear, spotty wear and camber wear [4]. Figure 2.5 shows some of the tread wear patterns. The wear of the tire is indicated by the amount of tread depth the tire has at every instant. Different experiments have been conducted on on-road vehicles equipped with tires of varying ply thickness, crown radius, sidewall depth, etc. [5]. Figure 2.6 shows the nonlinear dependence of the tread wear on the amount of miles the vehicle has run. Based upon this graph, the wear period of the tire can be broadly classified into three distinct zones: wearing-in zone, stable wear zone and critical wear zone. The effect of wheel slip, tire stiffness, and the local stress generation at the contact patch on tire wear has also been extensively studied through experimental testing [78, 79, 80].

Tire wear can be broadly classified into four main categories depending upon its interaction with the road surface:

- Adhesive Wear
- Abrasive Wear
- Fatigue Wear

Figure 2.5: Tire Wear Patterns [4]

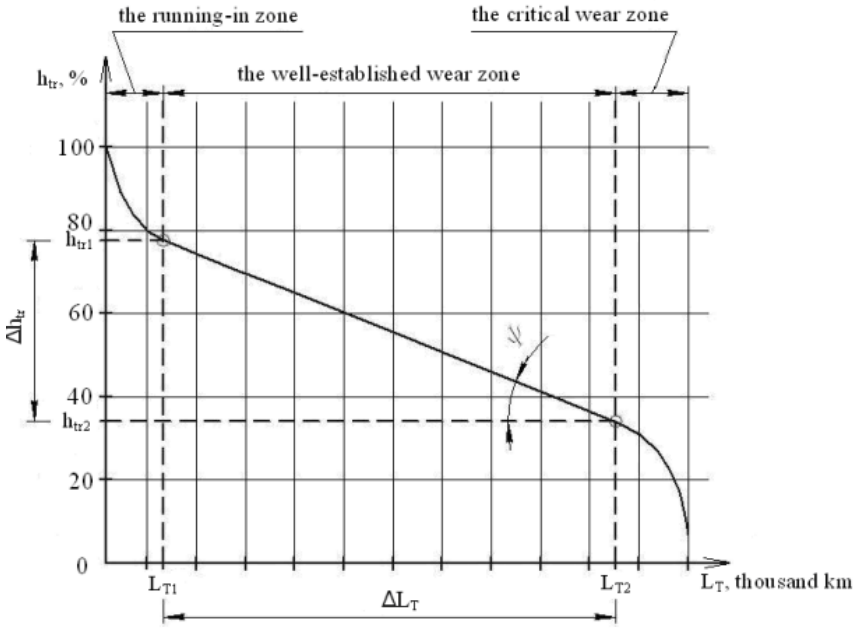

Figure 2.6: Tread Pattern Height dependence of tire life [5]

- Chemical Wear

Each of the above wear categories can be modelled either through math-based physical models or via experimental techniques.

Archard's wear model is one of the simplest and computationally easy model for tire wear analysis [81]. The amount of wear given by this model can be characterized by Equation 2.3.

$$Q_w = K * \frac{F_n S}{H_w} \tag{2.3}$$

where: Q_w = Amount of tire wear

H_w = Material Hardness

F_n = Total Normal Load

S = Sliding Distance

K = Probability Factor typical of the combination of materials used

Advancements have been made to the Archard's model to take into account the directional effects of the tire wear [82]. Similarly wear models have also been developed by considering the thermal and the frictional effects between the two sliding surfaces [83]. The authors in this paper discussed the effects of the reduced tread thickness, decreased strain energy loss and dissipative tread volume on the performance of the vehicle.

In order to have a real-time on-vehicle board tire wear detection systems, the concept of intelligent tires is being used. In [84], in-tire accelerometers have been used to detect cracks of various sizes within the radial tires and have been corroborated via FEA simulations. Similar to using accelerometers inside the tire, tread deflection measurement sensors have also been used to estimate the tire-road friction coefficient and further compute the wear of

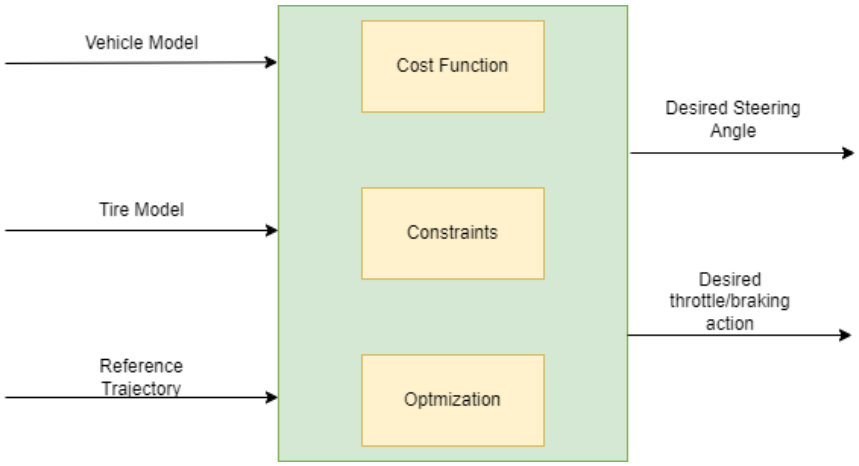

Figure 2.7: High Level Diagram for Trajectory Tracking Framework

the tire [85, 86].

2.5 Trajectory Tracking Control Algorithms

Trajectory tracking or path-following control algorithms are typically created to ensure that the vehicle follows a preset course and trajectory by determining and calculating the necessary actuation inputs for the vehicle to follow. This can be a correctional steering input to modify the vehicle's lateral position or a correctional brake or throttle setting to adjust the vehicle's longitudinal motion. Figure 2.7 shows a general overview of trajectory tracking control algorithms. The desired vehicle trajectory, the vehicle dynamic response variables, and the tire forces and moments are generally considered as inputs to these control algorithms.The output corresponds to the desired steering angle to track the reference trajectory along with the desired throttle/braking action.

Amer et al. [87] has summarized the framework of trajectory tracking control algorithms. Different vehicle models - kinematic and dynamic, full vehicle and half vehicle models which can be used as the plant in the trajectory tracking framework have been described. Along

Table 2.2: Overview of different trajectory tracking control algorithms

Control Strategy	Examples
Classical Control	PID and Sliding Mode Controllers (SMC) [88]
Geometric Controller	Stanley [89] and Pure Pursuit control [90]
Optimal Control	Full state feedback, LQR control [91]
Model Based	MPC, NMPC, Contingency MPC
Adaptive Control	Model Reference Adaptive Controller (MRAC) [92], Neural Network control

with this, different tracking algorithms have been discussed which have been summarized in Table 2.2.

Out of the above-mentioned trajectory tracking control algorithms, Model Predictive Control (MPC) offers added flexibility because of its ability to solve a receding horizon optimal control problem by incorporating complex cost functions, hard and soft constraints and plant dynamics [93, 94]. In [95], a Neural Network based MPC (NNMPC) was proposed that uses the vehicle operation data to develop a neural network model which is implemented in a MPC. Such a fused approach performs better than classical physics based MPC, especially at limits of vehicle handling maneuvers, due to its ability of predicting vehicle dynamics in complex and challenging maneuvers.

Cao et al. [96] has developed a Linear Time Varying (LTV) MPC framework to track a given vehicle trajectory.A three degrees of freedom (DOF) vehicle model was used coupled with a Pacejka tire model. The primary objective was to see how well such a framework tracks the trajectory in complex cornering maneuvers. The tracking accuracy was higher as compared to other conventional control strategies. However, the primary limitations being the use of simpler vehicle model and semi-empirical tire model, which excludes the tire transient dynamics. A similar MPC was developed in [97]] focusing on path following with an additional objective to prevent vehicle roll over.

Chen et al. [98] has proposed a MPC based trajectory tracking system with a module for

Adaptive Preview Time (APT) and Path Geometry Change (PGC) to adjust the preview time of the controller and it has been defined as the average value of the double derivative of the target path in the prediction horizon. Such an approach significantly reduces the jerk experienced during lateral maneuvers like Double Lane Change (DLC).

To account for the differences between the dynamics of a simple vehicle model and real-world vehicle, Kayacan et al. [99], Mata et al. [100] have developed a tube based robust model predictive control framework. Such a framework maintains all possible trajectories of a noisy plant model inside a sequence of admissible regions by using set theory metrics. To further improve the operating regime of the framework, in terms of dealing with more uncertainties, a multi-constrained model predictive control (MMPC) has been introduced in [101]. Such an approach computes the steer angle, to navigate a given turn, by embedding a 3D potential field of the surrounding environment. This ensures efficient obstacle avoidance while tracking the desired trajectory.

In most of the literature review conducted, the vehicle plant model comprises of a simplified 2DoF bicycle model coupled with or without a semi-empirical tire model. The bicycle model, even though being computationally inexpensive, is not able to capture the transient dynamics of the vehicle. This becomes extremely important in cases where the vehicle goes through complex limit handling maneuvers, like a double lane change. Due to this, more complex trajectory tracking control algorithms are required. Hence, in this research, high-fidelity vehicle and tire models have been proposed and implemented, and their trajectory tracking performance have been evaluated via a simple model predictive control framework.

Chapter 3

Tire Modeling Framework and Ride and Lateral Dynamics Vehicle Modeling

In this chapter, high fidelity tire and vehicle models have been developed for analyzing vertical and lateral dynamics of the vehicle. The first section consists of the two tire models which have been implemented in this research - STI (Systems Technology Inc) and Fiala tire models.

The second section of this chapter comprises of the development of a mathematical model for simulating the vertical and lateral dynamics of the vehicle. The vertical dynamics model is an 11-DoF model comprising of the vertical motions at the corners of the sprung and unsprung masses. Along with this, the vertical dynamics of the vehicle CG and its roll and pitch motion have also been modeled. The effect of relaxation length and vehicle roll have been considered while modelling the lateral dynamics. Table 3.1 lists the parameters and their corresponding values which have been used in this chapter.

Table 3.1: Vehicle Modelling Parameters

Parameter	Description	Value	Units
C_1, C_2, C_3, C_4	Tire Damping Coefficient	20000	Ns/m
K_1, K_2, K_3, K_4	Tire Stiffness	2000	N/m
L_f	Distance of front axle from vehicle CG	1.3	m
L_r	Distance of rear axle from vehicle CG	1.3	m
t_f, t_r	Front and Rear Trackwidth	1.5	m
M_s	Vehicle Sprung Mass	1200	kg
m_1, m_2, m_3, m_4	Vehicle Corner Unsprung masses	42.25	kg
x_1, x_2, x_3, x_4	Sprung Mass Corner Displacements	-	m
x_5, x_6, x_7, x_8	Unsprung Mass Corner Displacements	-	m
$F_{t1}, F_{t2}, F_{t3}, F_{t4}$	Tire forces at individual wheels	-	N

3.1 STI Tire Model

The STI Tire model can be divided into two different regimes based upon the magnitude of the slip angle and the tire-road contact interface. These regions are defined as the adhesion regions and the sliding region which are defined by combined lateral and longitudinal force distribution [102], [103]

By integrating the unit forces along the lateral and the longitudinal directions, the total of these forces can be obtained. These forces are integrated over an ellipsoid region (assumed contact patch distribution shape) as a function of the lateral and longitudinal slips as shown in Equation 3.1 and Equation 3.2.

$$F_y = \int_0^{a_p} f_y \, dl \tag{3.1}$$

$$F_x = \int_0^{a_p} f_x \, dl \tag{3.2}$$

The composite force function is specified as the sum of Root Mean Squares (RMS) of these

forces as given in Equation 3.3.

$$F(\sigma) = \sqrt{F_x^2 + F_y^2} \tag{3.3}$$

By integrating the above two equations and introducing the lateral and longitudinal stiffness, the total lateral and longitudinal forces can be obtained as shown in Equation 3.4 and Equation 3.5 respectively.

$$F_y = F_c . \frac{K_s . tan(\alpha)}{(K_s^2 . tan(\alpha)^2 + K_c . \frac{s^2}{(1-s)^2})} \tag{3.4}$$

$$F_y = -F_c . \frac{K_c . \frac{s}{(1-s)}}{(K_s^2 . tan(\alpha)^2 + K_c . \frac{s^2}{(1-s)^2})} \tag{3.5}$$

Equation 3.6 shows the composite slip function formulation which is essentially quadratic function of lateral and longitudinal slip.

$$\sigma = \frac{\pi . a_p^2}{8 . F_z} . \sqrt{((\frac{(K_s . tan(\alpha))^2}{\mu^2} + \frac{K_c^2}{\mu^2} . \frac{s^2}{(1-s)^2})} \tag{3.6}$$

Based on this composite slip function, the composite force function can be formulated using experimentally obtained coefficients as shown in Equation 3.7.

$$F(\sigma) = \frac{C_1 . (\sigma)^3 + C_2 . (\sigma)^2 + \frac{4 . \sigma}{\pi}}{C_1 . (\sigma)^3 + C_3 . (\sigma)^2 + C_4 . (\sigma) + 1} \tag{3.7}$$

The intermediate quantities of lateral and longitudinal stiffness can be computed via fitting curves on experimentally collected data and computing the slopes of these curves. This has been discussed in the subsequent section. These stiffness values are computed as shown in

Equation 3.8 and Equation 3.9.

$$K_c = \frac{2}{a_{p0}^2}.F_z.\frac{CS}{FZ} \tag{3.8}$$

$$K_s = \frac{2}{a_{p0}^2}.(A_0 + A_1.F_z - \frac{A_1.F_z^2}{A_2}) \tag{3.9}$$

The peak tire-to-road friction coefficient describes the effective tire friction coefficient using a priori defined Calspan parameters B1, B3, and B4 and the normal load as shown in Equation 3.10.

$$\mu_0 = 1.176.\mu_{norm}.(B_1.F_z + B_3 + B_4.(F_z)^2) \tag{3.10}$$

Figure 3.1 shows the variation of the lateral force with tire slip angle as computed by the STI tire model. Multiple curves have been plotted corresponding to different tire slip ratios. From these curves, it can be seen that at higher slip ratios, the slope of the lateral force curve is greater. Along with this, as compared to the conventional Pacejka Tire model, the lateral force plateaus at higher slip angle values.

The key feature of the STI Tire model is that it operates within both the adhesion region, as well as the transition and the saturation (sliding) regions. Along with this, the model with certain modifications in the normalized lateral force formulation can also be used for analyzing the tire forces in off-terrain conditions. This is accomplished by introducing shaping factors which depend on the surface irregularities, coefficient of friction and road roughness properties. Due to the formulation of a composite slip and force function, the combined effects in both lateral and longitudinal directions at the limit of friction can be studied which

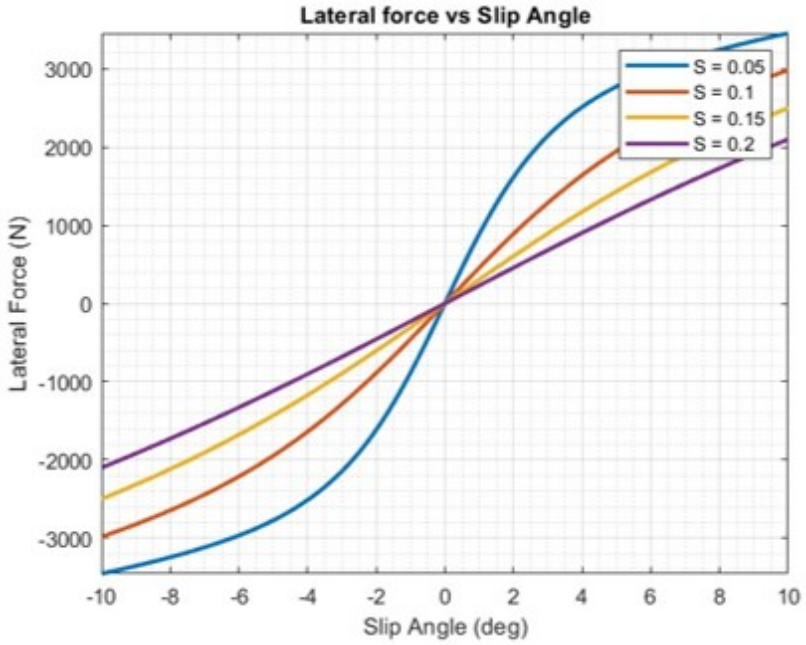

Figure 3.1: Lateral Force variation with respect to slip angle for varying slip ratios

otherwise is not possible for similar low computationally expensive semi-empirical models such as the Fiala Tire Model.

Upon further simplifying the composite force function, it can be seen that the STI Tire model does not depend on the tire contact patch length.

Along with this, due to the presence of the tire pressure term while analytically computing the longitudinal and lateral tire stiffnesses, the STI tire model can also be used for analyzing the effects of tire inflation pressure variation on different vehicle dynamics characteristics.

The STI Tire Model is valid for both on road (asphalt and concrete surfaces) along with off-road (soft terrain) road conditions. However, the simplified form of the STI Tire Model assumes that the tire is rigid at all times. Due to this assumption there can be no relaxation of the tire structure, which leads to an overestimation or underestimation of the forces reacting from the soils especially while analyzing off-terrain vehicle dynamics.

Table 3.2: STI Tire Model Parameters

Parameter	Symbol
Lateral Stiffness Coefficient Parameters	A_0, A_1, A_2
Camber Thrust Parameters	A_3, A_4
Peak Tire-to-road friction coefficient	B_1, B_3, B_4
Composite Force Function Parameters	C_1, C_2, C_3, C_4

Also with the STI Model being a semi-empirical tire model, the composite force function parameters need to be determined experimentally via a Flat Trac Machine.

Apart from the parameters listed in the Nomenclature section, the following dimensionless parameters are required for evaluating different intermediate quantities - as mentioned in Table 3.2.

Each of the parameters listed in Table 3.2 are experimentally derived by fitting curves through derived quantities.

1. **Lateral Stiffness Coefficient Parameters:** These parameters relate on-center cornering stiffness to tire normal load. Quasi-static steering tests are used, and the cornering stiffness of each is computed for a slip angle range of 2°. A second order polynomial is fit through the three cornering stiffness (corresponding to three normal load values), and A0 , A1, A2 are determined.

2. **Camber Thrust Parameters:** These parameters relate on-center camber stiffness to tire normal load. Quasi-static discrete cambering tests are used at three specified normal loads, and the camber stiffness of each is computed about zero camber angle. A second order polynomial is fit through the three camber stiffness, and A3, A4 are determined.

3. **Peak tire-to-road friction coefficient:** These parameters relate the peak longi-

tudinal normalized force to tire normal load. Quasi-static braking are used at three specified normal load values, and for each test the average of the peak normalized lateral force is computed. A second order polynomial is fit through the three peak normalized forces, and B1, B3, B4 are determined.

3.2 Fiala Tire Model

The Fiala tire model [104] is one of the fundamental approaches in modeling tire-road interaction and is derived from brush tire model. This tire model utilizes a physical interpretation of the tire's characteristics to understand and predict the lateral forces developed during cornering maneuvers.

The Fiala model divides the lateral force into three regions:

- Linear region ($0 \leq |\alpha| < \alpha_0$): In this region, the lateral force is directly proportional to the slip angle, as defined by the linear elastic behavior of the rubber in the tire, characterized by the cornering stiffness (C). The mathematical relationship is given by $F_y = C * \alpha$.
- Non-linear region ($\alpha_0 \leq |\alpha| < \alpha_p$): In this region, the lateral force grows nonlinearly as the slip angle increases, as the rubber in the tire begins to slide on the road surface. The mathematical relationship is typically modeled as a polynomial function.
- Saturation region ($\alpha_p \leq |\alpha|$): In this region, the tire's lateral force reaches its maximum value, F_{ymax}, and remains constant as the slip angle continues to increase. This is because the tire's rubber is fully sliding on the road surface.

The transition points α_0 and α_p, are defined by the parameters of the tire, such as the tire

stiffness and peak tire-road friction coefficient.

Equation 3.11 shows the tire lateral force computation derived from the Fiala tire model. The lateral force is a function of three parameters - tire slip angle, coefficient of friction and the tire normal load.

$$F_y = \begin{cases} -C_\alpha \tan\alpha + \frac{C_\alpha^2}{3\mu F_z}|\tan\alpha|\tan\alpha - \frac{C_\alpha^3}{27*\mu^2 F_z^2}\tan\alpha^3, & \text{if } \tan\alpha < \alpha_{sli} \\ -\mu F_z sgn(\alpha), & \text{otherwise} \end{cases} \tag{3.11}$$

where:

α_{sli}: Tire slip angle at which full slip occurs as shown in Equation 3.12. After this slip angle limit is reached, the lateral force is no longer a function of the slip angle but purely depends upon the vehicle normal load and coefficient of friction.

$$\alpha_{sli} = \arctan(\frac{3\mu F_z}{C_\alpha}) \tag{3.12}$$

The key assumptions of the Fiala tire model are:

- No effect of longitudinal forces
- The tire-road friction coefficient is assumed to be constant
- The pressure distribution within the contact patch is parabolic

Figure 3.2 shows the variations of the lateral force against slip angle for different values of vehicle normal load. The curves correlate with those obtained by conventional Pacejka tire model with the primary difference being that in the Fiala model a peak in the lateral force, before plateauing, is not characterized.

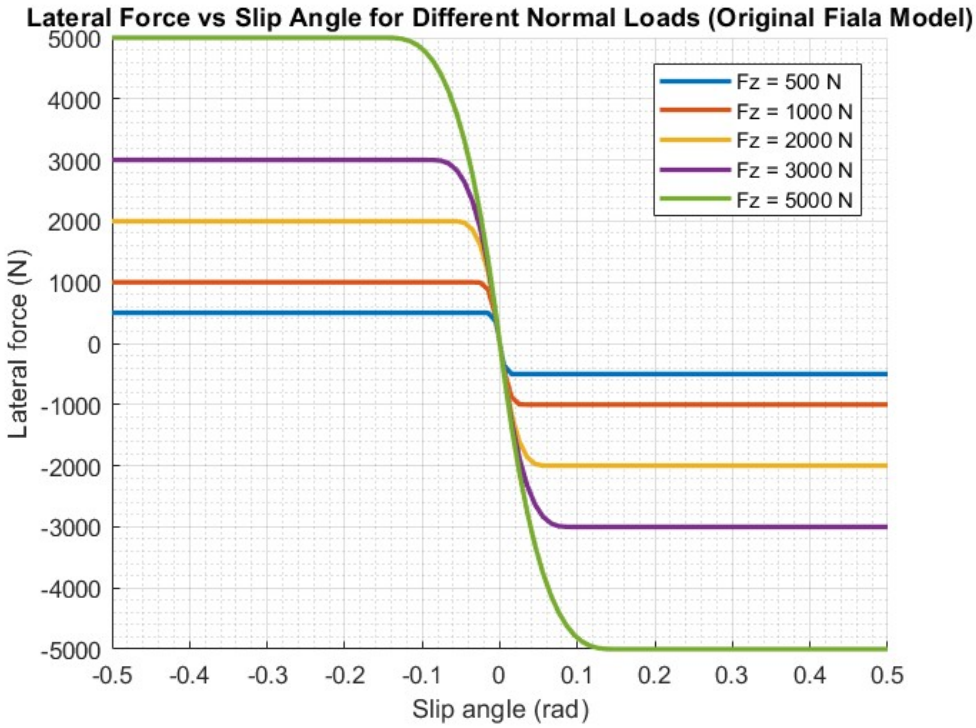

Figure 3.2: Lateral Force variation with respect to slip angle for varying normal load

3.2.1 Friction Circle/Ellipse

The Fiala tire model described in Equation 3.11, does not take into account the effect of tire longitudinal forces. This adversely affects the estimation of the tire lateral force in cases of limit handling maneuvers. Hence, in order to overcome this, a modified version of the Fiala tire model has been implemented, derived from the friction circle concept. Figure 3.3 shows the friction circle diagram for a vehicle taking a right turn.

The friction circle essentially represents the total amount of force which can be generated by a tire for a given number of operating conditions - tire inflation pressure, normal load, surface characteristics, and tire temperature. The radius of the friction circle provides the maximum force that can be generated by a tire and is given by Equation 3.13.

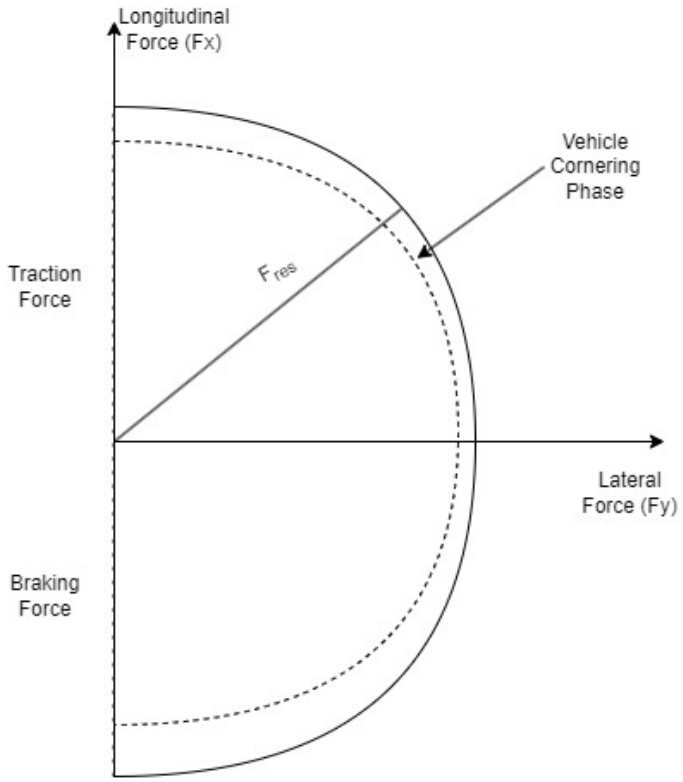

Figure 3.3: Friction circle for vehicle cornering

$$F_{max} = \sqrt{F_x^2 + F_y^2} \tag{3.13}$$

During cornering, the vehicle operates very close to the envelope of the friction circle and is represented by the dotted curve in Figure 3.3. Hence, in this regime, both the lateral and the longitudinal forces play a crucial role in determining the vehicle path. To take into account this coupling of longitudinal force, a modified version of the Fiala model has been used as shown in Equation 3.14.

$$F_y = \begin{cases} -C_\alpha \tan\alpha + \frac{C_\alpha^2}{3\mu F_z \sigma} |\tan\alpha| \tan\alpha - \frac{C_\alpha^3}{27*\mu^2 F_z^2 \sigma^2} \tan\alpha^3, & \text{if } \tan\alpha < \alpha_{sli} \\ -\sigma\mu F_z sgn(\alpha), & \text{otherwise} \end{cases} \tag{3.14}$$

where:

σ: Lateral force reduction factor

The term "σ" is introduced to take into account the reduction of the tire lateral force due to the increase in the longitudinal force during cornering and is represented by Equation 3.15. This factor has a range between 0 and 1, with 1 indicating no longitudinal force applied.

$$\sigma = \frac{\sqrt{(\mu F_z)^2 - (F_x)^2}}{\mu F_z} \tag{3.15}$$

The lateral force has been computed based upon this modified Fiala tire models and the results can be seen in Figure 3.4. At lower normal loads, due to the factor "σ", sharp discontinuities can be observed in the lateral force.

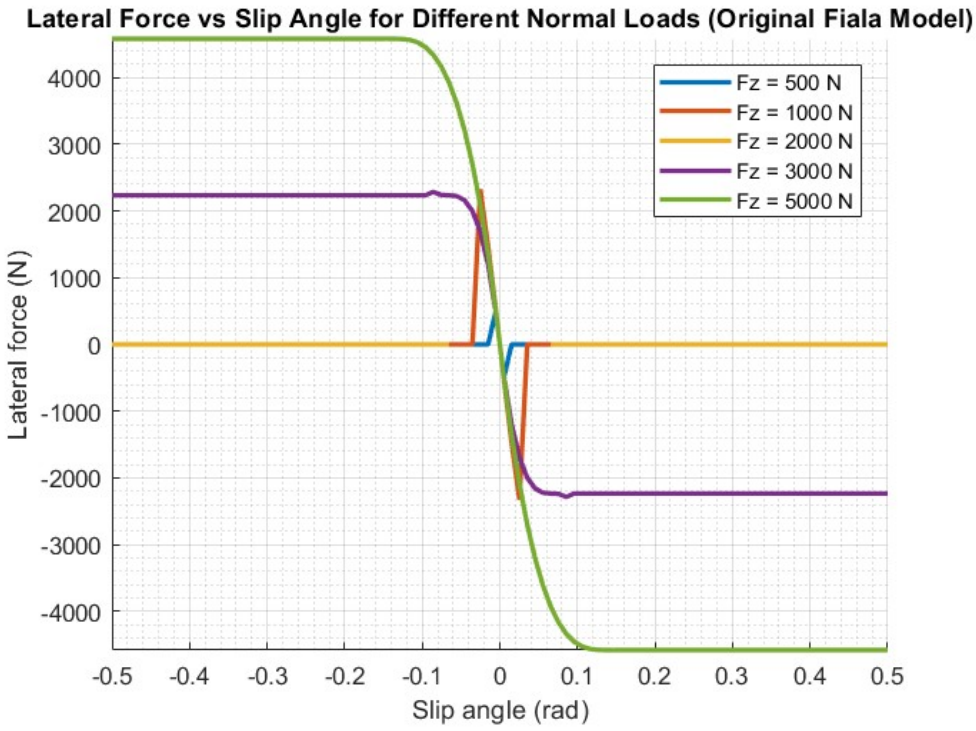

Figure 3.4: Lateral Force variation with respect to slip angle for varying normal load - Modified Fiala

The lateral forces estimated by the original and modified Fiala tire model have been compared for a given value of normal load as shown in Figure 3.5. From this figure, it can be seen that the lateral force generated from the modified Fiala model is lower as compared to that given by the original Fiala model. This is due to the lateral-longitudinal force coupling at cornering which reduces the lateral force to compensate for the traction force. The modified Fiala model provides more realistic lateral forces and hence has been used in this research.

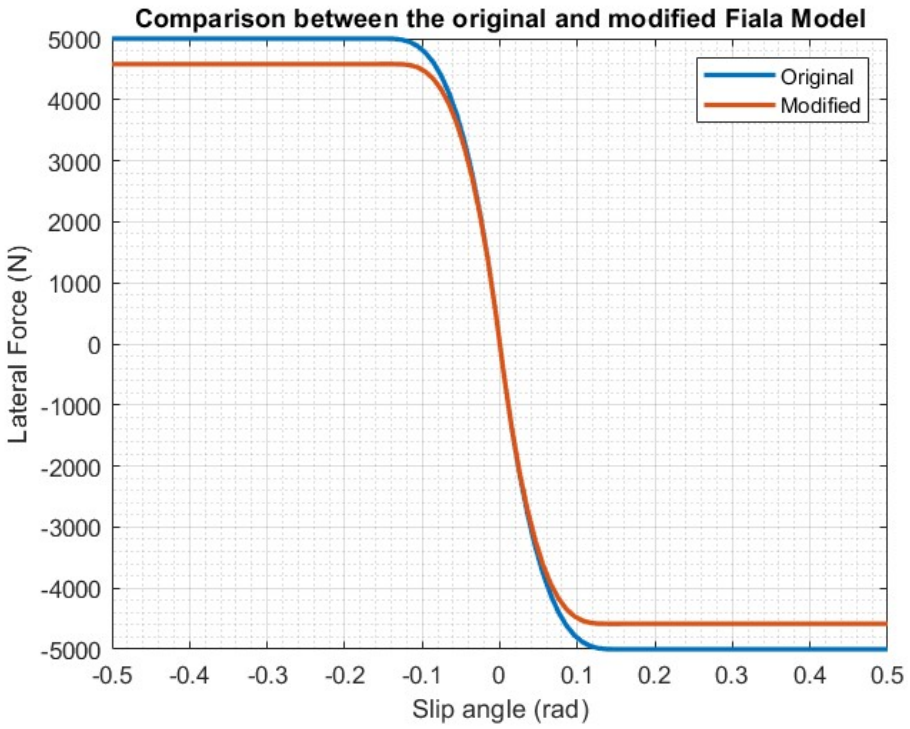

Figure 3.5: Comparison between the lateral force variation between original and modified Fiala model for a given F_z

3.2.2 Summary

In this research, two tire models have been implemented - STI and Fiala tire models. Based upon an extensive comparison between the two, it can be seen that though the Fiala tire model evaluates the lateral force via a simpler non-linear equation, it requires only three

variables for its parameterization. The STI model, on the other hand, requires 13 parameters which requires extensive tire testing - lateral, on-center, and camber thrust tests. The modified version of the Fiala tire model includes the effect of longitudinal tire force coupling with the lateral force and hence is more effective in analyzing vehicle cornering and slalom maneuvers.

Along with this, the Fiala model is much more computationally inexpensive as compared to the STI model. Hence, further in this research, the modified Fiala tire model has been used for the development of the vehicle plant model.

3.3 Vehicle Model for Ride Dynamics

To simulate the vertical dynamics of the vehicle, an 11 Degree of Freedom (DoF) rover model was developed. The model encapsulates the following vehicle motions:

- Vehicle CG Vertical Dynamics (Displacement, Velocity and Acceleration)
- Vehicle CG Roll and Pitch Dynamics
- Vehicle Sprung Mass Vertical Dynamics (corresponding to every wheel)
- Vehicle Unsprung Mass Vertical Dynamics (corresponding to every wheel)

Figure 3.6 shows the schematic vehicle diagram representing the different Degrees of Freedom. Based upon this, equations of motion have been derived representing the translational and rotational vehicular motions [11].

Equation 3.16, Equation 3.17, and Equation 3.18 represent the vertical displacement, pitch and roll of the vehicle CG respectively.

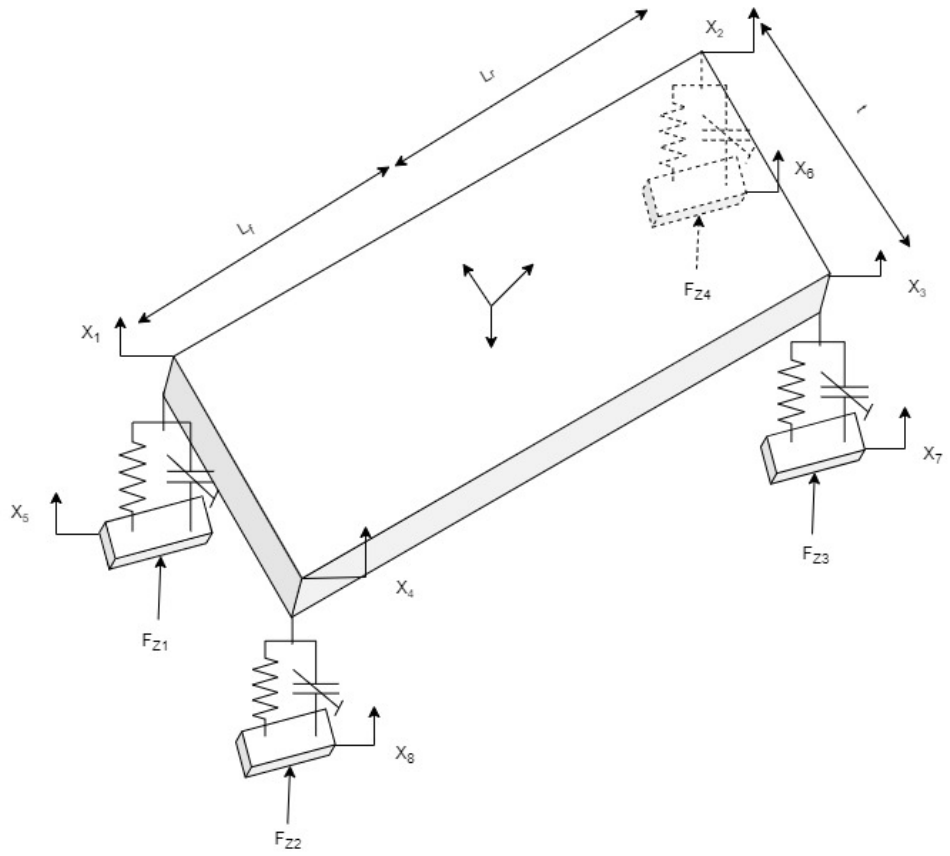

Figure 3.6: Schematic Diagram of the 11-DoF Vehicle Model

$$M_s\ddot{x_b} = C_1(\dot{x_5} - \dot{x_1}) + C_2(\dot{x_6} - \dot{x_2}) + C_3(\dot{x_7} - \dot{x_3}) + C_4(\dot{x_8} - \dot{x_4}) + K_1(x_5 - x_1) + K_2(x_6 - x_2) + K_3(x_7 - x_3) + K_4(x_8 - x_4) \quad (3.16)$$

$$I_p\ddot{\theta} = L_r[C_3(\dot{x_7} - \dot{x_3}) + C_4(\dot{x_8} - \dot{x_4}) + K_3(x_7 - x_3) + K_4(x_8 - x_4)] - L_f[C_1(\dot{x_5} - \dot{x_1}) + C_2(\dot{x_6} - \dot{x_2}) + K_1(x_5 - x_1) + K_2(x_6 - x_2)] \quad (3.17)$$

$$I_r\ddot{\phi} = \frac{t}{2}[C_2(\dot{x_6} - \dot{x_2}) + C_1(\dot{x_5} - \dot{x_1}) + K_2(x_6 - x_2) + K_1(x_5 - x_1)] + \frac{t}{2}[C_4(\dot{x_8} - \dot{x_4}) + C_3(\dot{x_7} - \dot{x_3}) + K_3(x_7 - x_3) + K_4(x_8 - x_4)] \quad (3.18)$$

Equation 3.19, Equation 3.20, Equation 3.21, and Equation 3.22 have been developed to determine the unsprung mass displacements at the 4 vehicle corners.

$$m_1\ddot{x_5} = C_1(\dot{x_1} - \dot{x_5}) + K_1(x_1 - x_5) + F_{t1} - m_1g \quad (3.19)$$

$$m_2\ddot{x_6} = C_2(\dot{x_2} - \dot{x_6}) + K_2(x_2 - x_6) + F_{t2} - m_2g \quad (3.20)$$

$$m_3\ddot{x_7} = C_3(\dot{x_3} - \dot{x_7}) + K_3(x_3 - x_7) + F_{t3} - m_3g \quad (3.21)$$

$$m_4\ddot{x_8} = C_4(\dot{x_4} - \dot{x_8}) + K_4(x_4 - x_8) + F_{t4} - m_4 g \tag{3.22}$$

Equation 3.23, Equation 3.24, Equation 3.25, and Equation 3.26 represent the vehicle sprung mass motion at the 4 corners. Small angle approximations for pitch and roll angle have been used to linearize these set of equations.

$$x_1 = x_b + \frac{t}{2}\phi - L_f\theta \tag{3.23}$$

$$x_2 = x_b - \frac{t}{2}\phi - L_f\theta \tag{3.24}$$

$$x_3 = x_b + \frac{t}{2}\phi + L_r\theta \tag{3.25}$$

$$x_4 = x_b - \frac{t}{2}\phi - L_r\theta \tag{3.26}$$

Equations 3.16 to 3.26 have been modelled in MATLAB/Simulink in order to evaluate the sprung and unsprung mass motion of the vehicle. Figure 3.7 shows the Simulink architecture of the model. The model essentially comprises of 11 subsystems with each system representing the above equations.

The inputs to the model comprise of the tire forces which have been generated from the road surface profile. This road surface profile is taken from VTTI institute and corresponds to an asphalt surface with a 10mm resolution. Figure 3.8 shows the tire forces at the individual wheels.

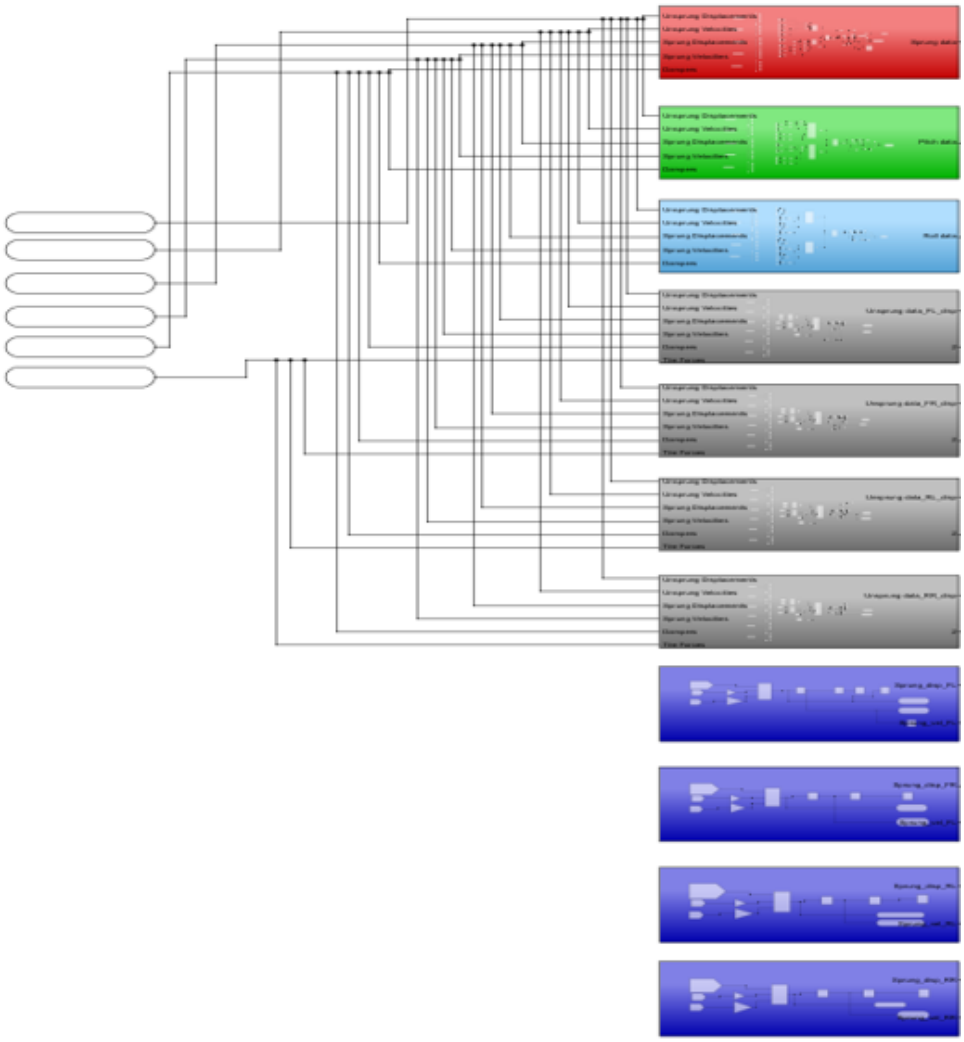

Figure 3.7: Simulink Vertical Dynamics Model Development

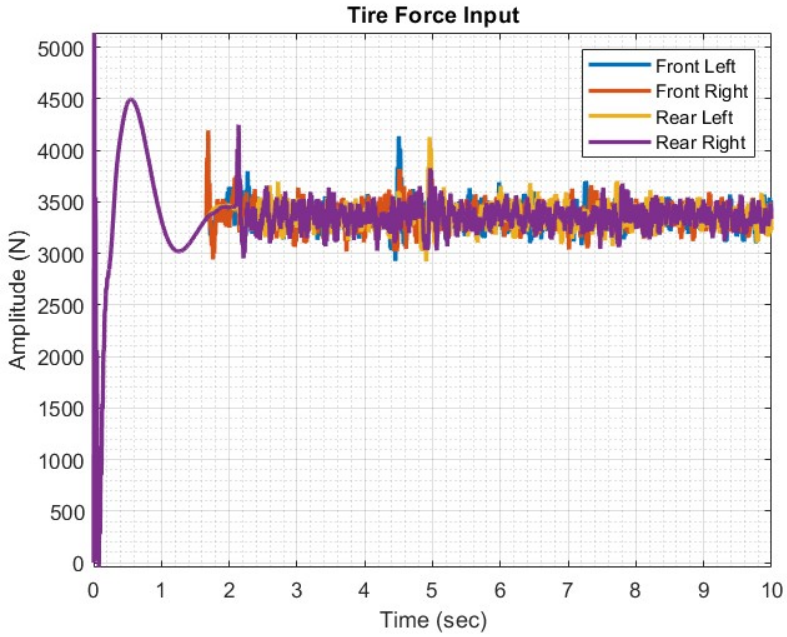

Figure 3.8: Tire Forces

The vehicle model has been simulated using the above inputs, the dynamics of which have been shown below. Figure 3.9 and Figure 3.10 show the pitch and roll angle of the CG of the vehicle and their corresponding rates respectively.

Similarly, Figure 3.11 and Figure 3.12 show the sprung mass and unsprung mass corner velocities, respectively. From each of these figures, it can be seen that the model is stable for the given tire force inputs.

To quantify the performance of the above vehicle model, the Root Mean Square (RMS) values of the angles and velocities have been calculated. Table 3.3 shows the RMS values of the above vehicle responses.

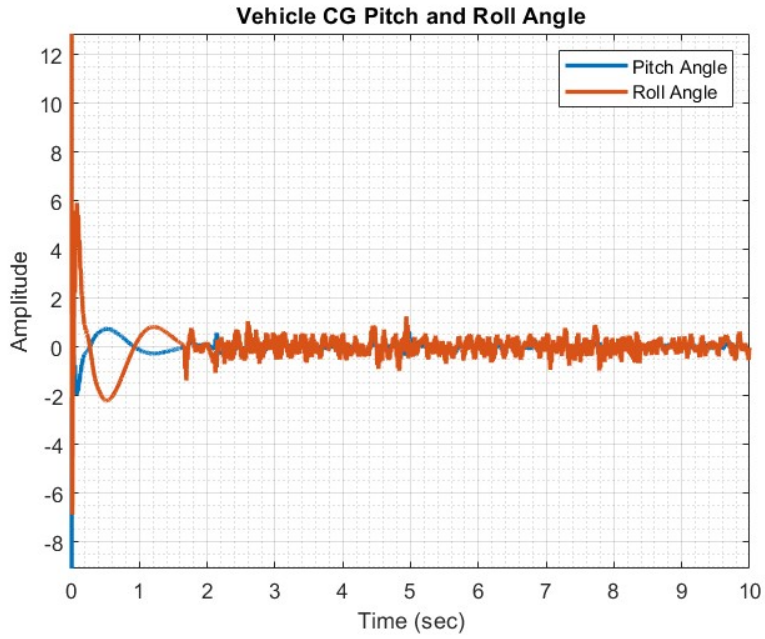

Figure 3.9: Vehicle CG Roll and Pitch Angle

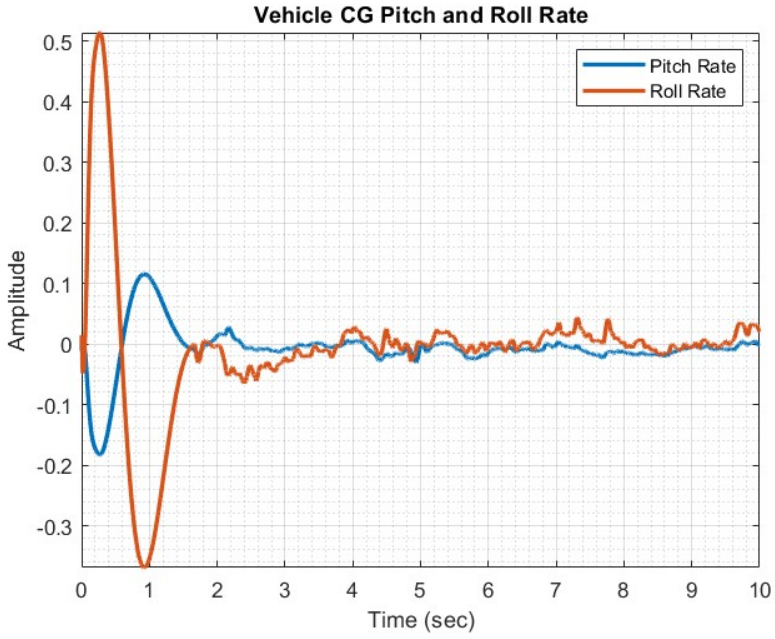

Figure 3.10: Vehicle CG Roll and Pitch Rate

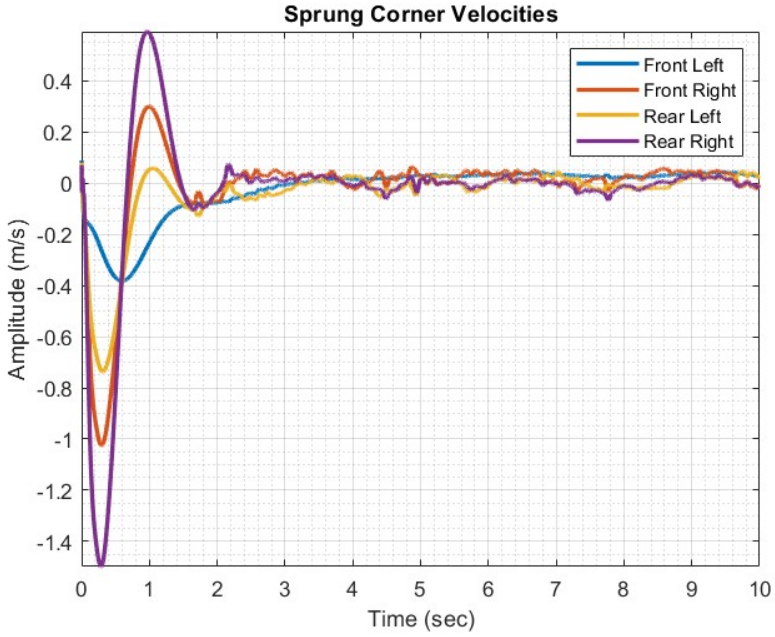

Figure 3.11: Sprung Mass Corner Velocities

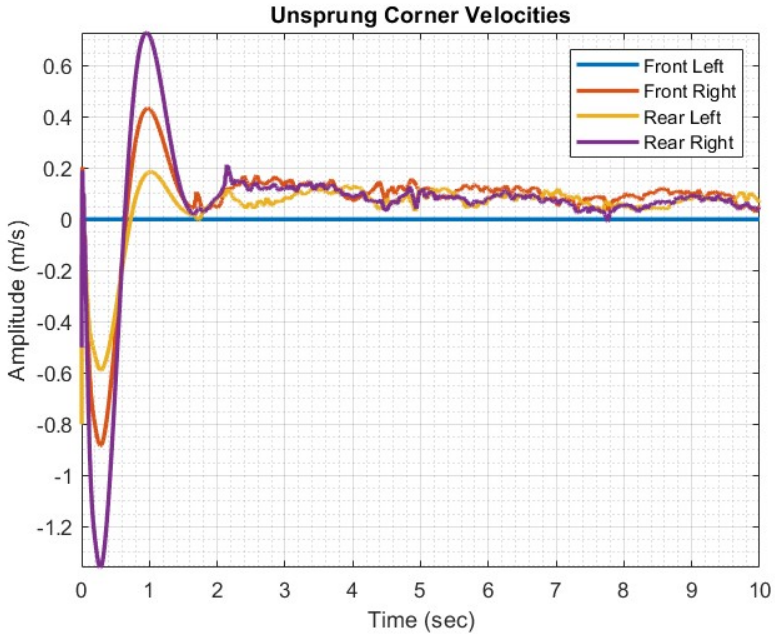

Figure 3.12: Unsprung Mass Corner Velocities

Table 3.3: RMS Values of Model Responses

Parameter	Value	Units
CG Pitch Angle	0.2634	deg
CG Roll Angle	0.7244	deg
CG Pitch Rate	0.0400	deg/s
CG Roll Rate	0.1156	deg/s
Sprung Mass Corner Velocities (FL, FR, RL, RR)	0.1052, 0.1979, 0.1484, 0.2899	m/s
Unsprung Mass Corner Velocities (FL, FR, RL, RR)	0.0125, 0.2041, 0.1376, 0.2891	m/s

3.4 Vehicle Model for Lateral Dynamics

The steady state vehicle and tire modelling discussed in Section 2.1.2 considers low variations in the input parameters of slip angle, normal load and vehicle speeds. To consider the transient effects of the tire and vehicle model, especially during maneuvers like Double Lane Change and Slalom, the tire lag dynamics need to be considered while modelling.

The tire lag dynamics represent the delay in the lateral force generation at the contact patch due to the tire sidewall deformation. Based upon literature review, it is seen that the tire lateral reaction force approximates the exponential law under step input of the wheel steering angle. The wheel covers a distance approximately equal to its static radius before the emerging lateral reaction varies by no more than 36.8% of its new steady-state value [15]. This travel covered by the wheel before the lateral force reaches its steady value is termed as the "relaxation length" and is used to represent the tire lag dynamics.

This relaxation length can be represented as a first order differential equation system given by Equation 3.27, [1].

$$\dot{y} + \frac{1}{\tau} y = F_y(t) \tag{3.27}$$

The solution of this differential equation yields Equation 3.28.

$$F_y = C_\alpha \alpha * (1 - e^{\frac{-t}{\tau}}) \tag{3.28}$$

where: $\tau = \frac{\lambda}{U}$ = Relaxation Time Constant

λ = Relaxation Length

U = Vehicle Velocity

The relaxation length depends upon the cornering stiffness and the lateral stiffness of the tire. Based upon different experimental studies, the value of relaxation length can vary from 0.3 - 0.5m for passenger car tires at longitudinal speeds of up to 15m/s [15].

In this section, a 5-DoF vehicle model has been developed to consider the effects of the tire lag dynamics by integrating the relaxation length into the model.

The vehicle model has been developed keeping the following assumptions under consideration:

- No motion exists along the vehicle pitch direction
- Longitudinal velocity is constant for the vehicle.
- Model has been linearized by taking into account small angle approximations.
- The aerodynamic effects of the model have been neglected.

The standard 2-DoF bicycle model has been modified to include the vehicle roll dynamics, and the tire relaxation lengths at the front and the rear tire [22]. Two separate models have been developed to understand the effects of tire lag dynamics. These models have been formulated as shown below:

Equation 3.29 and Equation 3.30 show the model state vector for without and with tire lag dynamics.

$$x_1 = \begin{bmatrix} V \\ r \\ \dot{\phi}_r \\ \phi_r \end{bmatrix} \tag{3.29}$$

$$x_2 = \begin{bmatrix} V \\ r \\ \dot{\phi}_r \\ \phi_r \\ F_f \\ F_r \end{bmatrix} \tag{3.30}$$

where:

V = Vehicle Lateral Velocity

r = Vehicle CG Yaw Rate

ϕ_r = Roll Angle

F_f = Front Tire Force

F_r = Rear Tire Force

State (A_1 and A_2) and input matrices (B_1 and B_2) have been formulated for each of the two models. Equation 3.31, 3.32, 3.33 and 3.4 shows the state and the input matrices for the

two models respectively.

$$A_1 = \begin{pmatrix} \frac{I_{xz}\, h_{sr}\, m_s\, \sigma_7}{U\, \sigma_1} - \frac{(c_{af}+c_{ar})\, \sigma_4}{U\, \sigma_1} & \frac{\sigma_6\, \sigma_4}{\sigma_1} - \frac{I_{zz}\, U\, {h_{sr}}^2\, {m_s}^2}{\sigma_1} + \frac{I_{xz}\, h_{sr}\, m_s\, \sigma_2}{U\, \sigma_1} & -\frac{I_{zz}\, d_\phi\, h_{sr}\, m_s}{\sigma_1} & -\frac{I_{zz}\, h_{sr}\, m_s\, \sigma_5}{\sigma_1} \\ \frac{I_{xz}\, h_{sr}\, m_s\, (c_{af}+c_{ar})}{U\, \sigma_1} - \frac{\sigma_7\, \sigma_3}{U\, \sigma_1} & \frac{I_{xz}\, U\, h_{sr}\, m\, m_s}{\sigma_1} - \frac{I_{xz}\, h_{sr}\, m_s\, \sigma_6}{\sigma_1} - \frac{\sigma_2\, \sigma_3}{U\, \sigma_1} & \frac{I_{xz}\, d_\phi\, m}{\sigma_1} & \frac{I_{xz}\, m\, \sigma_5}{\sigma_1} \\ \frac{I_{zz}\, h_{sr}\, m_s\, (c_{af}+c_{ar})}{U\, \sigma_1} - \frac{I_{xz}\, m\, \sigma_7}{U\, \sigma_1} & \frac{I_{zz}\, U\, h_{sr}\, m\, m_s}{\sigma_1} - \frac{I_{zz}\, h_{sr}\, m_s\, \sigma_6}{\sigma_1} - \frac{I_{xz}\, m\, \sigma_2}{U\, \sigma_1} & \frac{I_{zz}\, d_\phi\, m}{\sigma_1} & \frac{I_{zz}\, m\, \sigma_5}{\sigma_1} \\ 0 & 0 & 1 & 0 \end{pmatrix}$$

where

$$\sigma_1 = m\, {I_{xz}}^2 + I_{zz}\, {h_{sr}}^2\, {m_s}^2 - I_{zz}\, m\, {h_{sr}}^2\, m_s - I_{xx}\, I_{zz}\, m$$

$$\sigma_2 = c_{af}\, a^2 + c_{ar}\, b^2$$

$$\sigma_3 = -{h_{sr}}^2\, {m_s}^2 + m\, {h_{sr}}^2\, m_s + I_{xx}\, m$$

$$\sigma_4 = -{I_{xz}}^2 + I_{zz}\, m_s\, {h_{sr}}^2 + I_{xx}\, I_{zz}$$

$$\sigma_5 = k_\phi - g\, h_{sr}\, m_s$$

$$\sigma_6 = U\, m - \frac{\sigma_7}{U}$$

$$\sigma_7 = a\, c_{af} - b\, c_{ar} \tag{3.31}$$

$$B_1 = \begin{pmatrix} \frac{c_{\mathrm{af}}\left(-{I_{\mathrm{xz}}}^2+I_{\mathrm{zz}}\,m_s\,{h_{\mathrm{sr}}}^2+I_{\mathrm{xx}}\,I_{\mathrm{zz}}\right)}{\sigma_1} \_ \frac{I_{\mathrm{xz}}\,a\,c_{\mathrm{af}}\,h_{\mathrm{sr}}\,m_s}{\sigma_1} \\ \frac{a\,c_{\mathrm{af}}\left(-{h_{\mathrm{sr}}}^2\,{m_s}^2+m\,{h_{\mathrm{sr}}}^2\,m_s+I_{\mathrm{xx}}\,m\right)}{\sigma_1} \_ \frac{I_{\mathrm{xz}}\,c_{\mathrm{af}}\,h_{\mathrm{sr}}\,m_s}{\sigma_1} \\ \frac{I_{\mathrm{xz}}\,a\,c_{\mathrm{af}}\,m}{\sigma_1} \_ \frac{I_{\mathrm{zz}}\,c_{\mathrm{af}}\,h_{\mathrm{sr}}\,m_s}{\sigma_1} \\ 0 \end{pmatrix} \tag{3.32}$$

where

$$\sigma_1 = m\,{I_{\mathrm{xz}}}^2 + I_{\mathrm{zz}}\,{h_{\mathrm{sr}}}^2\,{m_s}^2 - I_{\mathrm{zz}}\,m\,{h_{\mathrm{sr}}}^2\,m_s - I_{\mathrm{xx}}\,I_{\mathrm{zz}}\,m$$

$$A_2 = \begin{pmatrix} 0 & \frac{U\,m\,\sigma_2}{\sigma_6} - \frac{I_{zz}\,U\,{h_{sr}}^2\,{m_s}^2}{\sigma_6} & -\frac{I_{zz}\,d_\phi\,h_{sr}\,m_s}{\sigma_6} & -\frac{I_{zz}\,h_{sr}\,m_s\,\sigma_3}{\sigma_6} & \frac{I_{xz}\,a\,h_{sr}\,m_s}{\sigma_6} - \frac{\sigma_2}{\sigma_6} & -\frac{\sigma_2}{\sigma_6} - \frac{I_{xz}\,b\,h_{sr}\,m_s}{\sigma_6} \\ 0 & 0 & \frac{I_{xz}\,d_\phi\,m}{\sigma_6} & \frac{I_{xz}\,m\,\sigma_3}{\sigma_6} & \sigma_5 - \frac{a\,\sigma_1}{\sigma_6} & \frac{b\,\sigma_1}{\sigma_6} + \sigma_5 \\ 0 & 0 & \frac{I_{zz}\,d_\phi\,m}{\sigma_6} & \frac{I_{zz}\,m\,\sigma_3}{\sigma_6} & \sigma_4 - \frac{I_{xz}\,a\,m}{\sigma_6} & \frac{I_{xz}\,b\,m}{\sigma_6} + \sigma_4 \\ 0 & 0 & 1 & 0 & 0 & 0 \\ \frac{c_{af}}{\sigma_f} & \frac{a\,c_{af}}{\sigma_f} & 0 & 0 & -\frac{U}{\sigma_f} & 0 \\ \frac{c_{ar}}{\sigma_r} & -\frac{b\,c_{ar}}{\sigma_r} & 0 & 0 & 0 & -\frac{U}{\sigma_r} \end{pmatrix}$$

where

$$\sigma_1 = -{h_{sr}}^2\,{m_s}^2 + m\,{h_{sr}}^2\,m_s + I_{xx}\,m$$

$$\sigma_2 = -{I_{xz}}^2 + I_{zz}\,m_s\,{h_{sr}}^2 + I_{xx}\,I_{zz}$$

$$\sigma_3 = k_\phi - g\,h_{sr}\,m_s$$

$$\sigma_4 = \frac{I_{zz}\,h_{sr}\,m_s}{\sigma_6}$$

$$\sigma_5 = \frac{I_{xz}\,h_{sr}\,m_s}{\sigma_6}$$

$$\sigma_6 = m\,{I_{xz}}^2 + I_{zz}\,{h_{sr}}^2\,{m_s}^2 - I_{zz}\,m\,{h_{sr}}^2\,m_s - I_{xx}\,I_{zz}\,m \tag{3.33}$$

Table 3.4: Vehicle Model Parameters

Parameter	Symbol	Value	Units
Sprung Mass	m_s	2956	kg
Longitudinal velocity	U	13.4	m/s
CG Distance from Front Axle	a	1.459	m
CG Distance from Rear Axle	b	1.895	m
Roll Center Height	h_{sr}	0.781	m
Front Cornering Stiffness	c_{alphaf}	120000	N/deg
Rear Cornering Stiffness	c_{alphar}	120000	N/deg
Moment of Inertia about X axis	I_{xx}	1830	kgm^2
Moment of Inertia about Z axis	I_{zz}	1830	kgm^2
Moment of Product	I_{xz}	1830	kgm^2
Roll Stiffness	k_ϕ	145330	Nm/deg
Front Relaxation Length	σ_f	0.7	m
Rear Relaxation Length	σ_r	0.23	m

$$B_2 = \begin{pmatrix} 0 & \frac{I_{zz}\, g\, {h_{sr}}^2\, {m_s}^2}{\sigma_1} - \frac{g\, m \left(-{I_{xz}}^2 + I_{zz}\, m_s\, {h_{sr}}^2 + I_{xx}\, I_{zz}\right)}{\sigma_1} \\ 0 & 0 \\ 0 & 0 \\ 0 & 0 \\ -\frac{U\, c_{af}}{\sigma_f} & 0 \\ 0 & 0 \end{pmatrix} \tag{3.34}$$

where

$$\sigma_1 = m\, {I_{xz}}^2 + I_{zz}\, {h_{sr}}^2\, {m_s}^2 - I_{zz}\, m\, {h_{sr}}^2\, m_s - I_{xx}\, I_{zz}\, m$$

The above state space model has been simulated by using parameters shown in Table 3.4.

The input to the vehicle model is the steer angle of the vehicle. A step input steering angle

has been provided as the input as shown in Figure 3.13.

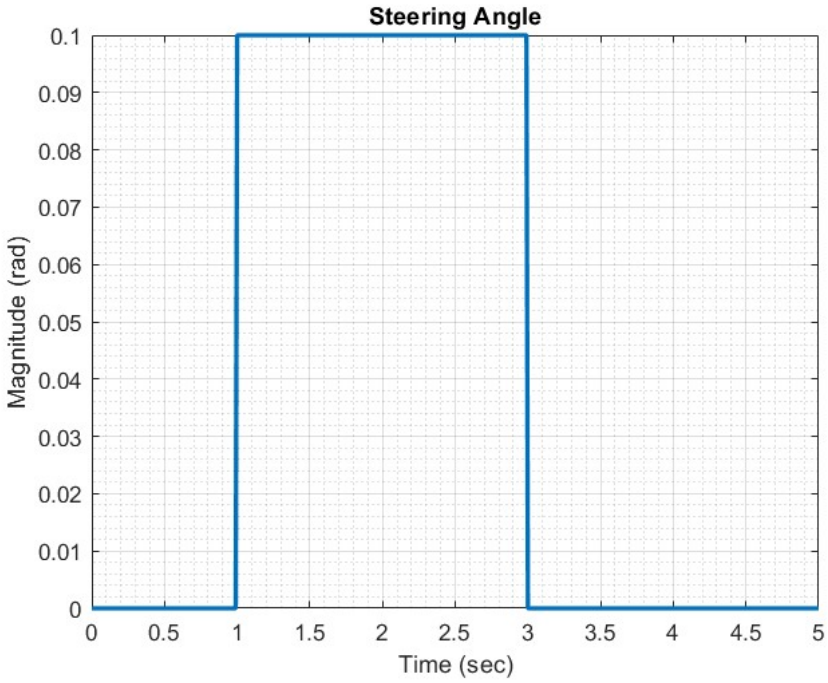

Figure 3.13: Steering Angle Input

The lateral velocity and the vehicle CG yaw rate are the model outputs and have been analyzed with and without tire lag dynamics respectively. Figure 3.14 and Figure 3.15 shows the two vehicle output parameters. From these plots, it can be seen that, the effect of tire lag is evident in the form of a phase shift within the lateral velocity and yaw rate. This is in agreement with the fact that introduction of lag dynamics, as a first order differential equation, helps to model the delay in the lateral force generation at the contact patch.

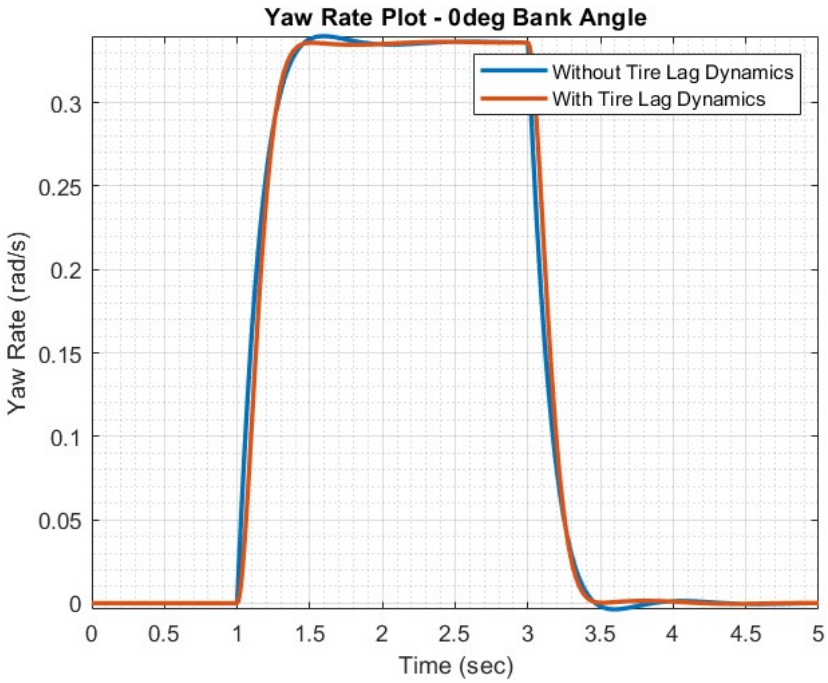

Figure 3.14: Vehicle CG Yaw Rate

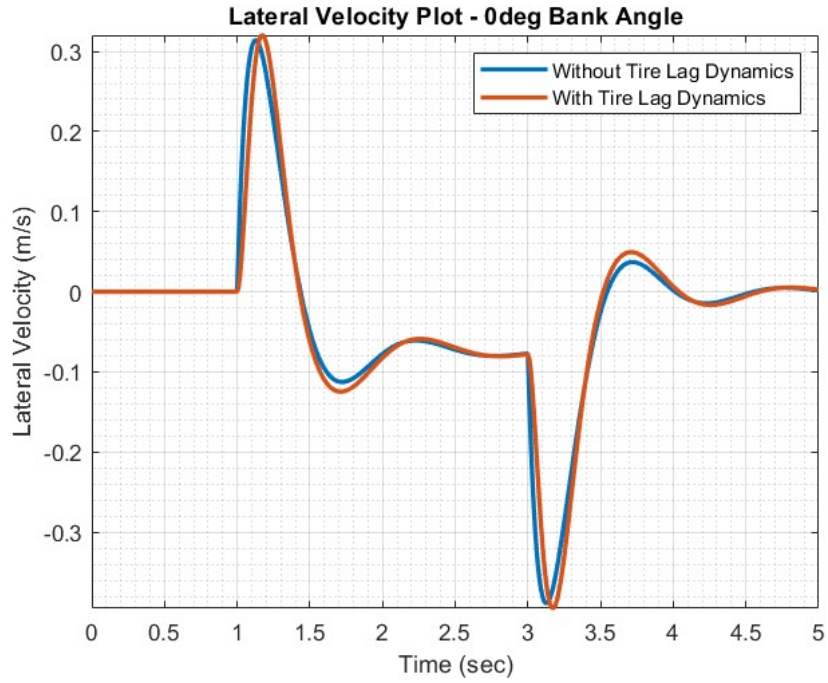

Figure 3.15: Vehicle CG Lateral Velocity

Chapter 4

Mathematical Modeling, Control Algorithm Development, and Experimental Validation of a Suspension Double Damper Setup

Some parts of this Chapter have been taken from Gorantiwar et al. [44].

4.1 Introduction

Automotive suspension systems are crucial to vehicle's road holding and ride comfort. When the tires traverse on uneven surfaces, the undulations in surface profile results in abrupt changes in the vertical forces on the tire which gets transmitted to the chassis via the axles and connecting mechanisms between the wheel hub and chassis. Such forces results in the tire not being in contact with the road at certain instants. Such effects are mitigated using energy dissipators like suspension systems. A major challenge faced in automotive suspension system design is the trade off between road-holding and ride comfort. Another bottleneck faced by suspension designers is the damping fluid used inside the shock absorber.

The state of the art automotive suspension system today include active dampers. As the name suggests, this system consists of an actuator component which could be either a hydraulic device or an electromagnetic actuator that generates forces to enhance road holding and ride comfort. While active suspension systems have been known to perform better than other existing suspension systems, namely the passive damper and semi-active dampers, several studies have concluded that active suspension systems are not commonly implemented simply because of the complexities in design and the higher cost.

Semi-active suspensions are currently the most widely used type of automotive suspension. While the performance of semi active dampers are not as close to the active counterparts, the lowered cost is definitely an incentive for commercial applications. These systems have the capability to vary the amount of damping fluid in the pressure chambers by essentially controlling the fluid flow across the pressure chamber in order to achieve either maximum ride handling or maximum road holding.

In [105], a non-linear parametric model of a mono tube damper has been developed and validated against experimental data. The bleed orifice flow has been modelled and the corresponding pressures in the compression and the rebound chambers have been analyzed . [106] has further improved upon this by modelling a mono tube damper taking into account the bleed orifice, shim stack and the leakage flows. This model has been further validated via performing a series of experimental tests on a shock dyno and the force-displacement, force-velocity plots have been analyzed for both the cases. Researchers in [107] have further studied the effect of varying the shim stack thickness and inducing a pre-deflection in the shims to conclude that increasing the shim stiffness increases the stiffness of the damper whereas pre-deflection of the shim stack increases the force transmission to the vehicle chassis.

The modelling of a double damper and the corresponding control algorithms are discussed in this chapter. The construction of the double damper can be seen in Figure 4.1. It can

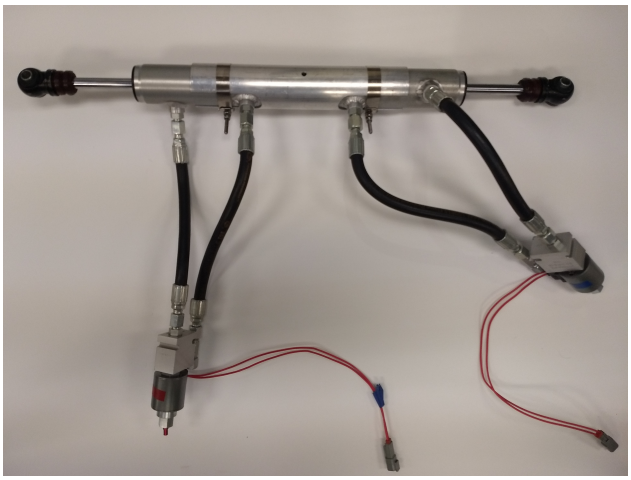

Figure 4.1: Semi-Active Double Damper

be essentially considered as two dampers connected to each other via a sleeve. The damper consists of 4 flow chambers characterizing the damper: Compression, Rebound, Gas ans By-pass. The gas chamber consists of compressed nitrogen gas and is located between the gas (floating) piston and the damper end. The compression chamber sits between the floating piston and the damper piston. The rebound chamber sits opposite to the compression chamber forming the lower pressure region. A semi-active valve forms the by-pass chamber, the area of which can be controlled which further results in having a control over the damping coefficient.

In this chapter, the double damper has been modeled taking into account the pressure and discharge variations corresponding to different road input displacements. Different control algorithms namely - Skyhook, Groundhook and Hybrid Skyhook-Groundhook control algorithms have been implemented on the double damper and its performance has been compared with the conventional passive and semi-active mono tube dampers. Different performance criteria - Sprung and unsprung mass displacement, suspension deflection and the comfort cost have been analyzed to determine the effectiveness of the dampers. This modeling has been further extended to compare with the experimental testing and validating the damper

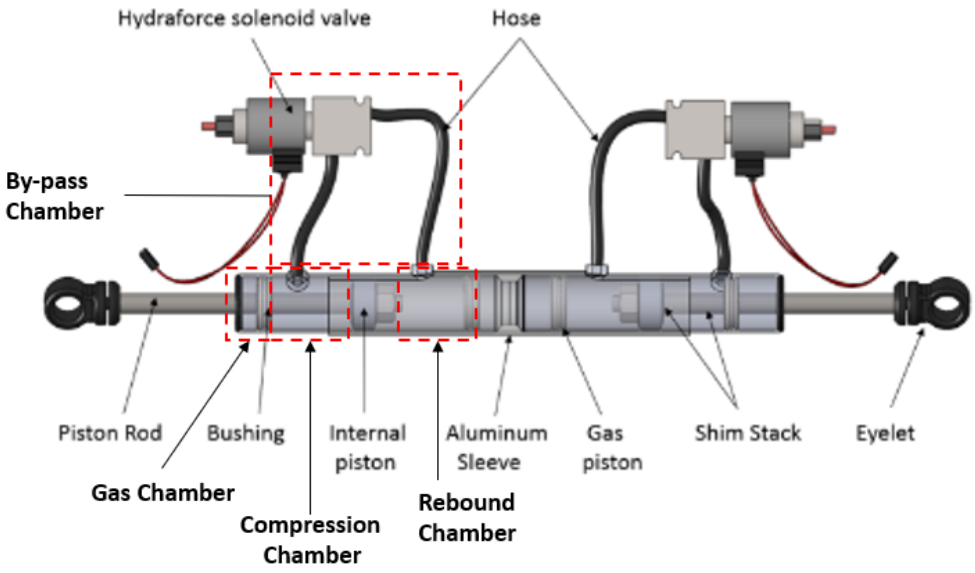

Figure 4.2: Construction of Double Damper

performance on a Shock Dyno Setup. Finally, Science Guided Machine Learning (SGML) framework has been developed as a control algorithm for improving the ride comfort and road holding properties.

4.2 Mathematical Modeling

4.2.1 Analytical Model of Single Passive Damper

As mentioned in the previous section, the damper consists of a compression chamber and the pressure chamber. The input to a damper in a "shock dyno" test rig is supplied at the suspension rod end. The force transmitted through this rod to the suspension body is measured by a force transducer. The transmission of this force involves the dynamic interaction of both solid components, which are assumed to behave as rigid bodies and fluid components, which in this case are the suspension fluid. The input force supplied at

the suspension rod is transmitted via the piston into the fluid, which results in the fluid compression. This compression force acted upon the fluid is then transmitted to the damper body which is finally measured by the force transducer.

The resultant damper force depends on certain parameters such as compression pressure, rebound pressure, gas chamber pressure, total discharge, valve discharge, leakage discharge, and bleed discharge.

The damper force can be modeled as follows:

$$F_{damper} = m_p\ddot{x} - p_r A_r + p_c A_c + F_f \tag{4.1}$$

where, m_p is the piston-rod assembly mass

$\ddot{x}$ is the piston-rod assembly acceleration along its longitudinal axis

p_r is the rebound pressure

p_c is the compression pressure

A_r is the effective area in the rebound chamber

A_c is the effective area in the compression chamber

F_f is the friction force acting on the piston-rod assembly.

The problem now becomes one of finding the values of p_c, p_r and F_f. In this model, the friction force, F_f and the areas, A_r and A_c are assumed to be constant. The unknown pressure terms can be solved using the conservation of mass principle. From Figure 4.2, it can be seen that during a compression stroke, the damping fluid moves into the rebound chamber. If the piston-rod velocity and the effective area of flow are known, then the total discharge due to the piston-rod movement can be calculated. However, the possible channels for the fluid to flow through are the bleed valve, the shim stack opening and leakage. If

Q_{bleed}, Q_{valve} and Q_{lp} are the flows either into the compression chamber or the rebound chamber, then the total flow rate denoted as $Q_{discharge}$, into a particular chamber is the sum of the flows through individual channels, which is expressed by Equation 4.2.

$$Q_{discharge} = Q_{bleed} + Q_{valve} + Q_{lp} \tag{4.2}$$

Since the input velocity of the piston-rod assembly is known and the effective flow area, which is A_r during the rebound stroke and A_c during the compression stroke is a constant, the total discharge can be obtained using,

$$Q_{discharge} = A_i \dot{x} \tag{4.3}$$

where, $i \, \epsilon \, \{r, c\}$

The bleed flow rate is modelled as shown in Equation 4.5.

$$Q_{bleed} = A_b C_d \sqrt{(2\Delta p_{CR})/\rho} \tag{4.4}$$

$$\Delta p_{CR} = p_{compression} - p_{rebound} \tag{4.5}$$

where, A_b is the bleed valve area

C_d is the coefficient of discharge of the bleed valve

ρ is the fluid density.

The flow rate through the shim stack valve is obtained using Equation 4.7.

$$Q_{valve} = A_v C_D \sqrt{2\Delta P_{VR}/\rho} \tag{4.6}$$

$$p_{VR} = p_{valve} - p_{rebound} \tag{4.7}$$

$$ky = \Delta p_{RV} A_v + \left(\frac{Q_v^2 c_f A_o}{\rho} \right) - F_{sp} \tag{4.8}$$

where

k is the shim stiffness

A_v is the valve area

A_o is the area of the orifice flow

c_f is the momentum coefficient.

The leakage flow rate is modeled by considering the viscosity of the fluid and the length of the leakage of the fluid as shown in Equation 4.9.

$$Q_{lp} = \left(\frac{\Delta p b^3}{12 \mu l} + \dot{x} \frac{b}{2} \right) \pi D_p \tag{4.9}$$

It can be seen from Equation 4.1 that the resultant force depends on the pressure terms. The compression chamber pressure is obtained as a function of the piston-rod assembly

acceleration and displacement and the initial gas pressure, which is then used along with Equations 4.2 to 4.16 to solve for the chamber pressures iteratively. The relation for compression pressure is as developed in Equation 4.10.

$$p_c = \frac{A_{rod} m_{gp}}{{A_{gp}}^2} \ddot{x} + p_{gi} \frac{A_{gp} L_g}{A_{gp} L_g - A_{rod} x} \tag{4.10}$$

where,

p_{gi} is the initial gas pressure

x is the piston-road assembly displacement

A_{gp} is the area of the gas piston

A_{rod} is the rod diameter

m_{gp} is the mass of the floating piston

$\ddot{x}$ is the piston-rod assembly acceleration

L_g is the thickness of the gas piston

4.2.2 Analytical Model of Double Passive Damper

As mentioned in the previous subsection, the double damper is made by combining two single dampers joined at the sleeve. The problem definition in comparison to the single damper changes in the sense that, the damper body can also be taken now as another degree of freedom. From a dynamics point of view, the double damper system now contains a moving lower piston-rod assembly, upper piston-rod assembly and the damper body. While the single damper was a single degree of freedom system, the double damper is a three degree of freedom system. The modeling of the double damper essentially comes down to determining

the resultant forces acting on the two piston-rods. The forces are obtained similar to the single damper, however, the only terms that change in the model are the rigid-body mechanics terms. The lower piston-rod is connected to the unsprung mass hence the subscript u and the upper piston-rod is connected to the sprung mass, hence the subscript s is used. Since the model now has the displacement and velocities as well as four pressure chambers, the notations are defined as the following: ${}^{i}\theta_{j}$, where i represents the damper configuration *i.e.* the upper or lower damper and i takes u, for the upper damper, l for the lower damper and b for damper body. j represents the pressure chamber and j takes c for the compression chamber and r for the rebound chamber. θ can represent any parameter in the modelling process like displacement, velocity or pressure.

It can be seen that the three bodies are moving relative to each other. The lower-piston rod connected at the unsprung mass moves relative to the body, hence the input displacement to the lower piston-rod end is taken as ${}^{b}x - {}^{u}x$ and the input-velocity is taken as ${}^{b}\dot{x} - {}^{u}\dot{x}$. Similarly, the input displacement at the piston-rod connected to the sprung mass is taken relative to the body displacement as ${}^{b}x - {}^{s}x$ and the input velocity to the upper piston-rod is taken as ${}^{b}\dot{x} - {}^{s}\dot{x}$.

4.2.3 Quarter Car Integrated with Damper Models

The double damper has been integrated with a 2 Degree of Freedom Quarter Car Model to evaluate the sprung and unsprung mass displacements corresponding to a step road input. The equations of motion of the sprung mass and unsprung mass are as below:

$$ {}^{s}m{}^{s}\ddot{x} = -k_d\left({}^{s}x - {}^{u}x\right) - F_{upper} \tag{4.11} $$

$$ {}^{u}m{}^{u}\ddot{x} = -k_t\left({}^{u}x - {}^{r}x\right) - c_t({}^{u}\dot{x} - {}^{r}\dot{x}) - F_{lower} \tag{4.12} $$

The F_{upper} and F_{lower} terms replace the damping force term $c({}^{s}\dot{x} - {}^{x}u)$. The values of F_{lower} and F_{upper} come directly from the double damper model instead. F_{lower} is the damping force that acts on the unsprung mass and F_{upper} is the damping force that acts on the sprung mass. ${}^{r}x$ denotes the road profile input. A key point to be noted is that, the damper model takes into account the dynamics of the damper body as well since it is not fixed to either the sprung or unsprung mass. The motion of the damper body is the result of the forces exerted by the fluids inside the damper. While the damping forces, F_{upper} and F_{lower} are obtained by solving the pressure models, the force experienced by the damper body is obtained as Equation 4.1. It can also be seen that there is no explicit displacement or velocities in the model to calculate F_{body}. However, the pressure models are dependent on the sprung and unsprung mass displacements and velocities, which in turn affects the damper body dynamics.

$$ {}^{b}m{}^{b}\ddot{x} = F_{body} \tag{4.13} $$

$$ F_{body} = {}^{s}p_c{}^{s}A_c + {}^{u}p_r{}^{u}A_r - {}^{u}p_c{}^{u}A_c - {}^{s}p_r{}^{s}A_r \tag{4.14} $$

The parameters of the Quarter Car are listed in Table 4.1.

Table 4.1: Quarter Car Parameters

Serial Number	Type	Value (in)
1	Tire Stiffness	704 N/m
2	Tire Damping Coefficient	88.6 Ns/m
3	Suspension Stiffness	600 N/m
4	Sprung Mass	180 kg
5	Unsprung Mass	40 kg

4.3 Control Strategies for Suspension Control

Different suspension control algorithms have been investigated in order to obtain a trade off between two performance metrics namely, ride comfort and road holding. Ride comfort emphasizes on the comfort of the passengers which is directly correlated with the sprung mass acceleration while the latter looks at maximizing the traction force between the wheel and the road surface. Two suspension control strategies have been implemented which take into account the sprung and unsprung mass velocities in deciding the damping coefficient of the system at that instant. The controllable terms F_u and F_s can be manipulated by controlling the flow through a solenoid valve. The model counterpart of the solenoid valve is defined as $Q_{control}$. The equations of motion and force models remain the same as above, however, the total discharge term is now updated as the damper fluid can pass through the added channel. The total discharge model now becomes,

$$Q_{total} = Q_{valve} + Q_{bleed} + Q_{lp} + Q_{control} \tag{4.15}$$

$$Q_{control,i} \triangleq 2^i A_{ct} C_d \sqrt{\frac{\Delta P R_i}{\rho}} \tag{4.16}$$

where, $i \epsilon \{s, u\}$ and A_{ct} is the controllable area. Suspension control algorithms like skyhook

control, groundhook control etc are modelled in terms of damping coefficients. Based on certain criteria, the damping coefficient, $c = c_{max}$ or $c = c_{min}$. Based on the solenoid valve control, c_{min} results when the valve is fully open which corresponds to $A_c = max(A_c)$ and c_{max} implies maximum damping which corresponds to the solenoid being fully closed, *i.e.* $A_c = 0$. Based on this control approach, two control algorithms were implemented on the quarter-car model integrated with a double damper.

4.3.1 Skyhook Control

Skyhook control is a semi-active suspension control strategy which assumes that the chassis is "connected" to the sky (fixed reference plane) in order to minimize the oscillations of the sprung mass i.e. the vehicle chassis. Figure 4.3 shows the schematic diagram of the Skyhook control on a quarter car model. On-off Skyhook control is one of the most commonly used control methodologies, which refers to the damping coefficient oscillating between only two fixed values depending upon the constraint equation.

$$\begin{aligned} \dot{x}_{sprung}(\dot{x}_{sprung} - \dot{x}_{unsprung}) \geq 0 \\ c_{sky} = c_{max} \\ \dot{x}_{sprung}(\dot{x}_{sprung} - \dot{x}_{unsprung}) < 0 \\ c_{sky} = c_{min} \end{aligned} \tag{4.17}$$

where, $\dot{x}_{sprung}$ is the Sprung mass velocity, $\dot{x}_{unsprung}$ is the Unsprung mass velocity and c_{sky} is the Damping Coefficient.

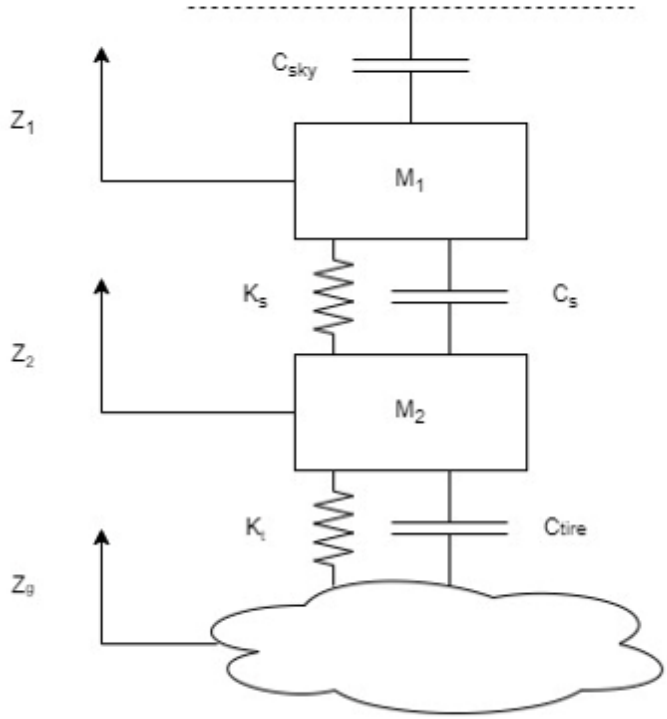

Figure 4.3: Skyhook Control Schematic Diagram

4.3.2 Groundhook Control

Groundhook control strategy modifies the Skyhook in the sense that it assumes that the unsprung mass is "connected" to a damper which is further connected to the ground i.e. a fixed reference plane. Figure 4.4 shows the schematic diagram of the Groundhook control on a quarter car model. Such a strategy allows to have a higher control on the unsprung mass displacements to improve the road holding characteristics.

$$-\dot{x}_{unsprung}(\dot{x}_{sprung} - \dot{x}_{unsprung}) \geq 0 \tag{4.18}$$

$$c_{ground} = c_{max}$$

$$-\dot{x}_{unsprung}(\dot{x}_{sprung} - \dot{x}_{unsprung}) < 0$$

$$c_{ground} = c_{min}$$

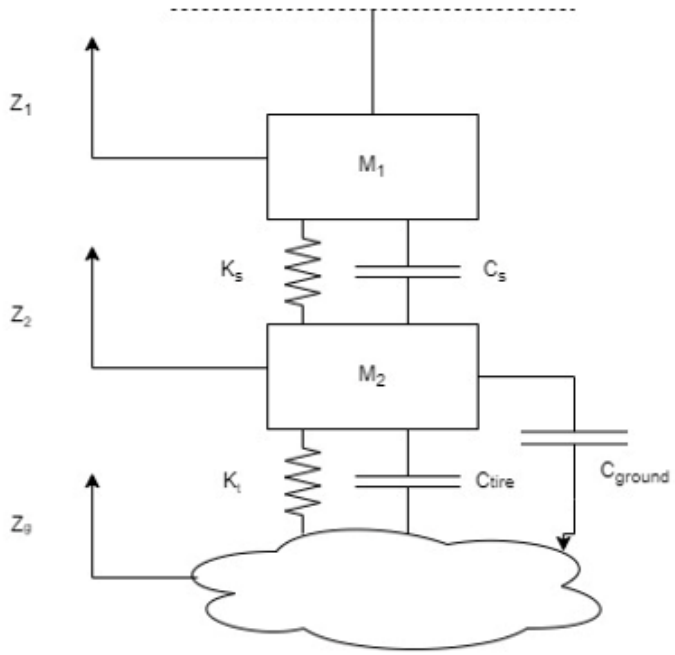

Figure 4.4: Groundhook Control Schematic Diagram

4.4 Results

This section comprises of the simulation results obtained for both the single and the double damper with different control strategies. Figure 4.5 shows the inner layer of the Simulink

architecture for modelling the compression and rebound zones of the double damper. Three metrics have been evaluated to compare the performance of the different damper configurations, namely: a)Sprung and Unsprung Mass Displacements b) Suspension Deflection and c) Comfort Cost - Chassis and Tire Hop Frequency Zones

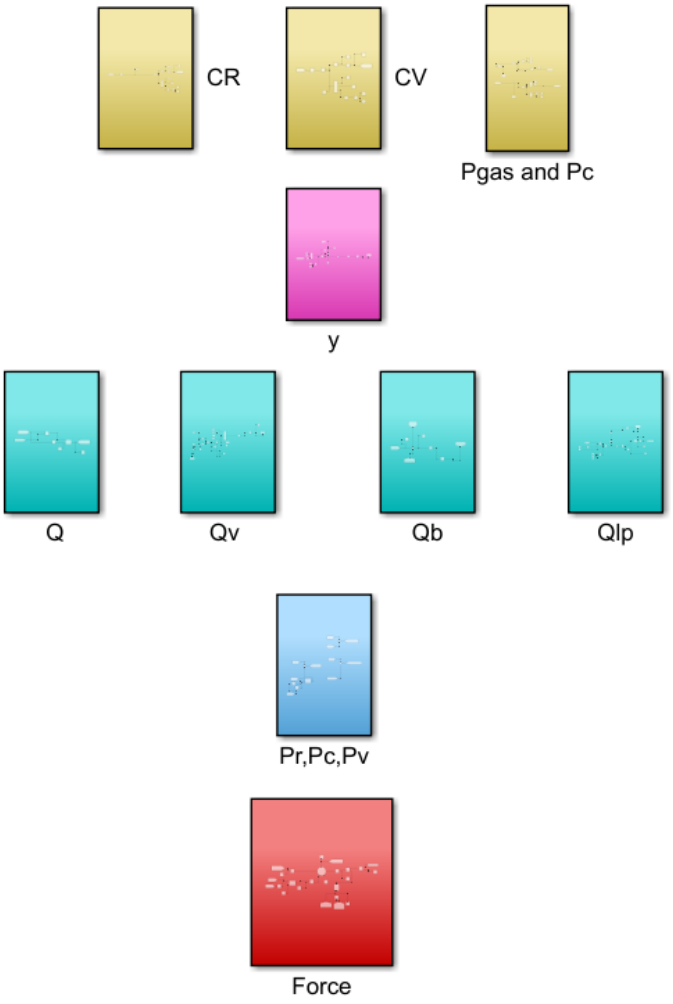

Figure 4.5: Simulink Architecture of the Double Damper Model

Sprung and Unsprung Mass Displacements

The damper performance has been studied for step road input which can be seen in Figure 4.6.

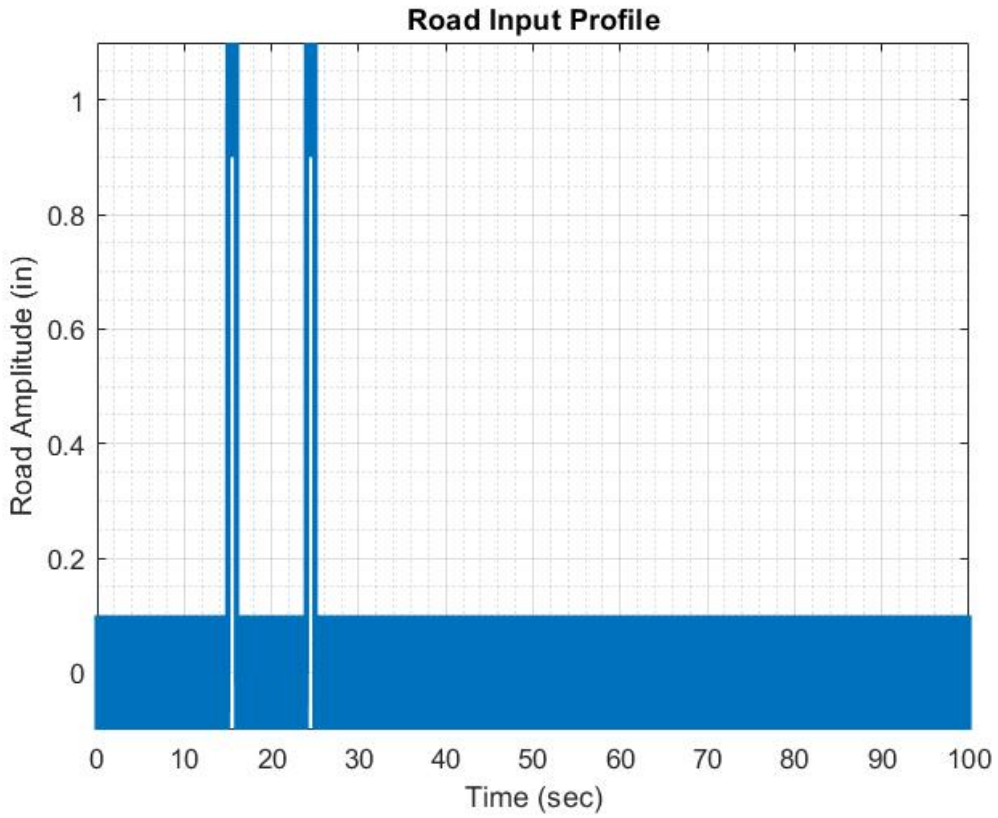

Figure 4.6: Road Profile

The sprung mass displacement can be perceived directly as the vertical motion experienced by the passenger which corresponds to ride-comfort. The unsprung mass displacement on the other hand could be perceived in terms of road holding. The sprung mass displacements of the different damper-control configurations can be seen in Figure 4.7. From the figure, it is seen that a single damper with sky-hook results in high amplitude oscillations. The settling time remains largely similar for all the configurations, however, the amplitude variation expressed in terms of Root Mean Squared value of the displacement, is seen to be the lowest for the double damper implemented with a Groundhook Control strategy. The Root Mean Squared of sprung mass displacements are summarized in Table 4.2.

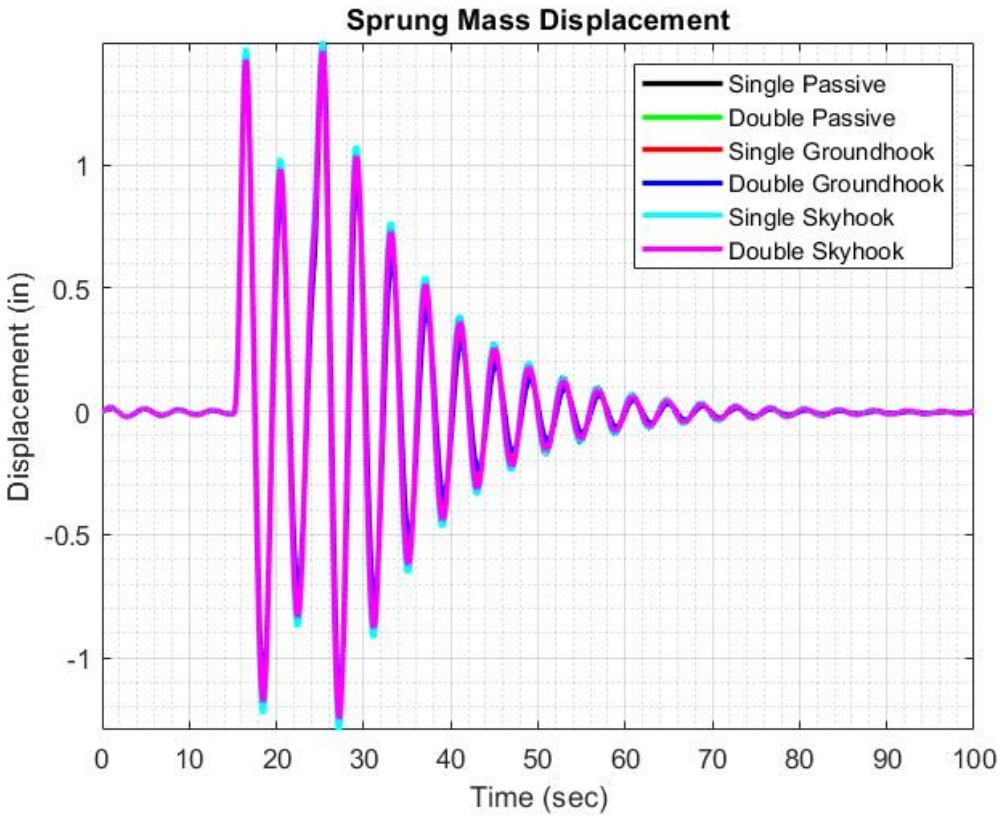

Figure 4.7: Sprung Mass Displacement

The variation of the unsprung mass displacements to the applied road input for different damper types can be seen in Figure 4.8. It can be seen that single dampers with both skyhook and ground hook control have significantly higher peak amplitudes. On the other hand, the double damper with the Groundhook control provides significant reduction in the unsprung mass displacement equating to a **47.2%** decrease as compared to the single passive damper.

From the above results, it is seen that the unsprung mass displacement is significantly reduced when using a double damper however, the sprung mass displacement reduction is not as much significant. This could be due to the movement of the damper body itself. While the force transmitted to the lower damper can be counteracted by the control mechanism,

Table 4.2: RMS Sprung Mass Displacement

Serial Number	Type	Value (in)
1	Single Passive	0.3623
2	Single Skyhook	0.3688
3	Single Groundhook	0.3471
4	Double Passive	0.3589
5	Double Skyhook	0.3544
6	Double Groundhook	0.2400

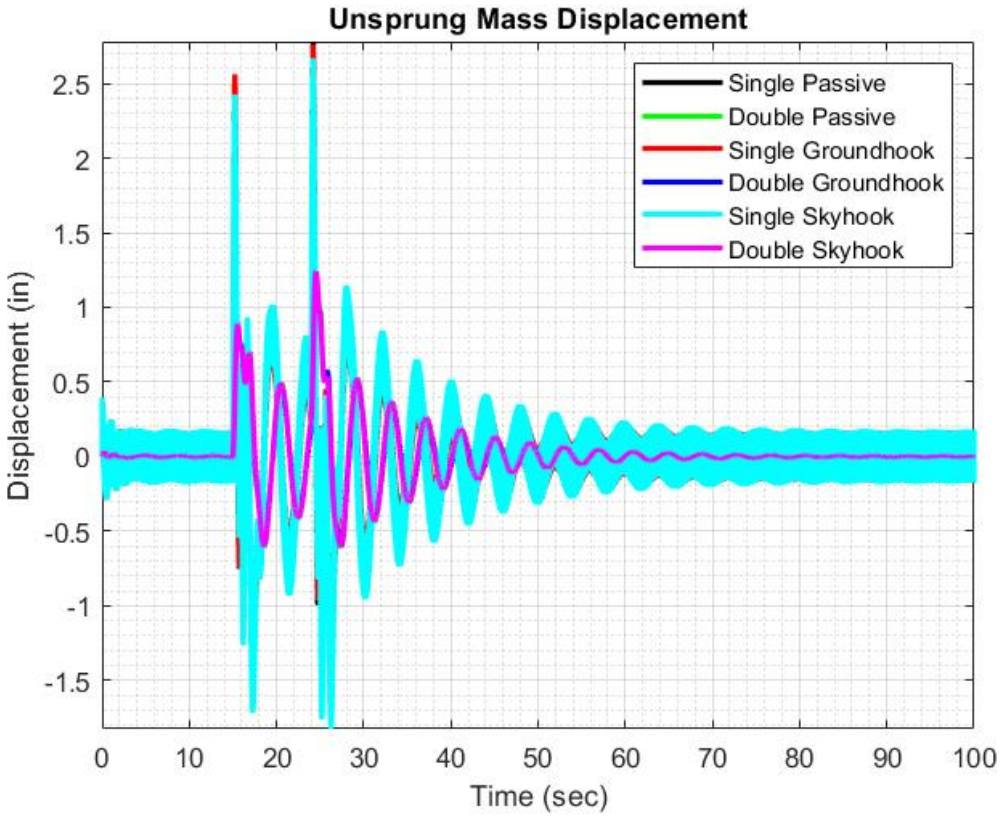

Figure 4.8: Unsprung Mass Displacement

the motion of the damper body is transmitted through the piston-rod into the sprung mass motion which results in the reduced decrease in sprung mass displacement.

Table 4.3: RMS Unsprung Mass Displacement

Serial Number	Type	Value (in)
1	Single Passive	0.3746
2	Single Skyhook	0.3751
3	Single Groundhook	0.3641
4	Double Passive	0.2091
5	Double Skyhook	0.2077
6	Double Groundhook	0.1973

Table 4.4: RMS Suspension Deflection

Serial Number	Type	Value (in)
1	Single Passive	0.5216
2	Single Skyhook	0.5261
3	Single Groundhook	0.5078
4	Double Passive	0.1838
5	Double Skyhook	0.1823
6	Double Groundhook	0.1716

Suspension Deflection

To have a better understanding of the damper performance in both the domains, the suspension deflection metric has been calculated which is given by Equation 4.19.

$$x_{deflection} = x_{sprung} - x_{unsprung} \tag{4.19}$$

where $x_{deflection}$ is the Suspension Deflection, x_{sprung} is the sprung mass displacement and $x_{unsprung}$ is the unsprung mass displacement.

The RMS values of the suspension deflection have been computed for these configurations and the double damper with groundhook control resulted in the least RMS deflection value.

Comfort Cost Analysis

Comfort Cost is a performance metric which is used to characterize the ride comfort/road holding felt by the passenger in terms of the sprung mass/unsprung mass displacement. Lower the value of this comfort cost, smoother is the ride quality. In order to quantify the ride comfort and obtain the comfort cost values, the frequency response of the suspension system is evaluated.

The general procedure to calculate the comfort cost is as follows:

1. Road input disturbance in the form of a continuous sinusoidal wave.
2. Measuring the sprung mass displacement as the response of the system
3. Calculating the Power Spectral Density (PSD) of the response by taking its discrete Fourier Transform.
4. Evaluating the comfort cost i.e.taking the ratio of the PSD of the developed suspension model and the PSD of a reference passive suspension system.

Comfort cost is evaluated for two frequency zones - Chassis Hop and Tire Hop. Each zone determines whether the suspension performs better in terms of the ride comfort or the road holding characteristics respectively.

The areas under the Power Spectral Density (PSD) plot of the signal in the frequency domain in both low-frequency (chassis responses) and high frequencies (tire-hop) are a measure of the damping characteristic of a damper, as in Equation (4.20).

$$G(X, f_1, f_2) = \int_{f_1}^{f_2} |X(f)|^2 df \tag{4.20}$$

where, $G(X, f_1, f_2)$ represents a function that calculates the squared area under signal $X(f)$, in the range of frequencies of interest f_1 and f_2.

However, since the system is a discrete time system, numerical integration by trapezoidal method is used as in Equation (4.21).

$$G(X, f_1, f_2) = \frac{f_2 - f_1}{2N} \sum_{n=1}^{N} (X(f_n) + X(f_{n+1}))^2 \tag{4.21}$$

where, N are the number of points in the signal. This normalized cost function Equation (4.22) represents the "Comfort Cost," which is used as a metric for evaluating the control algorithm.

$$J_{comfort} = \frac{G(F_z, 0, 20)}{G(F^{nom_z}, 0, 20)} \tag{4.22}$$

where, $G(F_z^{nom}, 0, 20)$ is the nominal (passive) reference suspension variance gains from 0 to 20 Hz; $G(F_z, 0, 20)$ is the variance gain of the system considered.

Chassis Hop Frequency Zone

Chassis Hop Frequency Zone is generally characterized between 1-5Hz of the frequency response of the sprung mass displacement.

From Figure 4.9 we can see that the double damper with the Groundhook control has the smallest value of the comfort cost indicating a smoother ride whereas the single damper with Skyhook control performs the worst in this aspect.

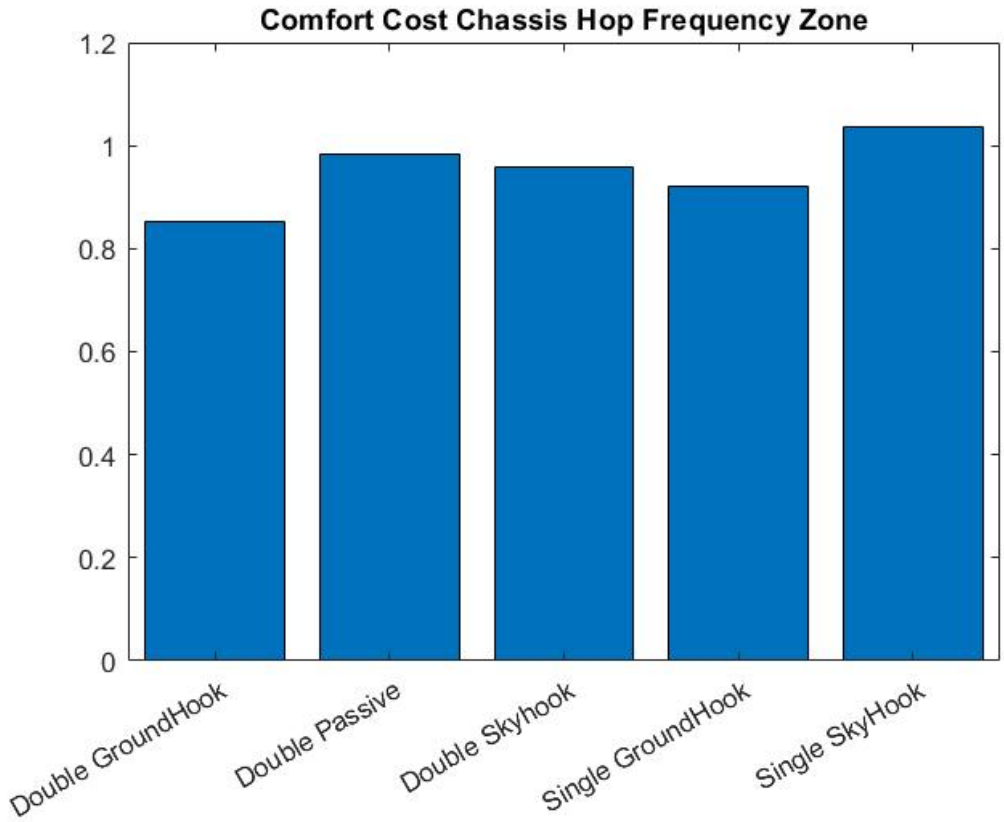

Figure 4.9: Comfort Cost for Chassis Hop Zone

Tire Hop Frequency Zone

Tire Hop Frequency Zone is generally characterized between 6-15Hz of the frequency response of the sprung mass displacement.

From Figure 4.10, the Groundhook double damper resulted in the least value of comfort cost.

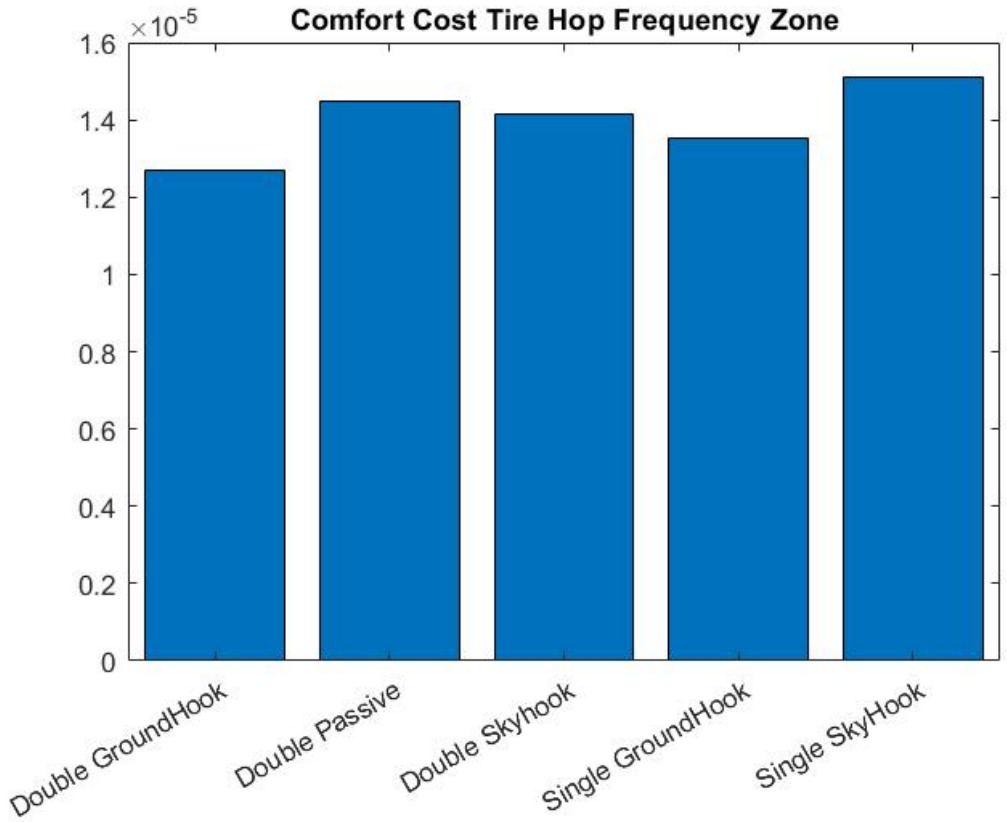

Figure 4.10: Comfort Cost for Tire Hop Zone

4.5 Experimental Testing and Validation

A Double Damper (Figure 4.1) consists of two controllable dampers placed in series and was used for carrying out the experiments. Tyagi [108] designed, developed, and manufactured this damper in-house at the Center for Tire Research (CenTire). The internal construction of the double damper is as shown in Figure 4.2. The damper consists of 4 main chambers—compression, rebound, gas, and by-pass, respectively. The gas chamber is at the top of the tube, and it is separated from the compression chamber by a floating piston. This piston separates the nitrogen in the gas chamber from the oil in the compression chamber. The compression chamber sits between the floating piston of the gas chamber and the piston. On the other side of the piston and opposite to the compression chamber is the

rebound chamber. The rebound chamber is connected to the piston of the damper by a rod. Also, it is connected to the compression chamber throw the by-pass valve. These by-pass valves are essentially solenoid valves, one for each damper. These valves control the flow rate of oil passing from the compression chamber to the rebound chamber for each individual damper. The damper was modeled, taking into account pressure and flow variations within the damper. The damper, as shown in Figure 4.1 has two controllable by-pass valves. Figure 4.2 illustrates different part of the double-damper.

For experimentation, a set of two springs is attached in parallel to the double damper. These springs correspond to the typical configuration of mounting a shock absorber in a vehicle. For the single damper, due to geometrical constraints, a single spring is attached in parallel to this damper. The spring attached in parallel with the single damper has a stiffness coefficient equivalent to the combined stiffness of the two springs in parallel with the double damper. The entire setup consisting of the double damper and springs mounted on the Shock Dyno can be seen in Figure 4.11.

This study's primary goal is to develop and implement a control algorithm for controlling the damping coefficient of the double damper based on the relative velocity difference between the sprung and unsprung mass in real-time. A dedicated experimental setup was developed for evaluating the performance of the semi-active double damper for different operating conditions. The control algorithm and its implementation for the double-damper are explained in the subsequent sections. Later results were compared to a semi-active single as a benchmark to evaluate the performance of the double-damper.

Different control strategies were implemented to minimize the vertical acceleration of the sprung mass and to improve the road-holding capabilities by varying the orifice area of the solenoid valves [109, 110, 111]. A hybrid control algorithm is developed that employs Groundhook control on the lower damper and Skyhook control on the upper damper [41].

Figure 4.11: Double Damper with springs system mounted on the Shock Dyno.

This algorithm is developed on MATLAB/Simulink and effectively deployed on the valves mounted on the Double Damper.

4.5.1 Hybrid Skyhook–Groundhook Control

Valášek et al. [41] performed an in-depth study on the combination of Groundhook and Skyhook control strategy for semi-active suspension systems mainly for trucks. In the case of the double-damper, the Groundhook control algorithm is implemented on the lower damper to ensure better road handling characteristics and Skyhook control algorithm on the upper damper. This strategy provides improved ride comfort. This concept of a hybrid control algorithm was reviewed by Goncalves and Ahmadian [40] in which they concluded that such an algorithm reduced the peak to peak displacements and accelerations of both sprung

and unsprung masses. A similar simulation study was conducted in [39] which showed the comparison between Skyhook, hybrid and a fuzzy hybrid control algorithm. They also found that the hybrid control algorithm proved to perform better than the individual Skyhook control. The control strategy is based upon the relative velocity difference obtained from three accelerometers mounted on the damper and Shock Dyno mounts. Skyhook control is based on the velocity difference between the double damper (Body Accelerometer) and the sprung mass (Upper Accelerometer) whereas the Groundhook control is based on the velocity difference between the unsprung mass (Lower Accelerometer) and the double damper (Body Accelerometer) as shown in Equation (4.23).

$$\begin{aligned} \dot{x_{upper}}(\dot{x_{upper}} - \dot{x_{body}}) \geq 0 \qquad & c_{sky} = c_{max} \\ \dot{x_{upper}}(\dot{x_{upper}} - \dot{x_{body}}) < 0 \qquad & c_{sky} = c_{min} \\ -\dot{x_{lower}}(\dot{x_{body}} - \dot{x_{lower}}) \geq 0 \qquad & c_{ground} = c_{max} \\ \dot{x_{lower}}(\dot{x_{body}} - \dot{x_{lower}}) < 0 \qquad & c_{ground} = c_{min} \end{aligned} \tag{4.23}$$

where

$\dot{x_{upper}}$: Sprung mass velocity

$\dot{x_{body}}$: Double damper velocity

$\dot{x_{lower}}$: Unsprung mass velocity

c_{sky} : Upper damping coefficient

c_{ground} : Lower damping coefficient

This section covers the complete system hardware of the system along with the description of each equipment and the overall process flow. Figure 4.12 shows the experimental setup

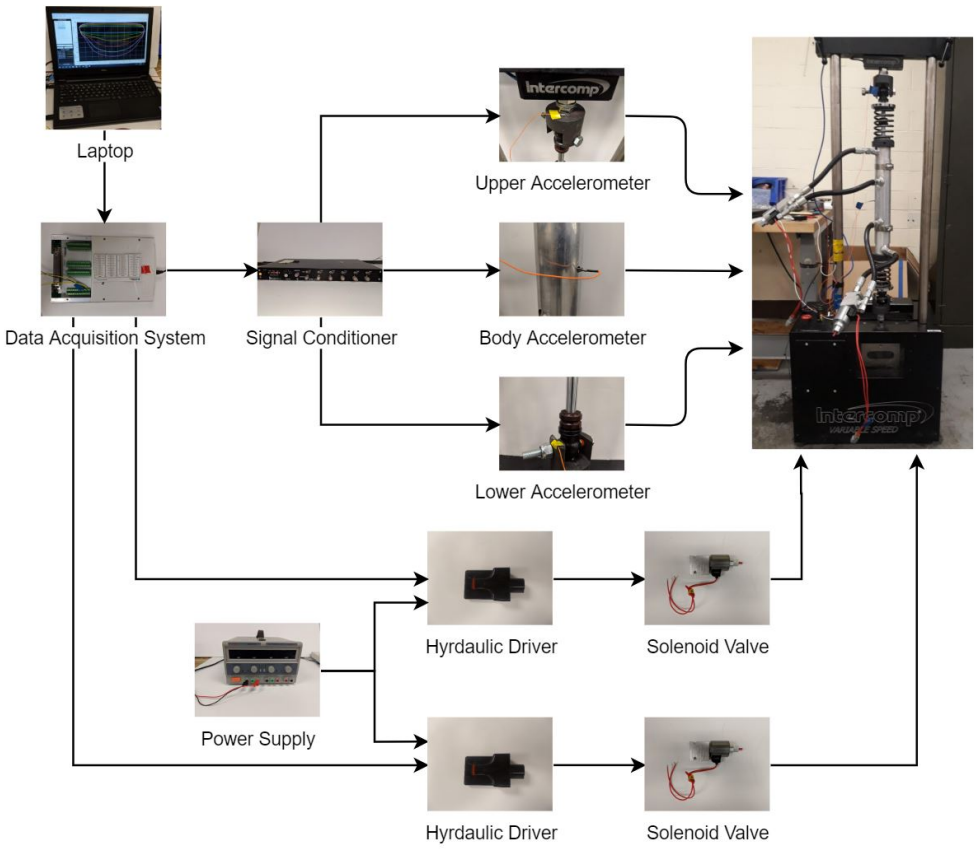

Figure 4.12: Assembly of Hardware Implementation.

used for data collection and testing of the damper on the Shock Dyno. Damper testing is carried out on the Shock Dyno covering frequencies from 0.25–3 Hz [112] that helps capture damper effects on yaw, roll, and pitch dynamics of a typical vehicle.

The experimental setup for testing the performance of the Double Damper system comprises of the components mentioned in Table 4.5.

Shock Dyno

An Intercomp Variable Speed Shock Dyno is used for providing the input excitation to the damper system. The parameters of the Shock Dyno are mentioned in Table 4.6. A load

Table 4.5: Experimental Apparatus.

Component	Quantity	Model
Double Damper	1	Built In-house
Data Acquisition System (DAQ)	1	NI DAQ USB 6225
Signal Conditioner	1	Dytran 4122b
Test Rig	1	Intercomp Variable Speed Shock Dyno
Valve Driver	2	Hydraforce EVDR-0101A
Solenoid Valve	2	Hydraforce SP10-24
USB-TTL-232R Cable	2	FTDI
Single Axis Accelerometer	3	Dytran 3225F1
Oscilloscope	1	Techtronix CDS-200B
DC Power Supply (12 V)	2	-

Table 4.6: Shock Dyno Specifications.

Parameter	Value
Adjustable Stroke	0.0254 m, 0.0381 m, 0.0508 m, 0.05715 m
Load Cell	907 kg
Variable Speed	0.0127–0.4826 m/s

cell is mounted on top of the upper eyelet of the damper. This arrangement ensures the measurement of the damper force transmitted to the vehicle chassis. The construction of the Shock Dyno is such that it has a provision of tightening or loosening the top eyelet (sprung mass) of the damper. This provision of loosening the top end is further used for adding different weights on top of the Dyno mimicking the sprung mass. In order to reduce the vibrations at the upper and the lower ends of the Shock Dyno, mounts were specifically designed corresponding to the eyelet dimensions of the dampers.

Accelerometers

Three single-axis accelerometers (Dytran Model 3225F1) are used for obtaining the accelerations at three different points of the Double Damper System. Three mounting points

Table 4.7: Single Axis Accelerometer Specifications

Parameter	Value
Sensitivity	10 mV/g
Frequency Response	1.6–10,000 Hz
Thermal Coefficient of Sensitivity	0.054/°C
Supply Current	2–20 mA
Compliance Voltage	+18 to +30 V

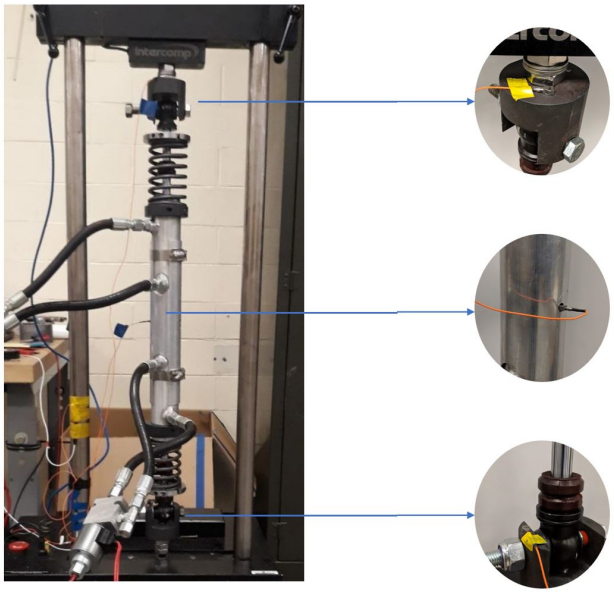

Figure 4.13: Double Damper with Three Single Axis Accelerometers.

are chosen on the damper and the Shock Dyno, as shown in Figure 4.13, which correspond to the unsprung, sprung, and the body accelerations. These are further used as inputs to the control algorithms. The primary reasons for choosing these accelerometers were their low sensitivity and wide frequency response. Petro wax is used as an adhesive for securing the accelerometers at their respective locations. The specifications of the accelerometer are mentioned in Table 4.7

Table 4.8: Signal Conditioner Specifications

Parameter	Value
Amplifier Gain	×1 , ×110, ×1100
Output Voltage Swing	±10 V
Sensor Supply Current Range	2–20 mA

Signal Conditioner

A Dytran 4122b signal conditioner is used for providing the required power supply to operate the accelerometers. The inputs to the signal conditioner are the three accelerometers, and the outputs are passed to the Data Acquisition System, which is explained in the subsequent sections.The key specifications of the signal conditioner have been stated in Table 4.8

Solenoid Valves

Two by-pass valves are mounted on the double damper to control the amount of fluid flow through the damper. van Rensburg et al. [113] focused on modeling the by-pass valve for a semi-active damper from which it was concluded that the involvement of fast-acting dynamics makes it necessary to use valves capable of handling high pressure and flow rates during damper testing. In order to take this into account, a Hydraforce SP10-24 valve is used for controlling the flow rate of oil from the compression end to the rebounding end in the experiment. It is a proportional solenoid-operated, 2-way, spool-type, normally closed, providing bi-directional fluid metering valve. The response time for the valve from fully closed to open fully is approximately 40 ms. It is acceptable to use these experiments since the sample rate chosen for sending the signal to the solenoid valve from the DAQ is 240 Hz. The gas chamber of the double damper is pressurized to an initial value of 1.37 Mpa. The nitrogen gas in the chamber attains the maximum pressure of 3.79 MPa when the damper is subjected to a velocity of 0.3048 m/s, which is the maximum velocity in this study).

Table 4.9: EVDR-0101A Driver Specifications

Parameter	Value
Power Requirements	9–32 VDC
Control Inputs Digital-Frequency	50–10,000 Hz
Control Output Current	50–2000 mA
Control Output PWM	40–400 Hz

The orifice area of the valve can be varied from 0–0.2 in^2 (0–0.005 m^2) thus allowing flow rate of the fluid flow to go upto 0.5 L/s (0.0005 m^3). The input to this solenoid valve is given by the digital output port of the DAQ via the valve driver.

Valve Driver

To accurately meter the opening and closing of the solenoid valve, an EVDR-0101A valve driver is used. This driver is a microprocessor-based valve driver mainly used in hydraulic proportional valve applications. It takes inputs from the Data Acquisition System, which drives the output current to the pre-defined ramp rate, enabling accurate and proportional metering control of the solenoid valve. HF-Impulse software is used for calibrating the driver corresponding to the input signal ratings. The valve driver specifications can be seen in Table 4.9.

The valve driver is calibrated using the HF-Impulse software, which enables the user to communicate with the EVDR driver as well as the solenoid valve. It can also be used to visualize the input as well as the control output signal, which will be given to the solenoid valve. The driver is calibrated such that it takes inputs from 0–5 volts and provides a current output for the solenoid valve to go from fully closed (0 A) to fully open (1.2 A) state. The current output of 1.2 A is as per valve specifications.

Table 4.10: Data Acquisition System Specifications.

Parameter	Value
Number of channels (Analog Input)	40 differential or 80 single-ended
ADC Resolution (Analog Input)	16 bits
Sample Rate (Analog Input)	250 kS/s (Multi Channel Maximum)
Counters/Timers	2 (32-bit resolution)

Data Acquisition System

A NI DAQ USB 6225 is used for collecting the accelerometer data. The analog outputs from all three accelerometers are fed to the analog input ports of the DAQ. A differential connection is used at the input port of the DAQ for connecting the three accelerometers. This sensor output data is then acquired using MATLAB/Simulink.

The specifications of the NI DAQ are mentioned in Table 4.10.

The sampling frequency was chosen as 240 Hz, which is the real-time limit of the highest sampling rate that could be achieved with the solenoid valve. Also, the 'Asynchronous' data collection method is used, which ensures that the data acquisition from the device and the simulation happen in parallel enabling quicker simulation time than the synchronous mode. Data from the device is continuously acquired into a FIFO (First In First Out) buffer in parallel as the simulation runs.

Figure 4.14 shows the process flow of the experimental setup and the interaction of each hardware with components within the system. Two separate laptops are used—one for operating the Shock Dyno and one for implementing the control algorithms and sending the control signals to the Data Acquisition System. This ensures faster processing for simultaneously running both the Shock Dyno and the control algorithms.

The testing and data collection process for the damper is carried out at different operating

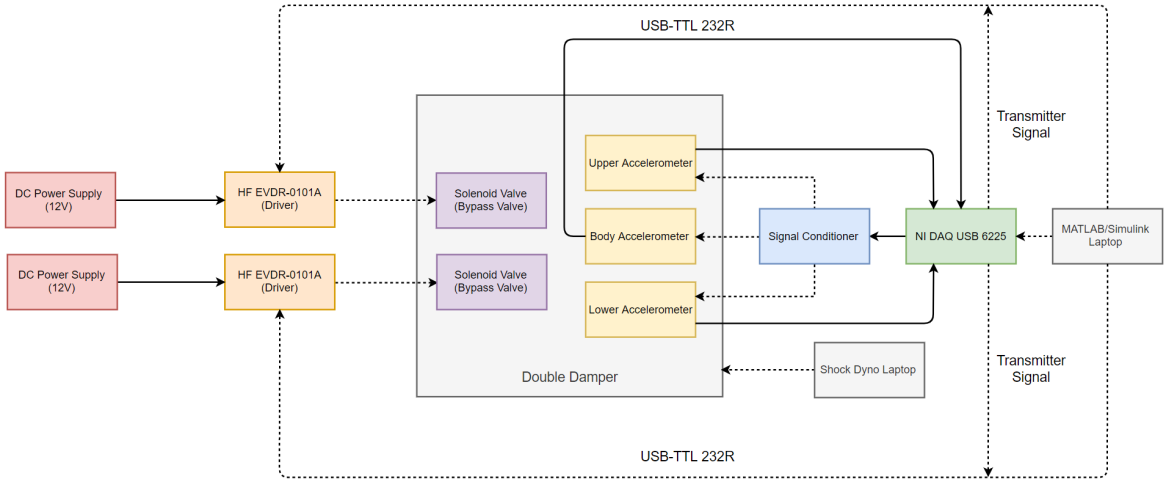

Figure 4.14: Block Diagram of the experimental setup for testing the Double Damper on Shock Dyno.

conditions to evaluate their effect on the damper performance. These parameters, which are varied during the testing, are explained in the subsequent subsection.

4.5.2 Testing Conditions

Loading Conditions

The damper is tested under two types of loading conditions. In the first scenario, the upper mount, on which the damper is mounted, is not free to move. This resembles the conventional damper testing on a Shock Dyno. Due to this kind of loading condition, the force characteristics of the double damper can be obtained for varying displacements and velocities. For the second scenario, as shown in Figure 4.15, in order to take into consideration the effect of sprung mass on the damper characteristics, an external load is added on top of the Shock Dyno, and the upper mount is made free to move. This provision also enables the

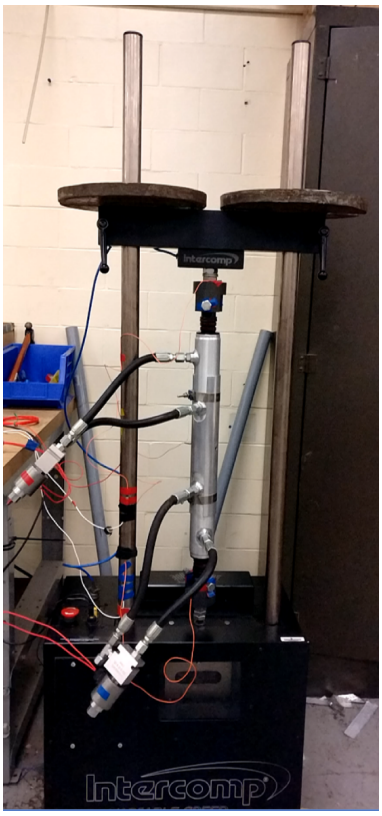

Figure 4.15: Application of Normal Load on the Shock Dyno.

use of control algorithms as the entire control logic is based on the velocity difference of the upper and lower mounting points. The upper limit of the normal load is taken to be 150 lbs (68 kg). This limit is decided based on the gas pressure inside the damper, which is in the order of 1.37 MPa. Exceeding the applied normal load above 68 kg, compresses the damper entirely up to its bottom dead center, and it starts behaving as a rigid body. The lower limit of the normal load is taken as 50 lbs (23 kg) based on the fact that loads less than this have no effect in compressing the piston and the damper starts behaving as a solid body.

Table 4.11: Different operating conditions for Damper Testing.

Normal Load lbs (kg)	Input Velocity in/s (m/s)	Control Algorithm
No Load (Upper Clamp Closed)	8 (0.20)	Hybrid Groundhook Skyhook
50 (22.6)	10 (0.25)	Skyhook
100 (45.35)	12 (0.30)	Groundhook

Input Velocity

In order to cover all the road frequencies, the damper is tested with different input velocities. The velocity range is between 8–12 in/s (0.2–0.3 m/s). The upper limit of the velocity is based on the constraint of the Shock Dyno; as above this speed, high-frequency vibrations are induced, resulting in corrupted accelerometer data. At lower velocities, after evaluating the accelerometer data, no significant difference could be found between the sprung and the unsprung accelerations. Hence the lower limit of the velocity was kept at 8 in/s (0.2 m/s).

Control Algorithm

The semi-active double damper is tested with a Hybrid Skyhook Groundhook control strategy and the single semi-active damper with Skyhook and Groundhook control to measure their ride comfort characteristics. Each control algorithm was modelled in Simulink with identical input parameters.

A brief overview of the testing conditions is summarized in Table 4.11.

The passive double damper characteristics are obtained by performing the conventional Shock Dyno test routine of clamping the upper end of the Dyno and evaluating the Force variations of the damper to changes in the input displacements and velocities. Each of these graphs is plotted for different velocities ranging from 0.025–0.15 m/s (1–6 in/s), as shown in the legend of each plot, respectively. The contours in blue represent the operating condition

of the damper at the lowest velocity i.e., 1 in/s (0.1 m/s). The velocities increase up to 6 in/s (0.15 m/s), in-unit increments, with the highest velocity shown by the pink contour.

Figure 4.16 shows the Force vs. Displacement plot of the double damper when it is subjected to no control algorithm, and the upper end of the Shock Dyno is not free to move. This condition resembles a passive damper as modeled by [108]. In this case, a continuous signal of +5 V is supplied to the solenoid valve which ensures that the valve is fully open during the entire test and the damping characteristics of the damper is at its minimum value. Each closed contour indicates the force-displacement plot at a specific velocity of the damper. The area under each contour shows the amount of energy absorbed by the damper for that cycle. The results agree with the literature that; as the velocity increases, the area under the contour plot increases.

Figure 4.17 shows the Force vs. Velocity plot of the damper when the solenoid valve is fully open. Similar to Figure 4.16, each contour indicates the force at a specific damper velocity. The hysteresis loop is observed during each cycle, indicating the presence of friction between the piston and the inner walls of the damper during the compression and the rebound stroke.

In order to observe the frequency domain characteristics and compare the dampers better, a method described in [114] is followed. In these experiments, the accelerometer data of the sprung mass and unsprung mass accelerations are recorded. The dampers are excited with a constant velocity in order to compare the response of the dampers to control logic.

This process for comparison of semi-active single damper and double damper performances can be seen in Figure 4.18. The single damper is initially tested for an unsprung input velocity of 0.2 m/sec, with a sampling frequency of 240 Hz. Fast Fourier transform of the signal is calculated by using Welch's method to see the frequency domain characteristics and differentiate between the control algorithms better. Since the conversion of a signal from

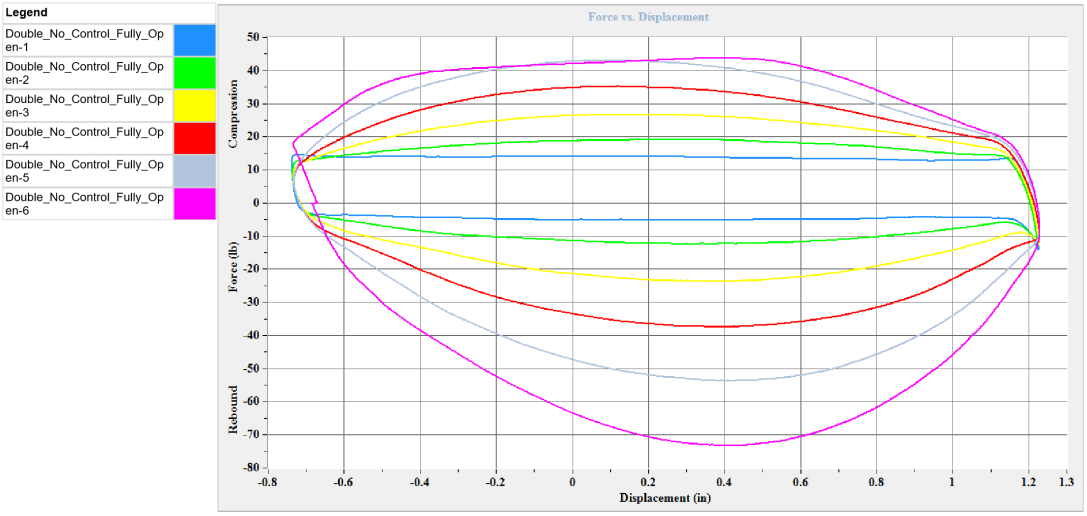

Figure 4.16: Force vs Displacement Plot for Passive Double Damper with Fully Open Valve (No Control).

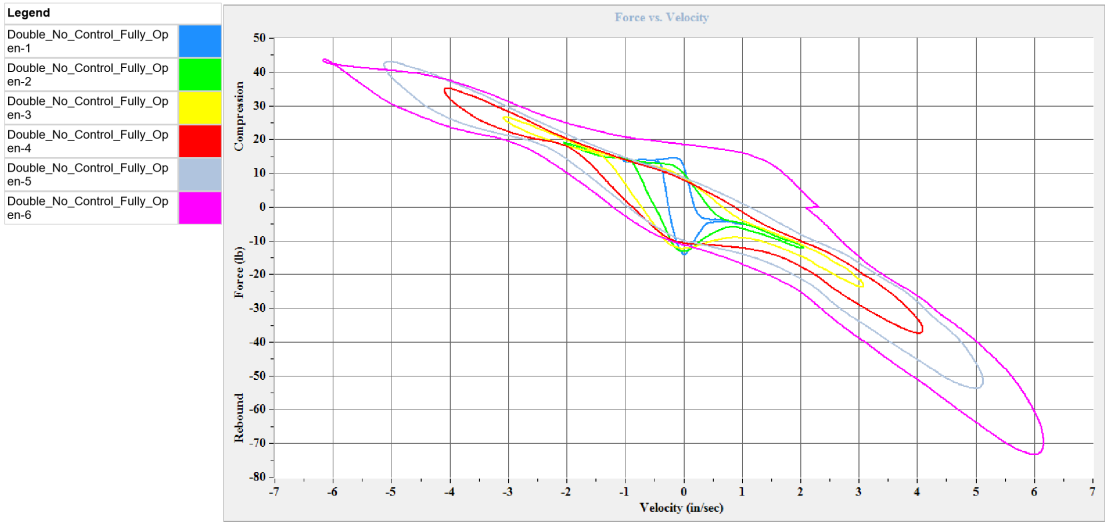

Figure 4.17: Force vs Velocity Plot for Passive Double Damper with Fully Open Valve (No Control).

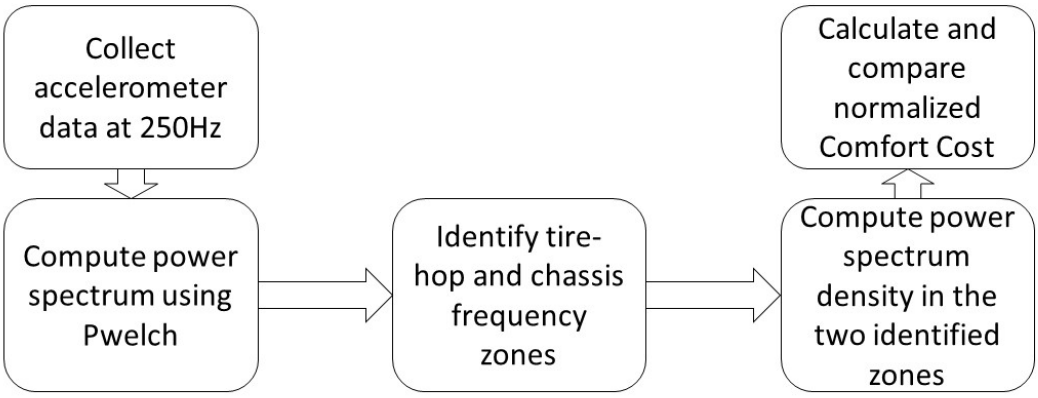

Figure 4.18: Data processing workflow.

time domain to frequency domain is sensitive to effects of noise, it is necessary to have a method that would not be affected by the presence of stochastic noise in the signal. Instead of extracting the Fourier coefficients of the time domain signal, Welch's method involving averaging and Hamming windowing Equation (4.24) is used.

$$w(n) = 0.54 - 0.46cos(2\pi\frac{n}{N}) \tag{4.24}$$

where,

$0 \leq n \leq N$

Window length L = N + 1

N is the total number of points

w are the coefficients of the Hamming window

The given signal is split into several sections using windowing techniques, and overlap. There is an overlap present between two consecutive sections in the signal. The power spectrum of each section, or window is computed, and overlapped hence eliminating effect of stochastic noise.

With this, the frequency domain plots for a single semi-active damper with Skyhook con-

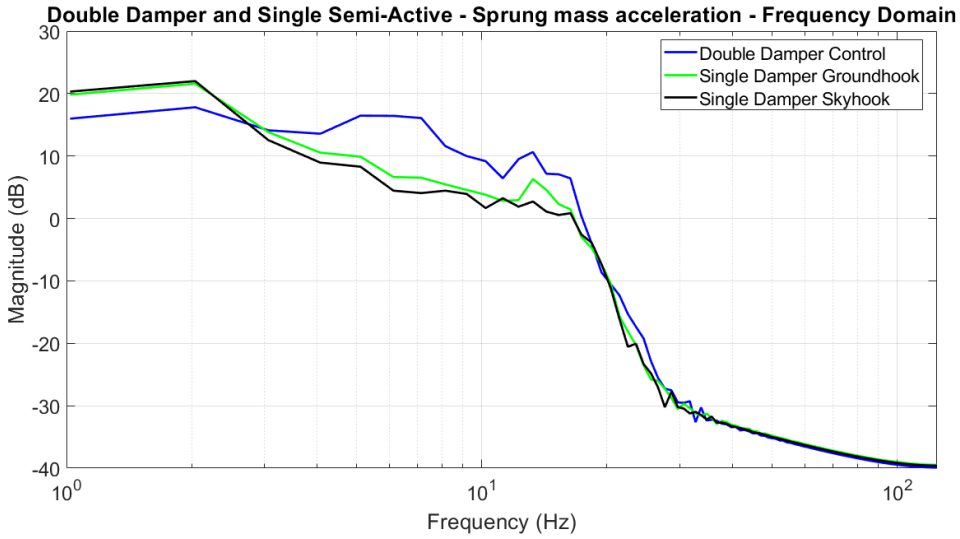

Figure 4.19: Frequency Domain sprung mass acceleration plot for semi-active single and double damper.

trol, single semi-active damper with Groundhook control, and double-semi active damper with Skyhook–Groundhook control are obtained. Two distinct zones of frequencies can be observed from Figure 4.19 , around 1 Hz and 10 Hz. These are the chassis/sprung mass frequency and tire-hop frequency, respectively. As seen in Figure 4.19, the area under the PSD plot in the chassis frequency zone is less for double damper with control, which signifies that the resonant peaks in that zone are damped, and the ride will be softer. In a nutshell, the smaller the "Comfort cost," the smoother is the ride quality. Following this, the "Comfort cost" is evaluated by using the method shown in Figure 4.20. This "Comfort cost" is the power spectrum density around the chassis frequency zone (Figure 4.21) and the tire-hop frequency zone.(Figure 4.22).

It can be concluded from "Comfort costs" that the double-damper with Groundhook- Skyhook controller has a smaller cost value. Hence giving a much smoother and softer ride as compared to the traditional Skyhook control and Groundhook control of the single-semi active damper. In addition to this, it is seen that in the tire-hop frequency zone, the double

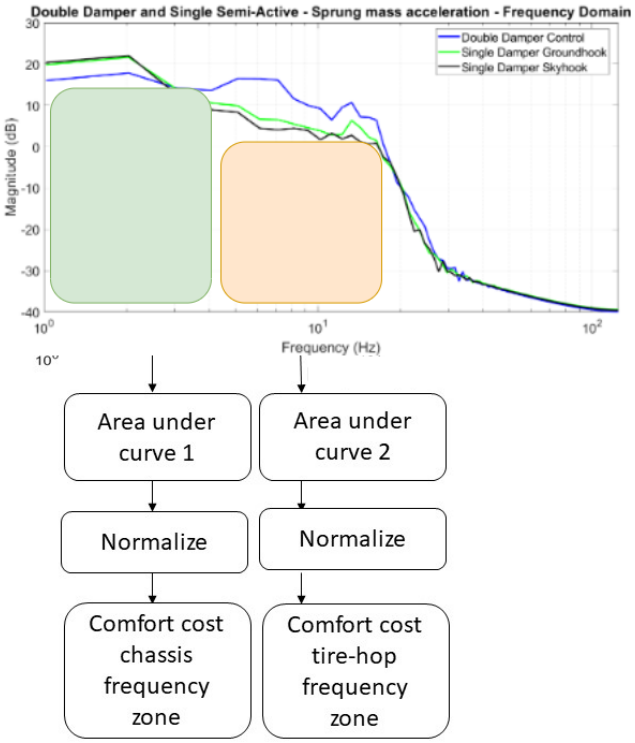

Figure 4.20: Method of computing comfort cost.

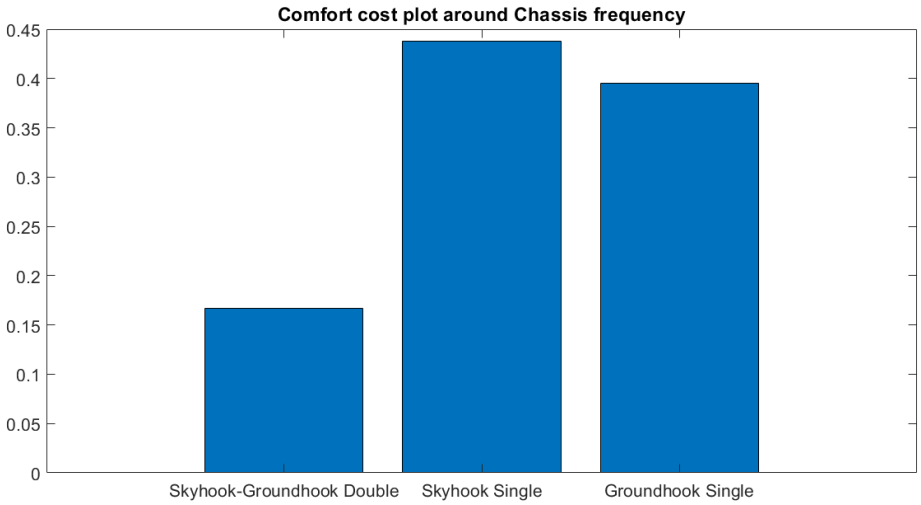

Figure 4.21: Normalized comfort cost plot—Comparing double-damper with control and single-damper with control, in Chassis frequency zone.

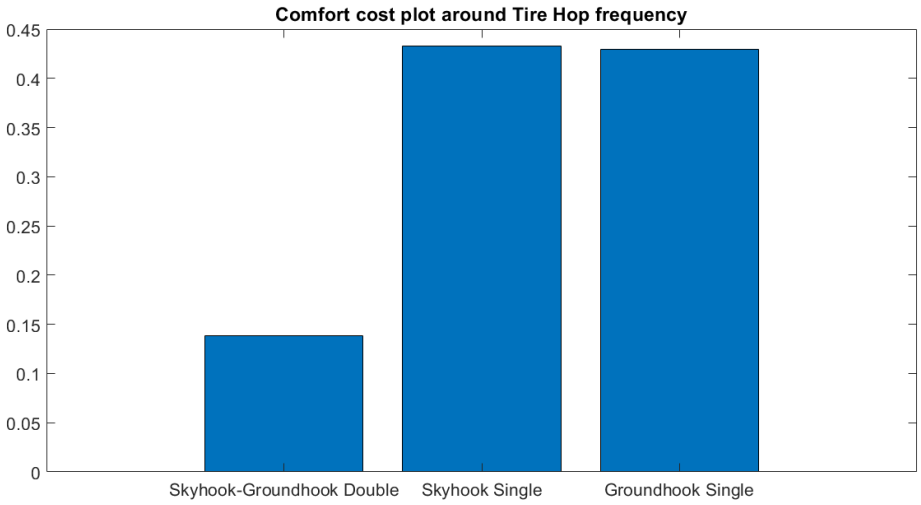

Figure 4.22: Normalized comfort cost plot—Comparing double-damper with control and single-damper with control, in Tire-hop frequency zone.

damper with control performs slightly worse than the single damper with control. This shows that the double damper with control is better suited for a softer ride, rather than for road holding. However, the performance of double damper with control in the tire-hop frequency zone can be better evaluated by using a dedicated quarter car test rig.

4.6 Science Guided Machine Learning based Control Development

In this section, a Science Guided Machine Learning (SGML) model has been developed to estimate and control the damping coefficient of a semi-active damper to minimize the sprung mass acceleration. A combined model based and data driven approach has been developed to take into account both the experimental characteristics of the damper as well as its behaviour corresponding to its analytical formulation. The system architecture can be seen in Figure 4.23.

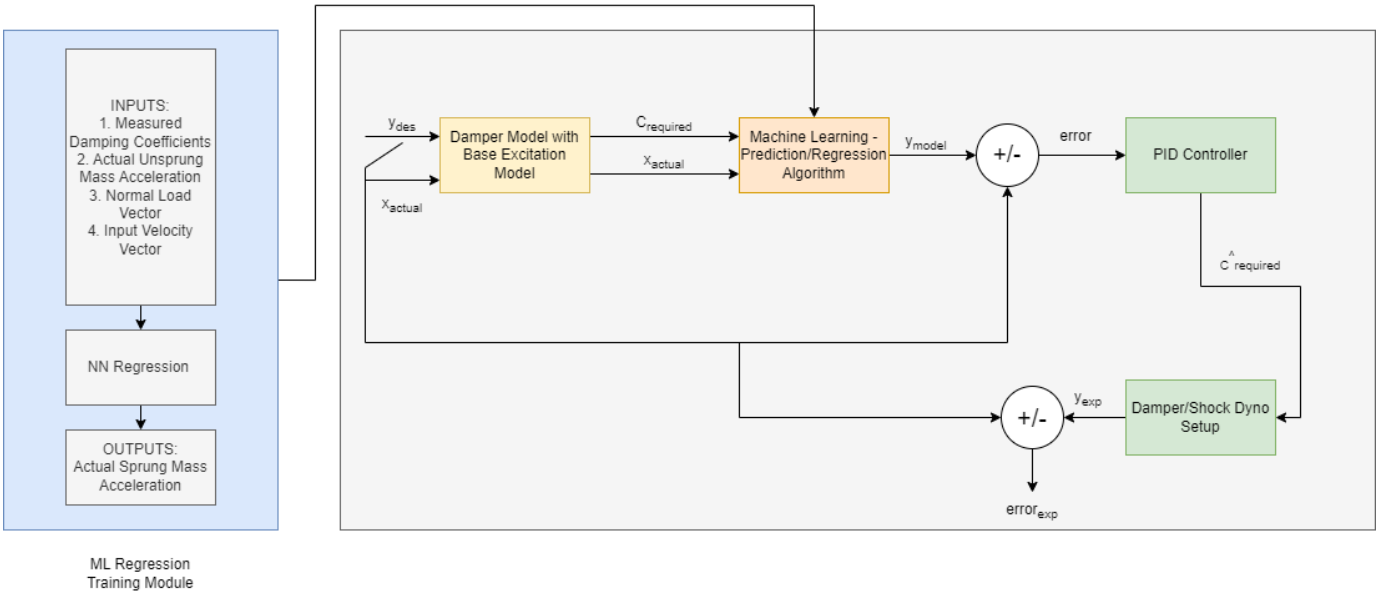

Figure 4.23: System Architecture

The entire framework can be broadly classified into three stages mentioned below:

- Regression Model Development (Training)
- Base Excitation Model Development
- Sprung mass acceleration predictions using the trained regression model

4.6.1 Regression Model Development (Training)

The data collected from the experimental testing - sprung mass acceleration, unsprung mass acceleration, damping coefficient, normal load, and the input velocity, have been used to train a regression model. The former is used as an output of the regression model and the latter 4 have been used as model inputs. Two types of regression models have been run and their performance have been evaluated based upon the R-square and RMSE values, respectively.

Kernel Approximation Support Vector Machine (SVM) Regression Model

A Kernel Approximation using SVM kernel has been used as a regression model for modelling the sprung mass acceleration as a function of the above discussed 4 input parameters. The model is essentially a Gaussian kernel-based regression model used especially for nonlinear regression of data. This model maps the sprung mass predictors into a higher order space and then fits a linear SVM through these transformed predictors. The performance of the kernel has been evaluated via the metrics given in Table 4.12.

Table 4.12: SVM Kernel Approximation Results

Parameter	Value
R-square	0.70
RMSE	0.0014586
MSE	2.1275e-6
Mean Absolute Error (MAE)	0.0010149

Neural Network Regression Model

A Neural Network based regression model has been trained based on the data described above. A Grid Search method was applied to tune the network hyper-parameters for obtaining the minimum Mean Squared Error (MSE). Table 4.13 shows the final hyper-parameter values obtained after tuning.

Figure 4.25 shows the progression of the hyper-parameters tuning and the corresponding MSE at every iteration.

Based upon this, the sprung mass acceleration has been predicted as shown in Figure 4.24. The R-square and Root Mean Square Error (RMSE) have been used as performance metrics in evaluating the model. Table 4.14 shows the performance metrics.

Table 4.13: Hyper-parameter Tuning

Parameter	Value
Number of Fully Connected Layers	3
Activation Function	Tanh
Regularization Strength	3.3647e-10
First Layer Size	293
Second Layer Size	300
Third Layer Size	14

Table 4.14: NN Model Results

Parameter	Value
R-square	0.74
RMSE	0.0013586
MSE	1.8457e-6
Mean Absolute Error (MAE)	0.0010327

4.6.2 Base Excitation Model Development

To estimate the dynamics of the Shock-Dyno test rig, a base excitation model has been developed which correlates with the dynamics of the Shock Dyno test rig. The inputs to this model are the desired sprung mass acceleration and the actual unsprung mass acceleration derived from the accelerometer data. The sprung mass acceleration is essentially a low amplitude signal with added white Gaussian noise to simulate the desired values. Figure 4.26 shows the plot of the desired sprung mass acceleration. The model output comprises of the damping coefficient for given set of input conditions.

The damping coefficient has been computed by taking the slope of the total force transmitted and the relative velocity between the sprung and the unsprung masses. Table 4.15 shows the damping coefficient values at different levels of valve openings.

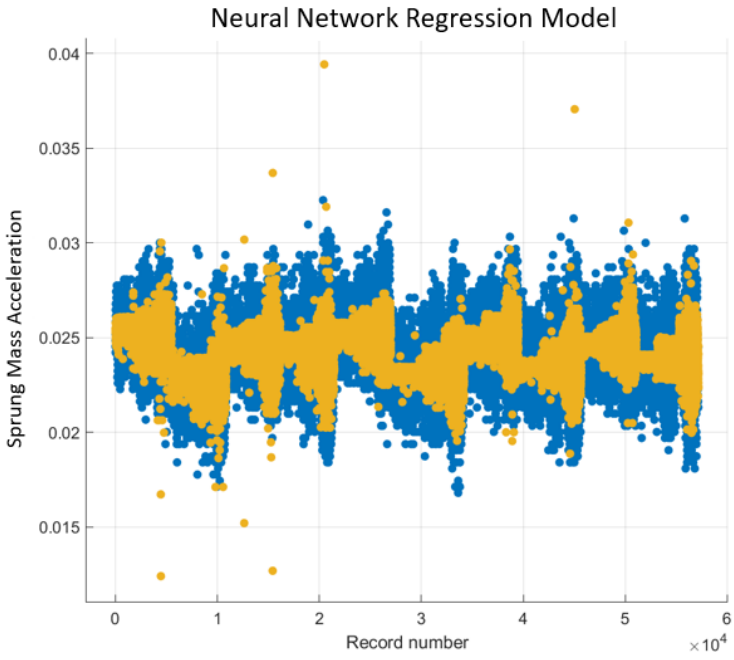

Figure 4.24: Sprung Mass Acceleration Response

4.6.3 Sprung mass acceleration predictions using the trained regression model

Using the damping coefficients obtained from the base excitation model and the previous set of actual unsprung mass accelerations, normal load vector and input velocity vector, the previously trained regression model has been tested to determine the sprung mass acceleration.

The performance of the SGML based control of the damper has been compared with that of the conventional Skyhook and Groundhook control. With the primary objective being to minimize the sprung mass acceleration, the algorithms have been evaluated against one another by computing their 'Comfort Cost'.

Figure 4.27 shows the Power Spectral Density Plot for the different damper configurations.

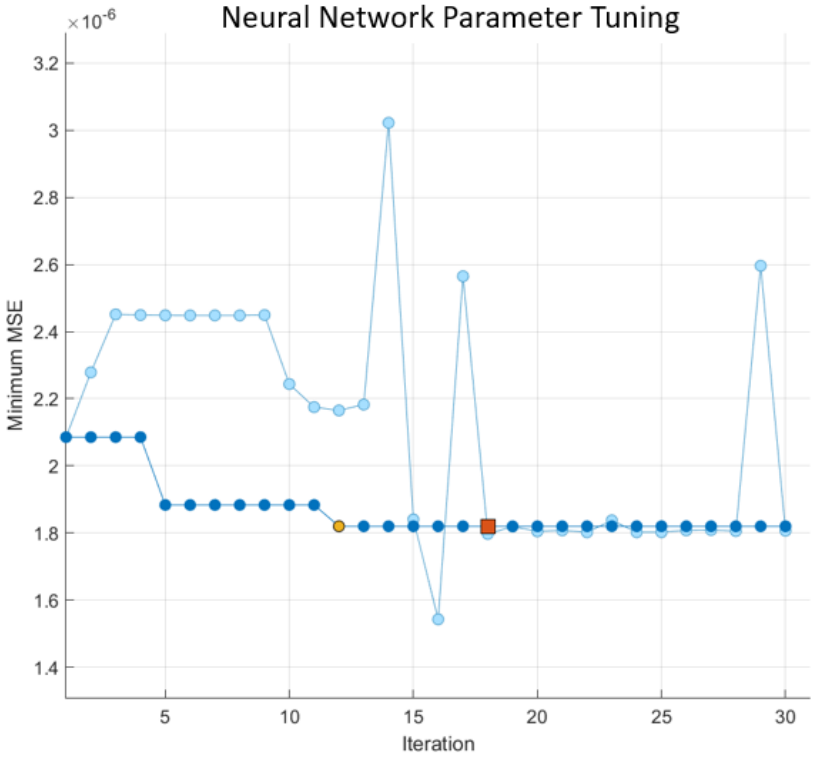

Figure 4.25: Hyper-parameter Tuning

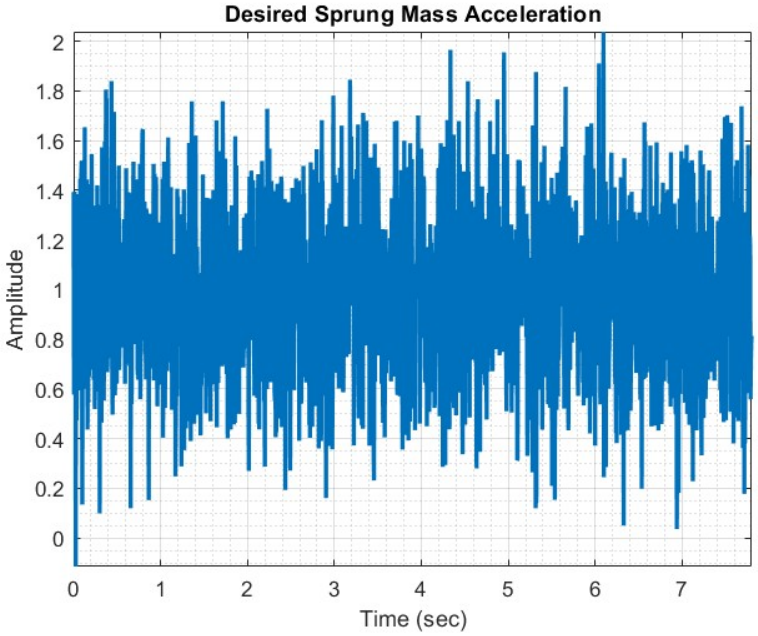

Figure 4.26: Desired Sprung Mass Acceleration

Table 4.15: Damping Coefficient Values

Valve Opening	Actual Values (N-s/m)	Model Values (N-s/m)
0%	4722.6	8516.4
25%	5411.9	8307.3
50%	4957.0	8267.1
75%	5484.1	8289.3
100%	6143.2	8458.9

It can be seen that area under the curve for the SGML based control is significantly lower than the other control strategies.

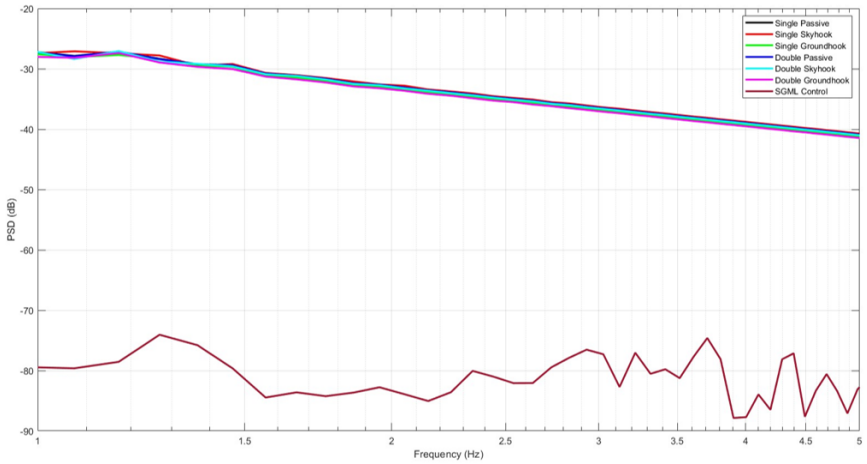

Figure 4.27: Power Spectral Density Plot

Based upon the above procedure, the comfort cost has been computed for 5 configurations of the damper control and are shown in Figure 4.28. It can be seen that the SGML based control performs significantly better with an average comfort cost of 0.0275 as compared to the conventional Skyhook and Groundhook control, respectively.

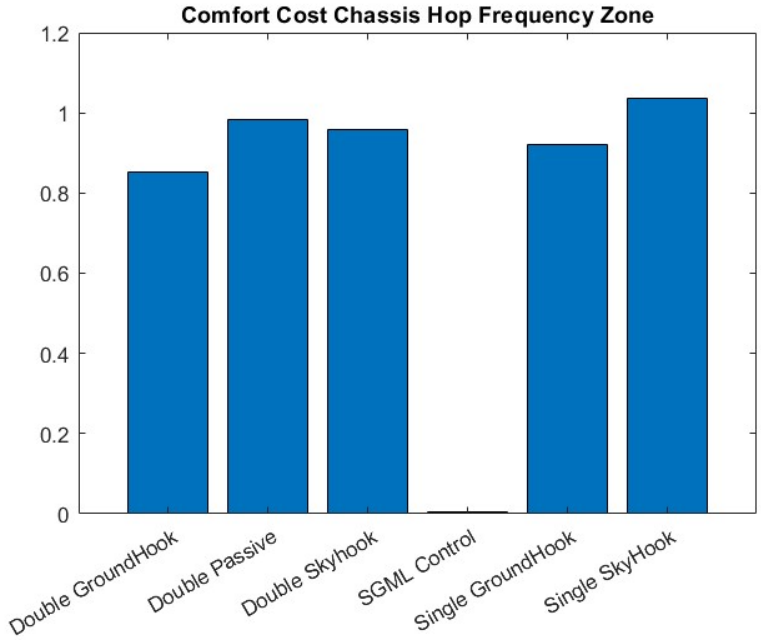

Figure 4.28: Comfort Cost - Chassis Zone

Chapter 5

Experimental Setup

To validate the developed tire, vehicle and the vertical dynamics model, a dedicated hardware test rig has been developed. This chapter has been further divided into three subsections describing the following:

- **Instrumented Vehicle Setup**: This section discusses the different exteroceptive and proprioceptive sensors used in instrumenting the vehicle along with the data acquisition and processing stations to analyze the data.

- **Scaled Unmanned Ground Vehicle (UGV)**: This section discusses the hardware architecture developed for implementing different control algorithms on the UGV platform setup.

- **Structural Health Monitoring Setup**: As discussed in Chapter 1, in this research, ML-based algorithms have also been developed to classify between a new tire and a completely worn out tire. Since these experiments have to be run for a significant amount of time, in order to validate some of the algorithms, a separate hardware setup has been developed as a precursor to tire wear classification. This section describes this preliminary hardware setup (rotatory ball bearing setup).

5.1 Instrumented Vehicle Setup

A 2003 VW Jetta vehicle has been instrumented for on-vehicle and track testing. Figure 5.1 shows the instrumented vehicle. The vehicle has been de-instrumented from its previous state and re-instrumented to accommodate the requirements of this test.

Figure 5.1: Instrumented Jetta Vehicle

The framework of the instrumented vehicle can be broadly divided into 5 different categories which completely govern the system. This division can be seen in Figure 5.2. The following subsections details the working of each of these subsystems respectively.

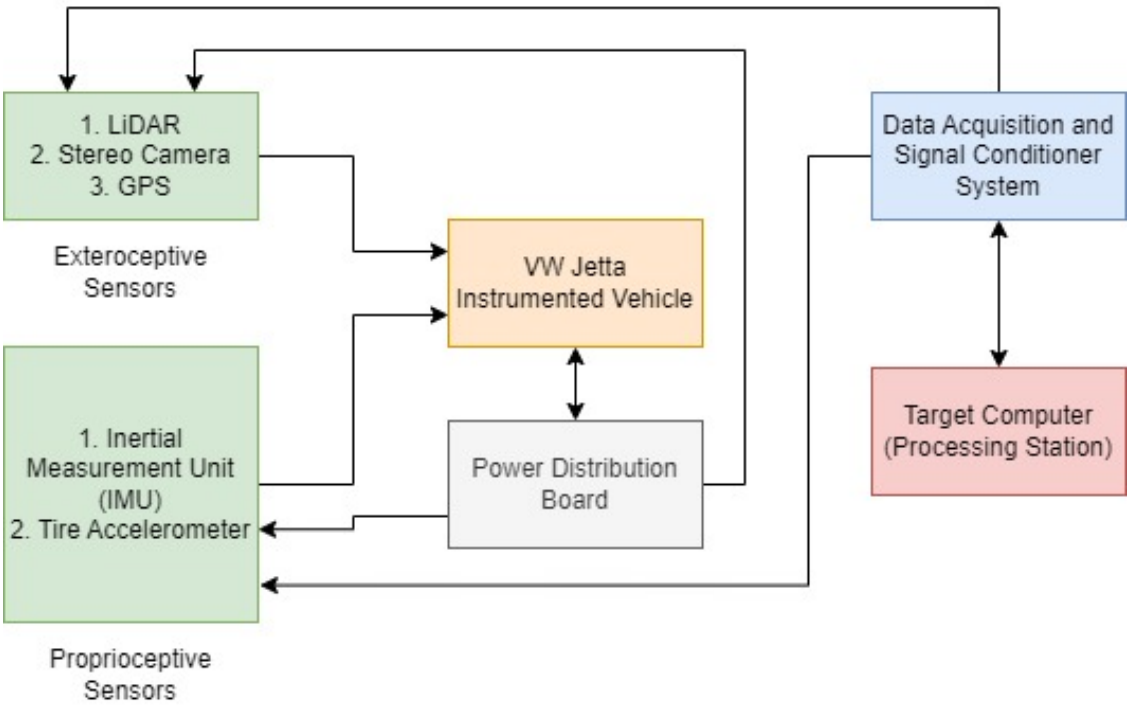

Figure 5.2: Instrumented Vehicle Hardware Architecture

5.1.1 Proprioceptive Sensors

Proprioceptive sensors are used to measure the systems internal states - for example, vehicle orientation and position, wheel speed, structure-borne noise etc. Three proprioceptive sensors have been used in instrumenting the vehicle as described below:

Inertial Measurement Unit (IMU)

A 6-axis IMU has been placed at the vehicle CG to measure the following three translational and rotational degrees of freedom:

- Longitudinal Acceleration
- Lateral Acceleration

- Vertical Acceleration
- Pitch Rate
- Roll Rate
- Yaw Rate

Figure 5.3 shows the IMU which has been mounted approximately on the vehicle CG.

Figure 5.3: IMU Unit

Some of the key specifications of the IMU have been listed in Table 5.1.

Table 5.1: IMU Specifications

Parameter	Value
X Axis Accelerometer Range	± 3G
Y Axis Accelerometer Range	± 3G
Z Axis Accelerometer Range	± 5G
Gyroscope Range	$50^0/s$
X Axis Accelerometer Sensitivity	666 to 400 ± 2% mV/G
Y Axis Accelerometer Sensitivity	666 to 400 ± 2% mV/G
Z Axis Accelerometer Sensitivity	400 to 100 ± 8% mV/G
Gyroscope Sensitivity	20 mV/G

Tire Accelerometer

Two tri-axis accelerometers have been mounted on the center of the inner lining of the tire. This essentially constitutes the formation of the "Intelligent Tire". The two accelerometers have been mounted diametrically opposite to ensure data repeatability along with serving as a redundant backup sensor in the scenario of one sensor failing. Figure 5.4 shows the accelerometer mounted on the tire inner lining. A glue has been used to mount the accelerometer with a curing time of 24hrs to ensure robust mounting.

Figure 5.4: Tire Accelerometer

Some of the key specifications of the accelerometer have been listed in Table 5.2.

Table 5.2: IMU Specifications

Parameter	Value
Sensitivity	5mV/G
Range	2500 G pk
Resolution	0.0035 G RMS
Weight	2.4 gms

Slip Ring - Encoder Arrangement

To acquire the data from the tire accelerometers, a slip ring mounted on the center of the wheel rim has been used. The slip ring essentially converts the rotation of the wheel to a stationary setup which enables the wires to be extracted from within the tire back to the vehicle where the data processing setup lies. Figure 5.5 shows the slip ring unit and Figure 5.6 shows it being mounted on the wheel rim.

The slip ring also comprises of an optical encoder to measure the tire revolutions. Some of the key encoder specifications have been described in Table 5.3.

Table 5.3: Encoder Specifications

Parameter	Value
Encoder Accuracy	0.25^o
Maximum Speed Without Seals	10000 RPM
Weight	425.24 gms

5.1.2 Exteroceptive Sensors

Exteroceptive sensors are used to measure parameters external to the vehicle, representing the environment. Three such sensors have been used in instrumenting the vehicle as described below:

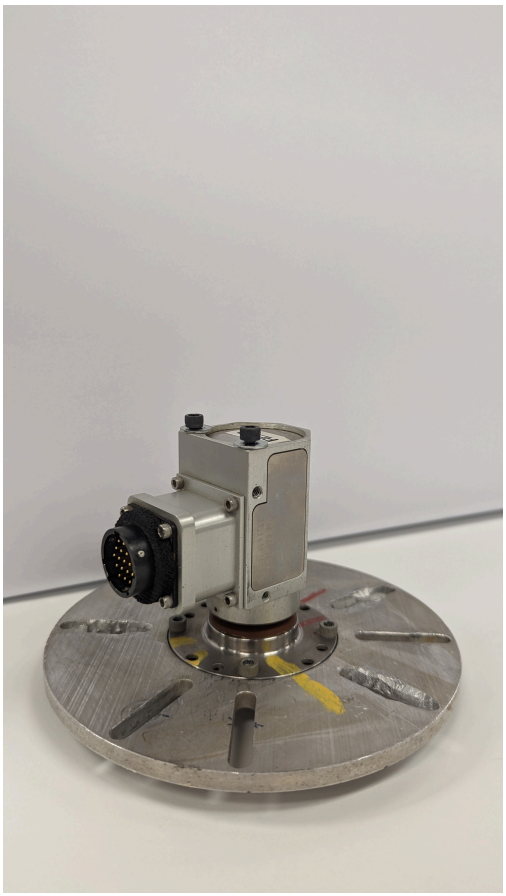

Figure 5.5: Standalone Slip Ring Unit

Global Positioning System (GPS)

To measure the longitudinal velocity of the vehicle, a Racelogic VBOX 3 unit has been used. Figure 5.7 shows the VBOX unit placed inside the vehicle. The system works by utilizing a GPS sensor and measuring the vehicle longitudinal velocity at every time instant. Figure 5.8 shows the GPS sensor mounted on the roof of the vehicle.

Some of the key VBOX specifications have been described in Table 5.4.

Figure 5.6: Slip Ring Assembly mounted on the wheel

Stereo Camera

Intel Real Sense Depth Camera D435 has been used in order to capture both the RGB images as well as the depth values associated with every pixel. It essentially works by combining two cameras at a set distance to triangulate pixels and obtain a disparity map. This disparity map is then used to get the depth image associated with the RGB image. For the instrumented vehicle, the stereo camera has been mounted on the vehicle roof via a 3D printed mount. Figure 5.9 and Figure 5.10 shows the CAD model of the camera mount and the depth camera component visualization.

Some of the key specifications of the depth camera have been listed in Table 5.5.

Figure 5.7: VBOX mounted inside the vehicle

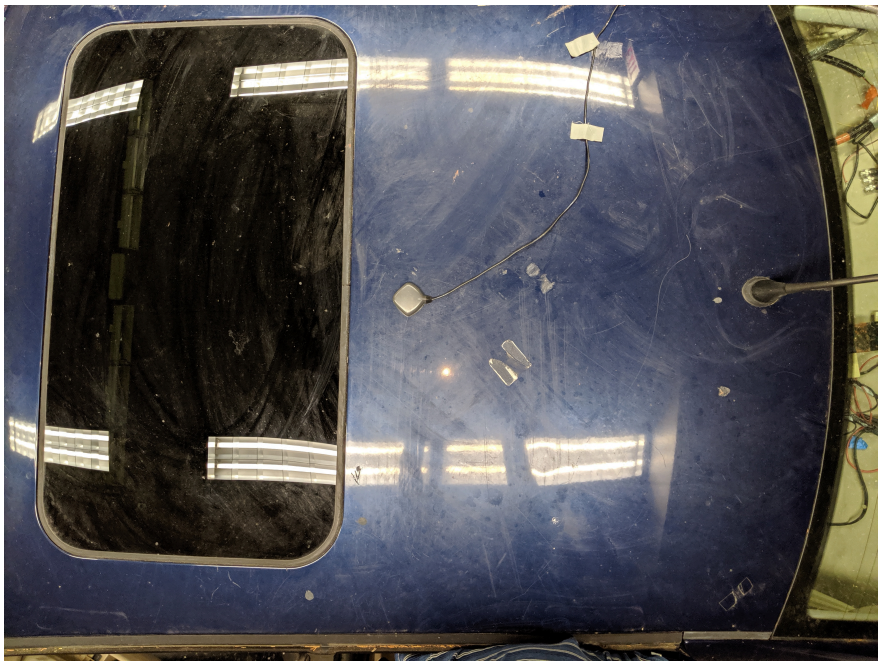

Figure 5.8: GPS Mounted on Vehicle Roof

Light Detection and Ranging (LiDAR)

To get a depth map of the surrounding environment, a 2D RPLiDAR A1 has also been used in conjunction with the stereo camera. Advantages of having such a sensor pair allows

Table 5.4: VBOX-GPS Specifications

Parameter	Value
Sample Rate	20Hz
Latency	12.5ms
Positional Accuracy	40cm

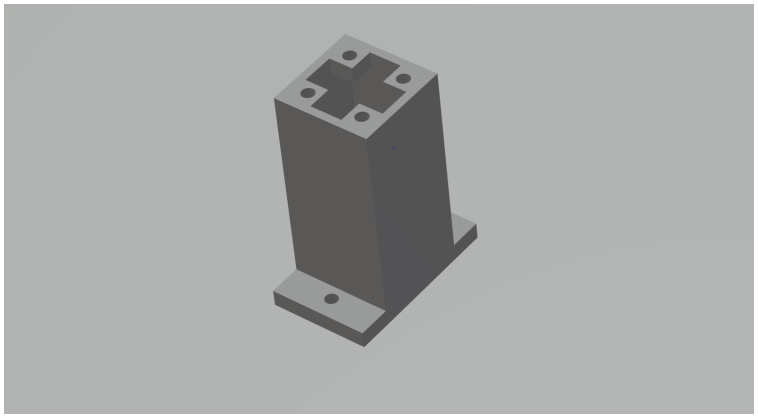

Figure 5.9: Stereo Camera Mount

Figure 5.10: Intel Real Sense Camera D435

Table 5.5: Depth Camera Specifications

Parameter	Value
Depth Field of View	87^o x 58^o
Depth Frame Rate	50 fps
Minimum Depth Distance	28 cm
RGB Frame Resolution	1920 x 1080
RGB Sensor Field of View	69^o x 42^o
RGB Sensor Resolution	2MP

continuous sensing in cases of poor environmental conditions - cases in which the LiDAR is not able to make accurate detections. Table 5.6 lists some of the key LiDAR specifications.

Table 5.6: LiDAR Specifications

Parameter	Value
Measuring Range	0.15m - 12m
Sampling Frequency	8kHz
Angular Resolution	1^o
Rotational Speed	5.5Hz
Accuracy	2.5% of range (5-25m)

5.1.3 Data Acquisition and Signal Conditioner System

To extract data from the exteroceptive and the proprioceptive sensors discussed in the previous section, a dedicated data acquisition and a power distribution setup has been built. The entire setup has been mounted inside the vehicle trunk as shown in Figure 5.11.

The key components involved in this subsystem have been enlisted below:

- Signal Conditioner Unit: To power the tire accelerometers.
- NI DAQ USB 6255: Data Acquisition System to acquire data from the exteroceptive and proprioceptive sensors.

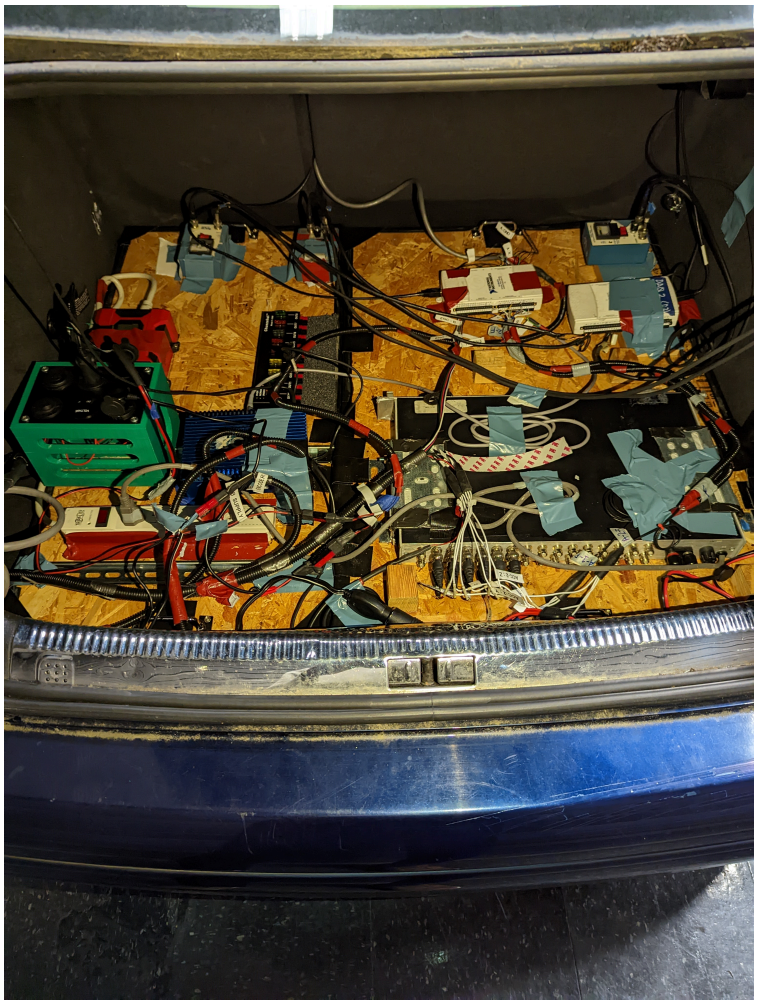

Figure 5.11: Data Acquisition and Processing Setup - Vehicle Trunk

- Power Distribution Board (PDB): To distribute power to the remaining sensors, namely - IMU, VBOX, Encoder and the Signal Conditioner. The PDB in itself is powered by the 12V supply of the vehicle.

5.2 Unmanned Ground Vehicle Setup

To test out some of the developed control and motion planning algorithms, a prototype scaled 1/10 RC car , derived from [115], has been developed and modified. Figure 5.12

shows the vehicle platform with the sensor, processing station and actuator packages.

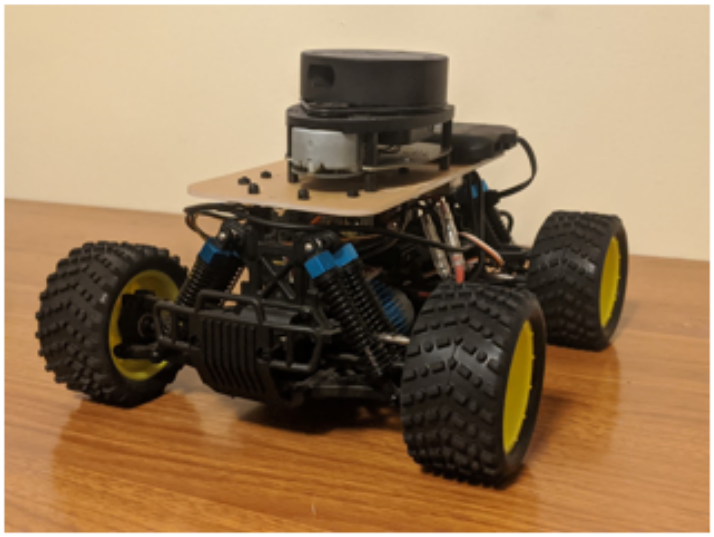

Figure 5.12: Scaled UGV Platform

The hardware architecture of the UGV platform can be seen in Figure 5.13 and a brief description of the components has been listed in Table 5.7.

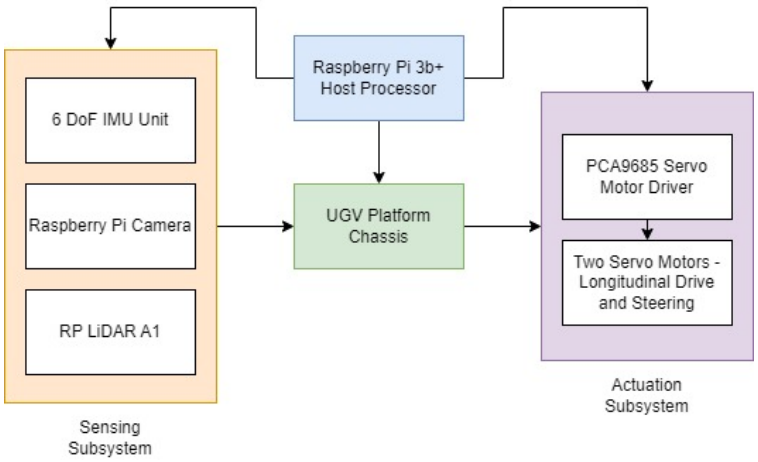

Figure 5.13: UGV Platform - Hardware Architecture

The primary reason for going with a scaled UGV setup was to achieve the following objectives:

Table 5.7: UGV Component Description

Component	Description
Raspberry Pi 3b+	Single Board Processors
Raspberry Pi Camera	Wide angle camera mounted at the front of the vehicle
RPLiDAR A1	LiDAR Unit mounted on tip of the vehicle
Servo Controller Board	PCA9685 Shield
Power Unit	LiPo 12.2V Battery
IMU Unit	MPU6050 6-DOF Measurement Board

- Understanding and implementation of different trajectory tracking control algorithms - MPC, PID and Lateral Stanley control and see their effect on the vehicle performance.
- Implementation of path planning algorithms - A*, and Dijkstra's in a mapped environment.

The following subsections briefly describe the sensors used on board the UGV platform.

5.2.1 Raspberry Pi Camera and LiDAR Setup

A Raspberry Pi Camera Module 2 has been used to collect the visual odometry data from the vehicle. The camera has been interfaced with the Pi module to continuously collect frames of data which have been further analyzed via a series of computer vision based algorithms. The camera has been mounted on the top front of the vehicle as seen in Figure 5.14.

Figure 5.15 shows a sample of raw images captured by the UGV camera.

Along with the camera, a 2D LiDAR has also been mounted on top of the vehicle chassis as shown in Figure 5.12. The key reason for this is to extract the depth data from the surrounding environment which can be further used for localization and object depth recognition. The LiDAR has been interfaced with the Raspberry Pi module to output the range and the bearing (angle) of the surrounding map. Figure 5.16 shows a sample of the collected

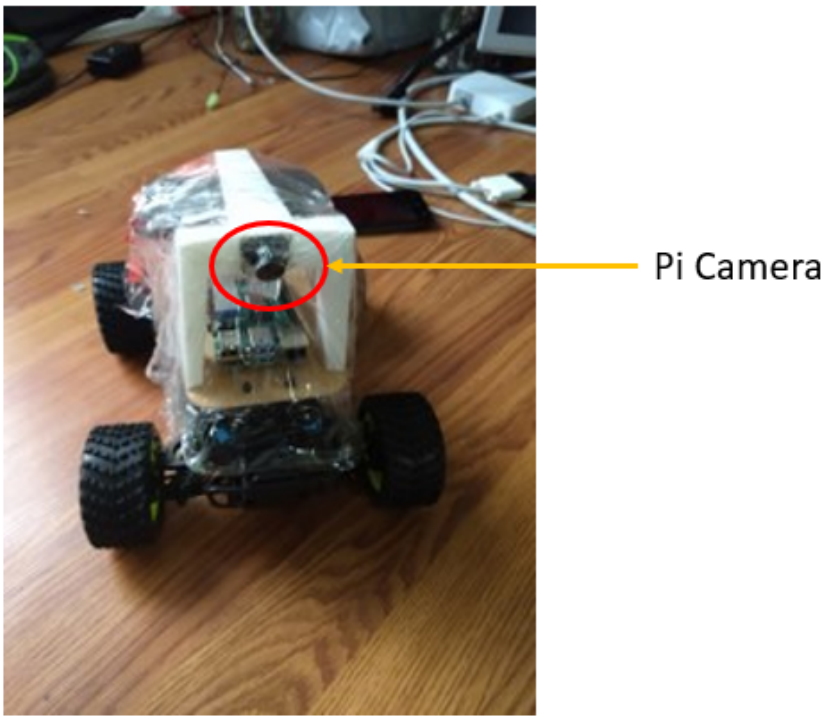

Figure 5.14: Pi Camera mounted on the UGV

Figure 5.15: Sample data from UGV mounted camera

LiDAR data.

5.2.2 IMU Setup

Two IMU sensors have been mounted on the UGV platform - one on the CG of the sprung mass and the second on the wheel axle in order to measure the sprung and unsprung mass

```
Angle = 344.202    degrees     Range  = 1.653      mm
Angle = 344.982    degrees     Range  = 1.647      mm
Angle = 345.515    degrees     Range  = 1.639      mm
Angle = 346.168    degrees     Range  = 1.633      mm
Angle = 346.948    degrees     Range  = 1.626      mm
Angle = 347.607    degrees     Range  = 1.619      mm
Angle = 348.261    degrees     Range  = 1.612      mm
Angle = 348.92    degrees      Range  = 1.606      mm
Angle = 349.453    degrees     Range  = 1.6      mm
Angle = 350.233    degrees     Range  = 1.599      mm
Angle = 350.887    degrees     Range  = 1.593      mm
Angle = 351.546    degrees     Range  = 1.581      mm
Angle = 352.216    degrees     Range  = 1.579      mm
Angle = 352.87    degrees      Range  = 1.576      mm
Angle = 353.529    degrees     Range  = 1.573      mm
Angle = 354.183    degrees     Range  = 1.553      mm
Angle = 354.842    degrees     Range  = 1.551      mm
Angle = 355.496    degrees     Range  = 1.553      mm
Angle = 356.155    degrees     Range  = 1.559      mm
Angle = 356.808    degrees     Range  = 1.553      mm
Angle = 357.451    degrees     Range  = 1.551      mm
Angle = 358.748    degrees     Range  = 0      mm
Angle = 359.731    degrees     Range  = 0.552      mm
(env) pi@raspberrypi:~/mycar/Lidar/build $
```

Figure 5.16: Sample data from UGV mounted LiDAR

orientation and position. Figure 5.17 shows the IMU sensor mounted on the wheel axle. Data from the IMU has been recorded using an I2C interface with the Raspberry Pi board.

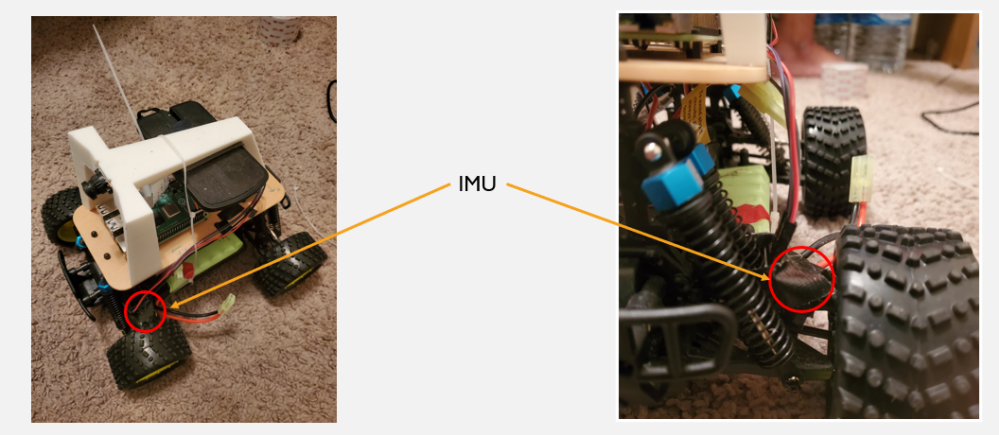

Figure 5.17: IMU Mounted on UGV unsprung mass

5.3 Structural Health Monitoring Setup

As discussed in Chapter 1, in order to develop a test bed for identifying defects within a tire, a preliminary setup comprising of defective ball bearings has been constructed. Real-time

bearing testing, data collection and defect classification has been carried on an in-house developed test-rig as shown in Figure 5.18.

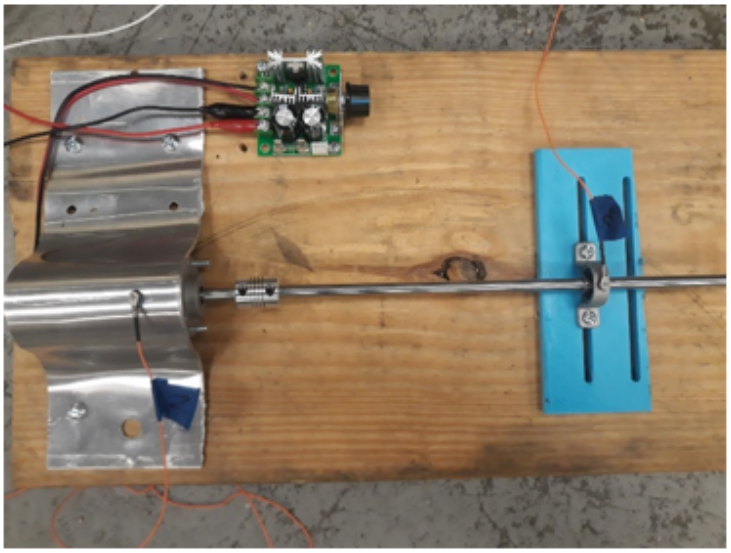

Figure 5.18: Experimental Setup - Bearing Test Rig

Table 5.8 shows the key components which have been used for developing the test rig. The following section enlist some of these components along with their functionalities.

Table 5.8: Bearing Test Rig - Component List

Component	Description
SpeedGoat	Target Computer
Dytran 3225F1 Accelerometer	Piezoelectric sensors for vibration data collection
Signal Conditioner	Power the accelerometers
Data Acquisition System	For accelerometer data acquisition
Bearing-Shaft-Motor Assembly	Primary components for defect and eccentricity classifications
Motor Controller	Vary the shaft speed in a controller manner

Figure 5.19 shows the inter-connections between the different subsystems of the test rig.

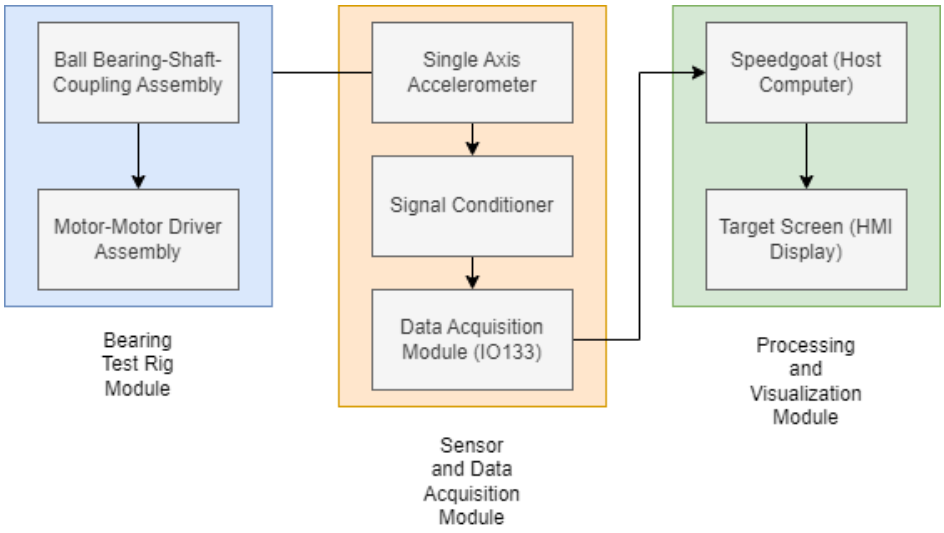

Figure 5.19: SHM - System Architecture

5.3.1 Speedgoat Target Computer

Speedgoat Baseline Model-M has been used as a real-time development platform for testing the data processing and ML algorithms. The key reason for choosing this hardware was its compatibility with Simulink and Simulink Real-Time from MathWorks. Along with this, Speedgoat has lower I/O and computation latency times which have been listed in Table 5.9. Figure 5.20 shows the Speedgoat hardware.

Table 5.9: SpeedGoat Latency Time Specifications

Parameter	Latency Time
CPU Computation Time	$53.1\mu s$
I/O Latency Time	$25\mu s$
Total Time	$78.1\mu s$

5.3.2 Single Axis Accelerometer

Dytran 3225F1 single axis accelerometers have been used for vibration data collection. These accelerometers have been placed on the outer casing of the bearing pillow block. The data has

Figure 5.20: SpeedGoat Target Machine

been sampled at 5kHz allowing to capture primary rotational harmonics present in defective bearings. Some of the key accelerometer specifications have been listed in Table 5.10.

Table 5.10: Accelerometer Specifications

Parameter	**Latency Time**
Sensitivity ±10%	10mV/g
Range	$\pm 4905 m/s^2 rms$
Frequency Response ±10%	1.6 - 10,000Hz

5.3.3 Signal Conditioner

A Dytran 4116 Model Signal Conditioner has been used to provide Direct Current (DC) power supply for operating the accelerometers. The signal conditioner has a total of 16 I/O ports allowing for powering multiple accelerometers simultaneously. Figure 5.21 shows the signal conditioner setup.

Figure 5.21: Signal Conditioner

5.3.4 Data Acquisition System

A IO133 module by SpeedGoat has been used as a data acquisition system for acquiring the accelerometer data. This module essentially serves as a connection between the Speedgoat Host Computer and the accelerometers. Differential connections have been utilized to connect the accelerometers to the data acquisition module and simultaneously sampling has been utilized between the different accelerometer data channels to allow for elimination of phase shift between the channels. The data acquisition module can be seen in Figure 5.22.

5.3.5 Bearing-Shaft-Motor Assembly

A pillow block ball bearing has been used as the primary component for classifying between the different types of bearing defects. The bearing comprises of the following 4 major components:

- Outer Race

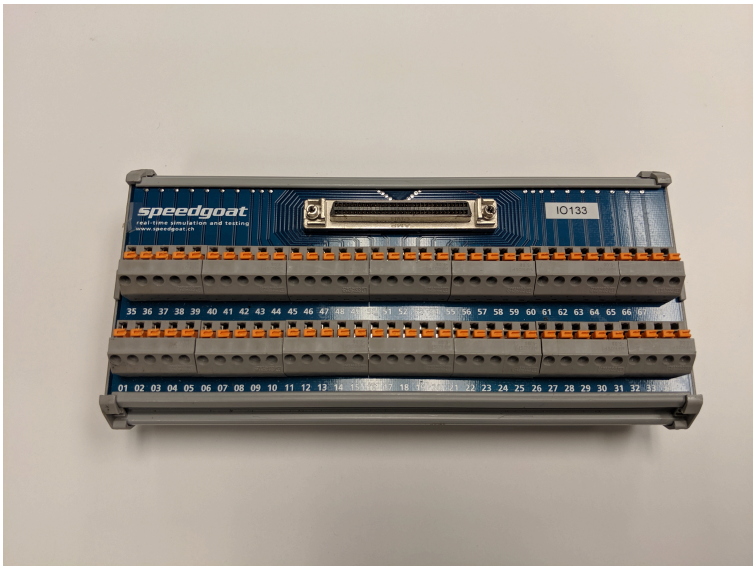

Figure 5.22: IO133 Data Acquisition System

- Inner Race
- Ball and Cage Arrangement
- Pillow Block

A permanent magnet DC motor has been used for rotating the shaft. A motor controller has been used to vary the shaft speed based upon the test conditions. Table 5.11 shows some of the key specifications of the bearings and motor driver.

Table 5.11: Bearing-Shaft-Motor Specifications

Parameter	**Values**
Bearing Properties	8mm bore diameter – Zinc Alloy
Motor Driver	1200 – 2700 RPM
Shaft Coupling Pair	8mm solid aluminum shaft with a flexible coupling attached to the motor shaft to allow for small eccentric inaccuracies

Chapter 6

Testing, Data Processing and State Estimation

In this chapter, the proprioceptive and exteroceptive sensor data collected during the vehicle testing has been analyzed. This chapter has been further divided into the following sections:

- Testing Procedure: This section describes the testing methodology followed for the VW Jetta Testing. This includes the design matrix for the input conditions as well as the different maneuvers followed.
- Data Processing: This section contains the different data processing techniques used to process the vehicle tire accelerometer, and IMU data.
- State Estimation: In this section, three algorithms have been developed for estimating the vehicle side slip angle, tire slip angle and the tire normal load.

6.1 Testing Procedure

6.1.1 VW Jetta Testing

Based upon the vehicle instrumentation discussed in Chapter 5, a testing procedure has been developed to collect the vehicle data for different values of normal load, tire inflation

pressure, vehicle longitudinal velocity, and the type of maneuver which has been performed. Table 6.1 lists the different input parameter conditions over which the testing has been carried out. A total of 24 test runs have been completed.

Table 6.1: Testing Procedure Design Matrix

Tire Inflation Pressure (bar)	**Normal Load (lbs)**	**Vehicle Velocity (mph)**	**Maneuver Type**	**Number of Runs**
2.8	150	20	Slalom Maneuver	3
2.3	0	30	Straight Line Maneuver	3

A slalom maneuver, which essentially comprises of multiple Double Lane Change (DLC) maneuvers, has been performed to evaluate the vehicle performance at the limits of handling. This maneuver has been performed in accordance with the ISO 13674-2:2016 and can be visualized in Figure 6.1.

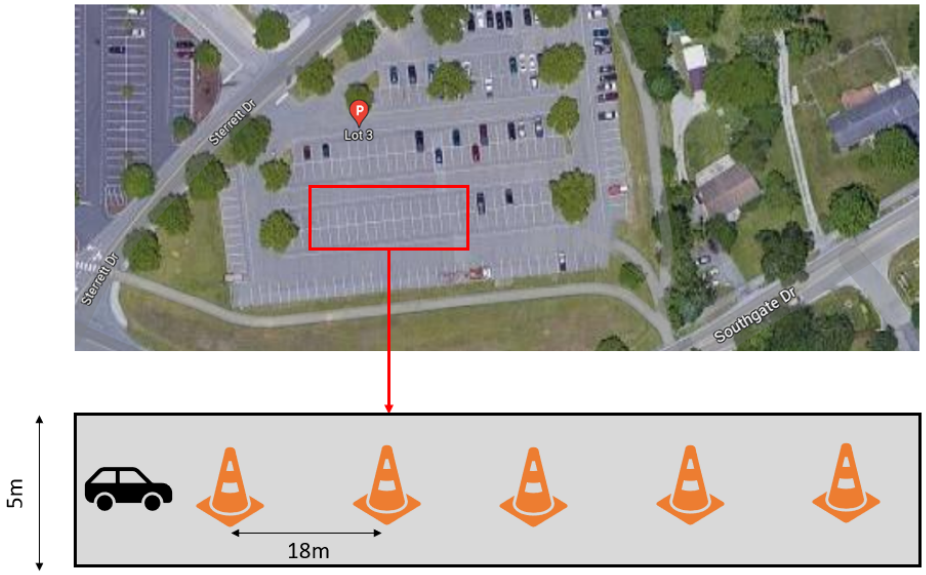

Figure 6.1: Testing Procedure - Lane Stadium Parking Lot

Figure 6.2 shows the layout of the test track.

Figure 6.2: Test Track Layout

The following testing methodology has been observed:

- The tire accelerometer and IMU data has been sampled at 9600Hz, and the GPS data has been sampled at 10Hz.

- The tire has been warmed up before starting actual testing to ensure further uniformity in the accelerometer data.

- The vehicle sensor data has been normalized by taking into account the noise data when the vehicle is stationary.

6.2 Data Processing

Vehicle sensor data has been collected for the above mentioned test conditions and post-processed to extract meaningful features from the data. Figure 6.3, Figure 6.4, and Figure 6.5 show the tire accelerometer data during one DLC action in the slalom maneuver corresponding to X, Y, and Z axis respectively. The data has been passed through a second order low pass Butterworth filter to reduce the high frequency noise content in the data. Each of these peaks represents when the tire accelerometer comes in contact with the ground and hence represents a single tire revolution.

From Figure 6.4, a low frequency variation can be seen which represents the time period when the vehicle undergoes the first lane change in the slalom maneuver. This is much more significant in this Y-axis acceleration data as the slalom maneuver essentially represents a lateral acceleration movement.

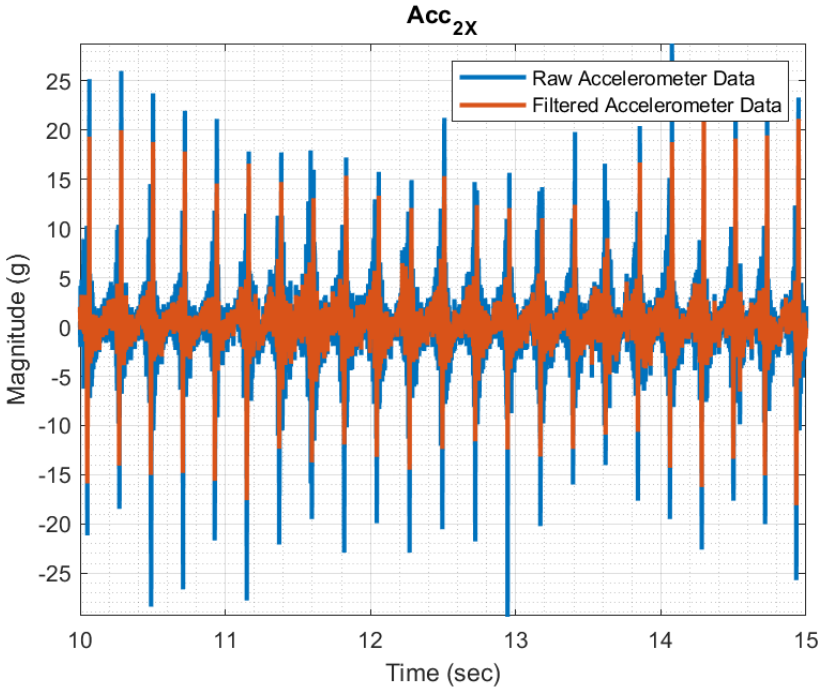

Figure 6.3: Longitudinal Tire Acceleration - X Axis

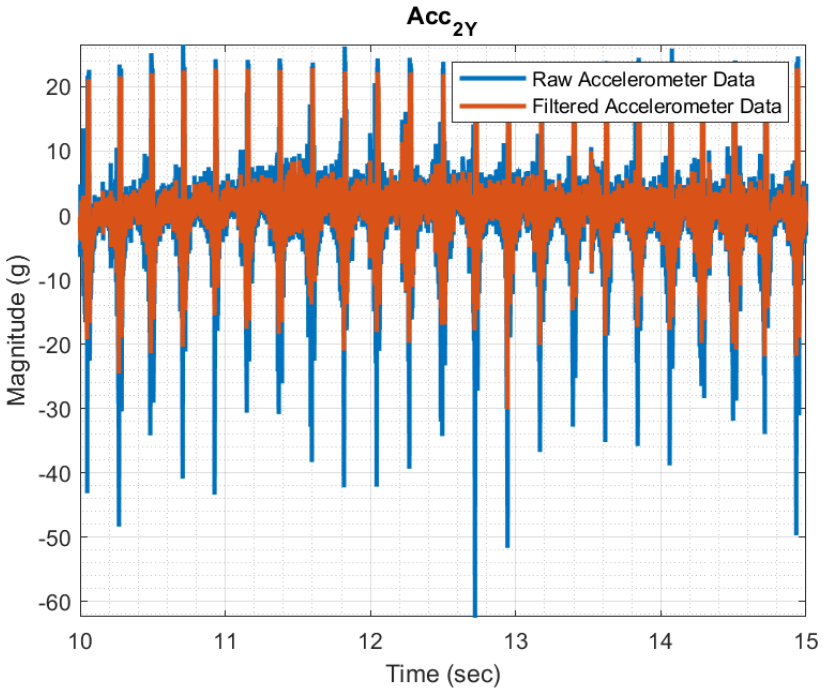

Figure 6.4: Lateral Tire Acceleration - Y Axis

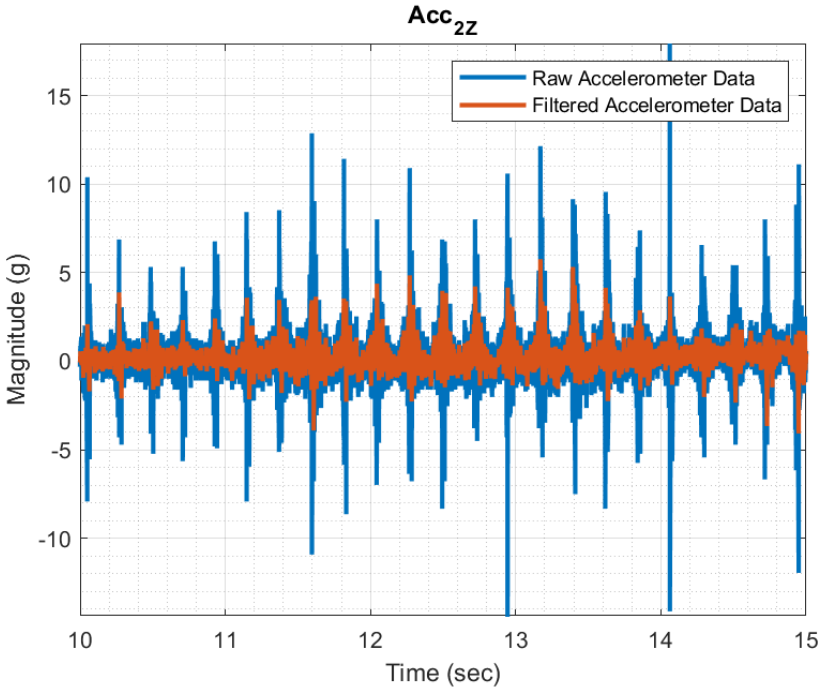

Figure 6.5: Radial Tire Acceleration - Z Axis

This lateral axis of the vehicle has been further explored by analyzing the lateral acceleration at the vehicle CG and its corresponding yaw moment. This data has been collected by an IMU placed at the vehicle CG as shown in Figure 6.6 and Figure 6.7 respectively. The slalom maneuver starts at t = 10sec and the vehicle goes through a series of 5 cones as can be seen in Figure 6.7.

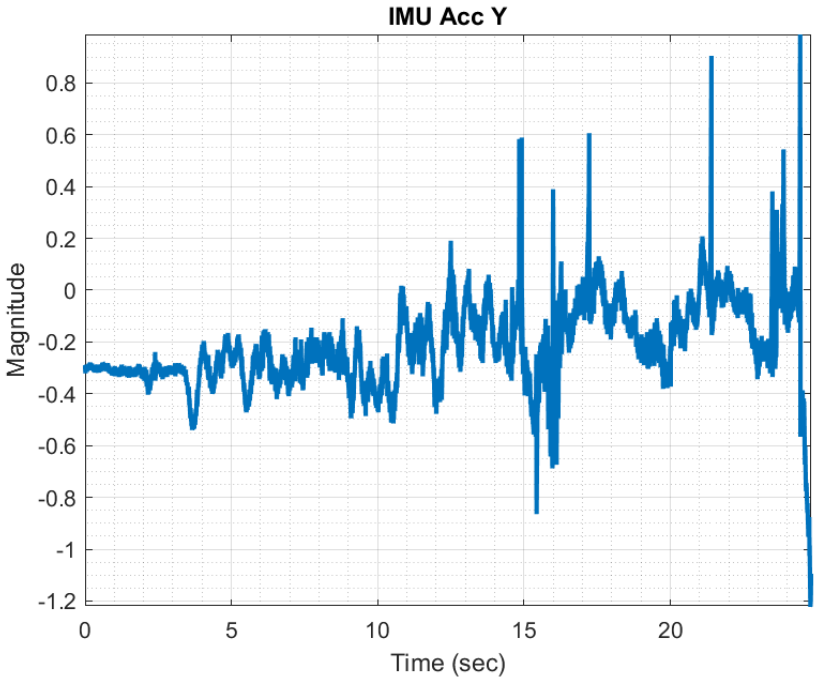

Figure 6.6: Vehicle CG Lateral Acceleration - IMU Data

6.3 State Estimation

6.3.1 Vehicle Normal Load Estimation

The Fiala Tire model developed in Chapter 3, is parameterized by three variables: vehicle normal load, tire slip angle and the coefficient of friction between the tire and road surface. To model the tire lateral forces, an accurate measurement or estimation system is required to

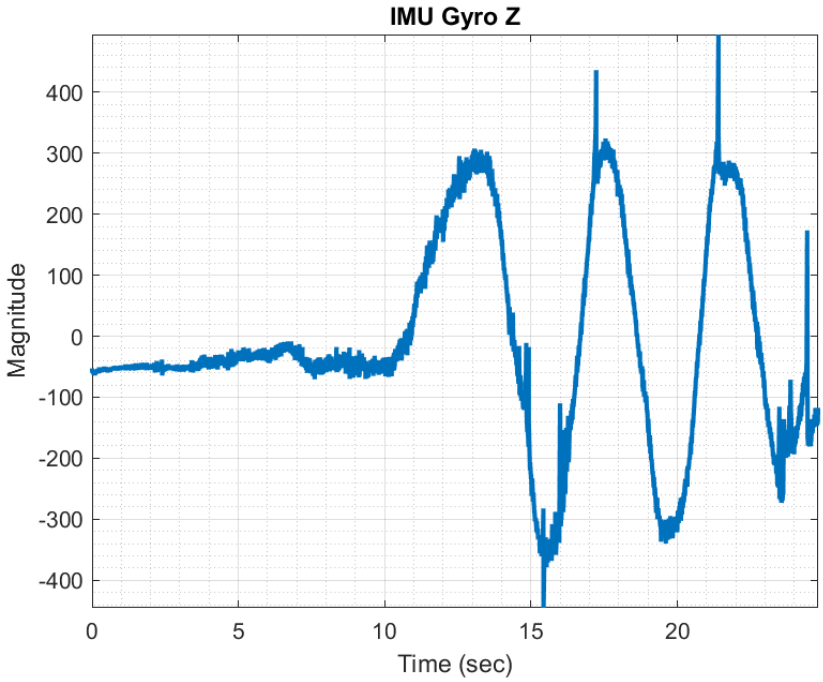

Figure 6.7: Vehicle CG Yaw Moment - IMU Data

compute these parameters. Hence, in this section, an estimation strategy has been developed to evaluate the vehicle normal load. The 11 DoF model developed in Section 3.3, coupled with the normal load equations used in [116] has been further expanded for this vehicle normal load estimation.

The normal load, based upon the 11 DoF model, depends upon the acceleration vector at the CG, the roll and pitch rates, and the vehicle mass and geometric properties. Based upon this, the normal load at the individual wheels has been modeled as shown in Equation 6.1, Equation 6.2, Equation 6.3, and Equation 6.4 respectively.

$$F_{fr} + F_{fl} = mg * (\frac{L_r}{L} - \frac{h * \ddot{x}}{Lg}) \tag{6.1}$$

$$F_{rr} + F_{rl} = mg * (\frac{L_f}{L} + \frac{h * \ddot{x}}{Lg}) \tag{6.2}$$

$$F_{fr} + F_{rr} = mg * (\frac{t_f}{D} + \frac{h * \ddot{y}}{Dg}) \tag{6.3}$$

$$F_{fl} + F_{rl} = mg * (\frac{t_r}{D} - \frac{h * \ddot{y}}{Dg}) \tag{6.4}$$

These set of equations are the linearized equations, wherein the effect of the roll and pitch rates have not been considered.

The above equations have been modeled in CarSim-Simulink environment. The primary objective of this was to compare the normal load values obtained from the estimation framework against those given CarSim (considering these values the the true vehicle values). Figure 6.8 shows the higher level architecture of the normal load estimation model.

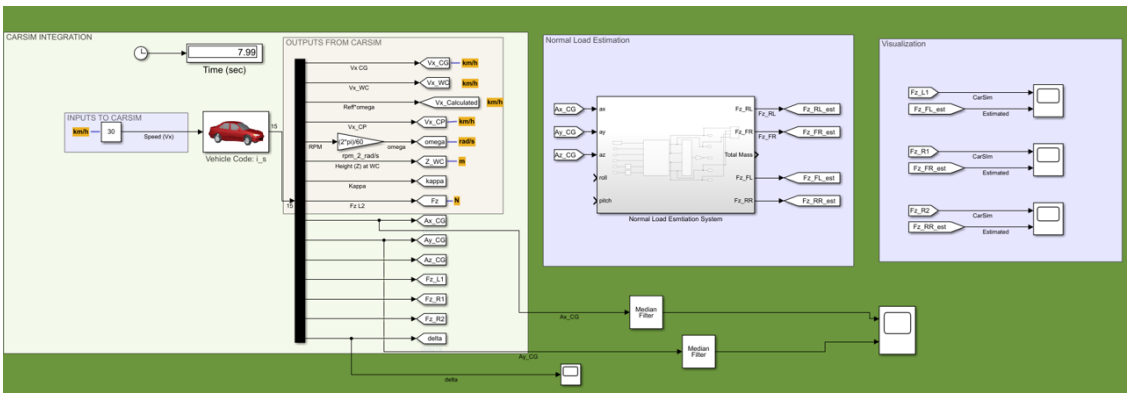

Figure 6.8: CarSim-Simulink Model for Normal Load Estimation

The vehicle parameters required for the simulation have been derived from the CarSim environment. Based upon these parameters and the normal load estimation framework, Figure 6.9, Figure 6.10, Figure 6.11, and Figure 6.12 show the normal load values for the

front left, front right, rear left, and rear right tires respectively.

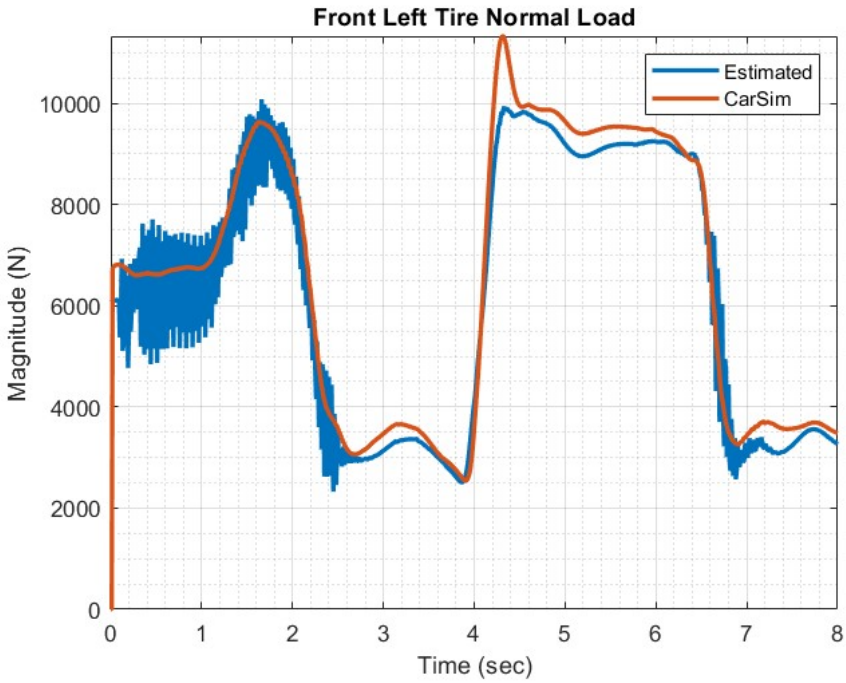

Figure 6.9: Front Left Tire Normal Load Estimation

The CarSim values represent the true normal load values. From these figures, it can be seen that the values outputted by the estimation framework are less over the entire time frame as compared to the true values. However, the average percentage difference between the true and the estimated values stands at **6.451%**.

6.3.2 Vehicle Side-slip and tire slip angle estimation

The vehicle side slip angle (β) and the tire slip angle (α) are required in the Fiala tire model to model the lateral forces at the contact patch. The side slip angle is essentially defined as the angle the velocity vector makes with the longitudinal axis at the vehicle CG.

Similarly, the tire slip angle is defined as the angle between the orientation of the tire and the orientation of the velocity vector of the tire. Figure 6.13 shows the slip angle developed at the

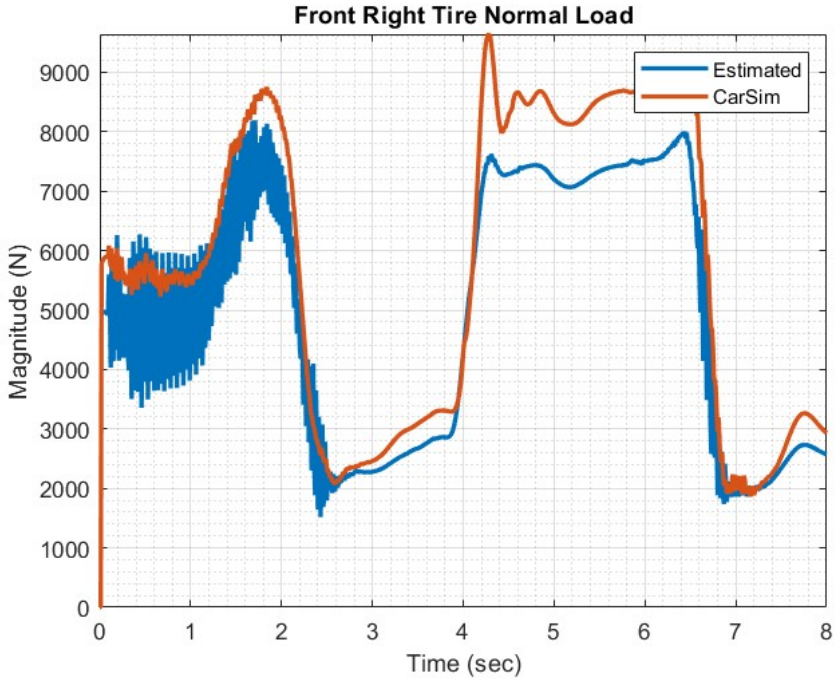

Figure 6.10: Front Right Tire Normal Load Estimation

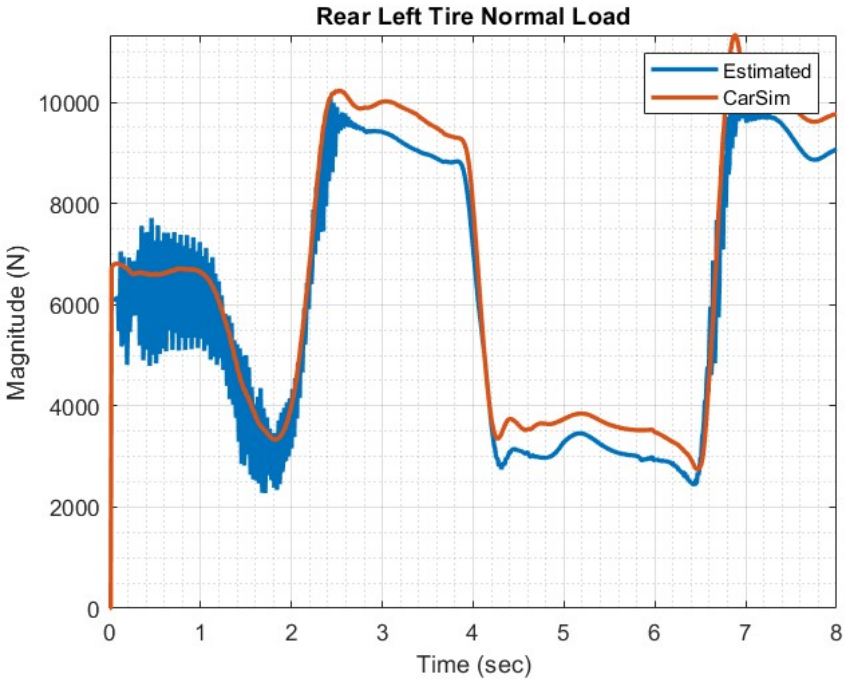

Figure 6.11: Rear Left Tire Normal Load Estimation

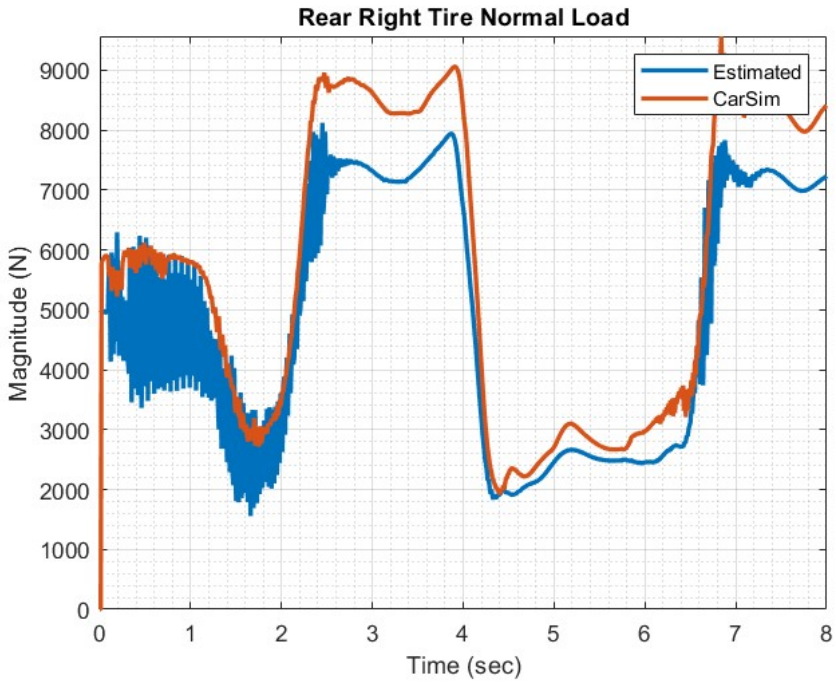

Figure 6.12: Rear Right Tire Normal Load Estimation

front wheel and is mathematical represented by Equation 6.5. Slip angle plays a crucial role in vehicle handling, tire wear, vehicle stability, and control algorithm performance. Hence accurate slip angle estimation is of prime importance for developing a robust and high fidelity vehicle-tire model

$$\alpha = \delta - \theta \tag{6.5}$$

Sideslip Angle Estimation

The lateral dynamics vehicle model developed in Section 3.4 has been used to estimate the vehicle side slip angle. The equations of motion derived for this model have been re-formulated so as to compute the side slip angle (β). Equation 6.6 shows the non-linear dynamics of the developed vehicle model.

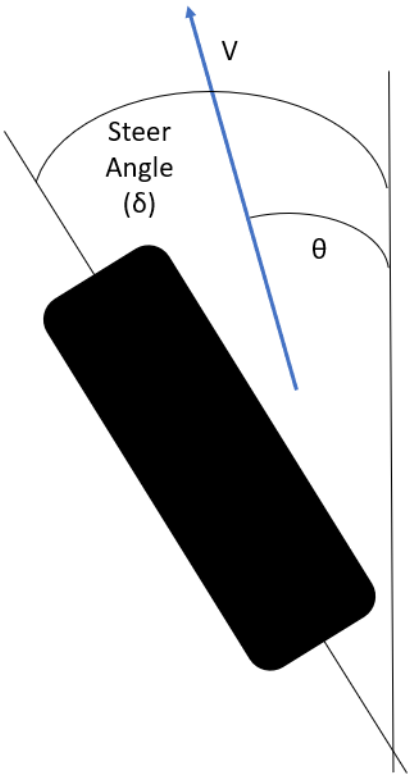

Figure 6.13: Tire Slip Angle Description

$$m\dot{v} = F_{yf} + F_{yr} + F_{yf} + F_{yr} - (mru) + mg\sin\theta - mh\sin\phi r^2 - mh\dot{\phi}^2\sin\phi + mh\cos\phi\ddot{\phi} \quad (6.6)$$

The key assumptions of this model, other than those listed in Section 3.4 are listed below:

- The effect of longitudinal forces has not been considered
- The effect of relaxation length on the front and rear tire has been neglected.

Assuming no road bank angle and using small angle approximation, Equation 6.6 can be written as follows:

$$m\dot{v} = 2F_{yf} + 2F_{yr} - mru - mh\phi r^2 - mh\dot{\phi}^2\phi + mh\ddot{\phi} \tag{6.7}$$

Rearranging equation 6.7 such that the lateral acceleration at the vehicle CG for the 3DoF vehicle roll model accounts for the roll acceleration and lateral acceleration.

$$m(\dot{v} + ru - h\ddot{\phi}) = 2F_{yf} + 2F_{yr} - mh\phi r^2 - mh\dot{\phi}^2\phi \tag{6.8}$$

$$mA_y = 2F_{yf} + 2F_{yr} - mh\phi r^2 - mh\dot{\phi}^2\phi \tag{6.9}$$

Considering a linear tire model, Equation 6.9 can be written as follows

$$mA_y = 2C_f\alpha_f + 2C_r\alpha_r - mh(\phi r^2 - \dot{\phi}^2\phi) \tag{6.10}$$

Now, from the bicycle model, the slip angle at the front and rear can be computed as follows:

$$\alpha_f = \delta_f - (\beta + \frac{ra}{u}) \tag{6.11}$$

$$\alpha_r = (\frac{rb}{u} - \beta) \tag{6.12}$$

Using Equation 6.11 and 6.12, Equation 6.10 can be simplified and rewritten as follows:

$$mA_y = 2C_f\delta_f - 2C_f\beta - \frac{2C_fra}{u} + \frac{2C_rrb}{u} - 2C_rb - mh(\phi r^2 - \dot{\phi}^2\phi) \tag{6.13}$$

Equation 6.13 can be further simplified and rearranged as follows

$$mA_y = 2C_f\delta_f - 2\beta(C_f + C_r) + \frac{2r}{u}(bC_r - aC_f) - mh(\phi r^2 - \dot{\phi}^2\phi) \tag{6.14}$$

To simplify the above equations, two terms have been introduced as shown below:

$$A_0 = C_f + C_r \tag{6.15}$$

$$B_0 = bC_r - aC_f \tag{6.16}$$

Using Equation 6.14, 6.15 and 3.26, the following equation can be written

$$mA_y = 2C_f\delta_f - 2\beta A_0 + \frac{2rB_0}{u} - mh(\phi r^2 - \dot{\phi}^2\phi) \tag{6.17}$$

Rearranging Equation 6.17 an estimate of the side slip angle can be formulated as given in Equation 6.18.

$$\beta = \frac{2C_f\delta_f + \frac{2rB_0}{u} - mh(\phi r^2 - \dot{\phi}^2\phi) - mA_y}{2A_0} \tag{6.18}$$

Equation 6.18 can be further simplified by assuming the vehicle undergoes negligible roll during steady-state maneuvering. This condition is represented by Equation 6.19 which has been used to estimate the vehicle side slip angle.

$$\beta = \frac{2C_f\delta_f + \frac{2rB_0}{u} - mA_y}{2A_0} \tag{6.19}$$

From Equation 6.19, it can be seen that the only dynamic parameters required for side slip angle estimation are:

- Vehicle CG Yaw Rate (r): Yaw rate can be obtained from the IMU placed at the vehicle CG.
- Vehicle CG Longitudinal Velocity (u): Longitudinal velocity can be obtained from the VBOX-GPS sensor.
- Vehicle CG Lateral Acceleration (A_y): Lateral acceleration can be measured from the CG IMU sensor.
- Steering Angle (δ_f): Tire steering angle can be obtained from the steering wheel sensor data and multiplying that with the steer ratio (The vehicle testing conducted did not have a steering angle sensor and hence CarSim data has been used).

To validate the above estimation method, CarSim has been used to simulate the true vehicle side slip angle. Figure 6.14 shows the CarSim-Simulink model which has been developed to estimate the side slip angle angle and compare it with the true value given by CarSim.

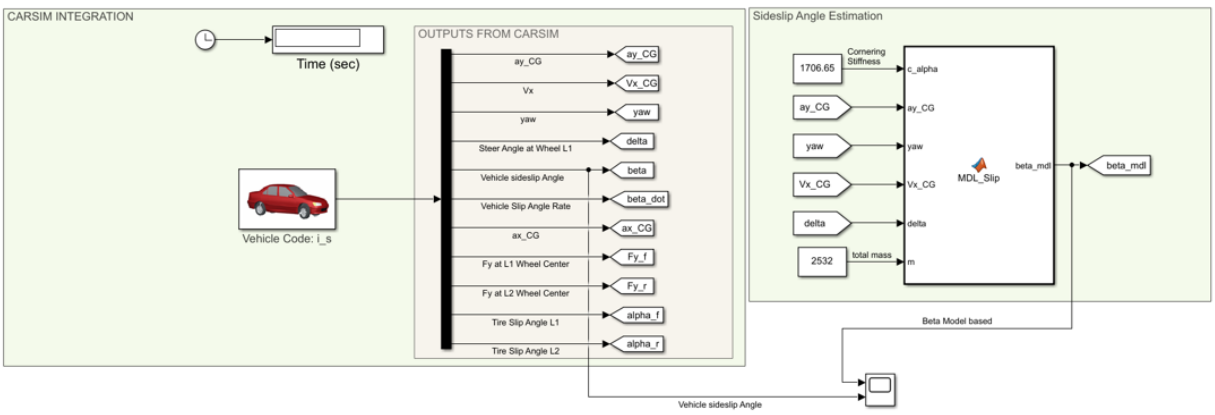

Figure 6.14: CarSim/Simulink Interface for Side Slip angle estimation

Figure 6.15 shows the estimated side slip angle plotted against the CarSim side slip angle (true value) for a Double Lane Change (DLC) maneuver. From this figure, it can be seen that the estimator is able to track the true value with a $\mp$ 0.5° error margin.

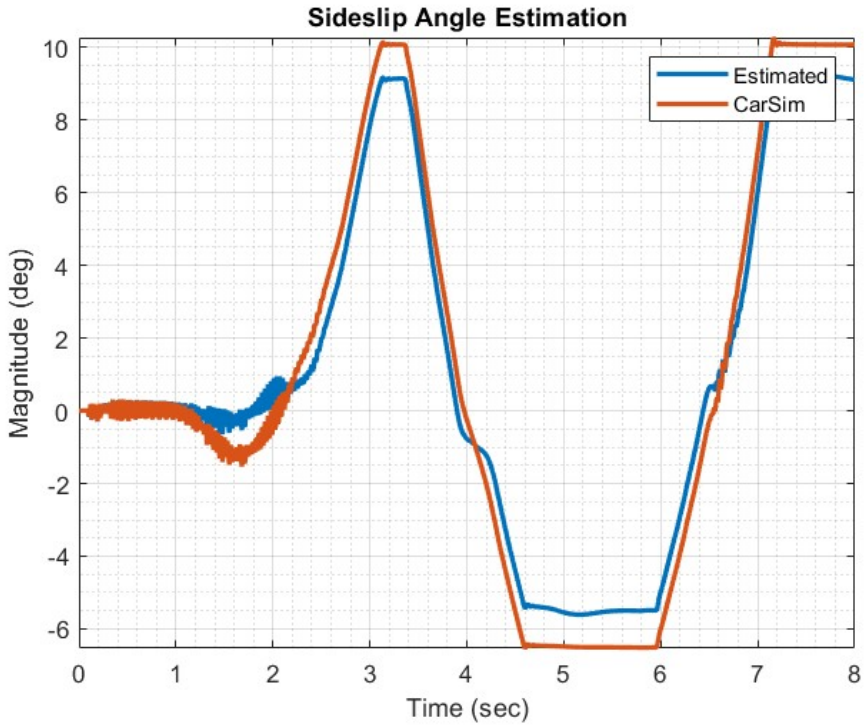

Figure 6.15: Vehicle side slip angle estimation results

Slip Angle Estimation

With the estimation of the vehicle side slip angle, the front and the rear tire slip angle can be obtained by using the kinematic relations shown in Equation 6.20 and Equation 6.21 respectively.

$$\alpha_f = \delta - (\beta + \frac{rL_f}{V_x}) \tag{6.20}$$

$$\alpha_r = -\beta + \frac{rL_r}{V_x} \tag{6.21}$$

Figure 6.16 shows the comparison between the estimated slip angle of the front tire and the CarSim true value. Sharp discontinuities can be seen at the inflection points which correspond to the turns of the DLC maneuver.

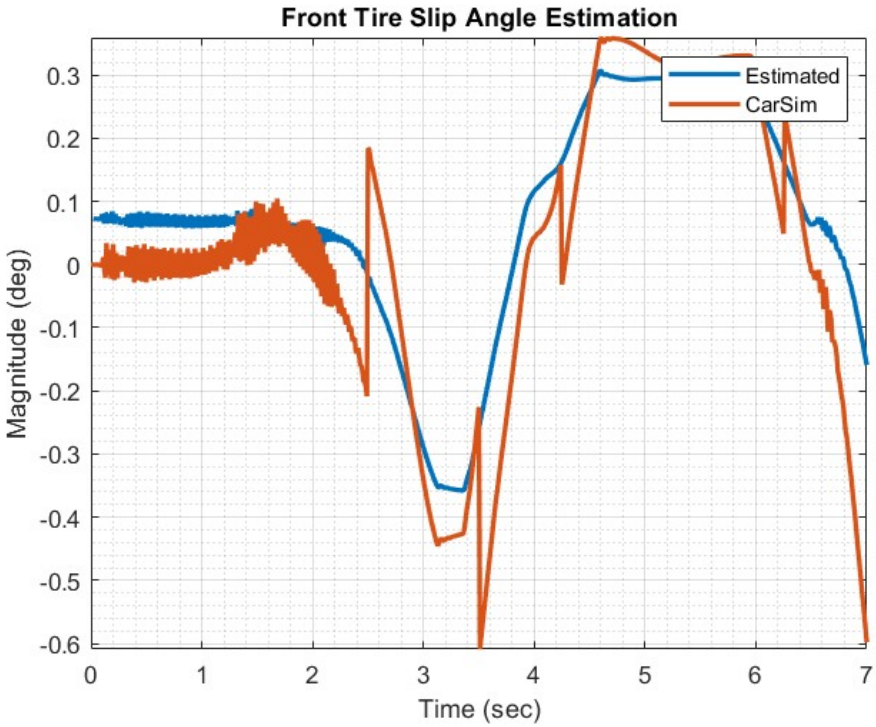

Figure 6.16: Front Tire Slip Angle Estimation

Chapter 7

Structural Health Monitoring

Some parts of this Chapter have been derived from Gorantiwar et al. [117] and Gorantiwar et al. [118].

7.1 Introduction

Structural Health Monitoring (SHM) plays a crucial role in the following two aspects:

- Identifying and classifying between different mechanical defects present within a system.
- Determining the Remaining Useful Life (RUL) of the system based upon a historic collection of vibration data.

The tire models and the vehicle models developed in Chapters 3, specifically the Fiala tire model, have an inherent assumption in them stating that changes in the tire composition, inflation pressure and tire abrasion, do not affect the lateral and longitudinal stiffness of the tire. This directly affects the lateral and the longitudinal forces generated by the tire model. Hence, it is necessary to have a parallel running estimation system which would determine the health of the tire at every time instant to ensure that the estimations given by the plant model fall within the working range of the system.

In this Chapter, the following objectives have been met:

- Time and Time-frequency based defect classification algorithms have been developed to distinguish between a normal ball bearing and a ball bearing with an inner race defect.
- This algorithm has been further extended to classify between different intensities of the defect.
- The combined ML algorithm has been validated on an in-house built test rig to classify between the two different bearing defect classes.
- The developed algorithm has been tested to classify between a completely worn out tire and a new tire.

7.2 Defect Classification

The experimental setup discussed in Section 5.3 has been used to acquire accelerometer data and further develop different signal processing and machine learning algorithms.

7.2.1 Time Domain Analysis

The accelerometer data has been analyzed in time-domain to identify features which can be used as potential indicators to classify between the two different bearings. Figure 7.1 shows the time domain signal for the normal bearing and the bearing with the inner race defect, respectively. Different statistical features have been extracted from the raw accelerometer data to quantify the bearing defect signatures. The entire dataset has been divided into batches of 100 points each and the features have been extracted for each of these batches.

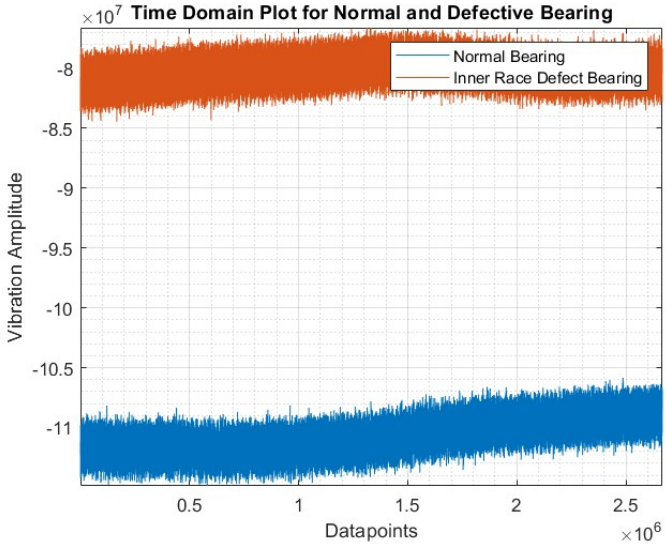

Figure 7.1: Time Domain Plot for Bearing Defect Analysis

- Mean(μ): Average value of the vibration signal

$$\mu = \frac{1}{N}\sum_{i=1}^{N} x_i \tag{7.1}$$

- Standard Deviation (σ): Dispersion of accelerometer data relative to mean.

$$\sigma = \sqrt{\frac{1}{N-1}\sum_{i=1}^{N}(x_i - \mu)^2} \tag{7.2}$$

- Skewness (μ_3): Measures the accelerometer data asymmetry of its probability distribution.

$$\mu_3 = \sum_{i=1}^{N}\frac{(x_i - \mu)^3}{(N-1)\sigma^3} \tag{7.3}$$

- Kurtosis (μ_4): Measures whether the accelerometer data is light tailed with respect to

its normal distribution

$$\mu_4 = \sum_{i=1}^{N} \frac{(x_i - \mu)^4}{(N-1)\sigma^4} \tag{7.4}$$

- Crest Factor (f_{crest}): Measures the peak value of the vibration data divided by its RMS.

$$f_{crest} = \frac{x_p}{\sum_{i=1}^{N} x_i^2} \tag{7.5}$$

- Impulse Factor ($f_{impulse}$): Measure of the peak value of the signal with respect to its mean

$$f_{impulse} = \frac{x_p}{\sum_{i=1}^{N} |x_i|} \tag{7.6}$$

- Peak-to-peak Factor: Computes the difference between the maximum and the minimum value within a given accelerometer signal.

- Root Mean Square (x_{RMS}): Computes the Root Mean Square value of the accelerometer signal.

$$x_{RMS} = \sqrt{\frac{1}{N} \sum_{i=1}^{N} (x_i)^2} \tag{7.7}$$

- Shape Factor (f_{shape}): Provides a measure of the shape of the signal while being independent of its dimensions

$$f_{shape} = \frac{x_R MS}{\frac{1}{N} \sum_{i=1}^{N} |x_i|} \tag{7.8}$$

- Margin Factor (f_{margin}): Computes the maximum absolute value of the accelerometer vibration signal with respect to its RMS value

$$f_{margin} = \frac{max(x_i)}{(\frac{1}{N}\sum_{i=1}^{N}\sqrt{x_i})^2} \tag{7.9}$$

- Spectral Mean: Computes the mean value of the signal in frequency domain.

- Spectral Standard Deviation: Computes the standard deviation of the signal in the frequency domain.

- Spectral Skewness: Computes the skewness of the signal i.e., the third moment in frequency domain.

- Spectral Kurtosis: Computes the kurtosis of the signal i.e., the fourth moment in the frequency domain.

- Energy: Computes the spectral energy content of the accelerometer vibration signal.

Figure 7.2 shows the statistical feature visualization for both the normal and the defective bearing respectively.

To quantify the effects of each of these 14 statistical features, monotonicity analysis has been conducted. Monotonicity essentially determines the monotonic trends in the different health indicators as the bearing system approaches failure. A monotonicity value of 1 indicates that the given feature is completely monotonic and accurately represents the health of the bearing. Similarly, monotonicity value of 0 indicates that the feature is completely non-monotonic and does not describe the bearing health as it approaches failure. Monotonicity for every statistical feature has been evaluated as given in Equation 7.10.

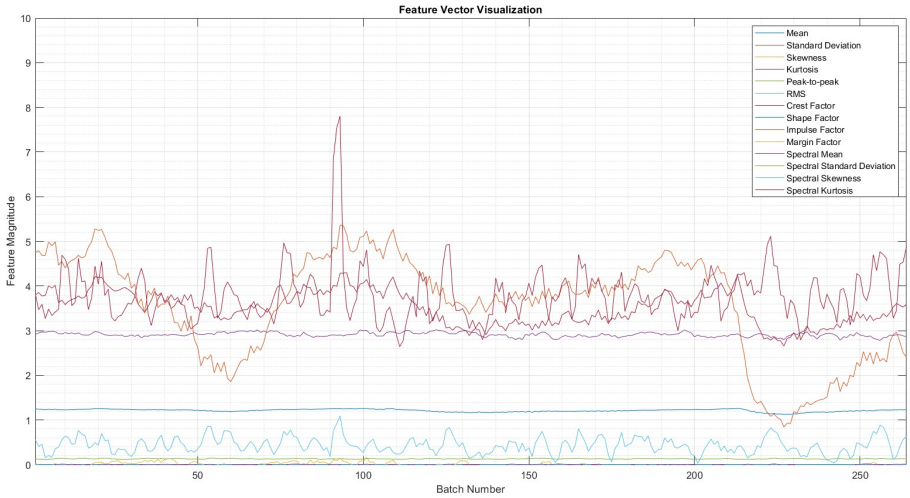

Figure 7.2: Feature Vector Visualization

$$Monotonicity = \frac{1}{N}\sum_{i=1}^{N}\left|\sum_{j=1}^{M}\frac{sgm(x_i(j+1)-x_i(j))}{N_i-1}\right| \tag{7.10}$$

Figure 7.3 shows the monotonic trends for the different features for a bearing with an inner race defect. Based upon a qualitative analysis of the monotonicity plot and literature review, a threshold value of 0.025 has been selected.

Machine Learning Algorithm Development

The statistical features described in the previous section were used as inputs to the developed machine learning algorithms for bearing defect classification. A bi-layered Neural Network (NN) Model was developed to classify between the two bearings. The model hyperparameters were tuned and are listed in Table 7.1. The tuning of parameters was performed via a Grid Search method.

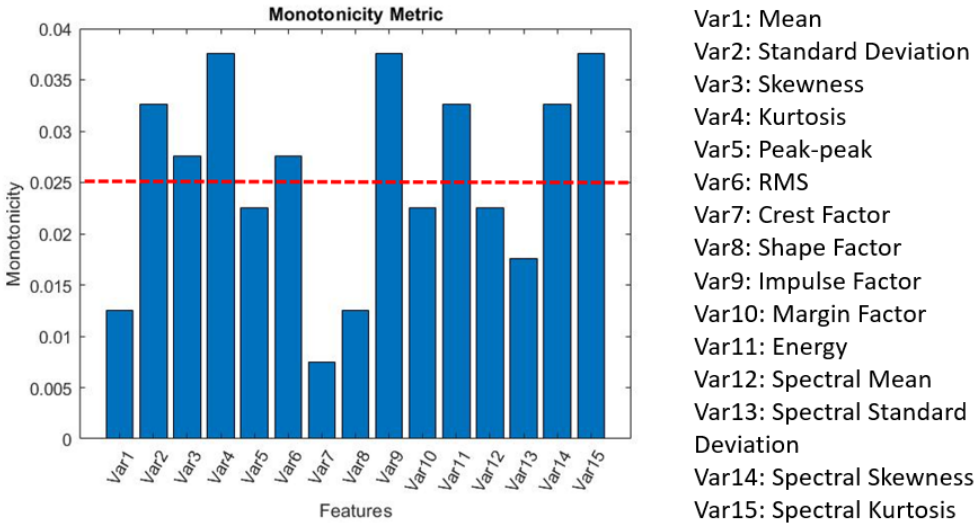

Figure 7.3: Monotonicity Analysis

Table 7.1: NN Model Hyper-parameters

Parameter	**Values**
Number of Fully Connected Layers	2
First Layer Size	2.6
Second Layer Size	2
Activation Function	ReLU
Maximum Number of Iterations	1500

Using the above described NN architecture, the classification metrics were analyzed via its confusion matrix and scatter plot variations respectively. Figure 7.4 shows the scatter variations for the two bearings. Principal Component Analysis (PCA) was performed for feature dimensionality reduction.

Figure 7.5 shows the confusion matrix results for this binary classification. Here, Class 0 represents the normal "healthy" bearing and Class 1 represents the bearing with the inner race defect.

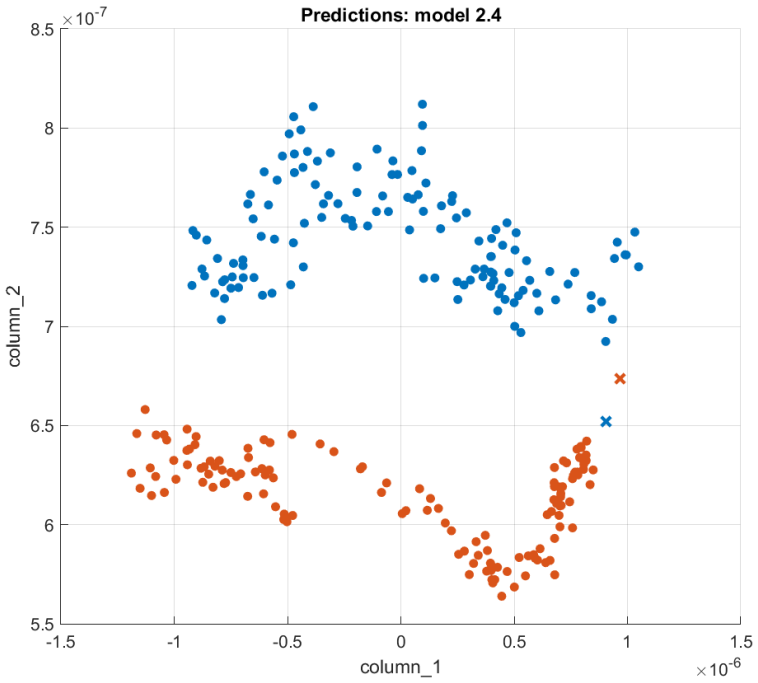

Figure 7.4: Scatter Plot for bearing defect classification - Blue (Inner Race Defect), Red (Normal Bearing)

7.2.2 Time-Frequency Domain Analysis

The second approach for the defect classification lies in the time-frequency domain based analysis. As opposed to the previous approach, in which time domain signals were studied, having a spectral approach enables gaining useful insight on the information available in both the time-frequency and spatial space. A wavelet-based approach is proposed over using Short Term Fourier Transforms (STFT) as the required window length can be changed by dilating and translating the wavelets, which provide the freedom to choose the time and frequency resolutions, respectively. For wavelet transform, the frequency resolution is better at lower frequencies and the time resolution is enhanced at high frequencies.

Based on an extensive literature review and having equal variance in both time and frequency domains, continuous Morlet wavelet was selected.

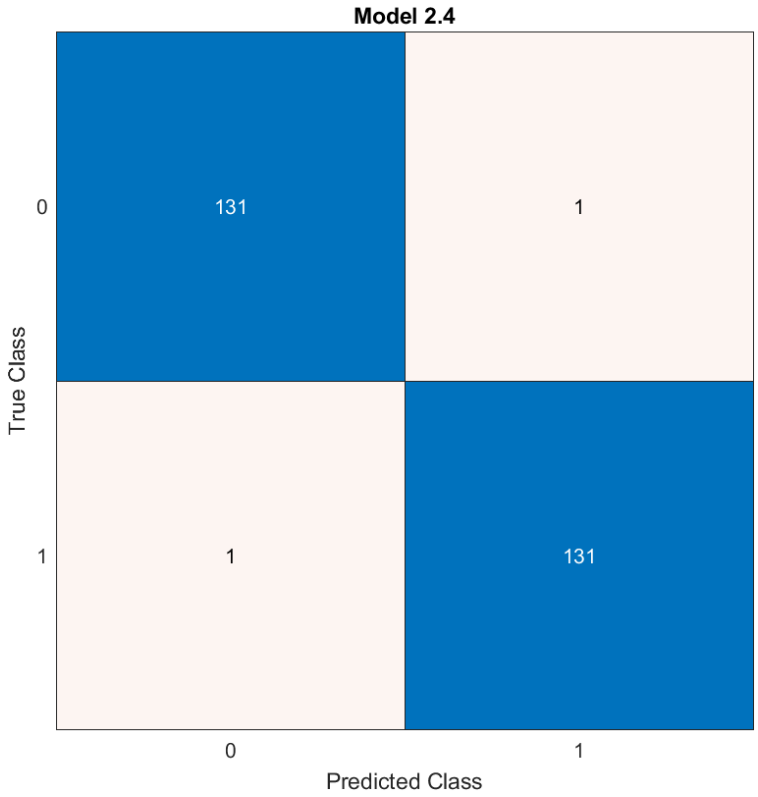

Figure 7.5: Confusion Matrix for Bearing Defect Classification

An important reason for going with this approach is that the bearing failure, due to these defects, can be further classified based on different frequency bands. This helps in determining what type of failure occurs at what frequency level. These zones are listed as follows:

- Stage 1: Acoustic emission: During the bearing operation, bursts of acoustic emissions (AE) result from the passage of the defect through the roller and raceway contacts. Defects at different locations of a bearing (inner race, roller and outer race) have characteristic frequencies at which bursts are generated – above 100kHz. The data corresponding to these frequency ranges can identify subtle defects like lack of lubrication.

- Stage 2: Ultrasonic frequencies: In ball bearings, as the metal in the raceway, roller or ball elements begins to fatigue, a subtle deformation begins to occur. This deforming

of the metal produces irregular surfaces, which cause an increase in the emission of ultrasonic sound waves (24 to 100kHz).

- Stage 3: Rotational harmonics: Defects start to ring at the bearing's natural frequencies. This generally occurs between 500 and 5,000 Hz. These natural frequencies may be resonances of either bearing support structures or components of the bearings themselves such as races or rolling elements. Side-band frequencies also start to appear above and below these frequencies.

Figure 7.6 shows the scalograms for different defect conditions of the bearing. From this Figure, we can see that, especially at lower frequencies, there is a substantial difference in the energy content between the different test conditions

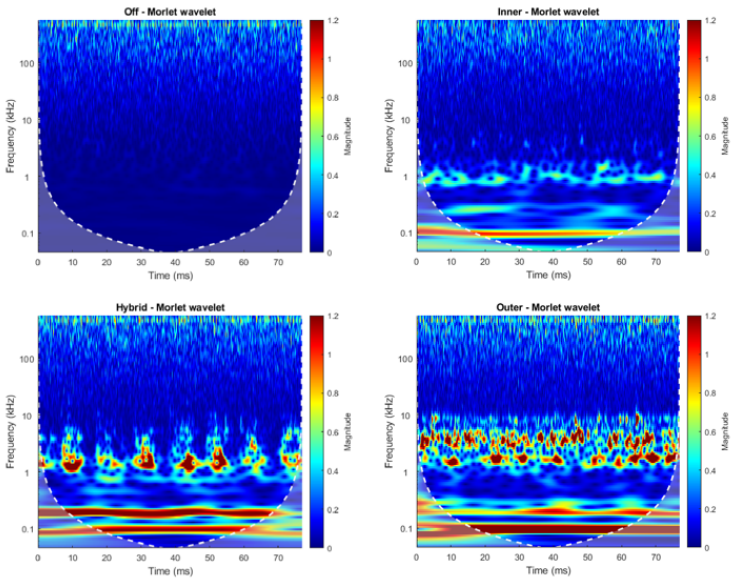

Figure 7.6: Scalograms for different bearing defect types

The overall process followed for the time-frequency analysis can be seen in Figure 7.7. Initially, the raw accelerometer data is normalized and converted to micro-strain values for better evaluation. The entire data is then sub-sampled into smaller batch sizes of 10000

data points each and the continuous Morlet wavelet transformation is performed for each of these batch sizes. The resulting time-frequency matrices was given as input to the machine learning based classification algorithm.

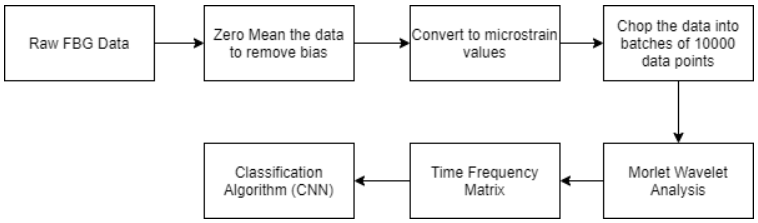

Figure 7.7: Time-Frequency Methodology

Machine Learning Algorithm Development

As discussed in the previous subsection, continuous Morlet wavelet has been used to generate spectral maps for the four defect classes which have been then fed as input tensors to a Convolutional Neural Network (CNN) architecture. Deep learning based CNN framework has been selected because by keeping the time-frequency image as a matrix, the spatial variation is preserved, which otherwise would have been lost by flattening the data.

The input feature is the time-frequency matrix, which is essentially a grayscale image, and the output is the condition of the bearing. In order to characterize the noise within the system, accelerometer data was also collected when the test rig was in an idle condition and this scenario has been treated as a separate class while performing the defect classification. Since there are 5 classes – Normal bearing, Inner race defect, outer race defect, hybrid defect, and static noise (bearing not running), this is a 5-class classification problem.

The architecture of the CNN model is described below:

- The input feature vectors are grayscale images of size 221x221.

- These feature images are then fed to a convolution layer with a 3x3 Gaussian kernel and 10 filters in each convolution layer.

- The activation function used is 'Rectified Linear Unit' due to its reduced likelihood of the gradient to vanish, being computationally efficient (as only 'max' operation needs to computed) and having better convergence performance.

- The resulting feature map is then fed to a Max pooling layer to generate a feature map containing the most prominent features of the previous feature map.

- This has been repeated for three convolution layers followed by a flatten layer and fully connected dense layers to make classifications.

A Key point to notice is that the entire time-frequency matrix is given to the CNN architecture in the form of an image input. In this way, the model can focus on all 3 frequency zones and can identify the slight damages in a bearing. This also makes the approach very scalable. CNN's help preserve the spatial variation of time and frequency data. The input image can be transformed into various domains, by multiplying with kernels, and better features can be extracted. The model automatically understands which frequencies to focus on, corresponding to the severity of the defect in the bearing.

Figure 7.8 shows the confusion matrix and the corresponding precision and recall scores for the 5-class classification algorithm. A classification accuracy of **98%** was obtained using this approach. This is significantly higher than the previous two approaches indicating that the wavelet based approach, due to its ability of focusing on all frequency ranges, gives a higher classification performance.

	precision	recall	f1-score	support
hybrid	1.00	0.98	0.99	50
normal	0.96	0.96	0.96	50
outer	1.00	1.00	1.00	50
inner	0.96	0.98	0.97	50
noise	1.00	1.00	1.00	50
accuracy			0.98	250
macro avg	0.98	0.98	0.98	250
weighted avg	0.98	0.98	0.98	250

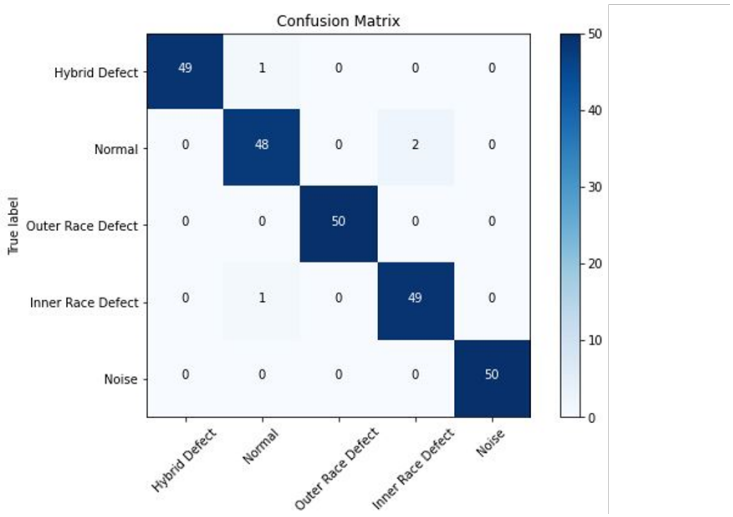

Figure 7.8: Confusion Matrix - Time Frequency Domain - Bearing Defect Type

7.3 Defect Intensity Classification

Along with classifying different types of defects, the levels of intensity of a particular defect were also analyzed by progressively increasing the depth of the indentation/cut on the inner race of the bearing. Six different depth defects were developed on the inner race of the bearing which can be seen in Figure 7.9.

Based on an in-depth analysis of the three defect classification algorithms developed, it can be seen that the time-frequency based approach has the highest values of classification performance metrics. A key reason for this is that the physics based models of time and frequency domains do not necessarily capture the non-linear effects created by the defects

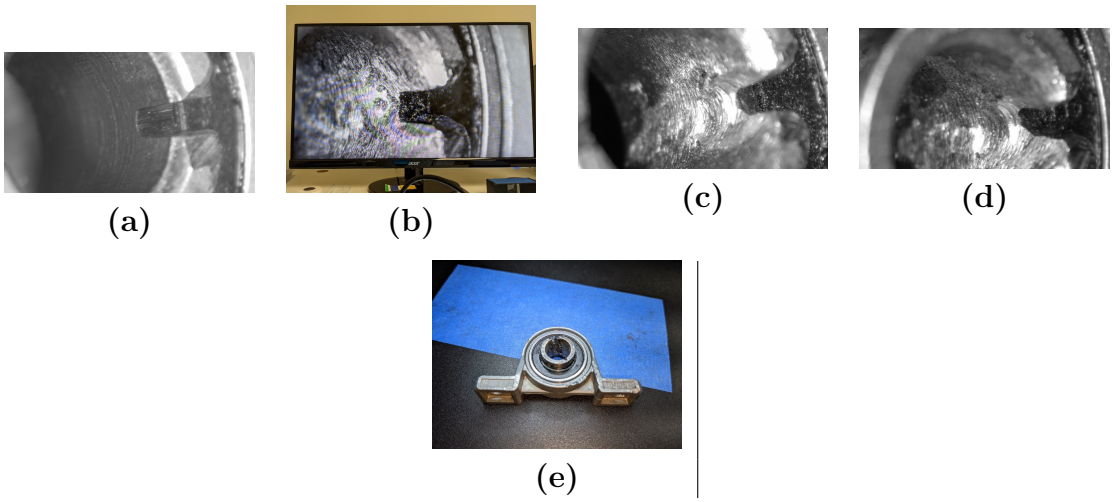

Figure 7.9: **(a)** First Cut **(b)** Third Cut **(c)** Fourth Cut **(d)** Fifth Cut **(e)** Sixth Cut

in the bearing. Hence, the same framework has also been used to characterize an inner race bearing defect of varying intensity and classify between these intensities of defect.

Figure 7.10 shows the time series plot of the six different intensities of the inner race defects discussed. Levels 1-6 indicate progressively higher intensities of the defect.

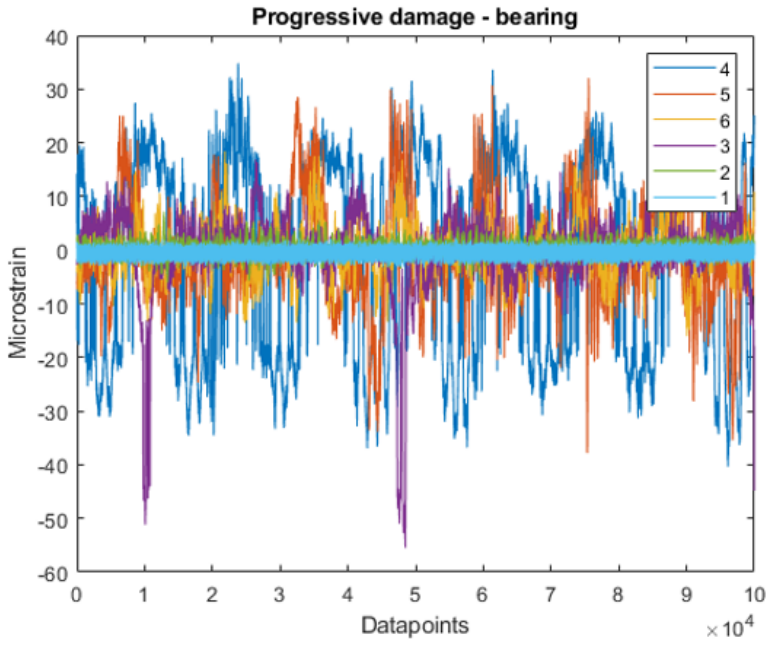

Figure 7.10: Varying Defect Intensity Time Series Plot

A wavelet process similar to that for classifying the different defect types has been followed. Figure 7.11 shows the scalograms for the 6 levels of the intensity of the defect. From this Figure, it can be seen that as the defect size increases, the energy content increases in the lower frequency ranges.

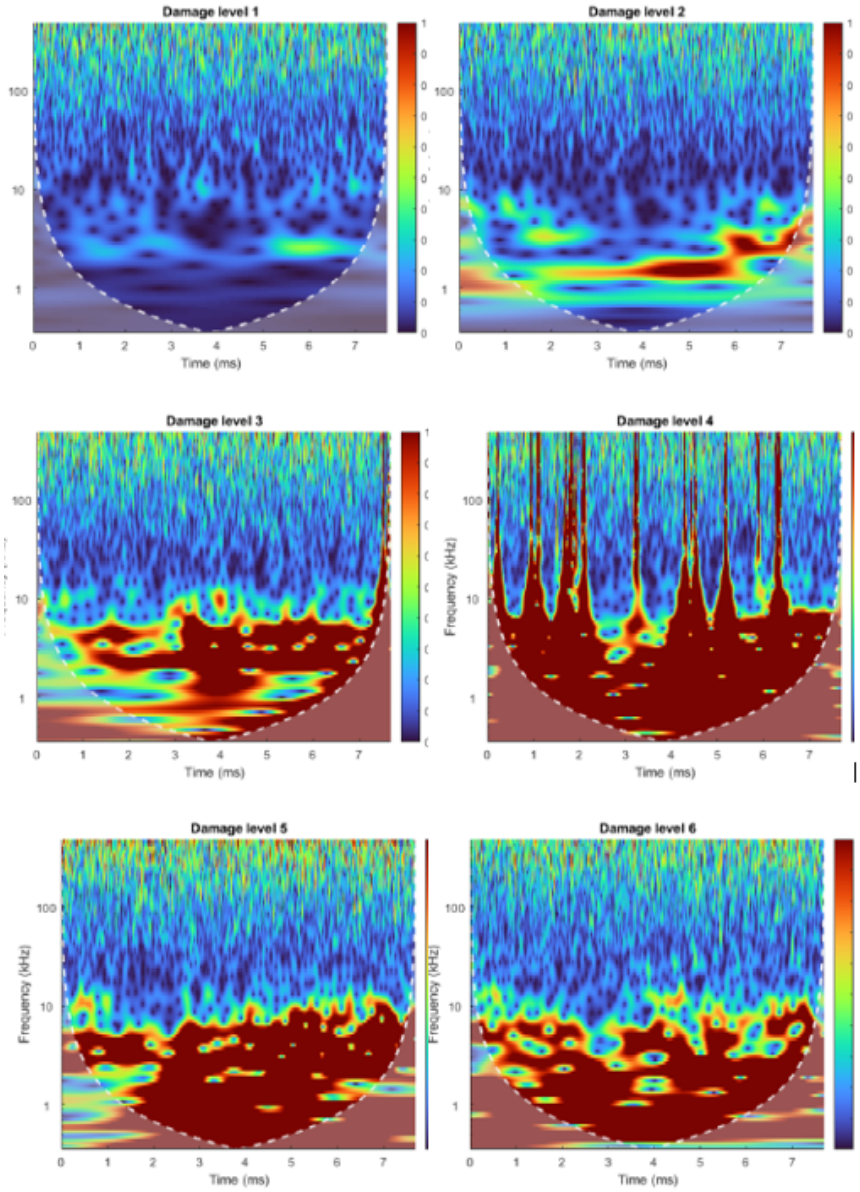

Figure 7.11: Scalograms for varying defect intensity

The CNN algorithm developed for classifying the bearing defect types has been re-implemented

for defect intensity classification. Figure 7.12 shows the confusion matrix for intensity classification along with the corresponding precision, recall and F1-scores for the different damage levels. A classification accuracy of **98.9%** has been obtained for defect intensity classification using this approach.

	precision	recall	f1-score	support
dam1	1.00	0.96	0.98	50
dam2	1.00	1.00	1.00	50
dam3	0.96	0.98	0.97	50
dam4	0.98	1.00	0.99	50
dam5	1.00	1.00	1.00	50
dam6	1.00	1.00	1.00	50
accuracy			0.99	300
macro avg	0.99	0.99	0.99	300
weighted avg	0.99	0.99	0.99	300

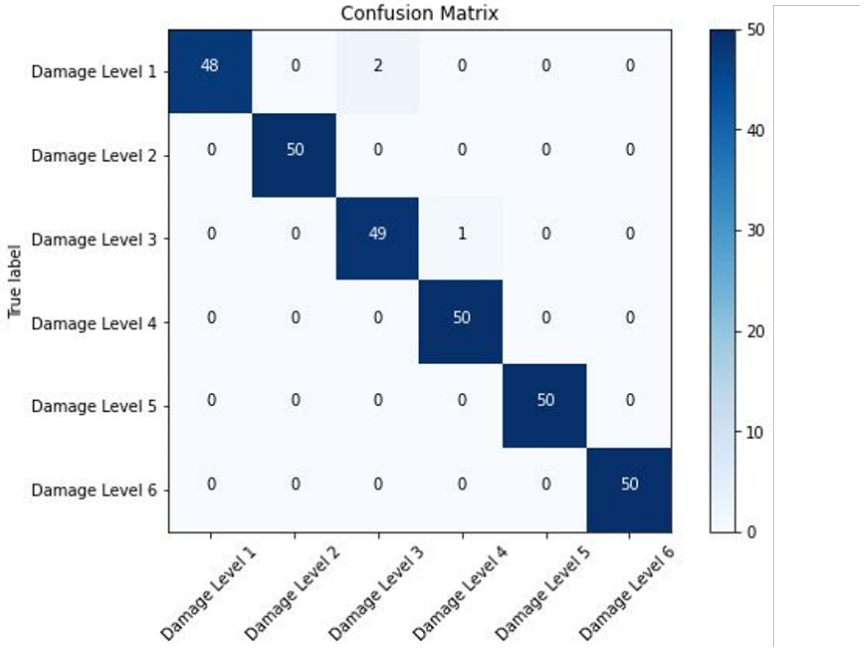

Figure 7.12: Confusion Matrix - Time Frequency Domain - Defect Intensity

7.4 Real Time Algorithm Implementation

Based upon the above discussed methodologies and the experimental setup, tests have been conducted to perform binary defect classification – normal bearing and bearing with inner race defect, in real time. Figure 7.13 shows the system architecture of the Simulink Real-Time code which has been used to perform real-time defect classification. The experimental test rig has been modified such that it can house two bearings, normal and inner race defect bearing, on the same shaft to better evaluate the efficiency of the algorithm in real time.

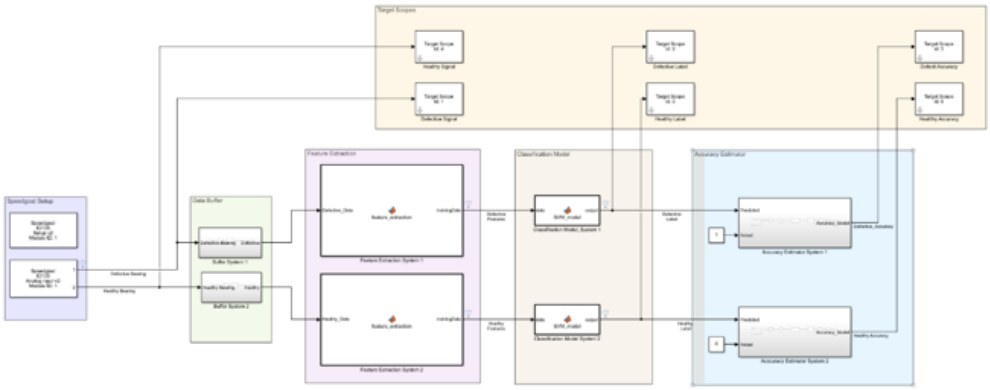

Figure 7.13: Simulink Real Time Architecture

The code block consists of the following key sub-blocks:

- Buffer Module: This module is used to hold the data for one period, to acquire 5000 data points before sending it to further modules for processing.
- Feature Extraction Module: This module is used to compute the time-domain based statistical features as discussed in the previous section.
- Normalization Module: This module has been used to zero-mean the data to achieve standardization.

- ML Module: This module has been used to perform different ML based defect classification algorithms. Pre-trained models, trained on the previously collected data, have been utilized and the real-time data is essentially the test data being fed to the ML model.

- Visualization Module: This module is used to display the accelerometer data, and the classification metrics on the Target Display. Figure 7.14 shows the HMI display which has been used. The following observations can be made via the target display:

  - Raw Accelerometer
  - Classification Accuracy
  - Predicted Class Labels

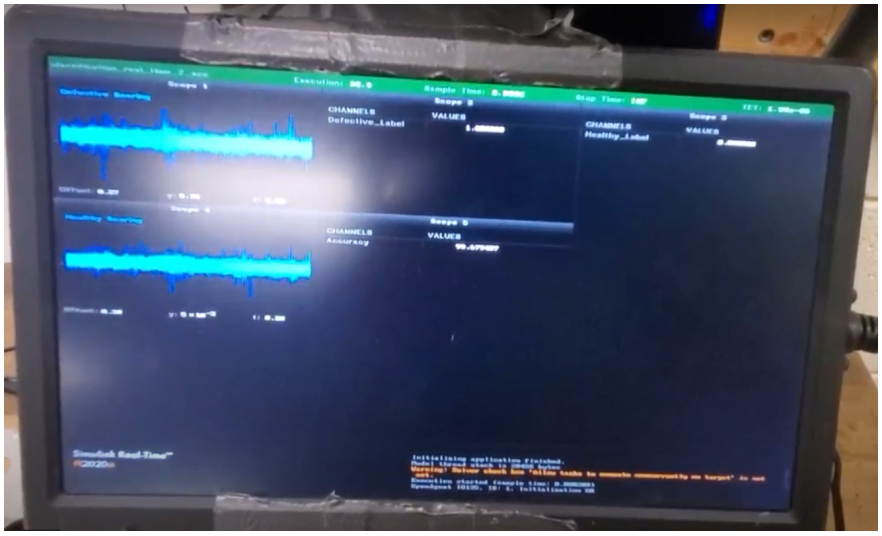

Figure 7.14: HMI Display for Real-Time Classification

Two test cases have been developed to evaluate the efficacy of the developed algorithm as discussed in the following subsections.

7.4.1 Test Case 1: 'Stethoscope Test'

In this test case, only one single axis accelerometer has been used. The accelerometer is initially placed on the normal bearing and the class label given by the algorithm has been stored. Similarly, the accelerometer position was then shifted to the pillow block casing of the defective bearing and the change in class label has been evaluated. The proposed system architecture was able to correctly predict between the two bearings with a class label accuracy of 96.8%.

7.4.2 Test Case 2: Simultaneous Classification Test

In the second test case, two single axis accelerometers have been used and they have been placed on the pillow block of the two bearings. The F1-score is then evaluated in real-time to classify between the normal bearing and the defective bearing. Figure 7.15 shows the test setup and the target display for this test case. An average classification accuracy of 97.8% was obtained for this test case.

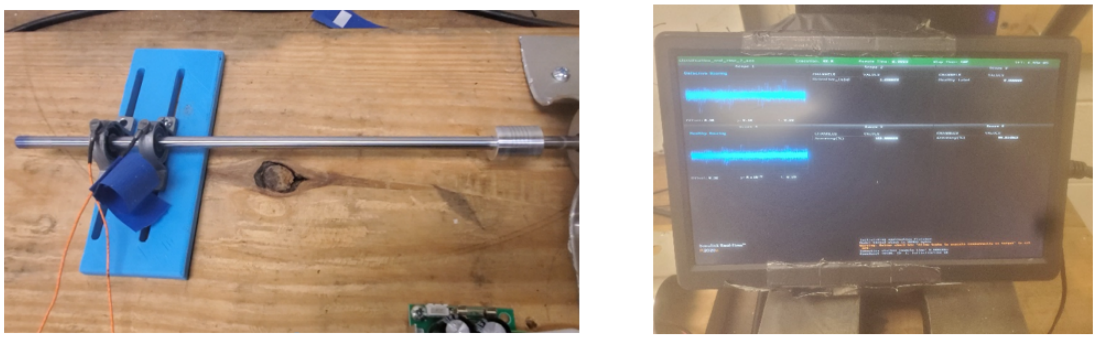

Figure 7.15: Simultaneous Classification Test Case

7.5 Tire Defect Analysis and Classification

The algorithms, which have been discussed in the above 4 subsections, have been further extended to classify between a completely new tire and a completely worn out tire. This section enlists the testing matrix followed, different data processing used and the machine learning algorithm results in classifying between the two tires.

7.5.1 Testing Procedure

The instrumented vehicle (VW Jetta) as discussed in Section 5.1, has been used for data collection for the new tire and a completely worn out tire. Data has been collected for varying conditions of input parameters - tire inflation pressure, normal load, vehicle longitudinal velocity and road surfaces. Table 7.2 enlists the different variations of the input parameters to collect the data

Table 7.2: Test Matrix for Data Collection

Parameter	**Values**
Tire Inflation Pressure (bar)	1.7, 2.1, 2.5
Vehicle Longitudinal Velocity (km/hr)	20, 30, 40, 50
Normal Load (kg)	0, 100
Road Surface	Dry Asphalt, Dry Concrete

The "intelligent tire" has been mounted on the rear right side of the vehicle. The tire has two accelerometers mounted diametrically opposite on the inner lining of tire to collect the vibration data along the X,Y, and Z axis. To measure the wear of the tire, a tread depth measurement device has been used and the tire tread depth has been recorded for the new tire and the old tire. Table 7.3 describes the tire used along with the tread depth values.

Straight Line maneuvers have been conducted for each of the two tires for the above men-

Table 7.3: Test Tire Information

Parameter	Values
Tire Description	Radial Tire 195/65R15
New Tire Tread Depth	6.33mm
Old Tire Tread Depth	3.38mm

tioned test conditions. The tests have been performed on two test tracks at Virginia Tech corresponding to the two different road surfaces:

- Dry Asphalt - Parking Lot behind Perry Street closed parking lot.
- Dry Concrete - Perry Street Parking Lot - P2 Parking Level (Closed)

7.5.2 Data Processing

The accelerometer data has been analyzed in time and frequency domain to extract key features differentiating the new and the worn out tire. These features have then been fed to the ML classification algorithms.

Time Domain Analysis

As discussed in Chapter 6, the tire accelerometer data has been pre-processed via the following steps:

- Splitting the data into individual tire revolutions based on the X axis acceleration data.
- Filtering the data via a low pass 2nd order filter.

Figure 7.16 and Figure 7.17 shows the time domain plot of the tire accelerometer data along the X and Z axis respectively. The worn out tire has approximately 20% higher magnitudes as compared to the new tire. This is attributed to

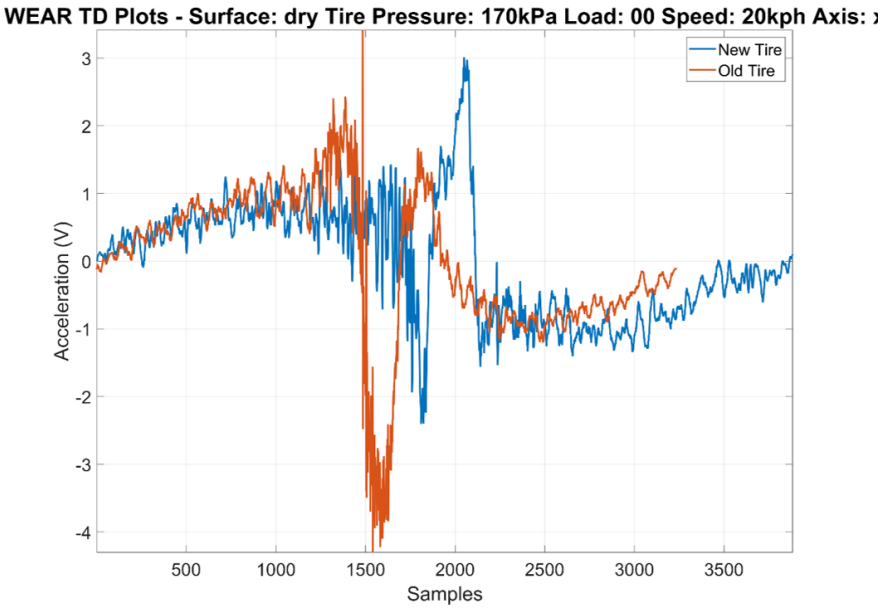

Figure 7.16: Time Domain Analysis - X Axis Data

Frequency Domain Analysis

The time domain data for a single tire revolution has been converted to the frequency domain by using the Welch's method has been used. This method essentially uses Hamming windowing to convert data from time domain to the frequency domain. Equation 7.11 shows the methodology to compute the Hamming coefficients.

$$\omega(n) = 0.54 - 0.46\cos(\frac{2\pi n}{N}) \tag{7.11}$$

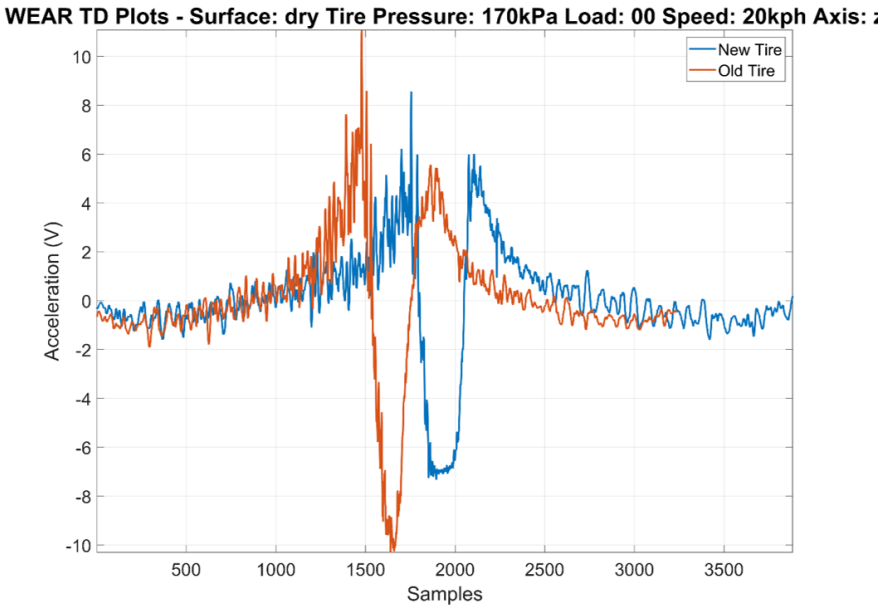

Figure 7.17: Time Domain Analysis - Z Axis Data

where;

N = Total number of data points

ω = Coefficients of the Hamming window

Figure 7.18 and Figure 7.19 shows the Power Spectral Density (PSD) plot for the two axes of the accelerometer data.

From this analysis, it can be concluded that, differences can be seen between the PSD estimates of the old tire and new tire for different frequency regimes. The PSD estimates have been calculated for each of the different test run cases and have been stored in a cell structure.

To extract suitable features from the PSD analysis, the "Mean Square Value (MSV)" of the accelerometer data, for each of the three axis, and for each test run has been computed. MSV corresponds to the Area Under the Curve (AUC) of the PSD plot estimates. Figure 7.20 shows the AUC values for each of the test conditions. From this figure, it can be observed

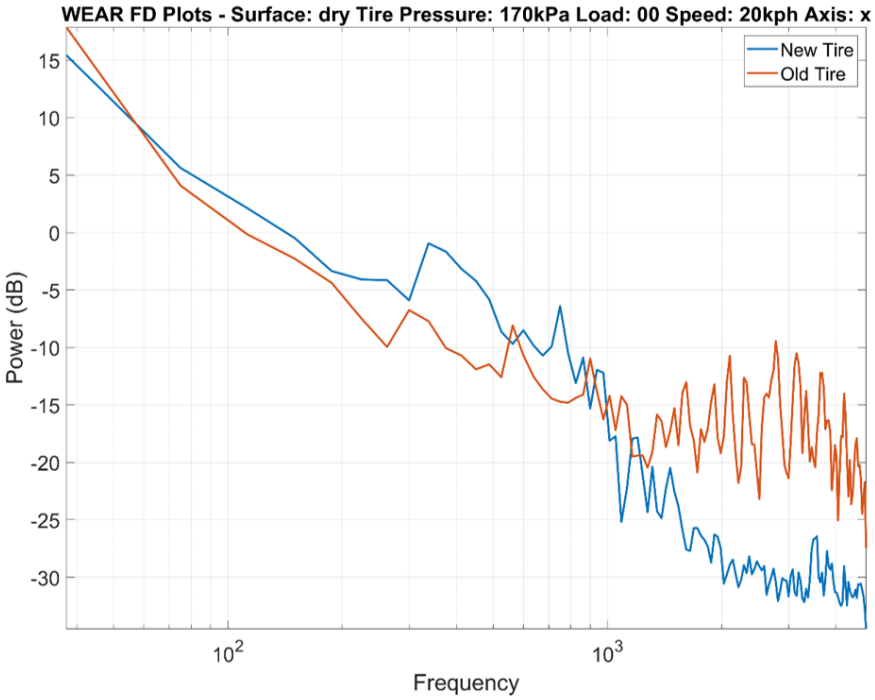

Figure 7.18: Frequency Domain Analysis - X Axis Data

that the worn-out tire has less AUC for almost all test conditions. AUC has been used as the feature vector for further development of the ML classification algorithms.

To analyze the standard deviation of the AUC parameter for each test condition corresponding to the number of tire revolutions, an error bar plot has been developed. Figure 7.21 shows this error bar diagram visualized for a subset of test conditions.

To quantify the AUC differences for tire revolutions, the mean and standard deviation for each test case has been computed, and some of these have been tabulated in Table 7.4, along with the average values for all the 47 test cases.

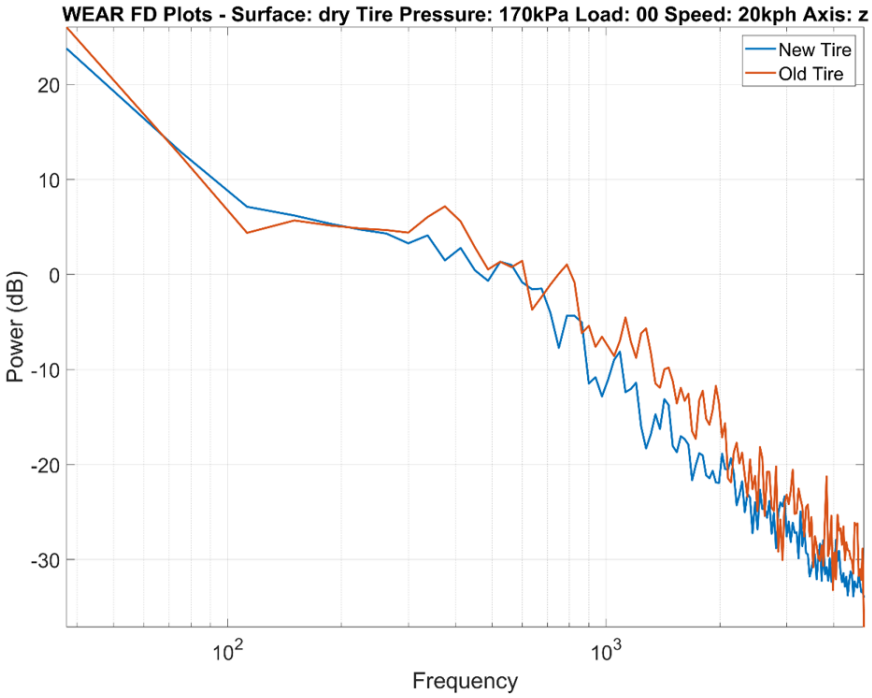

Figure 7.19: Frequency Domain Analysis - Z Axis Data

Table 7.4: Mean and Standard Deviation AUC values for New and Worn Tire

Test (Condition) Number	**New Tire (Mean)**	**Worn Tire (Mean)**	**New Tire (Deviation)**	**Worn Tire (Deviation)**
5	$8.27e^4$	$8.11e^4$	$1.41e^3$	$1.42e^3$
10	$1.07e^5$	$7.51e^4$	$7.16e^3$	$3.30e^3$
15	$1.06e^5$	$9.51e^4$	$1.09e^4$	$2.16e^3$
20	$7.44e^4$	$6.95e^4$	$1.15e^3$	$2.47e^3$
25	$1.27e^5$	$5.50e^4$	$5.09e^3$	$9.85e^2$
30	$1.28e^5$	$8.68e^4$	$1.71e^3$	$7.68e^3$
35	$1.273e^5$	$8.47e^4$	$1.32e^3$	28.53
40	$7.81e^4$	$6.57e^4$	$6.75e^2$	$6.47e^3$
45	$1.075e^5$	$4.53e^4$	$1.54e^3$	$7.80e^2$
Average	$\mathbf{1.04}e^5$	$\mathbf{7.09}e^4$	$\mathbf{3.23}e^3$	$\mathbf{2.98}e^3$
where, Me^n means $M \times 10^n$				

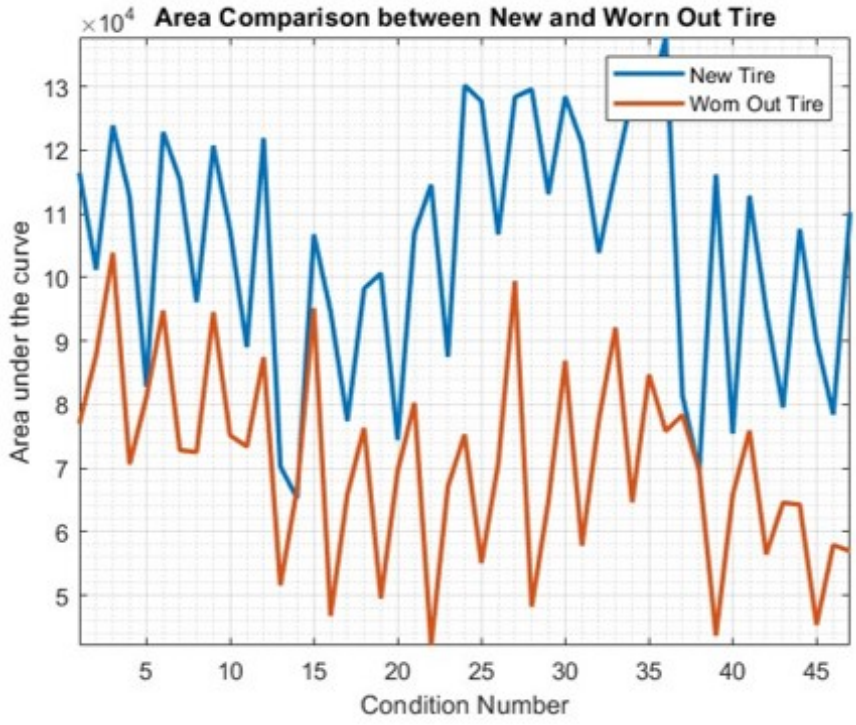

Figure 7.20: Area Under the Curve (AUC) Analysis

7.5.3 Machine Learning Classification Algorithms

Different binary classification algorithms have been developed and implemented to classify between the two tire cases:

- Gaussian Naive Bayes
- Support Vector Machine (SVM)
- K-Nearest Neighbor (KNN)
- Bagged Trees
- Neural Networks

Out of the above mentioned algorithms, it was observed that Gaussian Naive Bayes (GNB)

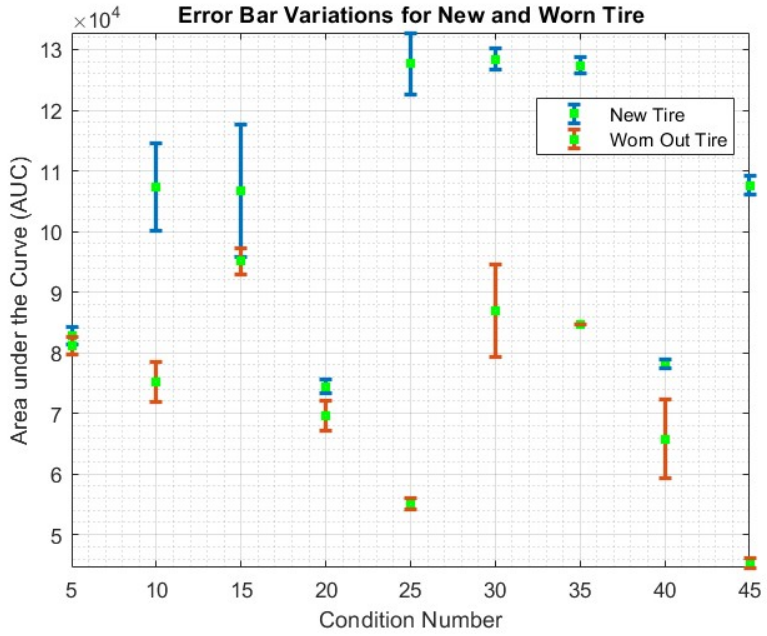

Figure 7.21: Standard Deviation for New and Worn Tire AUC corresponding to number of tire revolutions for subset of test conditions

performed the highest in terms of its precision and recall scores. The primary reason for this is that the AUC values follow a Gaussian distribution having the likelihood given by Equation 7.12. A comparative analysis between the different machine learning algorithms can be seen in Table 7.5.

$$P(x_i|y) = \frac{1}{\sqrt{2\pi\sigma}} exp(-\frac{(x_i - \mu)^2}{2\sigma^2}) \tag{7.12}$$

GNB algorithm has been used to classify the new tire from the worn out tire for two cases: by observing the X, Y, and Z axis tire accelerometer data simultaneously and by looking at the individual axis data. A total of 47 conditions have been used to train the algorithm, each condition corresponding to different variations of the input parameters (tire pressure, vehicle velocity, normal load, and road surface). Each condition comprises 127 PSD data

points which have been averaged to evaluate the AUC resulting in 94 data points being passed to train the model

Based on all multi-axis data

Figure 7.22 shows the GNB confusion matrix with the True Positive Rate (TPR) and False Negative Rate (FNR), respectively. TPR essentially represents the proportion of the correctly classified observations per true class, whereas FNR represents the proportion of incorrectly classified observations per true class. A classification accuracy of **80.9%** has been obtained by using the GNB classifier. 83% of cases with worn-out tires have been correctly classified while that for the new tire stands at 76.6%.

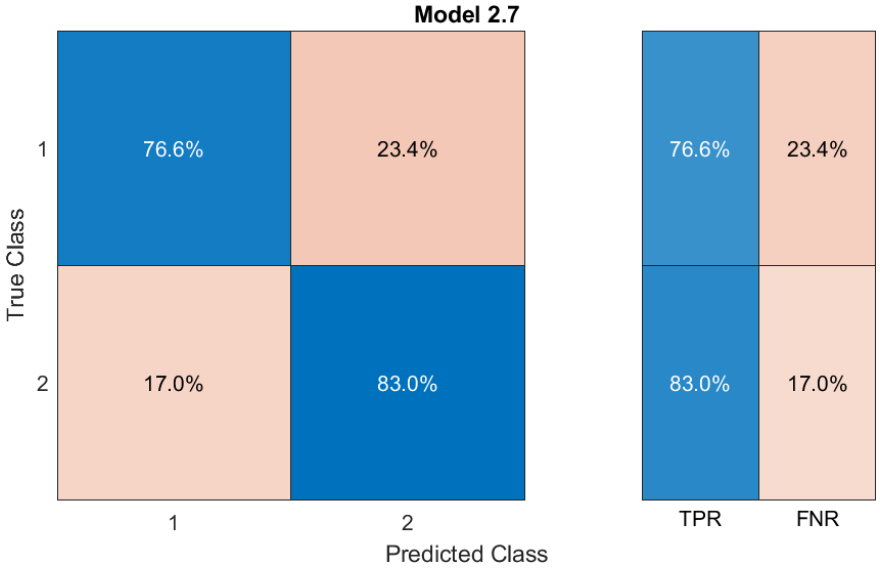

Figure 7.22: Gaussian Naive Bayes Confusion Matrix

Based on individual axis data

When the AUC values corresponding to only X axis tire accelerometer data were passed to the GNB classifier, the classification accuracy significantly increased to **93.8%** as seen in

Figure 7.23. Cases with worn tires have been correctly classified with 100% accuracy while new tires are correctly predicted with an accuracy of 87.5%

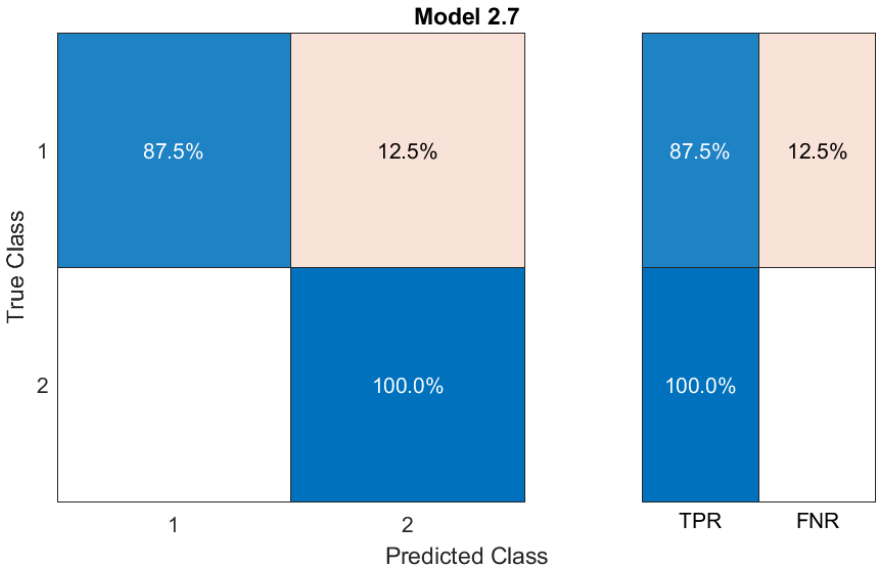

Figure 7.23: Gaussian Naive Bayes Confusion Matrix - X Axis

Table 7.5: Machine Learning Algorithm Performance Comparison

Model Type (X-Axis Acceleration Data)	**Classification Accuracy**
Gaussian Naive Bayes	93.8%
Support Vector Machine	90.6%
K-Nearest Neighbor	81.2%
Bagged Trees	81.8%
Wide Neural Network	87.5%

However, upon pass the Z-axis accelerometer data as the feature vector, the classification accuracy dropped down to **81.2%**. This still performed slightly better as compared to passing multi-axis data to the GNB classifier. The results of this can be seen in Figure 7.24.

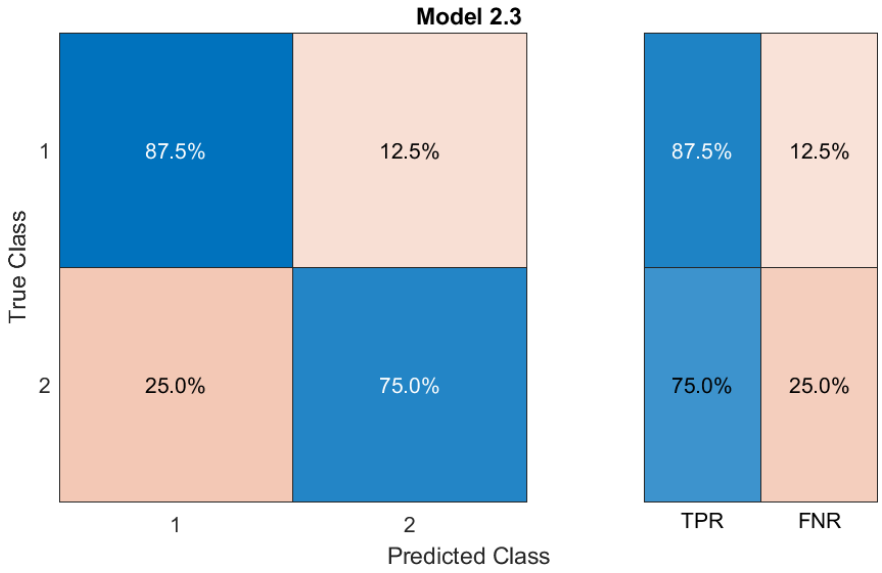

Figure 7.24: Gaussian Naive Bayes Confusion Matrix - Z Axis

7.6 Conclusion

In this section of tire wear detection, a framework has been developed to classify new and old worn-out tires based on the "Intelligent Tire" technology. Data has been collected for different vehicle speeds, tire inflation pressure, added normal load, and road surfaces for both tires. Various signal processing and Machine Learning based classification algorithms have been developed to classify between the two tires. It was found that the X-axis of the tire accelerometer was the most sensitive in differentiating between the two tires, which has been quantitatively evaluated by examining the TPR and FNR rates for the X-axis and Z-axis data, respectively. This can be attributed due to greater variations in the longitudinal stiffness of the tire as compared to the radial stiffness as the tire wears out.

Chapter 8

Tire Pneumatic Trail Estimation and Wear Correlation

8.1 Introduction

Tires play a critical role in determining the dynamics of the vehicle. The forces and moments generated at the contact patch interface prominently govern these vehicle dynamics properties. Along with this, the properties of the tire, such as tire construction, tire materials, and road surface characteristics, also determine the vehicle and tire dynamic responses. Amongst these parameters, the tire tread wear gradually affects the pneumatic trail, adversely affecting the aligning moment generated at the contact patch. The semi-empirical tire models do not account for these effects; hence, a framework is warranted to analyze the impact of tread wear on these vehicle dynamic properties.

In this chapter, the effect of tire tread wear on the pneumatic trail has been evaluated. The test setup described in Section 7.5 has been used to experimentally compute the pneumatic trail and has been briefly summarized below. Two tires, with identical mechanical and geometric properties, with different tread depths, have been instrumented with tri-axis accelerometers mounted on the tire's inner liner. These tires were sequentially mounted on an instrumented vehicle. Test data has been collected for various conditions, such as vehicle longitudinal velocity, tire inflation pressure, tire normal load, and the road surface. Algo-

rithms have been developed to estimate the tire pneumatic trail and see its variations with respect to the tread wear.

8.2 Tire Model based Pneumatic Trail Computation

The pneumatic trail can be computed analtically using the physical and semi-empirical tire models. The quantity in itself is a derived parameter which depends upon the lateral force and the aligning moment generated at the contact patch.

8.2.1 Pacejka Tire Model PT Computation

The Magic Formula (Pacejka Tire Model), is a semi-empirical tire model, which can be used to compute the forces and the moments generated at the contact patch. This is accomplished by calculating the intermediate parameters - curvature factor, shape factor, horizontal and vertical shifts, and peak factor. Each of these parameters is dependent upon a series of coefficients obtained via tire testing. Equations 8.1 to 8.9 show the computation of the lateral force. Similarly, Equation 8.10 is used to compute the aligning moment at the contact patch.

$$\alpha_y = \alpha + S_{hy} \tag{8.1}$$

$$C_y = a_0 \tag{8.2}$$

$$D_y = (a_1.(F_z^2) + a_2.F_z).(1 - (a_{15}.(\gamma^2))) \tag{8.3}$$

$$E_y = ((a_6.F_z) + a_7).(1 - ((a_{16}.\gamma) + a_{17}).sign(\alpha_y)) \tag{8.4}$$

$$K_y = a_3.\sin(2.\arctan(\frac{F_z}{a_4})).(1 - a_5.\gamma) \tag{8.5}$$

$$B_y = \frac{K_y}{C_y}.D_y \tag{8.6}$$

$$S_{hy} = a_8 F_z + a_9 + a_{10}\gamma \tag{8.7}$$

$$S_{vy} = a_{11} F_z + a_{12} + (a_{13} F_z + a_{14}) F_z \gamma \tag{8.8}$$

$$F_{y0} = D_y \sin(C_y \arctan(B_y \alpha_y - E_y(B_y \alpha_y - \arctan(B_y \alpha_y)))) + S_{vy} \tag{8.9}$$

$$M_{z0} = D_m \sin(C_m \arctan(B_m \alpha_m - E_m(B_m \alpha_m - \arctan(B_m \alpha_m)))) + S_{vm} \tag{8.10}$$

Table 8.1 lists the coefficients that have been used to calculate the magic formula parameters for a P225/60R16 tire dimensions.

Figure 8.1 and Figure 8.2 show the lateral force generated at the contact patch for the front and rear tires, respectively.

Similarly, Figure 8.3 and Figure 8.4 show the aligning moment for the front and rear tires, respectively.

Table 8.1: Tire Parameters (Front Tire)

Parameter	**Lateral Coefficients**	**Aligning Coefficients**
a_1	1.43	2.796
a_2	-16.77	1.856
a_3	-980.60	-0.067
a_4	-2480.61	2.888
a_5	-11.476	0.7861
a_6	0	-0.097
a_7	0.1901	0
a_8	0.8163	0.0162
a_9	-0.0160	0.1836
a_{10}	-0.107	0.404
a_{11}	0	0
a_{12}	-17.527	-0.0078
a_{13}	-71.954	-0.012
a_{14}	0	0
a_{15}	0	-0.197
a_{16}	0	1.931
a_{17}	0	2.80
a_{18}	0.2353	0.2365

The pneumatic trail has been calculated by dividing the aligning moment by the lateral force for every value of the slip angle as shown in Equation 8.11.

$$t_y = \frac{M_{z0}}{F_{y0}} \tag{8.11}$$

Figure 8.5 and Figure 8.6 show the pneumatic trail for the front and the rear tire as a function of the slip angle. From these figures, it can be seen that the pneumatic trail is the highest at 0 slip angle and decreases rapidly as the slip angle increases. It reaches an asymptotic state at higher slip angles.

The above process has been repeated for tires of different pitch circle diameters and radii to see tire geometry effect on the pneumatic trail. Figure 8.7 and Figure 8.8 detail the variation

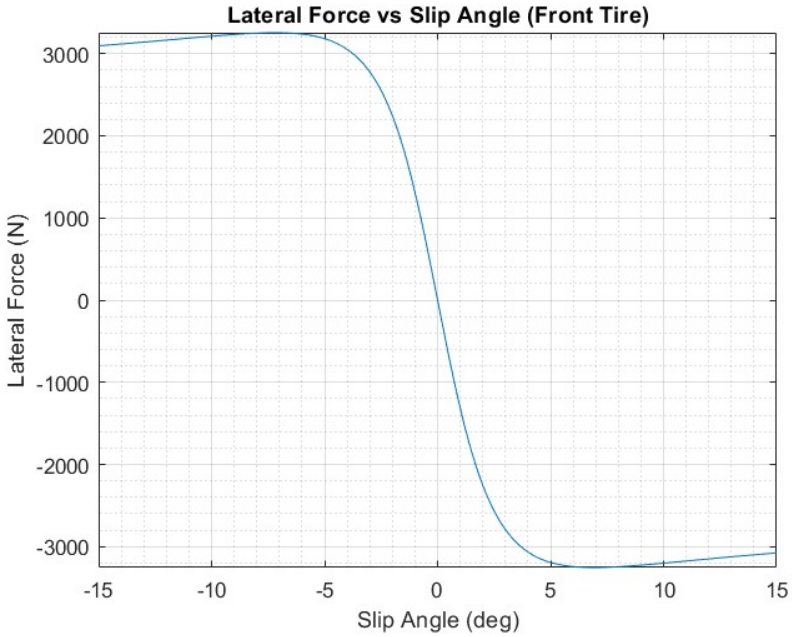

Figure 8.1: Lateral Force for Front Tire

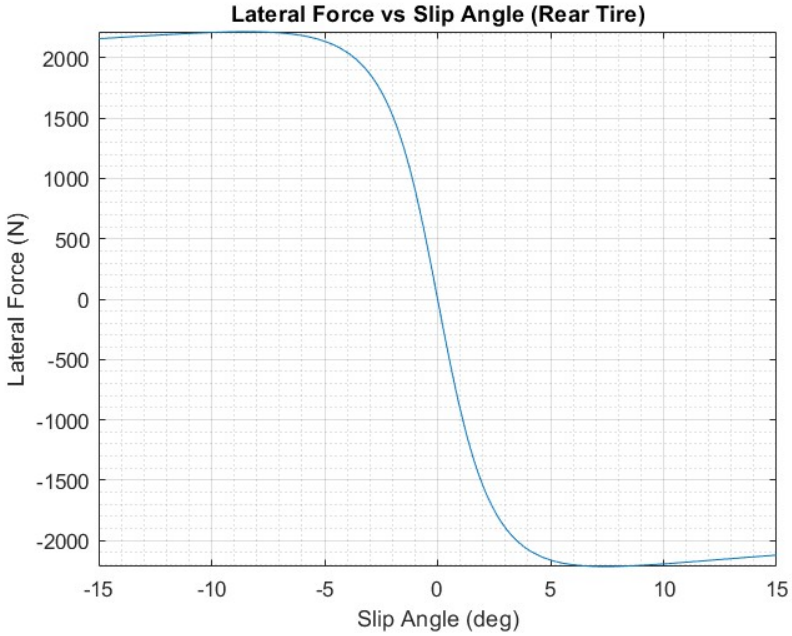

Figure 8.2: Lateral Force for Rear Tire

of pneumatic trail for different tire properties.

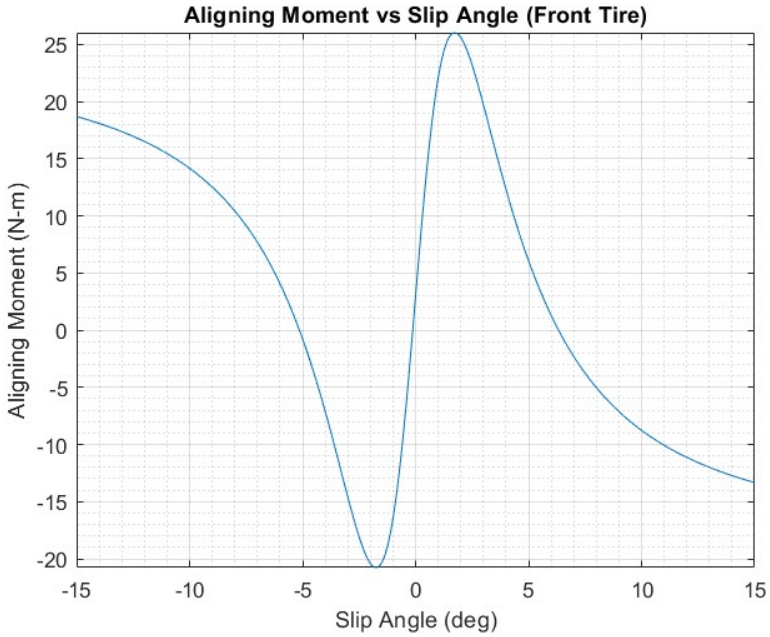

Figure 8.3: Aligning Moment for Front Tire

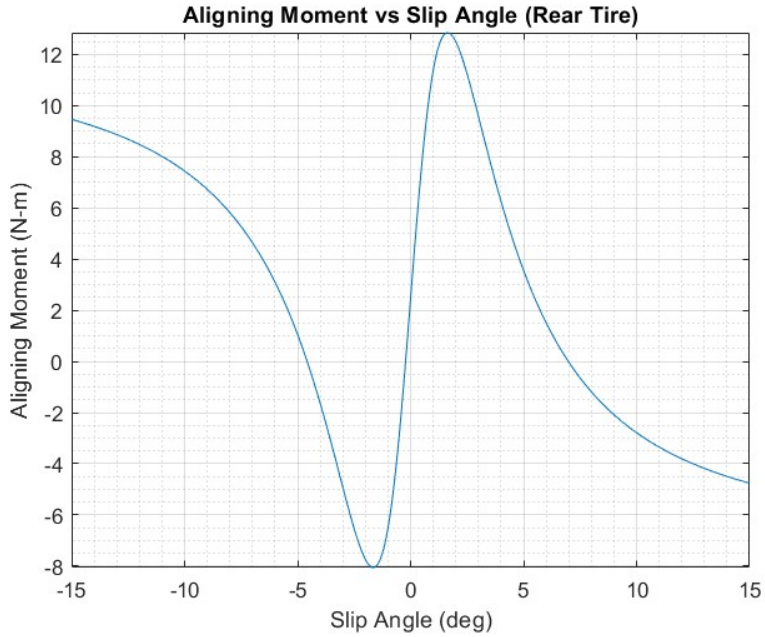

Figure 8.4: Aligning Moment for Rear Tire

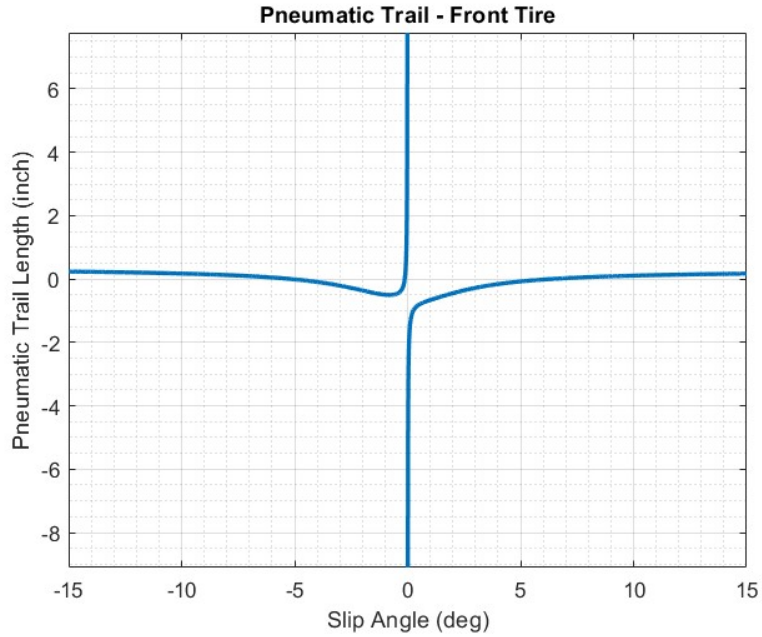

Figure 8.5: Pneumatic Trail - Front Tire

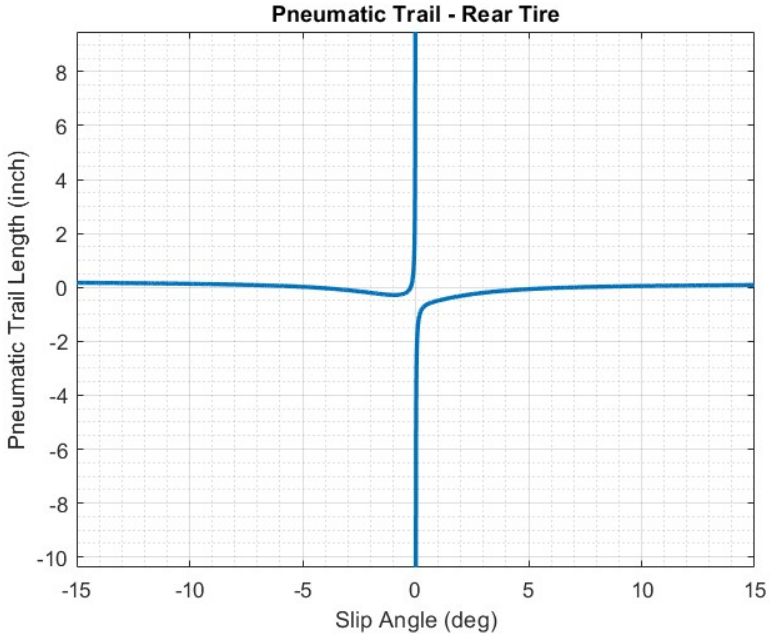

Figure 8.6: Pneumatic Trail - Rear Tire

8.2.2 Fiala Tire Model PT Computation

As discussed in Chapter 3, the Fiala tire model is a derivation of the brush model in which the lateral force at the tire contact patch is expressed as a function of three parameters -

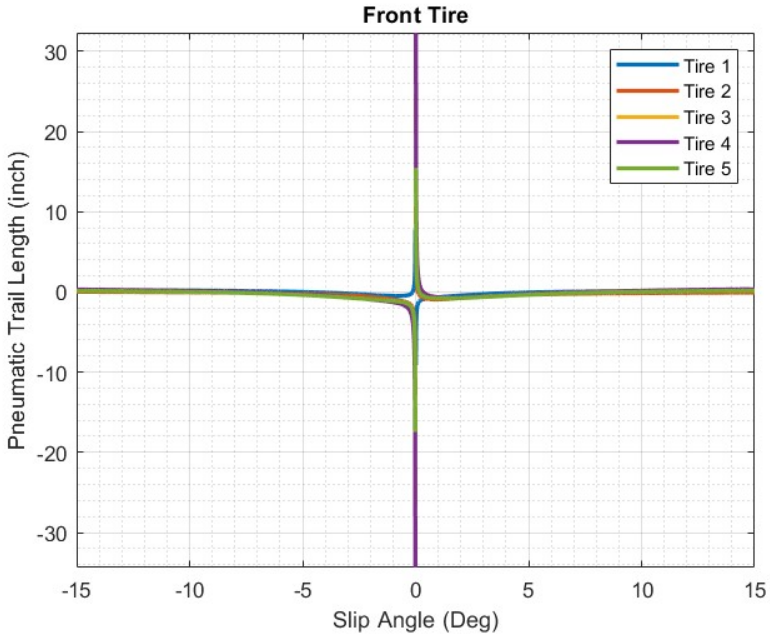

Figure 8.7: Pneumatic Trail - Multiple Front Tires

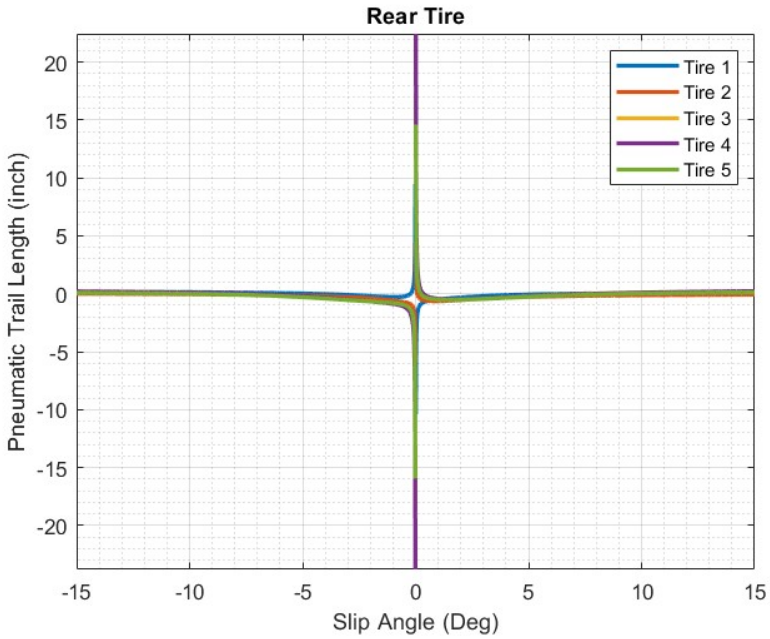

Figure 8.8: Pneumatic Trail - Multiple Rear Tires

cornering stiffness, slip angle and the tire-road friction coefficient. The tire pneumatic trail can also be computed analytically using the Fiala model as shown in Equation 8.12.

$$t_p = t_{p0} - \frac{t_{p0} C_\alpha |\tan\alpha|}{3\mu F_z} |\alpha| \leq \alpha_{slip} \qquad (8.12)$$

$$0 else$$

The cornering stiffness values obtained from the Pacejka Tire model simulation have been used to evaluate the pneumatic trail based on the Fiala model. A nominal friction coefficient of 1 has been chosen with a static contact patch length of 10 inches. The static pneumatic trail t_{p0} in Equation 8.12, is taken to be a quarter of the nominal contact patch length. Figure 8.9 shows the variation in pneumatic trail with the tire slip angle for 5 different tire specifications. The pneumatic trail drops sharply at 6.6 deg which is the saturated slip angle value at which the tire loses the lateral grip.

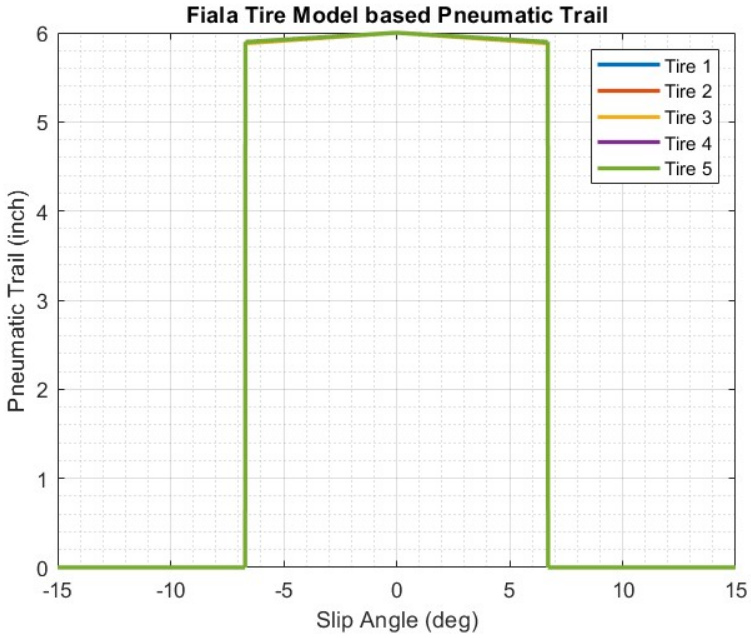

Figure 8.9: Tire Pneumatic Trail - Fiala Tire Model

Upon zooming in the lower slip angle region, as shown in Figure 8.10, a linear decrement is

observed from 2.5 inches to 2.46 inches for the 5 tire samples.

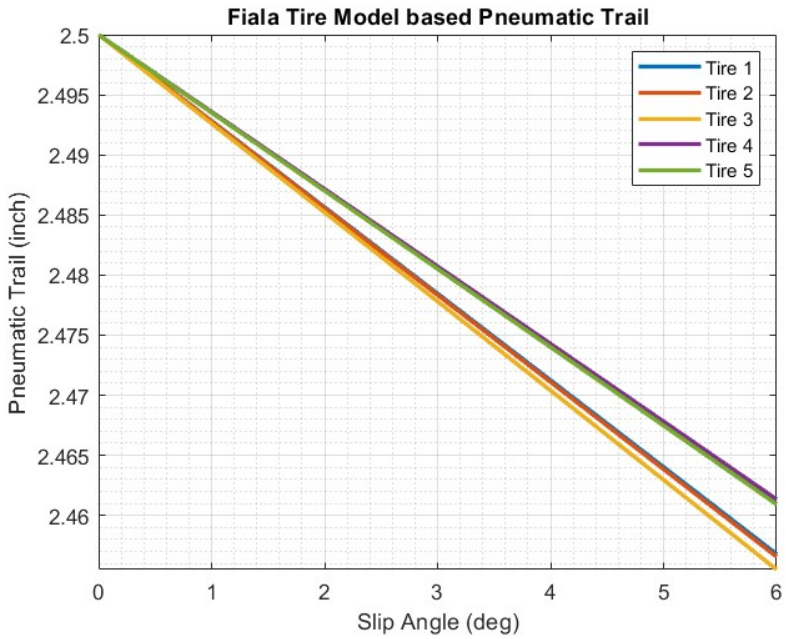

Figure 8.10: Tire Pneumatic Trail - Fiala Tire Model (Zoomed - Small Slip Angle)

8.3 Intelligent Tire based PT Estimation

The tire models which have been used to estimate the pneumatic trail do not take into account the effect of additional vehicle parameters such as the tire inflation pressure, vehicle longitudinal velocity, and vehicle suspension dynamics. These existing models also have an inherent limitation that the tire wear state cannot be incorporated in the analytical expressions for computing pneumatic trail.

Hence, the intelligent tire system has been used to derive the PT estimates. The data collected from Section 7.5 has been used to compute the pneumatic trail for the worn and the new tire respectively. A total of 47 test cases have been analyzed for different input parameter variations to get the estimation of the pneumatic trail.

Figure 8.11 shows the overall design of this framework and has been briefly described below:

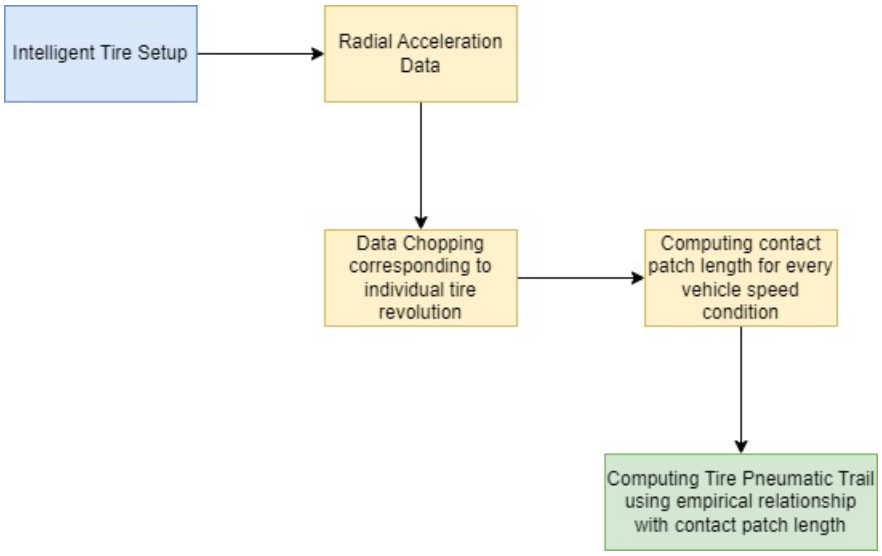

Figure 8.11: Tire Pneumatic Trail Estimation Framework

- Data Pre-processing: This step comprises of denoising the tire accelerometer data, removing the outliers, and converting them from electrical domain to mechanical units. Figure 8.12 and Figure 8.13 show the filtering of the raw radial acceleration data. A low pass filter has been used to remove the higher frequencies.

- Contact Patch Length Estimation: The next step consists of dividing the accelerometer data corresponding to individual tire revolutions using the wheel encoder data and computing the contact patch length for each tire revolution.

- Pneumatic Trail Estimation: The final step comprises of computing the pneumatic trail from the contact patch length using the empirical relation between the two.

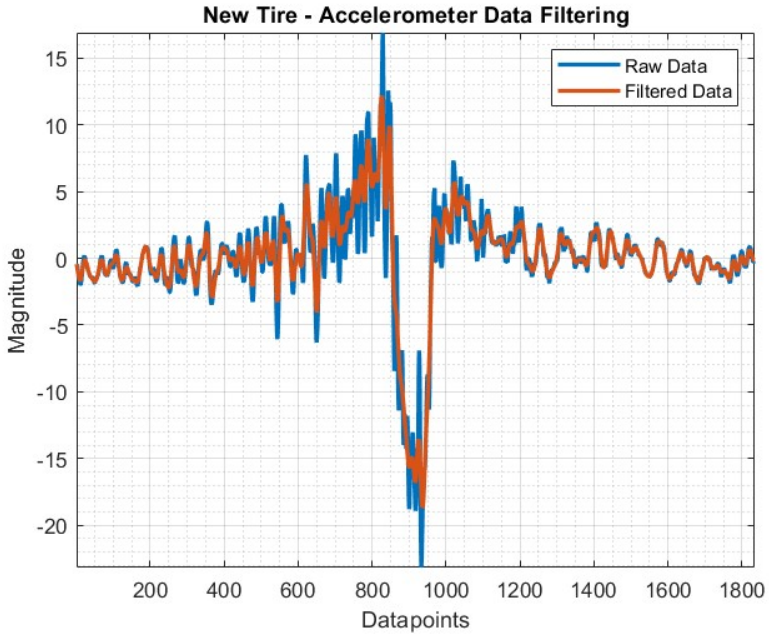

Figure 8.12: Radial Acceleration Data Filtering Process - New Tire

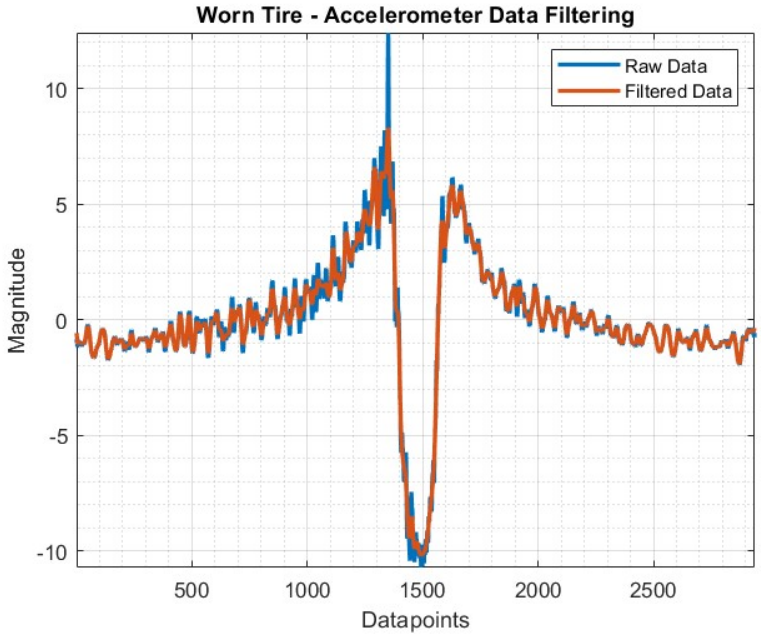

Figure 8.13: Radial Acceleration Data Filtering Process - Worn Tire

8.3.1 Contact Patch Length Estimation

With the individual tire revolutions extracted, the radial acceleration data (Z-axis data) has been further analyzed to compute the contact patch length. The peaks of the data have been extracted to isolate the leading edge and the trailing edge of the contact patch. This peak extraction process for the new and the worn tire can be seen in Figure 8.14 and Figure 8.15 respectively.

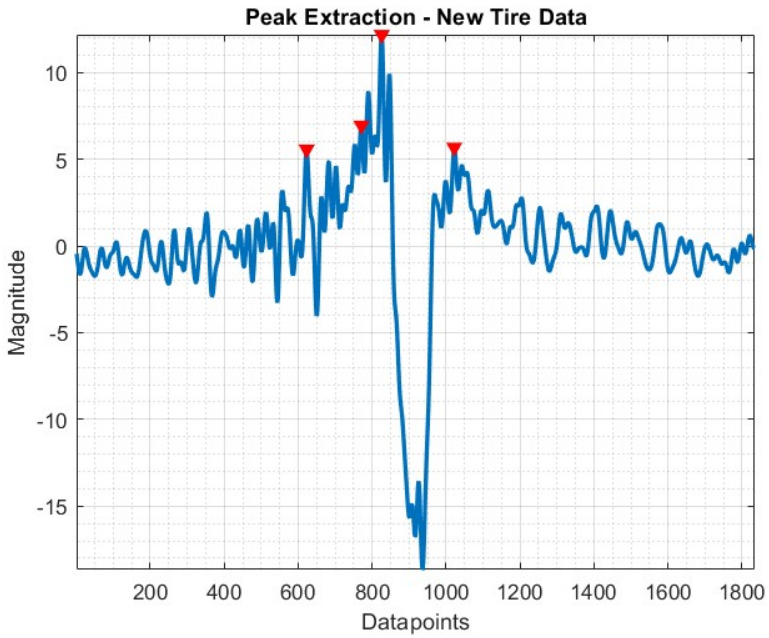

Figure 8.14: Peak Extraction Process for contact patch length estimation - New Tire

The number of data points between two successive peaks have been calculated and the contact patch length has been estimated by using Equation 8.13.

$$ContactPatchLength(C_p) = \frac{V * n}{f_s} \tag{8.13}$$

Where:

V = Vehicle Velocity $(\frac{m}{s})$

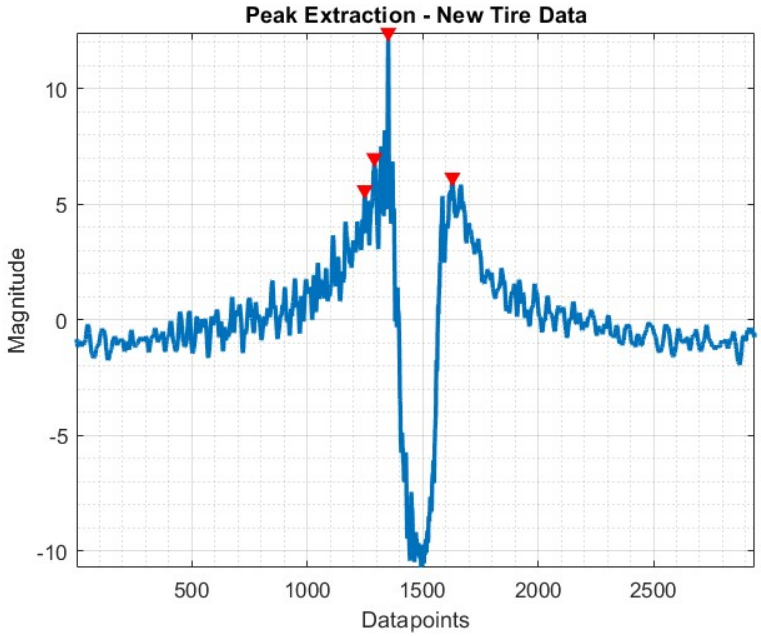

Figure 8.15: Peak Extraction Process for contact patch length estimation - Worn Tire

n = Number of data points between leading and trailing edge

f_s = Sampling Frequency (Hz)

Figure 8.16 shows the variation in the length of the contact patch with the number of revolutions for the new and worn tire. The test condition shown in this figure corresponds to 20MPH vehicle velocity, 2.5 bar tire pressure and 0kg added load.

8.3.2 Pneumatic Trail Computation

Once the contact path length is estimated, the next step comprises of getting the pneumatic trail estimates. A semi-empirical relationship has been used to derive these estimates as described in Equation 8.14.

$$t_{pe} = \frac{C_p}{4} \tag{8.14}$$

Figure 8.16: Contact Patch Length Estimation - Test Case 1

Figure 8.17 and Figure 8.18 show these PT estimates for the new and worn tire, respectively, for the different input parameter variations. Each of these curves represents a specific combination of the tire inflation pressure, normal load, vehicle velocity, and type of the road surface. From these figures, it can be seen that the average pneumatic trail values for the new tire are comparatively higher compared to those of the worn tire. For the new tire, initial peaks can be seen in the pneumatic trail estimates and this essentially represents the transient tire properties during which a steady state velocity has not been reached. The average pneumatic trail reduces to approximately 1-2in after 15-20 tire revolutions.

To obtain a qualitative and quantitative comparison between the pneumatic trails for the new and worn tires, eight test conditions that have the same input conditions for the two sets of tires have been analyzed. These conditions are summarized in Table 8.2.

Figure 8.19 and Figure 8.20 show the pneumatic trail estimates for the new and worn tire for concrete and asphalt surface respectively. The pneumatic trail for the new tire is higher

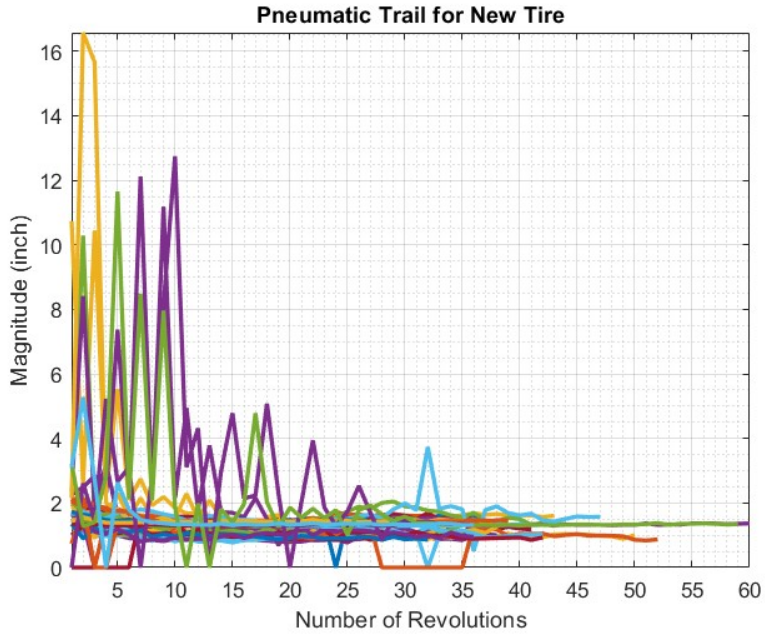

Figure 8.17: Pneumatic Trail for New Tire

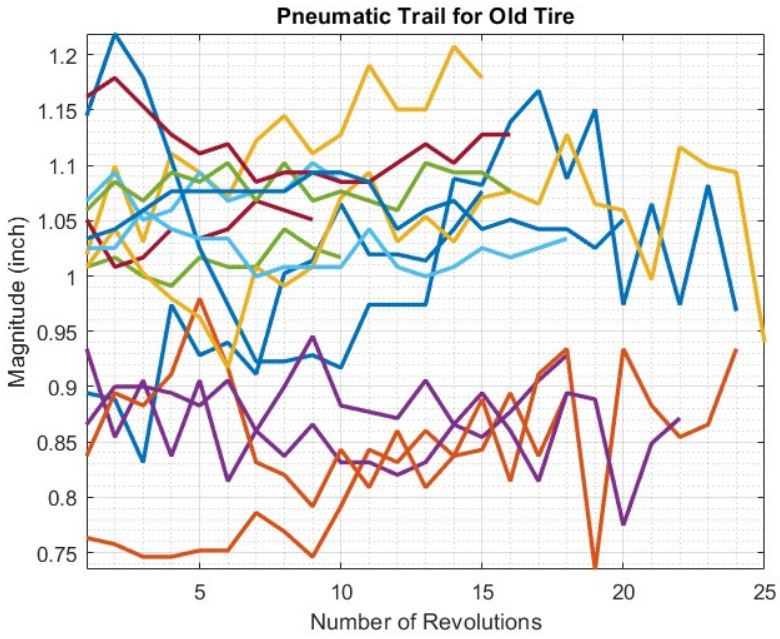

Figure 8.18: Pneumatic Trail for Worn Tire

than that of the worn tire for both surfaces and for all the analyzed test conditions within the range of 0.5-1.5in. This observation matches the conclusions which have been made in

Table 8.2: Condition Number - Pneumatic Trail Estimation

Condition Number	**Tire Inflation Pressure (bar)**	**Normal Load (lbs)**	**Vehicle Velocity (km/hr)**
1	1.7	0	20
2	2.5	0	20
3	1.7	100	20
4	2.5	100	20
5	1.7	0	40
6	2.5	0	40
7	1.7	100	40
8	2.5	100	40

the literature papers via Finite Element (FE) simulations. This phenomena can be traced to back to the following reasons:

- Tread pattern degradation: Tires with aggressive tread patterns or deep grooves rely on these features to maintain proper grip and traction on various surfaces. As the tread wears down, these patterns become less effective, which can result in a reduced or uneven contact patch area resulting in reduced nominal pneumatic trail
- Reduced tire flexibility: As the tire wears down, the rubber compound can become harder and less flexible, especially in older tires or those exposed to extreme temperatures. This reduced flexibility can affect the tire's ability to conform to the road surface, leading to a smaller contact patch area and diminished grip.
- Tire deformation: Excessive wear can cause the tire's structure to deform, affecting its overall shape and ability to maintain a consistent contact patch area which adversely affects the nominal pneumatic trail. This deformation can lead to reduced grip, handling, and performance.

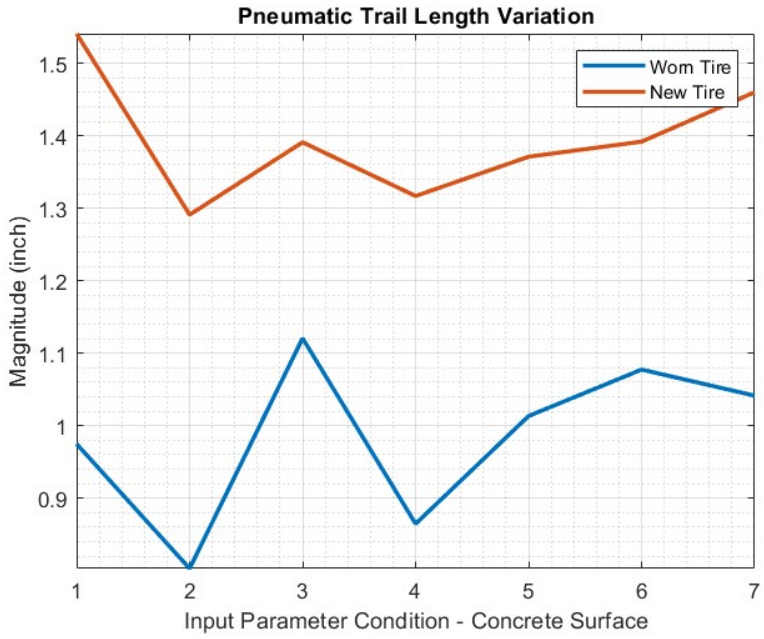

Figure 8.19: Pneumatic Trail Computation for Concrete Surface

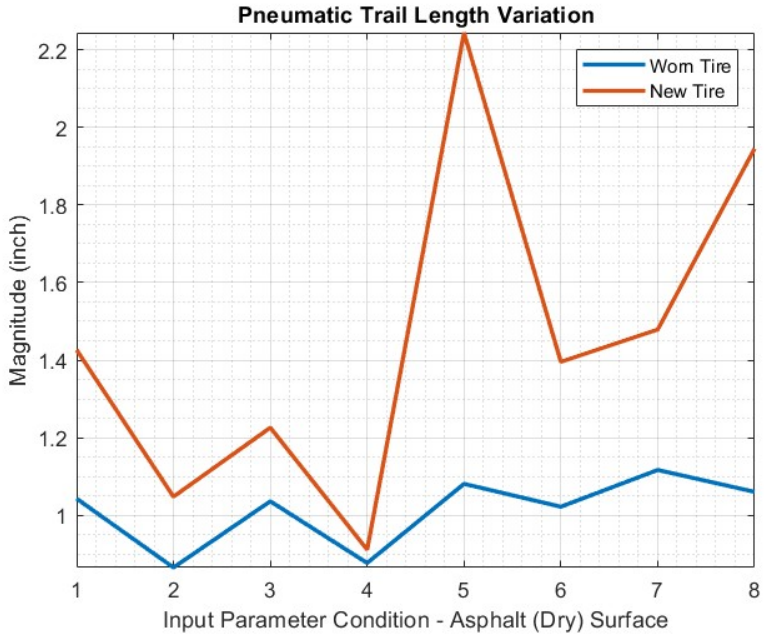

Figure 8.20: Pneumatic Trail Computation for Asphalt Surface

Chapter 9

Trajectory Tracking Control Algorithm

9.1 Introduction

With the development of the high fidelity vehicle and tire models, as discussed in Chapter 3, the final step comprises of testing the efficiency of these modes while tracking a given reference trajectory. In this chapter, Model predictive Control (MPC) has been used to perform vehicle trajectory tracking. The primary objective of this chapter is to compare the performance of the developed vehicle-tire plant model against the conventionally used bicycle model in trajectory tracking by implementing a preliminary MPC algorithm.

The primary steps involved in the implementation of a MPC algorithm have been listed below:

- System/Plant modeling: The 5DoF vehicle model and the modified Fiala tire model developed in Chapter 3 has been used as the plant model for MPC algorithm.

- Discretization: MPC operates on discrete-time models and hence the continous time plant model has to be converted into discrete time plant model. The zero order hold method has been used to discretize the model.

- Defining the cost function: The primary objective of the MPC controller is to minimize a cost function that includes two terms: Tracking error term - the difference between the reference trajectory and the vehicle's actual position and control effort term - the magnitude of the steering command

- Handling constraints: The next step comprises of defining the soft and hard constraints for the MPC framework. These comprise of the geometrical constraints of the vehicle, along with the permissible limits of the steering angle.

- Implementation of the MPC algorithm: Final step consists of solving a constrained optimization problem at each time step to find the control inputs that minimize the cost function.

Figure 9.1 shows the framework of the MPC algorithm for performing vehicle trajectory tracking.

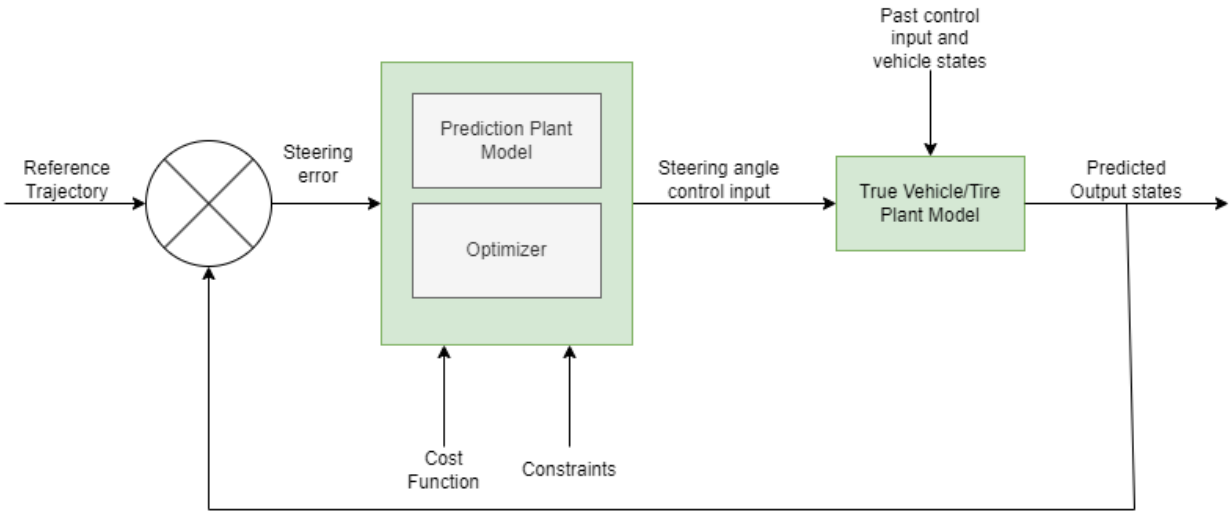

Figure 9.1: MPC Framework

9.2 MPC Framework

9.2.1 Baseline Model

A two degree of freedom (2DoF) bicycle model coupled with a linear tire model has been used as a baseline model to compare the trajectory tracking performance. This section describes the dynamics of the 2DoF model.

Based on the literature review conducted in Chapter 2, a linear tire model is the most commonly used model to evaluate the tire lateral and longitudinal forces. The linear tire model only works in the linear slip region of the tire wherein the lateral force generated by the tire is directly proportional to the tire slip angle. Equation 9.1 shows the lateral force generated by the linear tire model.

$$F_{ybase} = C_{\alpha} * \alpha \tag{9.1}$$

A 2DoF bicycle model has been used to simulate the lateral dynamics of a vehicle. These two degrees of freedom comprise the lateral velocity and the yaw rate at the vehicle CG. Figure 9.2 shows the bicycle model force distribution for a given slip angle.

The key assumptions of the bicycle model have been listed below:

- Rolling and pitching motion has been neglected.
- The effect of longitudinal load transfer has been neglected.
- Constant longitudinal velocity.
- The steering dynamics, along with the suspension compliance effects, have been ignored.

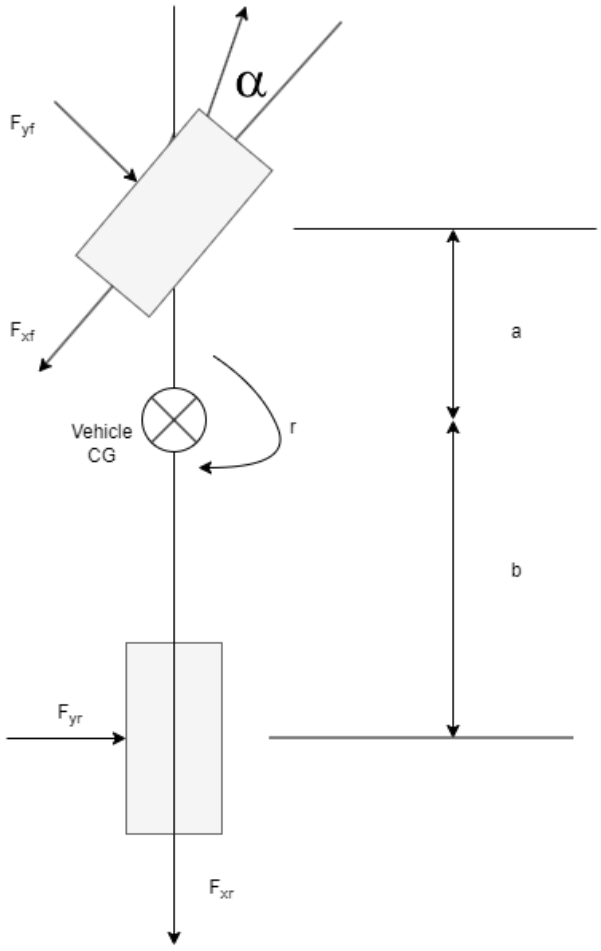

Figure 9.2: 2DoF Bicycle Model

- Small angle approximations taken throughout vehicle modeling.

The bicycle model equations can be derived by taking the summation of the lateral forces and the moment about the vehicle CG as shown in Equation 9.2 and Equation 9.3 respectively.

$$F_{yf} + F_{yr} = \frac{W(\dot{v} + ur}{g} \tag{9.2}$$

$$aF_{yf} - bF_{yr} = I\dot{r} \tag{9.3}$$

The above equations can be further expanded by representing the lateral force by the linear tire model. A state-space representation can be made for these dynamic equations as shown in Equation 9.4.

$$\begin{bmatrix} \dot{v} \\ \dot{r} \end{bmatrix} = \begin{bmatrix} \frac{-C_{\alpha f}+-C_{\alpha r}}{mu} & -u+\frac{-bC_{\alpha r}-aC_{\alpha f}}{mu} \\ \frac{-bC_{\alpha r}-aC_{\alpha f}}{I_z u} & \frac{b^2C_{\alpha r}-a^2C_{\alpha f}}{I_z u} \end{bmatrix} * \begin{bmatrix} v \\ r \end{bmatrix} + \begin{bmatrix} \frac{C_{\alpha f}}{m} \\ \frac{aC_{\alpha f}}{I_z} \end{bmatrix} * \delta_f \tag{9.4}$$

9.2.2 Developed 5-DoF Vehicle Model

As discussed in Chapter 3, a five degree of freedom model has also been developed which incorporates the effects of vehicle CG roll and tire lag dynamics along with the vehicle lateral velocity and yaw rate. The formulation of this model is summarized below in Equation 9.5 and Equation 9.2.2.

$$A_2 = \begin{pmatrix} 0 & \frac{U\,m\,\sigma_2}{\sigma_6} - \frac{I_{zz}\,U\,{h_{sr}}^2\,{m_s}^2}{\sigma_6} & -\frac{I_{zz}\,d_\phi\,h_{sr}\,m_s}{\sigma_6} & -\frac{I_{zz}\,h_{sr}\,m_s\,\sigma_3}{\sigma_6} & \frac{I_{xz}\,a\,h_{sr}\,m_s}{\sigma_6} - \frac{\sigma_2}{\sigma_6} & -\frac{\sigma_2}{\sigma_6} - \frac{I_{xz}\,b\,h_{sr}\,m_s}{\sigma_6} \\ 0 & 0 & \frac{I_{xz}\,d_\phi\,m}{\sigma_6} & \frac{I_{xz}\,m\,\sigma_3}{\sigma_6} & \sigma_5 - \frac{a\,\sigma_1}{\sigma_6} & \frac{b\,\sigma_1}{\sigma_6} + \sigma_5 \\ 0 & 0 & \frac{I_{zz}\,d_\phi\,m}{\sigma_6} & \frac{I_{zz}\,m\,\sigma_3}{\sigma_6} & \sigma_4 - \frac{I_{xz}\,a\,m}{\sigma_6} & \frac{I_{xz}\,b\,m}{\sigma_6} + \sigma_4 \\ 0 & 0 & 1 & 0 & 0 & 0 \\ \frac{c_{af}}{\sigma_f} & \frac{a\,c_{af}}{\sigma_f} & 0 & 0 & -\frac{U}{\sigma_f} & 0 \\ \frac{c_{ar}}{\sigma_r} & -\frac{b\,c_{ar}}{\sigma_r} & 0 & 0 & 0 & -\frac{U}{\sigma_r} \end{pmatrix} \tag{9.5}$$

$$B_2 = \begin{pmatrix} 0 & \frac{I_{zz}\, g\, {h_{sr}}^2\, {m_s}^2}{\sigma_1} - \frac{g\, m \left(-{I_{xz}}^2 + I_{zz}\, m_s\, {h_{sr}}^2 + I_{xx}\, I_{zz}\right)}{\sigma_1} \\ 0 & 0 \\ 0 & 0 \\ 0 & 0 \\ -\frac{U\, c_{af}}{\sigma_f} & 0 \\ 0 & 0 \end{pmatrix} \tag{9.6}$$

9.2.3 MPC Parameters

The MPC algorithm performance depends upon a set of design parameters which have been described below:

- Prediction Horizon (N_p): The prediction horizon is the future time window over which the MPC model predicts the future behavior of the system. A shorter horizon cannot capture future information whereas a longer prediction horizon results in the algorithm being computationally expensive. Hence, based upon an iterative approach and looking at the output yaw rate of the model, a prediction horizon of 12 intervals has been selected.

- Control Horizon(N_c): The control horizon denotes the number of future control moves that the MPC controller will compute at the current time step. A shorter control horizon results in a more reactive control policy, while a longer control horizon is computationally expensive. Hence, based upon literature review (as shown in Equa-

tion 9.7), and evaluation the steering angle effort, a control horizon of 4 intervals has been selected.

$$0.1N_p \leq N_c \leq 0.2N_p \tag{9.7}$$

- Constraints: Constraints in an MPC model define the feasible region for the states and control actions. A hard constraint has been given on the steering angle as shown in Equation 9.8.

$$-45^\circ \leq \delta \leq -45^\circ \tag{9.8}$$

- Sampling Time: The sample time is the discrete time step at which the MPC controller makes control decisions. A sample time of 0.1 sec has been selected.

- Weighing Factors: Weights in an MPC model are the coefficients that define the relative importance of different terms in the objective function. The weighing matrix consists of weights for the state error and the control effort.

Cost Function

A quadratic cost function has been used within the optimization module of the MPC controller. The primary objective of the MPC control then lies in finding a sequence of control inputs that minimizes the cost function, and at the same time falls within the set of the given hard constraint. Equation 9.9 shows the quadratic function used in this optimization problem.

$$minimize \quad J = \sum_{i=1}^{p} w_e e_{k+i}^2 + \sum_{i=0}^{p-1} w_\delta \delta_{k+i}^2 \tag{9.9}$$

where:

w_e and w_δ: Weights associated with the state error and the control input

δ: Control input (Steer angle)

e: State error (Lateral velocity)

9.3 Results

MATLAB/Simulink with the MPC control toolbox has been used to evaluate the performance of the MPC controller. The reference trajectory has been generated from CarSim corresponding to a Double Lane Change (DLC) maneuver. Both the state space models have been developed in such a way that the yaw rate is the desired output. Hence, corresponding to a DLC maneuver, the yaw rate data has been extracted.

Two MPC models have been developed for the bicycle model and the new 5DoF vehicle model. The MPC parameters, as discussed in the above section, have been kept constant for both the models and the performance of the MPC controller has been evaluated. Figure 9.3 shows the steering input control effort outputted by the MPC controller for the two models respectively. From this figure, it can be seen that the control effort required for the 5DoF model is much lesser than that for the 2DoF bicycle model to track the same reference trajectory.

Figure 9.4 shows the comparison of the yaw rate between the two models and the reference trajectory. The yaw rate outputttted by the new 5DoF model matches more closely to the desired reference trajectory than that given by the bicycle model, The primary reason for this

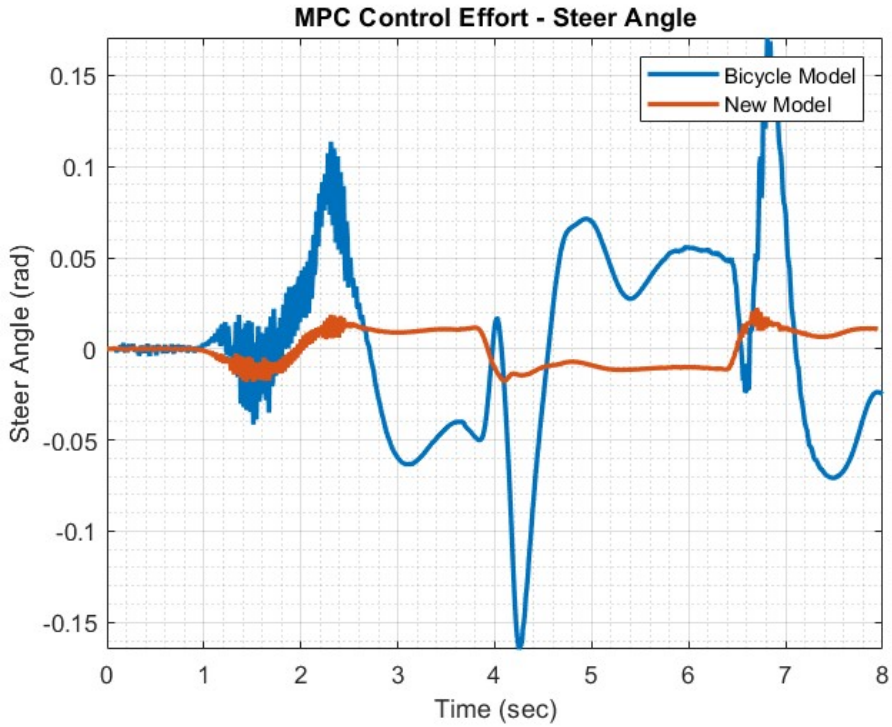

Figure 9.3: Steering Angle Control Effort

is that the new model incorporates the effects of tire lag dynamic which plays a crucial role in lateral force generation. This, in turn, affects the generation of the yaw rate, specifically during transient maneuvers like DLC.

Furthermore, the Root Mean Square Error (RMSE) has been used as the error metric to quantitatively compare between the bicycle model and the developed 5DoF model. RMSE values of the output yaw rate have been computed and Table 9.1 shows the comparison of these values.

Table 9.1: RMSE Metric for analyzing between reference trajectory and model outputs (yaw rate)

Model Type	**RMSE**
Bicycle Model	0.1133
5DoF Model	0.0239

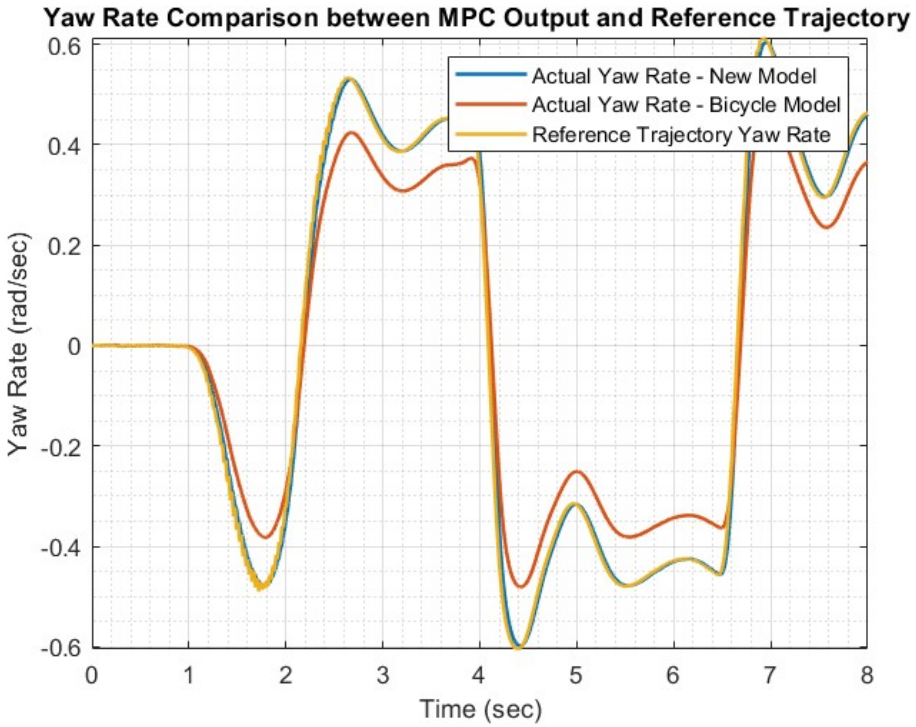

Figure 9.4: Comparison between the reference trajectory (yaw rate) and MPC output yaw rate for 2DoF Bicycle Model and the developed model

9.4 Conclusions

In this chapter, a Model Predictive Control (MPC) framework has been developed to track a reference trajectory. A conventional 2DoF bicycle model with a linear tire model has been used as the baseline model. The performance of the 5DoF vehicle model developed in Chapter 3 has been compared with this baseline model to track the reference trajectory. The primary observations are that the new model better tracks the reference yaw rate based-trajectory especially at the inflection points of the DLC maneuver.

Chapter 10

Conclusions and Future Steps

10.1 Summary of the Work

In this research, a framework has been developed to improve vehicle performance during cornering by developing a new integrated vehicle-tire model. The effects of relaxation length have been taken into account, which particularly affects the lateral force response. Along with this, mathematical modeling, control algorithm development, and real-time experimental validation have been achieved for a novel Double Damper suspension system to analyze the vehicle vertical dynamics. A tire health detection system has also been developed to classify between a new tire and a worn tire, and its effects on dynamic tire parameters (pneumatic trail) have been analyzed. Finally, the developed model has been tested for vehicle trajectory tracking algorithms. Figure 10.1 shows the complete high-level framework of the research.

In Chapter 1 and Chapter 2, a background survey has been conducted that focuses on the following research topics: Vehicle and Tire Modeling, Vehicle Vertical Dynamics, Intelligent Tires, Tire Health Monitoring, and Lateral Control Algorithms. These chapters dive deep into the existing work which has been done so far in this field and also provide the reasoning for undertaking the current research.

Chapter 3 introduces the tire and vehicle models which has been developed in this research. Two vehicle models have been discussed and developed for analyzing vertical dynamics and

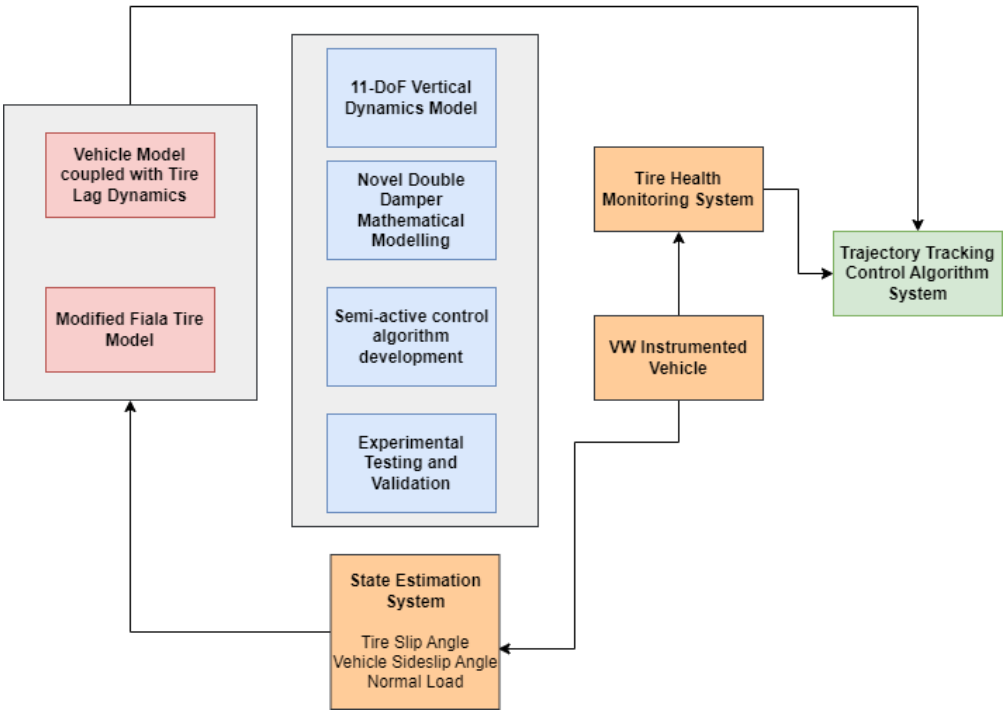

Figure 10.1: Complete Research Framework

vehicle lateral dynamics - 11 DoF Vehicle Vertical Dynamics Model and a 5-DoF Vehicle Lateral Model focusing on both transient and steady state phases of the vehicle dynamics. Simulations have been developed in MATLAB/Simulink to evaluate different vehicle states - lateral velocity, yaw rate, sprung and unsprung mass displacements, and Vehicle CG Pitch and Roll rates. Two tire models, STI and Fiala, have been implemented and parameterized. The primary objective of these models was to understand the physics behind each of these models and how the lateral force generation is modeled. The Fiala tire model was chosen for further modeling and control applications because of its relatively minimal time complexity and simpler parameterization.

In addition to understanding the lateral dynamics of the vehicle at limit handling, the vertical dynamics of the vehicle has also been analyzed in Chapter 4. This chapter can be broadly divided into three sections - Double Damper Modeling, Experimental Testing and Validation,

and SGML based semi-active control algorithm development. Different control algorithms have been developed to compare the performance of the semi-active double damper with that of the conventional single passive and semi-active dampers. The results of this chapter give two key insights: Double Groundhook Control Double Damper gave the highest road holding and ride comfort characteristics as compared to the other damper configurations. A good correlation has been observed between the modeling/simulation results with that of the experimental testing results. SGML based control has also been implemented and the results of this showed that such a control has the least values of ride comfort indicating a smoother ride.

Chapter 5 discusses the instrumentation of the vehicle - exteroceptive and proprioceptive sensors, data acquisition systems, and the corresponding processing stations mounted within the vehicle for data collection. Along with this, the development of the scaled UGV platform has also been discussed in this chapter. The primary purpose of the scaled UGV is to test out the control - trajectory tracking algorithms. The final section of the chapter comprises the experimental set-up developed for analyzing the health monitoring of a structure, which has been extended to tire defect analysis and classification.

In Chapter 6, data processing algorithms have been developed to analyze the data from proprioceptive and exteroceptive sensors. This mainly comprises cleaning and denoising the data. Along with this, state estimation algorithms have been developed to estimate the vehicle side slip angle, tire slip angle, and normal vehicle load.

In Chapter 7, data processing and ML algorithms have been developed for the following:

- Classifying between different bearing defects and classifying between different intensities of a particular defect. Algorithms have been developed for this in the time and time-frequency domain.

- These algorithms have been extended to classify between a new tire and a worn out tire based on the data collected on the instrumented vehicle. The results for this section showed that the algorithms developed are able to classify between the two tires with a classification accuracy of **98%**.

In Chapter 8, the effect of tire wear on pneumatic trail has been investigated. Pacejka and Fiala tire models have been used to analytically compute the pneumatic trail and its relationship with the tire slip angle has been evaluated. Intelligent tire data has been used to experimentally evaluate the effect of tire wear on the pneumatic trail and the results show that the worn tire has a lower magnitude of pneumatic trail compared to the new tire at all values of input normal load. tire inflation pressure, vehicle velocity, and road surface.

In Chapter 9, existing Model Predictive Control (MPC) framework has been implemented on the developed high fidelity vehicle-tire model to see how well the new model tracks a given trajectory. The performance of this model has been compared with the conventional 2DoF bicycle model and it was found that the new model is able to track the reference trajectory with minimum tracking error.

10.2 Conclusions

The crux of this research lies in the development of a high fidelity vehicle-tire model to simulate the lateral and vertical dynamics of the vehicle during limit handling maneuvers. The following lists the primary conclusions of this research:

- In this research, a 5DoF vehicle model has been developed that incorporates the effect of relaxation length on the generation of lateral forces. This model performed better than existing vehicle models in capturing the transient lateral force variation at higher

slip angles.

- The modified version of Fiala tire model has been used which encaptures the lateral-longitudinal force coupling near the limits of the handling diagram.

- An 11DoF vehicle model has been developed to simulate the vertical suspension dynamics by incorporating the motion of the sprung and unsprung mass of the vehicle. Along with this, a mathematical model of a novel double damper system has been developed by modeling the pressure and fluid discharge interactions. Different classical suspension control strategies (Skyhook and Groundhook control) and SGML framework have been implemented and its performance has been compared with conventional dampers. The developed model with SGML control performed better than the existing models in terms of the ride comfort and road holding comfort costs and minimizing suspension deflection.

- Experimental testing has been conducted on an instrumented vehicle comprising of different proprioceptive (intelligent tire, IMU, VBOX) and exteroceptive sensors (GPS) to collect data for slalom and straight line maneuvers. A test matrix has been developed to collect data for different tire inflation pressure, road surface type, normal load, and vehicle velocity.

- Machine learning-based algorithms have been developed to classify between a new tire and a worn tire for a given set of input operating conditions. The effect of tire wear on tire dynamics has been characterized by estimated the pneumatic trail of the tire using the "intelligent tire" data. It was concluded that the pneumatic trail of the new tire is 1.5-2 inches greater than that of the worn tire.

- The performance of the developed vehicle model in tracking a reference trajectory has been evaluated by implementing a standard Model Predictive Control (MPC). This

model has been compared with a conventional bicycle-linear tire. The results show that the developed model performs better in path tracking in terms of minimum yaw rate variations between reference values and actual model output values.

10.3 Future Work

The future work comprises of the following:

- **Development of a Finite State Machine (FSM) framework for integrating tire-road friction coefficient in the tire model:** The Fiala tire model described in Chapter 3, requires three parameters for lateral force computation - slip angle (α), vehicle normal load (F_z) and the tire-road friction coefficient (μ). Among the three, estimators have been developed in this research to quantify the first two parameters. To evaluate the effect of the coefficient of friction on the lateral force and, subsequently, the trajectory tracking algorithms, a framework for friction estimation is required. This estimation can be further integrated with an FSM to develop different operating regimes of the vehicle-tire plant model depending on the type of road surface.

- **Development of a Remaining Useful Life (RUL) Framework for estimating the life of the tire:** In this research, a framework has been developed to perform a binary classification between the new tire and the worn tire and see its effect on the pneumatic trail. One of the next steps in this involves developing a regression model to continuously monitor tire tread wear. For this, an accelerated wear testing needs to be carried out which can be completed by using the in-house rolling resistance machine as shown in Figure 10.2. The tire tread depth will be recorded at regular tire rotation intervals and tire accelerometer data will be collected before and after the

wear measurement. Based upon a preliminary study, an average run time 80 hours would be required for tire to go from 8mm tread wear to 2.5mm tread wear under accelerated testing conditions (75% rated normal load and 30psi tire pressure). The time-domain accelerometer data will be converted to spectral domain using wavelets to better understand the spectral energy content at different frequencies as the tire wears. Such an approach has been summarized in Figure 10.3. Furthermore, a Long Short Term Memory (LSTM) network can be used to predict the tire RUL based upon historic data.

- **Development of a framework to integrate the effect of tire tread wear to physics based tire models:** In this research, a relationship has been experimentally obtained between tire tread depth and the pneumatic trail for a given set of input operating conditions (tire inflation pressure, vehicle velocity, road surface type, and vehicle normal load). The key finding of this was that the pneumatic trail of a worn tire is 1-2 inches less than that of the new tire. The next step in this comprises of evaluating the effect of tread depth on the tire aligning moment and integrating it with existing physics based tire models. This can be accomplished with the introduction of a correction factor within the aligning moment equation, which depends on the tread depth of the tire.

- **Validation of the slip angle and normal load estimation algorithms against real vehicle data:** The estimation algorithms developed for the vehicle normal load, vehicle side slip angle and tire slip angle have been validated against CarSim data. However, the real world vehicle data - CG lateral and longitudinal acceleration, yaw rate, and longitudinal velocities may not match the CarSim data for a given maneuver due to environment noise and sudden disturbances. Therefore, one of the future goals of this research is to instrument the vehicle with a tire slip angle and a force hub sensor

to obtain real-time contact patch forces, moments and slip angle data.

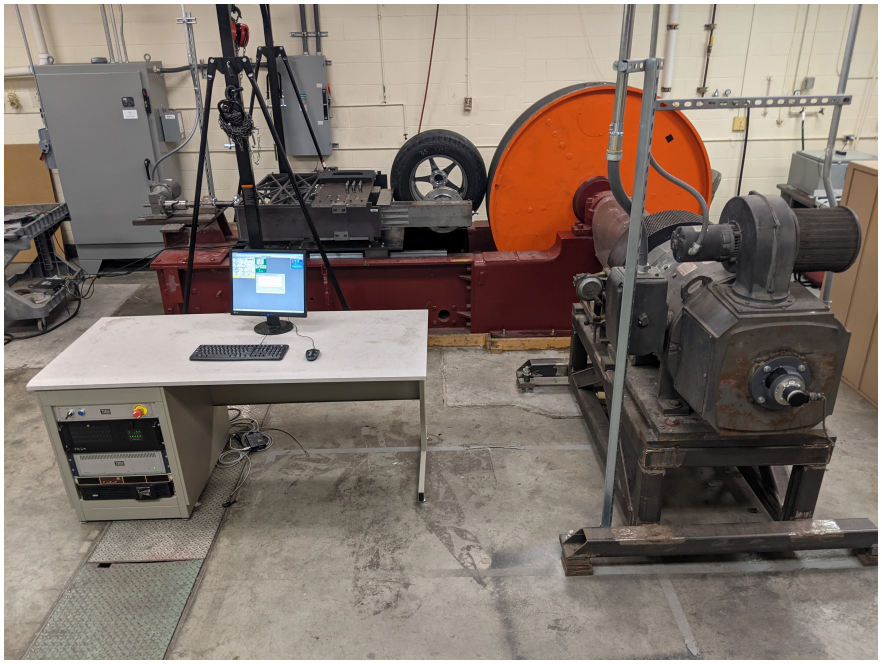

Figure 10.2: Rolling Resistance Machine Setup

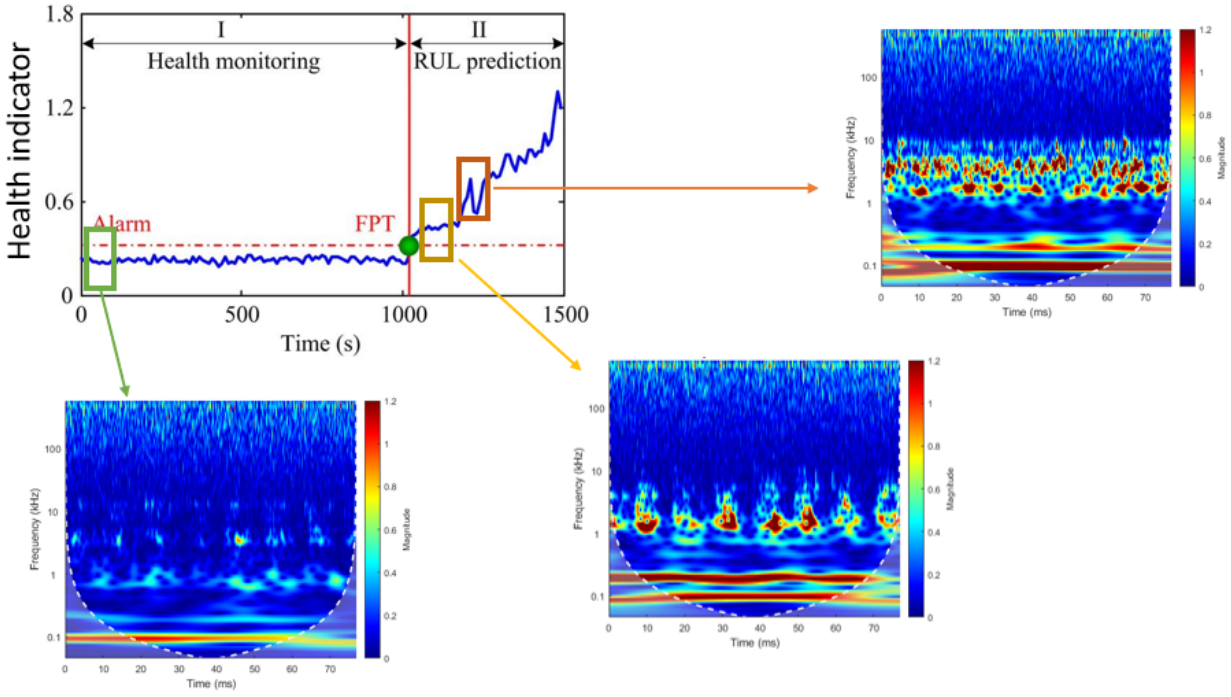

Figure 10.3: Proposed Tire RUL Estimation Framework

Bibliography

[1] Vehicle control - lecture slides, saied taheri, 2022. [Online; accessed 18-February-2023].

[2] Hans Pacejka. *Tire and vehicle dynamics*. Elsevier, 2005.

[3] Yi Xiong and Xiaoguang Yang. A review on in-tire sensor systems for tire-road interaction studies. *Sensor review*, 38(2):231–238, 2018.

[4] Guang Tong and Xiaoxiong Jin. Study on the simulation of radial tire wear characteristics. *WSEAS Transactions on Systems*, 11(8):419–429, 2012.

[5] Alexander Kravchenko, Olga Sakno, and Alexander Lukichov. Research of dynamics of tire wear of trucks and prognostication of their service life. *Transport problems*, 7 (4):85–94, 2012.

[6] First automobile vehicle, 2022. URL https://group.mercedes-benz.com/company/tradition/company-history/1885-1886.html#:~:text=On%20January%2029%2C%201886%2C%20Carl,1. [Online; accessed 18-February-2023].

[7] How many cars are there in the world in 2023?, 2023. URL https://hedgescompany.com/blog/2021/06/how-many-cars-are-there-in-the-world/. [Online; accessed 18-February-2023].

[8] Ryosuke Okuda, Yuki Kajiwara, and Kazuaki Terashima. A survey of technical trend of adas and autonomous driving. In *Technical Papers of 2014 International Symposium on VLSI Design, Automation and Test*, pages 1–4, 2014. doi: 10.1109/VLSI-DAT.2014.6834940.

[9] T Akasaka. Structural mechanics of radial tires. *Rubber Chemistry and Technology*, 54(3):461–492, 1981.

[10] F Frank and W Hofferberth. Mechanics of the pneumatic tire. *Rubber Chemistry and Technology*, 40(1):271–322, 1967.

[11] Yaswanth Siramdasu. *Discrete Tire Model Application for Vehicle Dynamics Performance Enhancement*. PhD thesis, Virginia Tech, 2015.

[12] Wolfgang Hirschberg, Georg Rill, and Heinz Weinfurter. Tire model tmeasy. *Vehicle System Dynamics*, 45(S1):101–119, 2007.

[13] Georg Rill. Tmeasy—a handling tire model based on a three-dimensional slip approach. In *Proceedings of the XXIII international symposium on dynamic of vehicles on roads and on tracks (IAVSD 2013), Quingdao, China*, pages 19–23, 2013.

[14] RT Uil. Tyre models for steady-state vehicle handling analysis. *Eindhoven University of Technology, Eindhoven*, 2007.

[15] Vladimir V Vantsevich and Jeremy P Gray. Relaxation length review and time constant analysis for agile tire dynamics control. In *International design engineering technical conferences and computers and information in engineering conference*, volume 57106, page V003T01A038. American Society of Mechanical Engineers, 2015.

[16] Georg Rill. First order tire dynamics. In *Proceedings of the III European Conference on Computational Mechanics Solids, Structures and Coupled Problems in Engineering, Lisbon, Portugal*, volume 58, 2006.

[17] Jeff S Loeb, Dennis A Guenther, Hung-Hsu Fred Chen, and John R Ellis. Lateral stiffness, cornering stiffness and relaxation length of the pneumatic tire. *SAE transactions*, pages 147–155, 1990.

[18] Jacob Svendenius and Björn Wittenmark. Brush tire model with increased flexibility. In *2003 European Control Conference (ECC)*, pages 1863–1868. IEEE, 2003.

[19] Joško Deur, Jahan Asgari, and Davor Hrovat. A 3d brush-type dynamic tire friction model. *Vehicle System Dynamics*, 42(3):133–173, 2004.

[20] Hiroki Yamashita, Paramsothy Jayakumar, and Hiroyuki Sugiyama. Physics-based flexible tire model integrated with lugre tire friction for transient braking and cornering analysis. *Journal of computational and nonlinear dynamics*, 11(3), 2016.

[21] Panagiotis Tsiotras, Efstathios Velenis, and Michel Sorine. A lugre tire friction model with exact aggregate dynamics. *Vehicle System Dynamics*, 42(3):195–210, 2004.

[22] Rajesh Rajamani. *Vehicle dynamics and control*. Springer Science & Business Media, 2011.

[23] RS Sharp and SA Hassan. The relative performance capabilities of passive, active and semi-active car suspension systems. *Proceedings of the Institution of Mechanical Engineers, Part D: Transport Engineering*, 200(3):219–228, 1986.

[24] William F Milliken. Active suspension. Technical report, SAE Technical Paper, 1988.

[25] XD Xue, KWE Cheng, Z Zhang, JK Lin, DH Wang, YJ Bao, MK Wong, and N Cheung. Study of art of automotive active suspensions. In *2011 4th International Conference on Power Electronics Systems and Applications*, pages 1–7. IEEE, 2011.

[26] Dean Karnopp, Michael J Crosby, and RA Harwood. Vibration control using semi-active force generators. *Journal of engineering for industry*, 96(2):619–626, 1974.

[27] Riccardo Caponetto, Olga Diamante, Giovanna Fargione, Antonino Risitano, and Domenico Tringali. A soft computing approach to fuzzy sky-hook control of semi-

active suspension. *IEEE Transactions on control systems technology*, 11(6):786–798, 2003.

[28] FH Besinger, D Cebon, and D Jo Cole. Force control of a semi-active damper. *Vehicle System Dynamics*, 24(9):695–723, 1995.

[29] KJ Kitching, DJ Cole, and D Cebon. Performance of a semi-active damper for heavy vehicles. *Journal of dynamic systems, measurement, and control*, 122(3):498–506, 2000.

[30] GZ Yao, FF Yap, G Chen, WHo Li, and SH Yeo. Mr damper and its application for semi-active control of vehicle suspension system. *Mechatronics*, 12(7):963–973, 2002.

[31] SB Choi, HK Lee, and EG Chang. Field test results of a semi-active er suspension system associated with skyhook controller. *Mechatronics*, 11(3):345–353, 2001.

[32] William Churchill Taliaferro Burke. *Large force range mechanically adjustable dampers for heavy vehicle applications*. PhD thesis, Virginia Tech, 2010.

[33] Chun Yu Lai and Wei-Hsin Liao. Vibration control of a suspension system via a magnetorheological fluid damper. *Modal Analysis*, 8(4):527–547, 2002.

[34] Ubaidillah Sabino, Khisbullah Hudha, and Hishamuddin Jamaluddin. Simulation and experimental evaluation on a skyhook policy-based fuzzy logic control for semi-active suspension system. *Int. J. Structural Engineering2*, (3):243–272, 2011.

[35] Youxiang Peng, Miao Yu, Xiumei Du, Xiaoying Xu, and Jie Fu. An experimental study of vehicle suspension semi-active control with skyhook controller and magneto-rheological dampers. In *2017 29th Chinese Control And Decision Conference (CCDC)*, pages 7427–7429. IEEE, 2017.

[36] Xin Tang, Haiping Du, Shuaishuai Sun, Donghong Ning, Zhiwei Xing, and Weihua Li. Takagi–sugeno fuzzy control for semi-active vehicle suspension with a magnetorheological damper and experimental validation. *IEEE/ASME transactions on mechatronics*, 22(1):291–300, 2016.

[37] Piotr Krauze, Jerzy Kasprzyk, Andrzej Kozyra, and Jaroslaw Rzepecki. Experimental analysis of vibration control algorithms applied for an off-road vehicle with magnetorheological dampers. *Journal of Low Frequency Noise, Vibration and Active Control*, 37(3):619–639, 2018.

[38] Mingde Gong and Hao Chen. Variable damping control strategy of a semi-active suspension based on the actuator motion state. *Journal of Low Frequency Noise, Vibration and Active Control*, page 1461348418825416, 2019.

[39] WG Ata and AM Salem. Semi-active control of tracked vehicle suspension incorporating magnetorheological dampers. *Vehicle System Dynamics*, 55(5):626–647, 2017.

[40] Fernando D Goncalves and Mehdi Ahmadian. A hybrid control policy for semi-active vehicle suspensions. *Shock and Vibration*, 10(1):59–69, 2003.

[41] Michael Valášek, M Novak, Z Šika, and O Vaculin. Extended ground-hook-new concept of semi-active control of truck's suspension. *Vehicle system dynamics*, 27(5-6):289–303, 1997.

[42] Sergio M Savaresi, Enrico Silani, and Sergio Bittanti. Acceleration-driven-damper (add): An optimal control algorithm for comfort-oriented semiactive suspensions. *Journal of dynamic systems, measurement, and control*, 127(2):218–229, 2005.

[43] Yilun Liu and Lei Zuo. Mixed skyhook and power-driven-damper: a new low-jerk semi-

active suspension control based on power flow analysis. *Journal of Dynamic Systems, Measurement, and Control*, 138(8):081009, 2016.

[44] Anish Gorantiwar, Rajvardhan Nalawade, Arash Nouri, and Saied Taheri. Experimental analysis of a novel double damper system with semi-active control. *Electronics*, 9 (9):1518, 2020.

[45] Mauro Da Lio, Daniele Bortoluzzi, and Gastone Pietro Rosati Papini. Modelling longitudinal vehicle dynamics with neural networks. *Vehicle System Dynamics*, 58 (11):1675–1693, 2020.

[46] Nathan A Spielberg, Matthew Brown, Nitin R Kapania, John C Kegelman, and J Christian Gerdes. Neural network vehicle models for high-performance automated driving. *Science Robotics*, 4(28), 2019.

[47] Hojong Lee and Saied Taheri. Intelligent tires? a review of tire characterization literature. *IEEE Intelligent Transportation Systems Magazine*, 9(2):114–135, 2017.

[48] Shichun Yang, Yuyi Chen, Runwu Shi, Rui Wang, Yaoguang Cao, and Jiayi Lu. A survey of intelligent tires for tire-road interaction recognition toward autonomous vehicles. *IEEE Transactions on Intelligent Vehicles*, 7(3):520–532, 2022.

[49] Kanwar Bharat Singh. *Development of an intelligent tire based tire-vehicle state estimator for application to global chassis control*. PhD thesis, Virginia Tech, 2012.

[50] O Yilmazoglu, M Brandt, J Sigmund, E Genc, and HL Hartnagel. Integrated inas/gasb 3d magnetic field sensors for "the intelligent tire". *Sensors and Actuators A: Physical*, 94(1-2):59–63, 2001.

[51] Alfred Pohl, Reinhard Steindl, and Leonhard Reindl. The" intelligent tire" utilizing

passive saw sensors measurement of tire friction. *IEEE transactions on instrumentation and measurement*, 48(6):1041–1046, 1999.

[52] Xiangwen Zhang, Zhixue Wang, Leifu Gai, Yunfeng Ai, and Feiyue Wang. Design considerations on intelligent tires utilizing wireless passive surface acoustic wave sensors. In *Fifth World Congress on Intelligent Control and Automation (IEEE Cat. No. 04EX788)*, volume 4, pages 3696–3700. IEEE, 2004.

[53] Ari J Tuononen. Optical position detection to measure tyre carcass deflections. *Vehicle System Dynamics*, 46(6):471–481, 2008.

[54] Sergio M Savaresi, Mara Tanelli, Peter Langthaler, and Luigi Del Re. New regressors for the direct identification of tire deformation in road vehicles via "in-tire" accelerometers. *IEEE Transactions on Control Systems Technology*, 16(4):769–780, 2008.

[55] Madhavendra Saxena, Olvin Oliver Bannett, and Vivek Sharma. Bearing fault evaluation for structural health monitoring, fault detection, failure prevention and prognosis. *Procedia Engineering*, 144:208–214, 2016.

[56] MS Safizadeh and SK Latifi. Using multi-sensor data fusion for vibration fault diagnosis of rolling element bearings by accelerometer and load cell. *Information fusion*, 18:1–8, 2014.

[57] Hwa Yaw Tam, T Lee, SL Ho, T Haber, T Graver, and A Méndez. Utilization of fiber optic bragg grating sensing systems for health monitoring in railway applications. *Structural Health Monitoring*, 2:1824–1831, 2007.

[58] F Bonnardot, RB Randall, J Antoni, and F Guillet. Enhanced unsupervised noise cancellation using angular resampling for planetary bearing fault diagnosis. *International journal of acoustics and vibration*, 9(2):51–60, 2004.

[59] Aditya Sharma, M Amarnath, and PK Kankar. Feature extraction and fault severity classification in ball bearings. *Journal of Vibration and Control*, 22(1):176–192, 2016.

[60] Jing Wang, Lingli Cui, Huaqing Wang, and Peng Chen. Improved complexity based on time-frequency analysis in bearing quantitative diagnosis. *Advances in Mechanical Engineering*, 5:258506, 2013.

[61] Omid Rahmani Seryasat, F Honarvar, A Rahmani, et al. Multi-fault diagnosis of ball bearing based on features extracted from time-domain and multi-class support vector machine (msvm). In *2010 IEEE International Conference on Systems, Man and Cybernetics*, pages 4300–4303. IEEE, 2010.

[62] LB Jack and AK Nandi. Genetic algorithms for feature selection in machine condition monitoring with vibration signals. *IEE Proceedings-Vision, Image and Signal Processing*, 147(3):205–212, 2000.

[63] Fengtao Wang, Jian Sun, Dawen Yan, Shenghua Zhang, Liming Cui, and Yong Xu. A feature extraction method for fault classification of rolling bearing based on pca. In *Journal of Physics: Conference Series*, volume 628, page 012079. IOP Publishing, 2015.

[64] Nagi Gebraeel, Mark Lawley, Richard Liu, and Vijay Parmeshwaran. Residual life predictions from vibration-based degradation signals: a neural network approach. *IEEE Transactions on industrial electronics*, 51(3):694–700, 2004.

[65] Abdenour Soualhi, Hubert Razik, Guy Clerc, and Dinh Dong Doan. Prognosis of bearing failures using hidden markov models and the adaptive neuro-fuzzy inference system. *IEEE Transactions on Industrial Electronics*, 61(6):2864–2874, 2013.

[66] Chandrabhanu Malla, Ankur Rai, Vaishali Kaul, and Isham Panigrahi. Rolling element bearing fault detection based on the complex morlet wavelet transform and performance evaluation using artificial neural network and support vector machine. *Noise & Vibration Worldwide*, 50(9-11):313–327, 2019.

[67] J Rafiee, PW Tse, A Harifi, and MH Sadeghi. A novel technique for selecting mother wavelet function using an intelli gent fault diagnosis system. *Expert Systems with Applications*, 36(3):4862–4875, 2009.

[68] Kun Feng, Zhinong Jiang, Wei He, and Qiang Qin. Rolling element bearing fault detection based on optimal antisymmetric real laplace wavelet. *Measurement*, 44(9): 1582–1591, 2011.

[69] Lajos Tóth and Tibor Tóth. On finding better wavelet basis for bearing fault detection. *Acta Polytechnica Hungarica*, 10(3):17–35, 2013.

[70] Olivier Janssens, Viktor Slavkovikj, Bram Vervisch, Kurt Stockman, Mia Loccufier, Steven Verstockt, Rik Van de Walle, and Sofie Van Hoecke. Convolutional neural network based fault detection for rotating machinery. *Journal of Sound and Vibration*, 377:331–345, 2016.

[71] Xiaojie Guo, Liang Chen, and Changqing Shen. Hierarchical adaptive deep convolution neural network and its application to bearing fault diagnosis. *Measurement*, 93:490–502, 2016.

[72] Min Xia, Teng Li, Lin Xu, Lizhi Liu, and Clarence W De Silva. Fault diagnosis for rotating machinery using multiple sensors and convolutional neural networks. *IEEE/ASME transactions on mechatronics*, 23(1):101–110, 2017.

[73] Long Wen, Xinyu Li, Liang Gao, and Yuyan Zhang. A new convolutional neural

network-based data-driven fault diagnosis method. *IEEE Transactions on Industrial Electronics*, 65(7):5990–5998, 2017.

[74] Levent Eren, Turker Ince, and Serkan Kiranyaz. A generic intelligent bearing fault diagnosis system using compact adaptive 1d cnn classifier. *Journal of Signal Processing Systems*, 91:179–189, 2019.

[75] Dalila Benmahdi, Lanto Rasolofondraibe, Xavier Chiementin, Sébastien Murer, and Ahmed Felkaoui. Rt-optics: real-time classification based on optics method to monitor bearings faults. *Journal of Intelligent Manufacturing*, 30:2157–2170, 2019.

[76] Yong Li, Shuguang Zuo, Lei Lei, Xianwu Yang, and Xudong Wu. Analysis of impact factors of tire wear. *Journal of Vibration and Control*, 18(6):833–840, 2012.

[77] DF Tandy, RJ Pascarella, JW Neal, JM Baldwin, and JD Rehkopf. Effect of tire wear on tire force and moment characteristics. *Tire Science and Technology*, 38(1):47–79, 2010.

[78] Edward A Saibel and Chenglung Tsai. Tire wear by ablation. *Wear*, 24(2):161–176, 1973.

[79] A Schallamach and DM Turner. The wear of slipping wheels. *Wear*, 3(1):1–25, 1960.

[80] Wade K Shepherd. *Diagonal wear predicted by a simple wear model*. ASTM International, 1986.

[81] JeFoa Archard. Contact and rubbing of flat surfaces. *Journal of applied physics*, 24 (8):981–988, 1953.

[82] VH Nguyen, D Zheng, F Schmerwitz, and P Wriggers. An advanced abrasion model for tire wear. *Wear*, 396:75–85, 2018.

[83] F Farroni, A Sakhnevych, and F Timpone. Physical modelling of tire wear for the analysis of the influence of thermal and frictional effects on vehicle performance. *Proceedings of the Institution of Mechanical Engineers, Part L: Journal of Materials: Design and Applications*, 231(1-2):151–161, 2017.

[84] Pooya Behroozinia, Saied Taheri, and Reza Mirzaeifar. Tire health monitoring using the intelligent tire concept. *Structural Health Monitoring*, 18(2):390–400, 2019.

[85] U Eichhorn and J Roth. Prediction and monitoring of tyre/road friction. In *XXIV FISITA CONGRESS, 7-11 JUNE 1992, LONDON. HELD AT THE AUTOMOTIVE TECHNOLOGY SERVICING SOCIETY. TECHNICAL PAPERS. SAFETY, THE VEHICLE AND THE ROAD. VOLUME 2 (IMECHE NO C389/321 AND FISITA NO 925226)*, 1992.

[86] Breuer Bert, Barz Michael, Bill Karlheinz, Gruber Steffen, Semsch Martin, Strothjohann Thomas, and Xie Chungyang. The mechatronic vehicle corner of darmstadt university of technology-interaction and cooperation of a sensor tire, new low-energy disc brake and smart wheel suspension. *International journal of automotive technology*, 3(2):63–70, 2002.

[87] Noor Hafizah Amer, Hairi Zamzuri, Khisbullah Hudha, and Zulkiffli Abdul Kadir. Modelling and control strategies in path tracking control for autonomous ground vehicles: a review of state of the art and challenges. *Journal of intelligent & robotic systems*, 86:225–254, 2017.

[88] K David Young, Vadim I Utkin, and Umit Ozguner. A control engineer's guide to sliding mode control. *IEEE transactions on control systems technology*, 7(3):328–342, 1999.

[89] Sebastian Thrun, Mike Montemerlo, Hendrik Dahlkamp, David Stavens, Andrei Aron, James Diebel, Philip Fong, John Gale, Morgan Halpenny, Gabriel Hoffmann, et al. Stanley: The robot that won the darpa grand challenge. *Journal of field Robotics*, 23 (9):661–692, 2006.

[90] Louis L Scharf, William P Harthill, and Paul H Moose. A comparison of expected flight times for intercept and pure pursuit missiles. *IEEE Transactions on Aerospace and Electronic Systems*, (4):672–673, 1969.

[91] Jarrod M Snider et al. Automatic steering methods for autonomous automobile path tracking. *Robotics Institute, Pittsburgh, PA, Tech. Rep. CMU-RITR-09-08*, 2009.

[92] H Philip Whitaker, Joseph Yamron, and Allen Kezer. *Design of model-reference adaptive control systems for aircraft*. Massachusetts Institute of Technology, Instrumentation Laboratory, 1958.

[93] John P Alsterda, Matthew Brown, and J Christian Gerdes. Contingency model predictive control for automated vehicles. In *2019 American Control Conference (ACC)*, pages 717–722. IEEE, 2019.

[94] John P Alsterda and J Christian Gerdes. Contingency model predictive control for linear time-varying systems. *arXiv preprint arXiv:2102.12045*, 2021.

[95] Nathan A Spielberg, Matthew Brown, and J Christian Gerdes. Neural network model predictive motion control applied to automated driving with unknown friction. *IEEE Transactions on Control Systems Technology*, 30(5):1934–1945, 2021.

[96] Jingwei Cao, Chuanxue Song, Silun Peng, Shixin Song, Xu Zhang, and Feng Xiao. Trajectory tracking control algorithm for autonomous vehicle considering cornering characteristics. *IEEE Access*, 8:59470–59484, 2020.

[97] Junyu Cai, Haobin Jiang, Long Chen, Jun Liu, Yingfeng Cai, and Junyan Wang. Implementation and development of a trajectory tracking control system for intelligent vehicle. *Journal of Intelligent & Robotic Systems*, 94:251–264, 2019.

[98] Bo-Chiuan Chen, Cheng-Ting Tsai, and Kangwon Lee. Path-following steering controller of automated lane change system with adaptive preview time. In *2015 IEEE International Conference on Systems, Man, and Cybernetics*, pages 2522–2526. IEEE, 2015.

[99] Erkan Kayacan, Herman Ramon, and Wouter Saeys. Robust trajectory tracking error model-based predictive control for unmanned ground vehicles. *IEEE/ASME Transactions on Mechatronics*, 21(2):806–814, 2015.

[100] Sara Mata, Asier Zubizarreta, and Charles Pinto. Robust tube-based model predictive control for lateral path tracking. *IEEE Transactions on Intelligent Vehicles*, 4(4): 569–577, 2019.

[101] Jie Ji, Amir Khajepour, Wael William Melek, and Yanjun Huang. Path planning and tracking for vehicle collision avoidance based on model predictive control with multiconstraints. *IEEE Transactions on Vehicular Technology*, 66(2):952–964, 2016.

[102] Qing Liu, Dario Solis, and Weidong Pan. Analysis of the sti tire model. Technical report, SAE Technical Paper, 2002.

[103] R Wade Allen, TJ Rosenthal, and HT Szostak. Analytical modeling of driver response in crash avoidance maneuvering. volume 2: Technical background. final report. Technical report, 1988.

[104] E Fiala. Seitenkrafte am rollenden luftreifen. *Z. VDI*, 96:11, 1954.

[105] Koenraad Reybrouck. A non linear parametric model of an automotive shock absorber. *SAE transactions*, pages 1170–1177, 1994.

[106] Michael S Talbott and John Starkey. An experimentally validated physical model of a high-performance mono-tube damper. *SAE Transactions*, pages 2422–2439, 2002.

[107] Alireza Farjoud, Mehdi Ahmadian, Michael Craft, and William Burke. Nonlinear modeling and experimental characterization of hydraulic dampers: effects of shim stack and orifice parameters on damper performance. *Nonlinear Dynamics*, 67(2):1437–1456, 2012.

[108] Sheetanshu Rajeev Tyagi. Development of a semi active suspension system for lightweight automobiles, 2016.

[109] E Valtolina, SM Savaresi, Sergio Bittanti, A Visconti, and Alberto Longhi. A coordinate approach for the control of road vehicles. In *2001 European Control Conference (ECC)*, pages 629–634. IEEE, 2001.

[110] Daniel Fischer and Rolf Isermann. Mechatronic semi-active and active vehicle suspensions. *Control engineering practice*, 12(11):1353–1367, 2004.

[111] Guoqing Geng, Yi Yu, Liqin Sun, and Hao Li. Research on ride comfort and driving safety under hybrid damping extension control for suspension systems. *Applied Sciences*, 10(4):1442, 2020.

[112] Nishant Bhanot. Artificial neural networks based modeling and analysis of semi-active damper system, 2017.

[113] N Janse van Rensburg, JL Steyn, and PS Els. Time delay in a semi-active damper: modelling the bypass valve. *Journal of Terramechanics*, 39(1):35–45, 2002.

[114] Spelta Sename Dugard Savaresi, Poussot Vassal. *Semi-Active Suspension Control Design for Vehicles*. Elsevier, 2010.

[115] Donkey car rc car setup, 2022. URL https://docs.donkeycar.com/. [Online; accessed 18-January-2023].

[116] Dasol Jeong, Seungtaek Kim, Jonghyup Lee, Seibum B Choi, Mintae Kim, and Hojong Lee. Estimation of tire load and vehicle parameters using intelligent tires combined with vehicle dynamics. *IEEE Transactions on Instrumentation and Measurement*, 70: 1–12, 2020.

[117] Anish Gorantiwar, Arash Nouri, Behzad Moslehi, Feraidoon Zahiri, Rajvardhan Nalawade, Vahid Sotoudeh, William Price, and Saied Taheri. Fiber optic sensor system for defect classification using novel physics based modelling and data driven approach. In *2022 IEEE Aerospace Conference (AERO)*, pages 1–12. IEEE, 2022.

[118] Anish Gorantiwar, Saied Taheri, Feraidoon Zahiri, and Bijan Moslehi. Real time bearing defect classification using time domain analysis and deep learning algorithms. Technical report, SAE Technical Paper, 2023.